

**68th Annual  
Technical Conference  
& Exposition  
Grand Rapids, Michigan**



# THANK YOU!

The Investment Casting Institute would like to thank  
the following companies who have sponsored the  
**ICI 68th Annual Technical Conference & Exposition**



**AUTOWAX INC.**  
AUTOMATED WAXROOM TECHNOLOGIES GROUP



Automated Wax Technologies, Booth 502  
Paramelt, Booth 309



The Investment Casting Institute would like to thank the following companies who have cast the awards for the **68th Technical Conference & Exposition.**



# ARISTO-CAST

## INVESTMENT CASTING

*Artcast inc*

**Aristo-Cast, Inc.**

7400 Research Drive  
Almont, MI 48003  
USA  
ph. (810) 798-2900  
fax (810) 798-2730  
[www.aristo-cast.com](http://www.aristo-cast.com)

**Artcast, Inc.**

14 Armstrong Avenue  
Georgetown, Ontario L7G 4R9  
CANADA  
ph. (905) 877-5455  
fax (905) 877-0205  
[www.artcast.com](http://www.artcast.com)



*Thank You*

The Investment Casting Institute would like to thank the following Member companies for their educational support and promotion of the industry. One scholarship is being offered in honor of the following individual:

Larry Blum of Aristo-Cast



The Investment Casting Institute would like to thank the following individuals who ran for the 2021 Board of Directors election.

Thank you to the following candidates listed below who have been nominated to fill the Regular Member openings on the Board of Directors:

Brad DeSplinter  
**TPM, Inc.**

Bob Johnson  
**Shellcast, Inc.**

Erich Knoespel  
**Artcast, Inc.**

Al Torok  
**Yamaha Marine Precision Propellers, Inc.**

Thank you to the following candidates listed below who have been nominated to fill the Affiliate Member opening on the Board of Directors:

Imed Bourega  
**Shell-O-Matic, Inc.**

Mike Hascher  
**Eagle Engineered Solutions, Inc.**

John Woodward  
**KnewMethod LLC**



The Investment Casting Institute would like to thank the following advertisers who have placed ads in INCAST Magazine and INCAST News.

*Thank*  
**YOU**

FOR YOUR SUPPORT

Air & Energy Systems  
AJAX Magnathermic  
Arnil C.F.S., Inc.  
ASK Chemicals Hi-Tech LLC  
Industrial Ceramic Products  
B&L Information Services, Inc.  
Barron Industries Inc.  
Bimac Precision Castings  
Bescast  
Buntrock Industries, Inc.  
Consarc Corporation  
Core Tech  
Covestro Additive Manufacturing  
Davis Alloys Manufacturing  
Eagle Engineered Solutions, Inc.

Elemental Metals  
Ergoflex  
Fireline Inc.  
Goff, Inc.  
Guardian Software Systems  
Imerys  
Inductotherm Corporation  
Industrial Ceramic Products  
Isostatic Toll Services  
Kyanite Mining Inc.  
LECO Corporation  
MAGMA Foundry Technologies  
Metsch Refractories Inc  
MK Technology  
MPI, Inc.

MORSA  
O'Fallon Casting  
Pacific Kiln & Insulations Co., Inc.  
Pillar Industries  
Pressure Technology, Inc.  
Ransom & Randolph  
REMET® Corporation  
SECO Warwick (Retch)  
SELEE™ Advanced Ceramics®  
Shell-O-Matic Inc  
Stoner Inc  
Synchro ERP Ltd  
VA Technology Ltd.  
Voxeljet of America  
Vulcan Engineering Co.



# **INVESTMENT CASTING INSTITUTE**

## **MISSION STATEMENT**

The Investment Casting Institute will market the investment casting industry and support its members by facilitating professional, academic, educational, and technical interests, and will provide a forum for advancement in technology and product quality for customers and manufacturers, while promoting free trade, fair competition, and adhering to U.S. laws and regulations regarding commerce and industrial trade.

## GENERAL RULES OF ANTITRUST COMPLIANCE

The following rules are applicable to all ICI activities and must be observed in all situations and under all circumstances, without exception or qualification other than as noted below:

1. Neither the ICI nor any committee, conference or activity of the ICI shall be used for the purpose of bringing about, or attempting to bring about, any understanding or agreement, whether written or oral, formal or informal, expressed or implied, among competitors with regard to prices, terms or conditions of sale, discounts, tying provision or purchase of a good or service with another, exclusive dealing arrangements, distribution, volume of production, allocation of territories or customers, restrictions on non-deceptive advertising, or credit of suppliers, customers or competitors or any understanding or agreement which could be perceived as restraining competition.
2. No ICI activity or communication shall (a) include discussion, survey, or action, for any purpose or in any fashion of costs, prices or pricing methods, rebates or other price discrimination, production quotas or other limitations on either the timing or volume of production or of sales; (b) take any action likely to raise prices or reduce quantity or quality of goods available, or (c) involve allocation of territories or markets or customers in any way. "Communication" includes but is not limited to electronic communications, such as emails, text messages, faxes, blog or web posts and/or social media posts.
3. No ICI committee shall undertake any activity, which involves exchange or collection and dissemination among competitors, of any information regarding prices, pricing methods, costs of production, or of sales or distribution or individual company statistics of any kind, without first obtaining the advice of legal counsel, provided by ICI, as to those proper and lawful methods by which these activities may be pursued.
4. No ICI activity or communication shall include any discussion or action which may tend to or may be construed as an attempt to prevent any person or business entity from gaining access to any market or to any customer for goods or services, or to prevent or boycott any supplier, competitor, customer, or other entity from obtaining, accessing, or selling a supply of goods or otherwise purchasing or distributing goods or services freely in the market.
5. No ICI activity or communication shall include any discussion or action which might be construed as an agreement or understanding to refrain from purchasing any raw materials, equipment, services or other supplies from any supplier.
6. Neither ICI nor any committee thereof, shall make any effort to bring about the standardization of any product or method of manufacture, credentialing, listing or certification of any product or program for the purpose of preventing the manufacture or sale of any product not conforming to a specified standard or which would tend to have the overall affect of either lessening competition or resulting in a degree of price stabilization.
7. No person or company shall be commercially disparaged nor shall any ICI Member make statements that are reasonably likely to have a negative reputational impact on another so as to exclude that person or company from ICI membership or participation in any ICI activity where such exclusion is designed to or may impair such person's or company's ability to compete effectively in the investment casting industry.
8. In conducting ICI committee meetings, the chairman thereof shall prepare and follow a formal agenda which shall be provided to all committee members prior to the meeting; else it shall not be considered. Agenda items listed as "Any Other Business" shall be prohibited. Minutes of each meeting shall be distributed to all persons who attended such meetings. Approval of the minutes shall be obtained from the membership of the committee at its next meeting. Copies of the minutes shall be transmitted to the headquarters staff.
9. ICI speakers and authors of conference papers shall be informed of the need to comply with ICI's antitrust policy in the preparation and presentation of their papers and addresses.
10. In informal or social discussions at the site of an ICI meeting (whether such meetings are conducted in-person or via telecommunications services), which are beyond the control of its officers and chairmen, all representatives are expected to observe the same standards of personal conduct required of ICI in its compliance with these antitrust guidelines. Members are reminded that even actions or discussions occurring outside of the U.S. may still be subject to federal antitrust laws. In addition, copies of the foregoing Antitrust Policy Statement and General Rules of Antitrust Compliance will be included in registration packets and will also be printed in the ICI Committee Directory. The Board may from time to time require all members to sign an acknowledgement that each member has read and understood these Rules of Antitrust Compliance.

## **ANTITRUST POLICY STATEMENT OF THE INVESTMENT CASTING INSTITUTE**

The Investment Casting Institute (ICI) is a trade and technical association of investment casting foundries (and their suppliers) where castings of metal are made.

The ICI is organized to promote the common interests of the investment casting industry. The ICI is not intended to become, and will not become, involved in the competitive business decisions of its members, nor will it take any action which would tend to restrain competition in the investment casting industry.

Nevertheless, it is recognized by the Board of Directors of ICI that the Institute itself, as well as its varied activities, could be regarded by some as a forum or opportunity to promote anti-competitive conduct. For this reason, the Board of Directors promulgates this statement of policy to make clear its unequivocal support for the policy of competition served by federal and state antitrust laws, as well as its uncompromising intent to comply strictly in all respects with those laws.

In addition to stating the ICI's firm commitment to the principle of competition served by antitrust laws, the ICI also wishes to advise that the penalties which may be imposed upon both ICI and its individual and corporate members involved in any violation of such laws are now so severe that prudent business judgment demands that every effort be made to avoid any such violation. In addition to injunctions and other equitable remedies, violations of the Sherman Act, such as price-fixing, are felony crimes for which individuals may now be imprisoned for up to ten (10) years and fined up to one million dollars (\$1,000,000.00), and corporations can be fined up to 100 million dollars (\$100,000,000.00) for each offense, or twenty percent (20%) of affected commerce. The Department of Justice has recently obtained fines of up to five hundred million dollars (\$500,000,000.00). Under the Sherman Act, state Anti Trust law, the Federal Trade Commission Act and Robinson-Patman Act, treble (triple) damage claims based on the amount of gain or loss by private parties (including class actions) for antitrust violations are extremely expensive to litigate and can result in judgments of a magnitude which could destroy the ICI and seriously affect the financial interests of its members. This includes attorney's fees and "joint and several liability" where one may be liable for an entire Judgement even though their role in the antitrust violation was rather small.

It is the responsibility of every member of the ICI to be guided by ICI's policy of strict compliance with antitrust laws in all ICI activities. It shall be the special responsibility of ICI officers, directors and committee chairmen to ensure that this policy is known and adhered to in the course of activities pursued under their leadership.

To assist the ICI staff and all its officers, directors and committee chairmen in recognizing situations which may raise the appearance of an antitrust problem, the Board will as a matter of policy furnish to each of such persons copies of ICI's General Rules of Antitrust Compliance. The ICI will also make available general legal advice when questions arise as to the manner in which the antitrust laws may apply to the activities of the ICI or to any committee thereof.

Antitrust compliance is the responsibility of every ICI member. If you have any questions or information concerning potentially anti-competitive conduct, please contact the Board's Executive Committee orally, in writing and even anonymously. Alleged violations of the ICI General Rules of Antitrust Compliance or of this policy statement will be vigorously investigated and reviewed with due process pursuant to the by-laws of the ICI; violations may result in revocation of membership in ICI and removal from any ICI office.

**SUNDAY, NOVEMBER 7, 2021**

3:00 p.m. - 6:00 p.m. **REGISTRATION – Lobby Outside of Ambassador Room**

6:00 p.m. - 7:30 p.m. **WELCOME RECEPTION - Ambassador Room**

**MONDAY, NOVEMBER 8, 2021 – 7:00 a.m. Registration at DeVos Place**

8:00 a.m. - 8:10 a.m. **WELCOME INTRODUCTION \*\*\*\* 68th Technical Conference & Expo 2021**

8:10 a.m. – 9:00 a.m. **Russ Gallagher, ICI Director**  
*Bescast, Inc.*

**Russ Rosmait, ICI Academic Advisor**  
*Pittsburg State University*

**Annual Awards Ceremonies - Scholarships, Casting Contest, Innovator of the Year & Cast in Steel**

9:00 a.m. – 9:15 a.m. **Benjamin Fahrney, ICI Intern**  
*Pennsylvania State University - Behrend*

**Paper No. 1**  
ICI Intern Project

9:15 a.m. - 10:00 a.m. **Jerrod Weaver**  
*Non-Ferrous Founders' Society*

**Booth 212**

**Paper No. 2**  
The Integrated Casting Order Network (ICON)

10:00 a.m. – 10:20 a.m. **BREAK**

10:20 a.m. – 11:00 a.m. **Chris Whitehouse**  
*3M Technical Ceramics, Inc.*

**Paper No. 3**  
Shell Drying – Effect of Ambient Conditions Upon Drying & Shell Properties

11:00 a.m. – 11:40 a.m. **Gerald Richard**  
*MAGMA Foundry Technologies, Inc.*  
**Booth 204**

**Paper No. 4**  
An Investigation into Misrun Defects in Investment Cast Stainless Steel Castings

11:40 p.m. - 12:00 p.m. **Gerard Thiel**  
*University of Northern Iowa*

**Paper No. 5**  
AM4IC Report Out

12:00 p.m. - 1:00 p.m. **Lunch**

1:00 p.m. – 1:40 p.m. **Tom Mueller**  
*Mueller Additive Manufacturing Solutions*

**Paper No. 6**  
Optimization of an Aerospace Casting: A Case Study

1:40 p.m. – 2:20 p.m. **Dan Z. Sokol**  
*Renaissance Services – PERFECT – 3D*  
**Booth 318**

**Paper No. 7**  
Rapid, Low-Cost Tooling for Small Engine Castings

2:20 p.m. – 3:00 p.m. **Lee Chamberlain**  
*VA Technology Ltd.*  
**Booth 107**

**Paper No. 8**  
Automated Methods of Slurry Testing, Monitoring & Control

3:00 p.m. – 6:00 p.m. **EXPO**

TUESDAY, NOVEMBER 9, 2021

## 68th Technical Conference &amp; Expo 2021

8:00 a.m. - 8:05 a.m.	<b>Greeting</b>	
8:05 a.m. - 8:45 a.m.	<b>Angelika Priese</b> <i>Imerys Fused Minerals Murg GmbH</i>	<b>Paper No. 9</b> Development of Investment Casting Shells Based on Calcia Stabilised Zirconia for Ti-6Al-4V
8:45 a.m. - 9:25 a.m.	<b>Nip Singh, ICI Director</b> <i>S&amp;A Consulting Group</i>	<b>Paper No. 10</b> Process Control Standards (PCS) for Investment Castings
9:25 a.m. – 10:00 a.m.	<b>Raymond Monroe</b> <i>Steel Founders' Society of America</i> <b>Booth 512</b>	<b>Paper No. 11</b> Steel Performance Initiative (SPI) and Digital Innovative Design (DID)
10:00 a.m. – 10:15 a.m.	<b>BREAK</b>	
10:15 a.m. - 10:55 a.m.	<b>Phil Geers</b> <i>Blasch Precision Ceramics</i> <b>Booth 316</b>	<b>Paper No. 12</b> Implementing Best Practices & Reducing Process Costs For Refractory Use in Investment Casting & Alloy Production Foundries
10:55 a.m. - 11:35 a.m.	<b>Samuel Holt</b> <i>Georgia Southern University</i>	<b>Paper No. 13</b> The Effect of Firing Temperature & Time on Silica Based Investment Shells Strength
11:35 a.m. – 12:15 p.m.	<b>Iñaki Vicario</b> <i>Consarc Engineering Ltd.</i> <b>Booth 308</b>	<b>Paper No. 14</b> Process Cycle Time Analysis & Optimisation for Efficient Vacuum Precision Investment Casting Furnaces
12:15 p.m. – 1:00 p.m.	<b>LUNCH</b>	
1:00 p.m. - 1:40 p.m.	<b>Mark Oles</b> <i>Pine Tree Castings</i> <b>Alfred Kaulius</b> <i>Paramelt</i> <b>Booth 309</b>	<b>Paper No. 15</b> Pattern Cleaning Study of Pattern Formulation Effects on Surface Energy Measurements
1:40 p.m. - 2:20 p.m.	<b>Dr. Sergejs Spitans</b> <i>ALD Vacuum Technologies</i> <b>Booth 202</b>	<b>Paper No. 16</b> Investment Castings with Unique Levitation Melting Technology FastCast
2:20 p.m. – 3:00 p.m.	<b>Dr. Sam Ramrattan</b> <i>Western Michigan University</i>	<b>Paper No. 17</b> Analysis of Thermal Distortion Data to Detect Issues in Investment Shell Materials
3:00 p.m. - 6:00 p.m.	<b>EXPO</b>	
6:30 p.m. - 8:00 p.m.	<b>EVENING RECEPTION</b>	

**WEDNESDAY, NOVEMBER 10, 2021**

**68th Technical Conference & Expo 2021**

8:00 a.m. - 8:05 a.m. **Greeting**

8:05 a.m. - 9:05 a.m. **Shayla Rivera – Keynote Speaker**

**Keynote Address: Awareness Brings Change**

9:05 a.m. – 9:45 a.m. **Noel O’Sullivan**  
*University of Limerick*

**Paper No. 18**  
Enhancing Porosity & Permeability of Ceramic Shells  
For Investment Casting through Pre-wetting

9:45 a.m. – 10:25 a.m. **Mark White**  
*IMPRO Industries USA*

**Paper No. 19**  
Tensile Bar Castings

10:25 a.m. – 10:30 a.m. **Joseph Fritz**  
*ICI Executive Director*

**Best Paper Award, Closing Remarks and  
Adjournment**

# SPEAKERS

**Benjamin Fahrney**                      **Paper No: 1**  
*ICI Intern*  
Pennsylvania State University - Behrend  
4701 College Drive  
Erie, PA 16563  
Phone: (717) 572-6749

**Jerrold Weaver**                      **Paper No: 2**  
*Executive Director*  
Non-Ferrous Founders' Society  
1480 Renaissance Drive  
Suite 310  
Park Ridge, IL 60068  
Phone: (847) 299-0950

**Chris Whitehouse**                      **Paper No: 3**  
*Specialist Engineer*  
3M Technical Ceramics, Inc.  
510 Midway Circle  
Midway, TN 37809  
Phone: (423) 422-2028

**Gerald Richard**                      **Paper No: 4**  
*Application Manager*  
MAGMA Foundry Technologies, Inc.  
10 N. Martingale Road  
Suite 425  
Schaumburg, IL 60173  
Phone: (847) 969-1001

**Gerard Thiel**                      **Paper No: 5**  
*Director*  
University of Northern Iowa  
76 Industrial Technology Center  
Cedar Falls, IA 50614  
Phone: (319) 273-7085

**Tom Mueller**                      **Paper No: 6**  
*President*  
Mueller Additive Manufacturing Solutions  
13830 Foxwood Drive  
New Berlin, WI 53151  
Phone: (224) 548-2191

**Dan Z. Sokol**                      **Paper No: 7**  
*Managing Partner*  
Renaissance Services, PERFECT-3D  
Division  
1 Herald Square  
Fairborn, OH 45324  
Phone: (937) 322-3227

**Lee Chamberlain**                      **Paper No: 8**  
*Director of Engineering*  
VA Technology Ltd.  
Halesfield 9  
Telford, UK TF7 4QW  
Phone: (44)1952-585252

**Angelika Priese, Ph.D**                      **Paper No: 9**  
*Science & Technology Director*  
Imerys Fused Minerals Murg GmbH  
Ferroweg 1  
Laufenburg, Germany 79725  
Phone: 49 (0)7763 933-515

**Nip Singh**                      **Paper No. 10**  
*Consulting Partner & CEO*  
S&A Consulting Group LLP  
2573 Butterwing Road  
Cleveland, OH 44124  
Phone: (216) 593-0050

**Brian Ferg**                      **Paper No. 10**  
*Engineer*  
Consolidated Precision Products  
34000 Lakeland Blvd.  
Eastlake, OH 44095  
Phone: (440) 953-0053

**Joseph Fritz**                      **Paper No. 10**  
*Executive Director*  
Investment Casting Institute  
1 Paragon Drive, Suite 110  
Montvale, NJ 07645  
Phone: (520) 245-0945

# SPEAKERS

**Craig Lanham** Paper No. 10  
*Member Emeritus*  
3054 Broad Vista Street NW  
Uniontown, OH 44685  
Phone: (330) 354-1906

**Thad Nykiel** Paper No. 10  
*Process Engineering Manager*  
BESCAST, Inc.  
4600 East 355th St.  
Willoughby, OH 44094  
Phone: (440) 946-5300

**Tom Planz** Paper No. 10  
*President*  
Kovatch Castings, Inc.  
3743 Tabs Drive  
Uniontown, OH 44685  
Phone: (330) 896-9944

**Raymond Monroe** Paper No. 11  
*Executive Vice President*  
Steel Founders' Society of America  
780 McArdle Drive  
Suite G  
Crystal, IL 60014  
Phone: (815) 263-8240

**Phil Geers** Paper No. 12  
*Senior Market Manager*  
Blasch Precision Ceramics Inc.  
580 Broadway  
Albany, NY 12204  
Phone: (620) 235-4375

**Samuel Holt** Paper No. 13  
*Master of Science Student*  
Department of Mechanical Engineering  
Georgia Southern University  
P.O. Box 8046  
Statesboro, GA 30460  
Phone: (912) 478-8449

**Iñaki Vicario** Paper No. 14  
*CASTING Technology Specialist*  
Consarc Engineering Ltd  
9 Woodside, Eurocentral, Holytown,  
Scotland, UK ML1 4XL  
Phone: 34/653 418 976

**Mark Oles** Paper No. 15  
*Process Engineering Manager*  
Pine Tree Castings  
411 Sunapee Street  
Newport, NH 03773  
Phone: (603) 863-2000

**Alfred Kaulius** Paper No. 15  
*New Product Development Engineer*  
Paramelt  
2817 McCracken Street  
Muskegon, MI 49441  
Phone: (231) 759-7304

**Dr. Sergejs Spitans** Paper No. 16  
*Process Engineer*  
ALD Vacuum Technologies GmbH  
Otto-von-Guericke-Platz 1  
63457 Hanau Germany  
Phone: (496) 181-3070

**Dr. Sam Ramrattan** Paper No. 17  
*Professor College of Engineering*  
Western Michigan University  
4501 Campus Drive  
Kalamazoo, MI 49008  
Phone: (269) 276-3373

**Shayla Rivera** Keynote Speaker  
*Aerospace Engineer*  
GDA Speakers  
3500 Oak Lawn Avenue  
Suite 740  
Dallas, TX 75219  
Phone: (214) 420-1999

**Noel O'Sullivan**                      **Paper No.18**  
*Mechanical Engineer Student*  
University of Limerick, Bernal Institute  
Castletroy, Limerick  
Munster, Ireland V94 T9PX  
Phone: 353/0-879-06338

**Mark White**                              **Paper No. 19**  
*Technical Director*  
Impro Industries USA  
21660 East Copley Drive  
Suite 100  
Diamond Bar, CA 91765  
Phone: (630) 538-6417

# SPEAKER BIOGRAPHIES

## **Benjamin Fahrney ..... Paper No: 1**

### ***Investment Casting Institute Intern***

Ben Fahrney is currently a junior, mechanical engineering student at Penn State University - Behrend. Over the summer of 2021, Ben completed a summer internship with Techcast LLC in Myerstown PA. Here, he took part in designing and running his own internship project as part of a grant from the Pennsylvania Department of Community and Economic Development. Ben has also been involved in a number of other projects both during his internship with Techcast and as an undergraduate research student under Dr. Paul Lynch. Here, the primary focus of his research has been the integration of different additive manufacturing techniques for rapid-prototyping applications in investment casting. One of Ben's career goals in the industry is to continue this work in integrating "industry 4.0" technologies into this industry. Ben will also be serving as the president of the Penn State Behrend Materials and Manufacturing Group for this coming year. The club has become one of the most active engineering clubs on campus; It's primary focus is on building connections between students who are passionate about the industry, with companies and organizations who are looking for interns and full time employees. Altogether, Ben enjoys building connections with these students and companies, and intends to make a career out of working with people and teaching them about the metalcasting industry and the great opportunities available to them.

## **Jerrod Weaver ..... Paper No: 2**

### ***Executive Director – Non-Ferrous Founders' Society (NFFS)***

Jerrod Weaver is the Executive Director of the Non-Ferrous Founders' Society. He has more than twenty five years of professional experience in association management, first as a staff member with NFFS beginning in 1996 and then as Executive Director since January of 2016. Mr. Weaver received a BS in Manufacturing Engineering (cast metals minor) from Western Michigan University in 1996. He earned the prestigious Certified Association Executive (CAE) designation from the American Society of Association Executives in 2010, as well as certified quality auditor, quality manager and lead auditor credentials issued by the American Society for Quality in 1998.

## **Chris Whitehouse ..... Paper No: 3**

### ***Specialist Engineer – 3M Technical Ceramics, Inc.***

Ceramist serving 3M Technical Ceramics and their fused silica customers with over 19 years focused upon investment casting and castable products. Over a dozen papers and presentations on investment casting presented both nationally and internationally. Design shell systems for optimizing select properties of interest for foundry applications. BS/ MS Ceramic Engineering from NYS College of Ceramics at Alfred University.

## **Gerald Richard ..... Paper No: 4**

### ***Application Manager – MAGMA Foundry Technologies, Inc.***

Gerald Richard is an Application Manager at MAGMA Foundry Technologies Inc., a software company that is committed to casting excellence and achieves this through its casting process simulation tool MAGMASOFT®. Before devoting his life to the foundry industry, Gerald achieved a Bachelor of Science degree in Mechanical Engineering from Marquette University. He went on to work in the chemical industry as an engineer for 5 years before pursuing an opportunity to work at Badger Alloys, a high alloy jobbing foundry locate in Milwaukee, WI. Gerald fell in love with castings and the casting process as he worked as a foundry engineer focusing mostly on gating and risering design. After 4 years of working at Badger Alloys, Gerald moved to the greater Chicago area and began working for MAGMA Foundry Technologies Inc. in 2015, where he focuses on client development and support for a number of sand and investment foundries. He has been heavily involved in Investment Casting Institute events, including contributing 4 consecutive papers at the annual technical conference.

## **Gerard Thiel ..... Paper No: 5**

### ***Director – University of Northern Iowa***

Jerry Thiel is the Director of the Metal Casting and Additive Manufacturing Centers at the University of Northern Iowa. He has a diverse industrial background and has held management positions in the metal casting and related industries for over 45 years. Jerry holds degrees in materials science, manufacturing and manufacturing process development and has published numerous research papers pertaining to molding and core materials for the foundry industry. He is a past chairman of the AFS Molding and Materials division, Additive Manufacturing division and Cast Metals Institute. Jerry has received multiple awards from the American Foundry Society for his service and technical contributions to the foundry industry.

# SPEAKER BIOGRAPHIES

**Tom Mueller.....Paper No: 6**

**President – Mueller Additive Manufacturing Solutions**

Shawn Franks is a second generation foundryman at HTC I who has worked in the aerospace aluminum casting industry for over 21 years. His specialty is making aluminum aerospace grade castings using the investment mold, plaster mold, and precision sand mold processes. Shawn has been involved on projects ranging from classified military grade castings and high-volume commercial aerospace castings to OEM automotive castings, aftermarket high-performance automotive castings, as well as medical grade castings. He learned his trade skills through hard work and dedication while working with pioneers of the aluminum casting industry. With decades of experience and continuous educational enrichment, Shawn has been able to successfully bring innovative casting approaches from ideas to reality. His most recent efforts include the introduction of 3D-printed ceramics into aluminum casting production.

**Dan Z. Sokol.....Paper No: 7**

**Managing Partner – Renaissance Services, PERFECT - 3D Division**

Mr. Dan Z. Sokol is the Managing Partner of Renaissance Services Inc. He is involved in leading complex technology integration projects for automotive, aerospace, and casting companies such as General Motors, Lockheed, and PCC. Dan has most recently been the technical lead for various projects focused on the improvement of investment casting, which involves the 3D-printing of ceramic cores, filters, and molds. He was the technical leader and principal investigator on additive manufacturing development efforts sponsored by the US Air Force and Defense Logistics Agency. Dan has also successfully managed technology projects funded by the National Institute of Standards and Technology, Missile Defense Agency, and the National Science Foundation. Dan has received multiple patents for software and engineering systems. He has published over thirty technical papers and he was recently awarded the Society of Automotive Engineers Excellence in Presentation Award. He was also a finalist for the Ernst & Young Ohio Entrepreneur of the Year award. Dan received a BS in Industrial & Systems Engineering and a BS in Computer Sciences from the Ohio State University, and an MBA from the University of Dayton.

**Lee Chamberlain.....Paper No: 8**

**Director of Engineering – VA Technology Ltd.**

Lee Chamberlain is Director of Engineering at VA Technology Ltd, the largest supplier of automated shell making systems in the world. Lee achieved a bachelor's degree in Mechanical Engineering at Leeds university before joining BAE Systems as a R&D engineer developing automated manufacturing systems for the military aircraft division. He subsequently went on to become a lead design engineer on the RAF Typhoon and F35 Lightning II military aircraft projects before moving to take up his post at VA Technology. Lee, along with his dedicated team, develops bespoke shell making systems for installation into customer foundries all around the world and is committed to continued integration of technologies into shellroom solutions.

**Angelika Priese.....Paper No: 9**

**Science & Technology Director – Imerys Fused Minerals Murg GmbH**

Angelika Priese has received her diploma degree in chemistry from Hamburg University (Germany) in 1996 and Ph.D. in earth sciences (mineralogy) from Cambridge University (UK) in 2001. She then joined the French industrial mineral company Imerys to work in various positions in Research and Development in the UK, France, Switzerland, P.R. China, Austria and Germany. Since 2019 Angelika is the Science & Technology Director for Advanced Ceramics at Imerys. She is member of the board of the German Ceramic Society and the Zircon Industry Association (ZIA) and chairperson of the technical committee of ZIA. Her research interests include solid state chemistry, mineral processing technology and all aspects of ceramics. In her spare time she is a keen rower.

**Nip Singh.....Paper No: 10**

**Consulting Partner & CEO – S&A Consulting Group LLP**

Nipendra (Nip) Singh has been an affiliate member of ICI for almost 30 years. He is also member of ICI Board of Directors representing affiliate members and working/chairing many key committees for the welfare of Investment Casting in general and both Affiliate and Regular members. Nip has almost 50 years of experience in the high technology aircraft engine components manufacturing business including nearly 20 years with Rolls Royce, General Electric and TRW/PCC Corporations. Since 1991 Nip is Consulting Partner and CEO of S&A Consulting Group LLP, Cleveland, USA.

# SPEAKER BIOGRAPHIES

**Brian Ferg.....Paper No. 10**  
**Engineer – Consolidated Precision Products**

With 45 years' experience in the investment casting industry, Mr. Ferg has worked in ceramics R&D, core manufacturing, and foundries. This includes stints at Sherwood Refractories, TRW, PCC, ESCO, and CPP. Mr. Ferg has been active in developing shelling processes and casting processes throughout his career and has been a leader in controlling key variables to reduce scrap and produce commercial, aerospace, and IGT castings for customers including GE, Honeywell, and Pratt & Whitney. Mr. Ferg holds a degree in Ceramic Science from the Pennsylvania State University and is a GE certified Black Belt.

**Joseph Fritz..... Paper No. 10**  
**Executive Director – Investment Casting Institute**

Joseph Fritz has been the Executive Director of the Investment Casting Institute since 2013. Under his leadership, the ICI has focused its initiatives on member services, educational resources, technological collaboration, industry sustainability and growth. With over 35 years' experience, Mr. Fritz has served the industry in a variety of capacities with a number of Fortune 100 as well as privately held companies, including operations management, quality assurance, engineering, marketing and sales. During this time, he has contributed to a number of programs, including the Navy's Trident II, Phalanx and Aegis programs, the Air Force's Joint Strike Fighter program and Boeing's 787 Dreamliner program. Mr. Fritz holds degrees in Engineering from the University of Connecticut and an MBA with a concentration in Strategic Marketing from Union College. He is the recipient of a number of management awards from General Electric and Howmet Corporation.

**Craig Lanham ..... Paper No. 10**  
**Member Emeritus**

Mr. Craig Lanham, retiring in 2014 from Ceradyne Inc., a 3M Company, received his BS Degree from Carroll College, Waukesha, Wisconsin in 1971. During his career Mr. Lanham spent over 44 years involved in the manufacturing of casting with 38 years of that experience in the Precision Investment Casting Industry. His experience included a healthy balance between direct investment casting manufacturing experience and management responsibilities at two investment casting foundries; Northern Precision Castings and Kovatch Castings and experience in the marketing and sales of consumables to Investment Casting Foundries; first with REMET and then Minco / Ceradyne.

**Thad Nykiel..... Paper No. 10**  
**Process Engineering Manager - BESCOAST, Inc**

Mr. Nykiel is the Process Engineering Manager for BESCOAST, Inc., located in Willoughby Ohio, where he has spent the last 19 years of his career. A graduate of Cleveland State University, where he was awarded a Foundry Engineering Society Scholarship, Mr. Nykiel has served the investment casting industry for 40 years, working for a number of prestigious manufacturers, including Precision Metalsmith's, Duradyne Technologies and PCC. Over the course of his career, he has held a number of key positions, including Part and Area Process Engineer, Supervisor of SPC and A.C.E. Supervisor. Mr. Nykiel has also served the industry through volunteerism. For many years served in a variety of roles including Chapter President of the Northeast Ohio Chapter of the American Society for Metals. He has also presented a number of papers for the FEF and the ICI.

**Tom Planz.....Paper No. 10**  
**President – Kovatch Castings, Inc.**

Mr. Planz Joined Kci As Director Of Operations In December 2014. In January 2020, Tom Stepped Into The Role Of President Of Kci, As Doug Kovatch Becomes Chairman Of The Board Of Directors. Tom Is A Proven Leader With 38 Years Of Experience In The Investment Casting Industry. Early In His Career, He Spent 17 Years In Various Engineering And Manufacturing Positions (For 4 Different Foundries) Working In A Range Of Functional Areas, Including Lab Tech, Product Engineer, Process Engineer, Production Manager And Plant Manager. He Moved To The Supplier Side Of The Industry And Spent 16+ Years Working For Several Different Wax Suppliers. He Oversaw The Construction, Startup And Operation Of M. Argueso Inc.'S First Wholly Owned Subsidiary, Cerita West Llc In Tempe. Tom Then Joined Kindt-Collins Llc Where He Held The Position Of President And Coo. During His Tenure At Kindt-Collins, Annual Sales Tripled And He Played An Integral Role In The Sale Of Kindt-Collins Llc To Paramelt Bv. Post-Acquisition, He Spent 4 Years At Paramelt As Its Vp Of Sales And Global Casting Wax Business Manager. Tom Studied Aerospace Engineering At The University Of Michigan And Mechanical Engineering At Illinois Institute Of Technology.

# SPEAKER BIOGRAPHIES

**Raymond Monroe..... Paper No. 11**

***Executive Vice President – Steel Founders’ Society of America (SFSA)***

Raymond W. Monroe joined the Steel Founders' Society of America SFSA as Executive Vice President in 1988. He holds a B.S. in Chemical Engineering from Auburn University, an M.S. in Engineering Science from the University of Alabama (Birmingham), and a Phd in Manufacturing Engineering from Worcester Polytechnic University. Raymond supports the U.S. Department of Defense as a panelist for the Joint Defense Manufacturing Technology Panel-Metals Sub-panel. This panel reviews the DoD MANTECH projects for advanced manufacturing. He is the instigator for the Steel Performance Initiative, a DoD program to invest in advanced specialty steel technology for U.S., domestic producers to meet strategic DoD requirements.

**Phil Geers ..... Paper No. 12**

***Senior Market Manager – Blasch Precision Ceramics, Inc.***

Phil Geers, Sr. Market Manager – Metals, has been with Blasch Precision Ceramics since 2001. Phil has over 30 years of industrial sales, engineering, marketing and management experience, where he has worked to develop partnerships with companies nationally, internationally, large and small. As the Sr. Market Manager for the Metals group, he leads a team whose goal is to provide solutions for improving processes using ceramic refractories by increasing life, reducing turnaround time and improving quality in all areas to our customers. Phil holds B.S. in Business and Marketing from SUNY Empire College.

**Samuel Holt ..... Paper No. 13**

***Master of Science Student – Georgia Southern University***

Samuel Holt is a second year Master of Science student in Mechanical Engineering at Georgia Southern University. He has been researching strength of fused silica investment shell molds, while assisting in teaching foundry, machine shop, and material science. For summer 2021, Samuel completed an internship at Nematik. There he was in charge of optimizing the heat treatment process and validating altered alloy chemistry with mechanical testing.

**Iñaki Vicario.....Paper No. 14**

***Casting Technology Specialist - Consarc Engineering Ltd***

Iñaki Vicario is the Casting Technology Specialist of Consarc Engineering. He belongs to the Technology Group of Consarc dealing with technical developments, and customer technical support. He has almost 13 years of experience in the aerospace industry, specifically in investment casting technology as a foundry process owner. He has also large experience in other metallurgical processes, such as vacuum heat treatment (10 years of experience in AMS 2750), VIM process for Ni based alloy manufacturing, HIP and gas phase aluminizing. Mr. Vicario has a Bachelor's degree from the University of the Basque Country in Industrial Engineering, specialized in Manufacturing Technologies.

**Mark Oles ..... Paper No. 15**

***Process Engineering Manager – Pine Tree Castings***

Mark Oles received his Bachelor of Technology degree from the University of Northern Iowa. Mark started his career at Hitchiner manufacturing in 1984, eventually rising to the position of Senior Process Engineer. He is a Six Sigma Black Belt and an instructor for the Investment Casting Institute Process Control Course.

**Alfred Kaulius.....Paper No. 15**

***New Product Development Engineer - Paramelt***

The author is the New Product Development Engineer for investment casting waxes for Paramelt. Alfred has over 30 years of experience in the investment casting industry working on formulations and process improvements in pattern materials, ceramic cores, crucible materials, and shell materials. He has also worked as a Six-Sigma Black Belt working on investment casting issues. Alfred holds a BS Degree in Ceramic Engineering from Rutgers University, and an MS Degree in Engineering Management from Western Michigan University.

# SPEAKER BIOGRAPHIES

**Dr. Sergejs Spitans.....Paper No. 16**

***Process Engineer – ALD Vacuum Technologies GmbH***

Dr. Sergejs Spitans worked as a researcher in the field of induction melting at the Institute of Electrotechnology (Leibniz University, Germany) and obtained his doctoral degree in Physics in 2015. He is a process engineer in the R&D department of the ALD Vacuum Technologies GmbH since 2016 with focus on simulation of coupled electromagnetic, gas/fluid flow, heat transfer and structural mechanics problems.

**Dr. Sam Ramrattan.....Paper No. 17**

***Professor College of Engineering – Western Michigan University***

Dr. Sam Ramrattan is a Professor in the Department of Engineering Design, Manufacturing and Management Systems, College of Engineering, Western Michigan University (WMU). He received his Bachelors & Masters from the University of Wisconsin-Stout, Ph.D. from Iowa State University and Post Doc. from Ames Lab. His area of specialization is materials & processes emphasizing casting. He is a member of the 4F and 4H Research Committees at the American Foundry Society (AFS), Technical Adviser to the WMU Student Chapter AFS, and a Key Professor for the Foundry Educational Foundation (FEF). He was a recipient of the AFS Scientific Merit Award, the AFS Service Citation, the British Foundry Medal and several outstanding teaching awards. He has published more than two hundred and fifty technical papers, presented in more than twenty different countries and has been awarded several patents. Sam has taught at the University of Wisconsin-Stout, Iowa State University, and University of Technology Malaysia. His current research projects involve casting issues at the mold/metal interface, rapid casting technologies, digital dynamic testing for process control for foundry sand systems.

**Shayla Rivera.....Keynote Speaker**

***Aerospace Engineer – GDA Speakers***

Shayla Rivera is an Aerospace Engineer and former Rocket Scientist with NASA turned salesperson, corporate trainer, and now International Keynote Speaker, TV & Radio host, Emcee/Host, Comedian, Actor, Writer, Producer, Awareness Expert, Seminar Facilitator and Panel Moderator. And as of 2017, Shayla is Director of the ENGR[x] program and Professor of Practice for the College of Engineering at Texas A&M University.

**Noel O’Sullivan..... Paper No. 18**

***Mechanical Engineer Student – University of Limerick***

Noel O’Sullivan graduated from the University of Limerick in 2017 with a bachelor’s degree in Mechanical Engineering as a mature student. Since then, he has started a PhD in collaboration with Stryker Orthopedics, Limerick, Ireland. Noel’s area of expertise is related to the development of the ceramic shell and the stability of the primary ceramic slurry. His PhD is titled “Continuous improvement of investment casting production techniques for biomedical castings through ceramic shell development”. After two years of Noel’s PhD process yield was increased by 3% through optimizing and stabilizing the primary ceramic slurry.

**Mark White..... Paper No. 19**

***Technical Director – Impro Industries USA***

Mark A. White is an Investment Casting Engineering Leader employed with Impro Industries USA, Inc. as Technical Director of Aerospace and Medical Components. He holds a B.S. in Applied Engineering from Kent State University where his research was in foundry science and a Master of Science, in Quality Systems & Improvement Management, from Cambridge College and holds a Six Sigma Black Belt, from Juran Global. Mark has supported many casting programs during his career which began in 1981, in Minerva, Ohio spanning involvement as an airfoil and structural casting engineer in casting plants and at the OEM level, with Pratt & Whitney.

# **INVESTMENT CASTING INSTITUTE**

## **ICI Intern Project**

Benjamin Fahrney  
Pennsylvania State University - Behrend

## **68<sup>TH</sup> TECHNICAL CONFERENCE & EXPO 2021**

Paper No 1

## **Investment Casting Institute Internship Overview**

**Ben Fahrney**

**Tech Cast LLC, Summer 2021**

During the summer of 2021 I took on a position as an engineering intern at Tech Cast LLC in Myerstown PA. This was among the most formative and challenging experiences that I have had in my professional or academic career so far. Although, because of the challenging nature of the work I was able to complete here, I was able to develop my technical, interpersonal, and critical thinking skills in a way that I had never been able to before. Altogether, the knowledge and skills that I have been able to take away from this experience have greatly exceeded my expectations. The structure of this internship allowed me to gain experience in every aspect of Tech Cast's process from the administrative work and procedures during the planning phase of a project all the way to the finishing and dimensional inspection on the final casting right before they go out the door. Altogether, the opportunity that I was given at Tech Cast LLC was as close to a true professional engineering experience that I could have achieved in an intern's role.

I was fortunate to make a connection at Tech Cast LLC through a research project that I had been working on since the summer of 2020 with the Penn State Behrend materials and manufacturing research group. This project aimed to investigate the capabilities of additive manufacturing (AM) technologies and their respective materials for use in investment casting pattern design and fabrication. The project was sponsored by a grant from the Pennsylvania Department of Community and Economic Development with the goal of demonstrating how Pennsylvania foundries can make extremely complex and efficient castings for low-volume

## **SHELL DRYING:**

### **The Effect of Ambient Conditions upon Drying and Shell Properties**

C. Whitehouse, A. Buchner

#### **1.0 ABSTRACT**

Shell drying and its effects upon shell properties is always one of the most important considerations for the investment casting industry. To further investigate this area, shell drying was studied here as a function of ambient room temperature and relative humidity at a fixed air speed but with oscillating movement. Shell temperature changes with evaporative cooling under four different temperatures (65/ 75/ 85/ 95°F) were studied, at three different relative humidity values (35/ 50/ 65%RH). Two different shell systems were used to denote dryness or lack thereof. Weight loss, shell temperature and room temperature are presented to help understand the completeness of the drying process for each of the conditions studied. Data sets are presented in 3D topographical map form. All told 1152 MOR test breaks were used to generate this extensive and fascinating data set. The comprehensive data will be presented with some very interesting results and discussion points.

#### **2.0 BACKGROUND**

Shell drying is always near the top of the list of areas of monitoring and concern for investment casters. Historically, the investment casting industry has focused dry room conditions around a comfortable 50%RH at 70°F/ 21°C. Operator comfort may have been a factor rather than shell property optimization in this choice. Differences in thermal expansion between the wax and ceramic shell dictate what level of variation from the desired setting is permitted. However, the target temperature and humidity can be set where it minimizes the overall cost to manufacture the final end castings.

A quick review of the drying papers in the last twenty plus years might first be in order. Snow and Scott presented the effects of temperature and air velocity on shell drying and shell strength in 1998 at a fixed 50%RH (1). Drying was monitored with a custom electroconductivity meter and automated drying loss measurements. Air temperature, relative humidity and air velocity were shown to impact shell performance, with higher air temperature suggested as a possible route to improved shell properties. These authors also explored the effects of flour particle size distribution and latex and/or wetting agent use in drying time. Shell weight changes with evaporation as well as capillary absorption

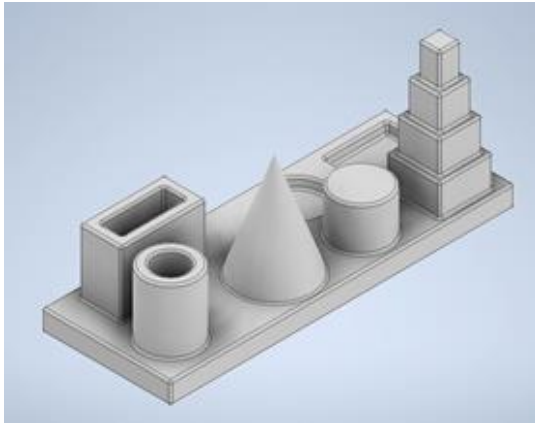


**Fig 1.** The “Investment Casting Test Artifact” used in this experiment

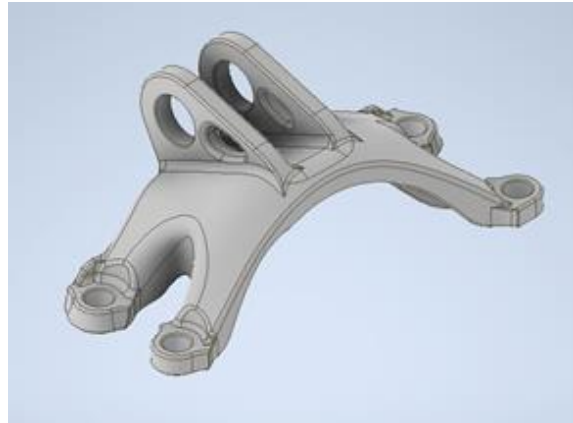


**Fig 2.** A jet engine bracket design from a GE-Sponsored competition

The first of these materials is a product known as MOLDLAY from the company LAY-Filaments, a polymer and wax blend designed to mimic the properties of the wax that is typically used for investment casting. The other FDM filament was known as Polycast from the company Polymaker, this material was designed to mimic the properties of PLA (arguably the easiest to use and the most widely available FDM filament) while achieving a better ash content through the burnout process. The final material was a photosensitive resin for SLA printing known as Accura 60 designed for making rigid and strong parts that are often used for investment casting.

To evaluate the dimensional accuracy of the patterns, 25 different measurements were taken from the investment casting test artifact shown in figure one. These measurements encompassed different features like simple curves and negative spaces to determine if certain geometries may be less accurate than others. This dimensional data will be compared across four artifacts of each material and will include a comparison between, intended dimensions, pattern dimensions, and casting dimensions.

The jet engine bracket shown in figure two serves the purpose of demonstrating the ability to produce complex organic geometry provided with this production method. The design of this part is a perfect use-case for AM patterns, hundreds of different designs were considered for a prototype part and instead of investing in expensive tooling for traditional wax patterns, AM patterns present the opportunity to obtain many more cast parts with a significantly lower investment of both time and money. Additionally, the fact that the organic geometry of the part is designed using FEA analysis and AI demonstrates how well this method of manufacturing can be tied into other industry 4.0 technologies.

During the casting design and simulation phase of this project, the GE bracket also demonstrated another interesting benefit to AM casting patterns. Most attempts to use traditional gating geometry resulted in poor castings based on data from solidification software. A move to more organically shaped gating (pictured in figure 3) proved to alleviate many of these problems. The organic gating design offers a gating solution to complex parts in unique cases, where traditional gate geometries may be inefficient or ineffective.



**Fig 3.** An organic gating design for the engine bracket model shown in figure 2

Throughout this internship I was truly able to get the best top-to-bottom engineering experience that I could hope for. I was able to design experiments that would meet the scope of the project, complete simulation and casting design, perform all of the administrative tasks required for a casting to work its way through Tech Cast's process, and even get hands-on technical experience as I walked my parts through the investment casting process.

In my opinion, this diverse range of experiences ended up being one of the most valuable portions of my time in this position. Over the course of my internship, I got to work in each position that Tech Cast offers for at least one day each as I pushed my parts through production. Not only would I work alongside the project engineers at Tech Cast, but I would also work alongside sales reps, machinists, technicians, as they taught me portions of their jobs as well. I also got the opportunity to work with several industry sponsors who had a part in the completion of this project. One of these project sponsors was a company known as ProtoCAM in Allentown PA. ProtoCAM is a large additive manufacturing company that has been working with Tech Cast for a number of years in the fabrication of SLA patterns used for investment casting. The patterns that they provide, at the slight penalty of cost, have proven to be far better in surface finish quality and dimensional accuracy than FDM patterns can achieve. Their partnership allowed me to study the benefits of different additive manufacturing technologies in addition to the traditional FDM printing method.

Learning all these new technical skills and pushing this project along in the extremely tight timeline of my internship was by far one of the most troublesome aspects of my project. I found myself competing with my project's timeline on a daily basis and the experience truly challenged my project management and planning abilities. This was my first major engineering

project that I had the opportunity to lead from start to finish and it has taught me countless lessons that I am excited to take into my career in the coming years.

Although this particular project concerning the use of additively manufactured patterns was the primary focus of my internship at Tech Cast, there were a number of other activities that I participated in my day-to-day work at the foundry. I often found myself working with other project engineers at Tech Cast, learning from the projects that they were working on alongside me, and picking up their knowledge as I went along. Some of these activities involved hot pressing parts to get them within tight tolerance requirements, dimensional inspections, tree assemblies, burnout operations, among many other smaller tasks. Although, what was really eye-opening to me was how often these project engineers had to tackle challenging problems throughout their projects. It was truly eye-opening for me to see how many problems can arise in the casting process even after the theoretical design work has been completed. It seemed that almost every day I was learning about another challenge to plan around in the casting design process. Although, what was arguably more impressive, is how the engineers at Tech Cast were able to tackle these challenges by analyzing the root cause and performing the corrective action to solve the problem. I often found myself involved in both processes with the project engineers at Tech Cast as we had parts that failed inspection. This analysis of root causes and the implementation of the corrective action was one of the most valuable skills that the engineers at Tech Cast had, and it is a skillset that I want to continue working on as I grow in the industry.

Altogether, I cannot express my thanks enough for my time at Tech Cast. The people I had the opportunity to work with really made the experience special. As my first real introduction into working the metal casting industry, I could not have asked for a better exposure to the industry. I also wanted to take this time to thank ICI for their support on this project and

this internship, the resources that I had access to through the ICI proved to be a great help throughout my time at Tech Cast, and the people that I worked with were nothing but helpful.



# **INVESTMENT CASTING INSTITUTE**

## **The Integrated Casting Order Network (ICON)**

Jerrold Weaver  
Non-Ferrous Founders' Society

## **68<sup>TH</sup> TECHNICAL CONFERENCE & EXPO 2021**

Paper № 2

Investment castings are among the most difficult items for our Government and Armed Forces to obtain from its supply base. Reviewing the thousands of bid solicitations issued by these agencies on a daily basis is time consuming and a barrier to participation for all but a few of the industry's largest casting suppliers. This has led to an environment where there are very low participation rates by many of our nation's investment casting foundries in the military and defense supply chains.

To address the diminished supply chain for investment castings available to our nation's military and defense customers, the Non-Ferrous Founders' Society (NFFS) has developed the Integrated Casting Order Network (ICON) program. ICON is a cloud-based B2B portal that identifies sales opportunities available from the Department of Defense, the Defense Logistics Agency (DLA), and other federal procurement agencies and directs them foundries that either have existing tooling for that part or have the right combination of material and process capabilities to manufacture the required component.

Join this session to learn more about the tremendous contracting opportunities that exist for investment casting foundries, and how the ICON program can help your foundry increase its sales volumes and expand its customer base.

Speakers: Sheila Rayburn, ICON program manager  
Jerrold Weaver, NFFS Executive Director



# **INVESTMENT CASTING INSTITUTE**

## **Shell Drying – Effect of Ambient Conditions Upon Drying & Shell Properties**

Chris Whitehouse  
3M Technical Ceramics, Inc.

### **68<sup>TH</sup> TECHNICAL CONFERENCE & EXPO 2021**

Paper № 3

## **SHELL DRYING:**

### **The Effect of Ambient Conditions upon Drying and Shell Properties**

C. Whitehouse, A. Buchner

#### **1.0 ABSTRACT**

Shell drying and its effects upon shell properties is always one of the most important considerations for the investment casting industry. To further investigate this area, shell drying was studied here as a function of ambient room temperature and relative humidity at a fixed air speed but with oscillating movement. Shell temperature changes with evaporative cooling under four different temperatures (65/ 75/ 85/ 95°F) were studied, at three different relative humidity values (35/ 50/ 65%RH). Two different shell systems were used to denote dryness or lack thereof. Weight loss, shell temperature and room temperature are presented to help understand the completeness of the drying process for each of the conditions studied. Data sets are presented in 3D topographical map form. All told 1152 MOR test breaks were used to generate this extensive and fascinating data set. The comprehensive data will be presented with some very interesting results and discussion points.

#### **2.0 BACKGROUND**

Shell drying is always near the top of the list of areas of monitoring and concern for investment casters. Historically, the investment casting industry has focused dry room conditions around a comfortable 50%RH at 70°F/ 21°C. Operator comfort may have been a factor rather than shell property optimization in this choice. Differences in thermal expansion between the wax and ceramic shell dictate what level of variation from the desired setting is permitted. However, the target temperature and humidity can be set where it minimizes the overall cost to manufacture the final end castings.

A quick review of the drying papers in the last twenty plus years might first be in order. Snow and Scott presented the effects of temperature and air velocity on shell drying and shell strength in 1998 at a fixed 50%RH (1). Drying was monitored with a custom electroconductivity meter and automated drying loss measurements. Air temperature, relative humidity and air velocity were shown to impact shell performance, with higher air temperature suggested as a possible route to improved shell properties. These authors also explored the effects of flour particle size distribution and latex and/or wetting agent use in drying time. Shell weight changes with evaporation as well as capillary absorption

measurements and electrical conductivity were used in this testing. Perhaps one of the most interesting points in this paper was the demonstration of improved overall shell properties with increased inter-dip and final dry times.

Brienza et. al. (2) studied the effect of dryness on shell strength at three levels of shell dryness while seeking a plateau for strength which was not determined. One of their conclusions was the need to better understand the effect of dryness with greater data collection. They commented that shell temperature and weight reduction due to evaporation was not an absolute measurement of dryness. Another conclusion from this research was that allowing each individual shell layer to dry completely may reduce the output of the shell room.

Snyder et. al. (3) attempted to study the effect of three levels of humidity upon shell properties, but some combination of technical and equipment difficulties prevented accumulation of significantly different shell data for trend analysis. This research attempted to provide the data not achieved at that time.

### 3.0 PROCEDURES

The temperature and humidity regions investigated for this work are depicted in Table 1.

		Temperatures (°F/°C)			
		65/ 18	75/ 24	85/ 29	95/ 35
RH%	35	x	x	x	x
	50	x	x	x	x
	65	x	x	x	x

Table 1. Temperatures and Relative Humidity Region Studied.

Two slurry systems were prepared for this study per the formulas given in Table 2. Slurries were creamed in overnight and the first two dips were applied in the morning. Both were stuccoed with 50x100 fused silica. These two dips were used to simulate a prime and intermediate. This combination was chosen to be equally discriminatory as most foundries have some unique and custom first dips. Both were dried in normal ambient 50%RH- 70°F air. The next three dips in each backup slurry were applied over the next workday. Each was stuccoed with 30x50 fused silica and then dried in its respective unique atmospheric conditions. Finally, a seal dip was applied. Inter-dip dry time was maintained at 2.25 hours regardless of whether shells were completely dried or not. This consistent drying schedule

was maintained across the board for all conditions and both shell systems to eliminate an added time variable. Both slurries were maintained at 20 seconds on an ISO 6mm mini dip cup. Final dry times after the seal dip were maintained at 18 hours and then samples were prepped and tested.

<b>FLOUR NAME</b>	<b>WDS2</b>	<b>WDS3</b>
COLLOIDAL NAME	1130	1030
FLOUR (lbs.)	29.8	31.1
COLLOIDAL (lbs.)	10.77	16.31
POLYMER (lbs.)	1.10	1.46
WATER (lbs.)	1.32	0.00
ANTIFOAM (mL)	40	40
WETTING AGENT (mL)	0	0
Total Weight (lbs.)	42.9	48.9
%SiO <sub>2</sub>	24.5%	27.5%
%Polymer	8.3%	8.2%
%Refractory Solids	76.8%	73.6%
	20sec	20sec
Target Visc	ISO6	ISO6

Table 2. Slurry Formulas

Invested samples included 1”x 0.125”x 18” steel bars coated in Johnson’s Paste Wax and ¾” schedule 40 PVC pipe with one end plugged with wax, but with its length also coated in wax to assist shell removal. Ten pipes were invested per temperature and humidity condition for each shell system for both permeability and burst testing. This technique was developed by Snyder and Snow in 2003 (4).

The same drying room and equipment used in the Snyder paper in 2019 on mold dryness and shell strength was used in this effort. Drying room area used was 5’x8’ with separate air conditioning and resistance heating. Two randomly oscillating fans moving air at 12mph/1000fpm from 8” diameter fan blades were implemented, as measured with a hot wire anemometer. A Dri-Eaze LGR Dehumidifier and ultrasonic humidifiers were balanced to maintain RH levels. Air velocity was not altered for this drying study.

Shells were built upon a PVC vehicle much like the Snyder/ Snow effort in 1998 (see Photos 1 and 2). Baseline weight of the system was recorded, and automatic data capture allowed recording of the change in weight with evaporation for each dip. Shell was of course removed

after completion of one iteration of this study, then reused. Weighing was accomplished with a Mettler scale and Mettler Balance Link software along with fans that were programmed to turn off at 20 seconds before data capture. Stucco was applied via fluidized bed for both 50x100 and 30x50.

A significant difference of this paper and the 1998 Scott/ Snow paper is that the shells were not necessarily allowed to completely dry. Shells were re-dipped after 2.25 hours of dry time, regardless of their dryness condition. Drying data was recorded throughout the entire dipping sequence. The baseline weight was zeroed just prior to the next dip. This allows clear display of how much water is evaporated at each dip. However, the downside is that this method does not display how much water might remain from a previous dip that was not completely dried.



Photos 1 and 2. PVC Shell Building Platform- Bare and Invested with Thermocouple.

MOR testing was performed on an Instron 3342 with a 500N/ 112 lbs. load cell. A cross head speed of 0.05"/min along with a two-inch span is used for testing. The thickness of the bar at the break is measured in six locations across the break, three on each side of the break; the width is measured twice and averaged. Burst and permeability shells were removed from the PVC pipes and cut into 6" lengths for permeability and burst testing.

## 4.0 RESULTS

### 4.1 Shell Drying Data

The following section is particularly helpful in pointing out the effects of different ambient conditions upon evaporative cooling shell temperatures as well as resultant weight loss. Each shell drying condition was determined by its weight as water evaporated. Shell temperature was recorded via thermocouple. All of this data is shown for each condition in each particular graph below. Shells for WDS2 and WDS3 are shown side by side for comparison. One should note that the shell weight was re-zeroed just prior to the next dip for these graphs. This may give the false impression that all the water evaporated from each dip; however, the author feels this gives a clearer representation on exactly what percentage of water did evaporate for each dip on its own. It should be clear that these shells were not necessarily completely dried, particularly for the lower temperature and higher humidity runs. This was chosen however to help depict the relative level of dryness for each dip that was achieved. All actual data is shown, even when there were occasional sporadic datapoints which are not easily explained.

Figures 1A and 1B report temperature and weight loss for the first atmospheric condition of 35%RH and 65°F for the backup dips on both shell systems. The WDS2 shell reached ambient temperature after the first dip but did not regain 65°F for any other dried dip except for the seal dip with its long final dry. WDS3 on the other hand, with its greater ability to soak back and build thicker layers, did not reach ambient room temperature after any of the dips until final dry. Both figures show that the first dip was able to evaporate the greatest percentage of water while the following dips evaporated noticeably less water from each dip due to soak back and the short dry interval of 2.25 hours between dips. One would correctly conclude from these graphs that WDS3 has greater difficulty drying at this temperature and humidity and short time than does WDS2.

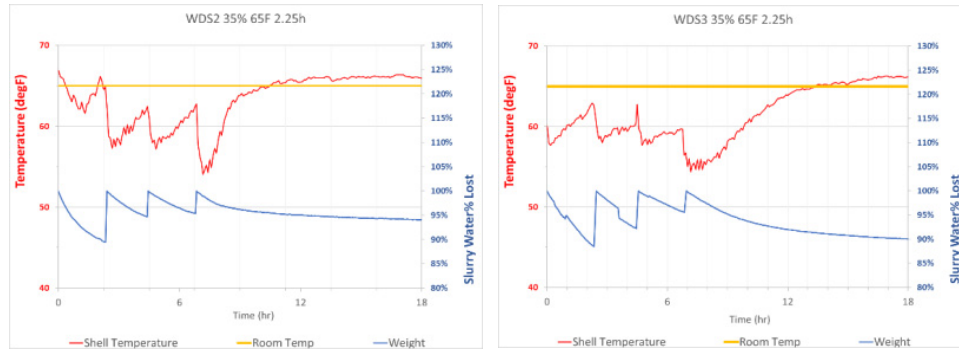


Fig. 1A and 1B. Drying for WDS2/ WDS3 at 35%RH/ 65°F

Figures 2A and 2B report temperature and weight loss for the slightly hotter atmospheric condition of 35%RH and 75°F. The WDS2 shell essentially reached ambient on the first dip but did not quite attain ambient temperature on subsequent dips. Subsequent dips did however reach closer to ambient temperature than the 65°F dry room condition showed in Figures 1A and 1B. The WDS3 shell’s drying temperature curve does not reflect the expected drying curve behavior and could not be explained. A greater degree of water loss was shown after the seal dip drying cycle of WDS2, again expectedly due to the reduced soak back this shell system exhibits. This is related to the increasing thickness of slurry (and water) applied at each subsequent dip due to greater soak back.

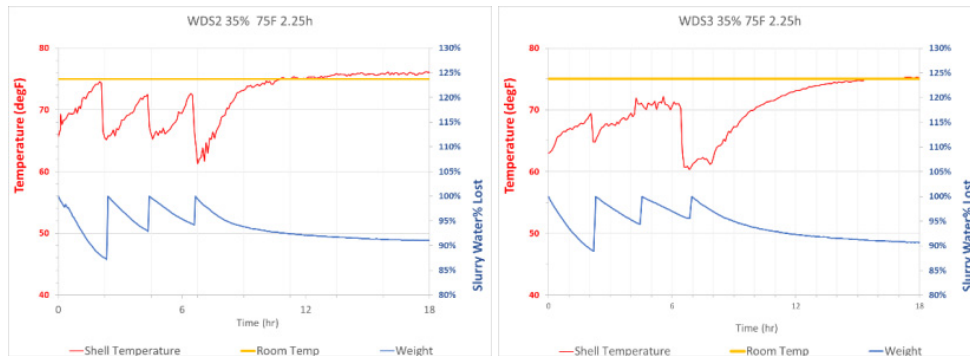


Fig. 2A and 2B. Drying for WDS2/ WDS3 at 35%RH/ 75°F

Figures 3A and 3B report the temperature and weight loss for a hotter atmospheric condition of 35%RH and 85°F. The WDS2 shell reached ambient after the first dry again; however, each subsequent dip came closer to ambient than previous lower room temperature conditions (Figures 1A/B and 2A/B). WDS3’s shell appeared to consistently struggle with reaching ambient with its higher ability to build a thicker shell faster, and the resulting need

to shed more water in a short dry time. It did however reach ambient with its final dip dry approximately seven hours after its seal dip was applied. The additional small drop in the WDS3 weight loss curve at just over five hours might be explained by the drying room door being left open inadvertently, allowing 70°F lab room into the drying area.

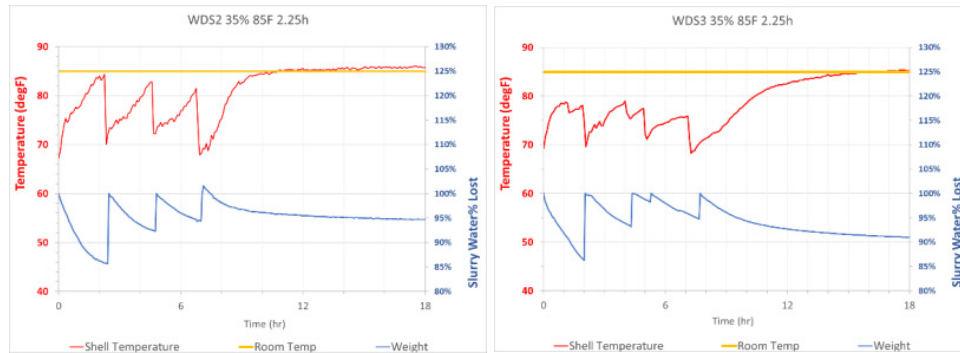


Fig. 3A and 3B. Drying for WDS2/ WDS3 at 35%RH/ 85°F

Figures 4A and 4B report the shell temperature and weight loss for the hottest condition of 35%RH and 95°F. The WDS2 shell reached ambient on the first dip and approximately 92°F on subsequent dips. The WDS3 shell reached ambient temperature on the first dip but gradually reached a somewhat lower maximum temperature prior to each next dip. The final seal dip dry did however reach the ambient room temperature. These results demonstrate that the fast building WDS3 shell can benefit from longer dry times between dips even at 95°F and a low 35%RH.

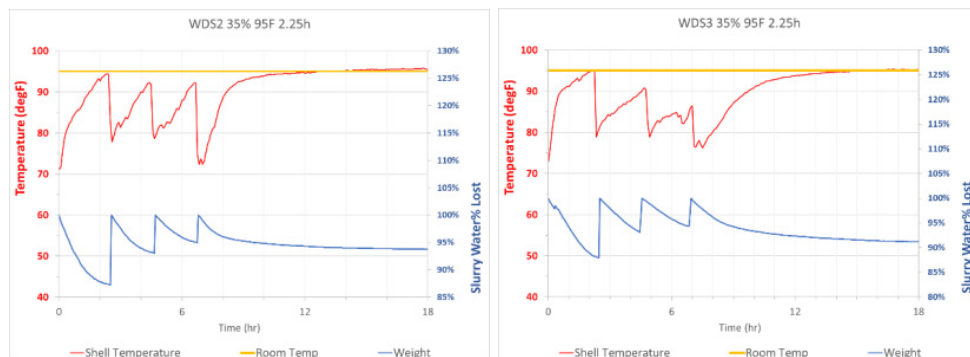


Fig. 4A and 4B. Drying for WDS2/ WDS3 at 35%RH/ 95°F

Figures 5A and 5B report the next higher humidity condition of 50%RH and 65°F. The WDS2 shell appears to have reached ambient room temperature on every dip. However, as the final dip dry temperature achieved 67°F, the author suspects the temperature was off slightly and was set two degrees higher. The WDS3 shell reached ambient temperature on the first dip and again, each subsequent dip reached a slightly lower temperature. As in prior graphs, the shell did reach ambient during its final dry. As WDS3 has an enhanced ability to build each subsequent layer faster and thicker than WDS2, this would explain the greater difficulty of achieving ambient as the shell is built.

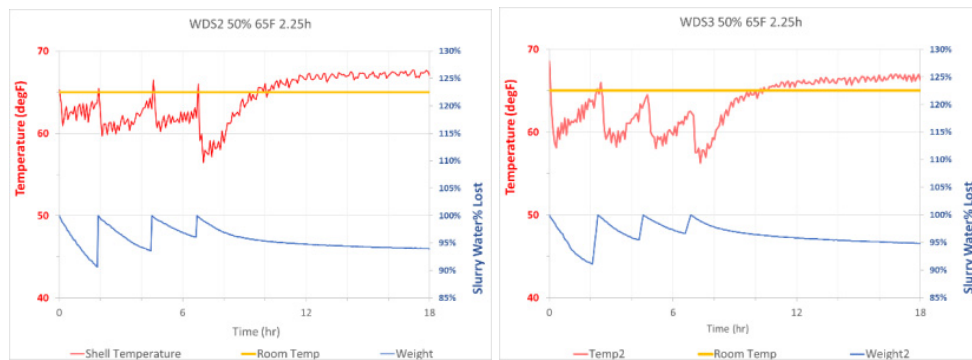


Fig. 5A and 5B. Drying for WDS2/ WDS3 at 50%RH/ 65°F

Figures 6A and 6B show the drying condition of 50%RH at 75°F. Room temperature appeared again to be set 2°F higher than planned. The WDS2 shell did not quite achieve ambient until final dry. WDS3 shell achieved room temperature on the first dip and again at final dry. Other dips achieved only a shell temperature of 70-72°F.

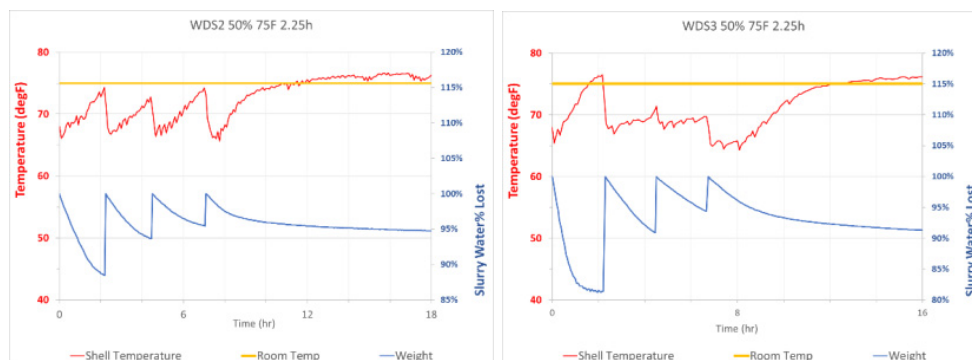


Fig. 6A and 6B. Drying for WDS2/ WDS3 at 50%RH/ 75°F

Figures 7A and 7B are reported for the condition of 50%RH at 85°F. The WDS2 shell attained ambient temperature with the first two backup dips. The third dip nearly achieved room temperature. The WDS3 shell temperature achieved room temperature after completion of the first dip drying. However, the next two dips had only reached 78/79°F instead of the 85°F. The shell did reach room temperature ultimately after seven hours of final dry time on the last dip.

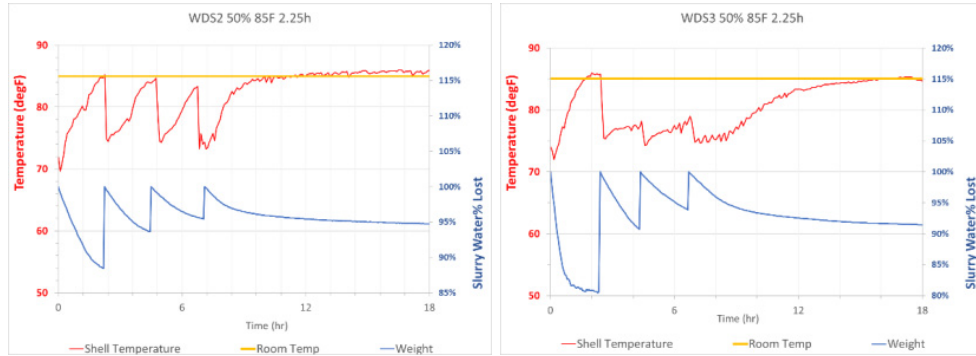


Fig. 7A and 7B. Drying for WDS2/ WDS3 at 50%RH/ 85°F

Figures 8A and 8B report the condition of 50%RH at 95°F. The WDS2 shell attained ambient temperature in the 2.25hr dry time for every dip. The WDS3 shell reached ambient on the first dip but only reached 77-78°F on the second and third dips. Ambient room temperature was reached at 11-hours after the last dip was applied at the 7-hour point on the x-axis.

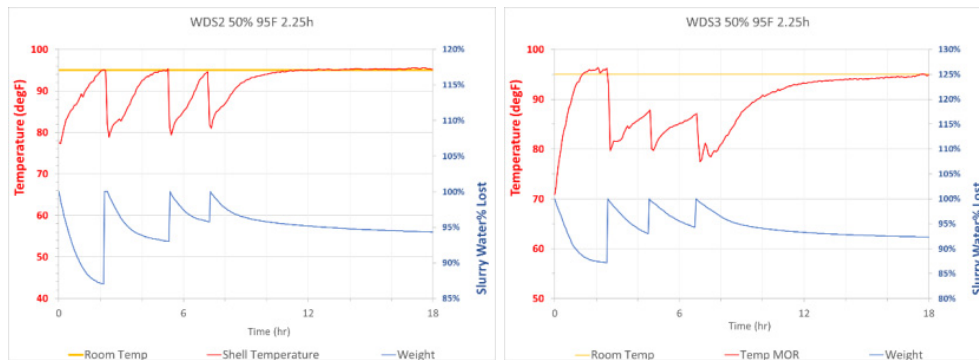


Fig. 8A and 8B. Drying for WDS2/ WDS3 at 50%RH/ 95°F

This next section depicts results for 65%RH, the highest relative humidity examined in this paper. Figures 9A and 9B report the drying attempts at 65°F. The typical sawtooth pattern seen at lower humidity values on WDS2 shells was not seen here. The first dip appears to

have reached near ambient at 64°F. Very little evaporative cooling took place after all of the dips at this temperature. The WDS3 shell showed some evaporative cooling on the first dip but the remainder of the temperature swings remained unclear as shell temperatures dropped from ambient 65°F down to 60°F. Final shell temperature plateaued around 63-64°F. These graphs suggest great difficulty achieving sufficient evaporation with the insufficient thermal energy to liberate the trapped water.

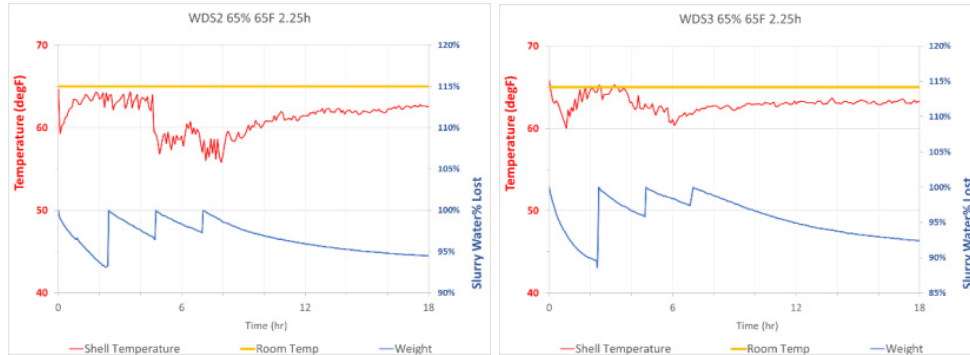


Fig. 9A and 9B. Drying for WDS2/ WDS3 at 65%RH/ 65°F

Figures 10A and 11B report the condition of 65%RH at the somewhat warmer 75°F. The WDS2 drying temperature curve shows some return of the typical sawtooth pattern, but ambient temperatures were not reached until the final dry some six hours later. The WDS3 curve shows a more standard sawtooth pattern and approached 73-74°F. However, it did not quite reach ambient on any dips. Shell temperatures never reached ambient during the final dry either.

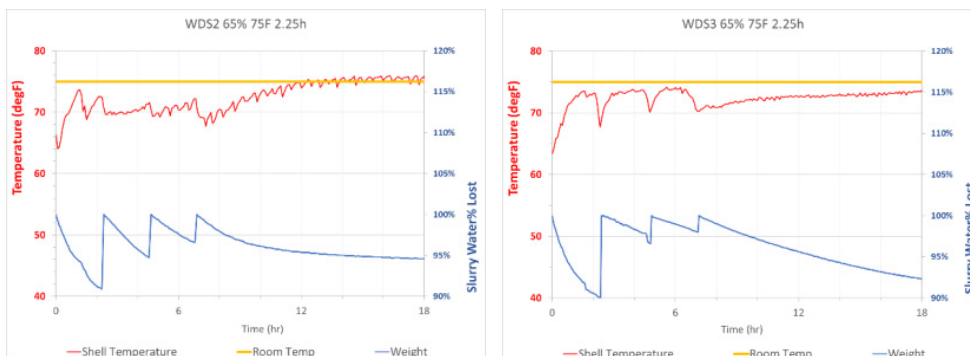


Fig. 10A and 10B. Drying for WDS2/ WDS3 at 65%RH/ 75°F

Figures 11A and 11B report the condition of 65%RH and 85°F. The WDS2 shell attained ambient temperature on the first dip’s drying condition; however, subsequent dips never showed shell temperatures over 80°F. Final shell temperatures reached 84°F. WDS3 shell drying curve showed a very rough sawtooth pattern with little change in overall shell temperature and kept within a range of 77 to 83°F. This data demonstrates the difficulty in drying at this high humidity even with temperatures of 85°F.

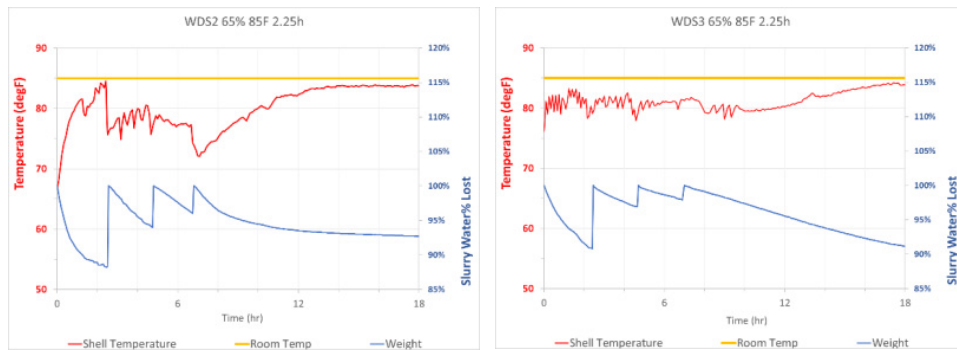


Fig. 11A and 11B. Drying for WDS2/ WDS3 at 65%RH/ 85°F

Figures 12A and 12B report drying efforts at 65%RH at 95°F. The WDS2 shell reached ambient at this higher humidity on the first dip, while subsequent dips reached 90-93°F. Final shell drying condition did reach ambient very quickly approximately 2 hours later. Clearly the increased temperature had a dramatic effect upon removing the water even with this high level of humidity. The WDS3 shell drying curve depicts better temperature curve, although the dry time did not allow it to reach ambient in the 2.25hrs dry time allotted. The shell did reach ambient after six hours. The high water retention (due to greater soak back) demonstrates the need for greater dry times between dips even at this higher temperature.

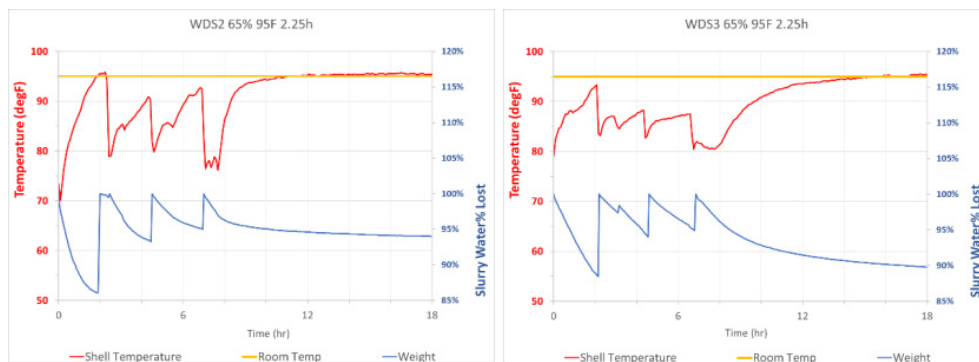


Fig. 12A and 12B. Drying for WDS2/ WDS3 at 65%RH/ 95°F

## 4.2 Shell Performance Data

Shell data from all of these humidity and temperature conditions were run through Minitab 17 statistical software package. This allowed generation of topographical plots to best represent the three-dimensional response surfaces. Due to the nature of Minitab, units are not shown on the graphs but will be listed in the figure description below.

### 4.2.1 Shell Thickness

Thickness of the shells built upon MOR bar substrates is shown in Figures 13A and 13B. The response surface in Figure 13A shows an increase in shell build thickness at lower humidity and temperatures above 70-75°F for WDS2. However, Figure 13B shows a flatter response surface for the enhanced WDS3 shell system. This suggests its shell thickness may be somewhat less sensitive to humidity variation except at the extremes of the humidity conditions tested.

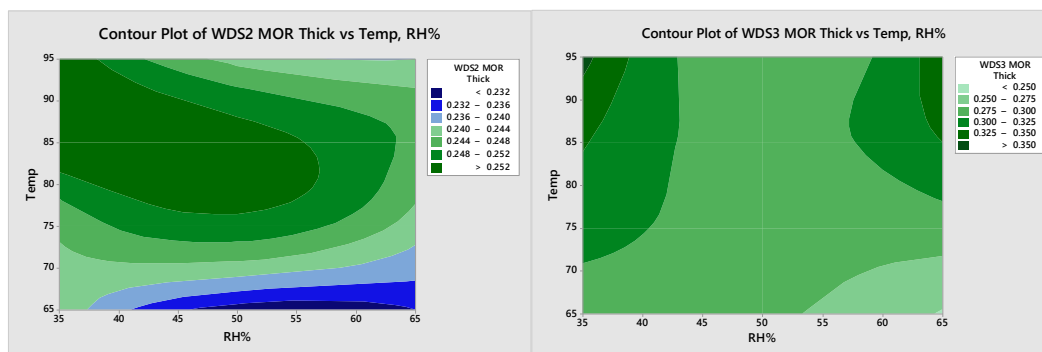


Fig. 13A and 13B. Shell MOR Thickness for WDS2/ WDS3 (in inches).

The shell thickness response surfaces generated from data on the shells built upon PVC pipes is shown in Figures 14A and 14B. Similar to Figure 13A, WDS2 shell thickness showed a significant increase (approximate 20%) in thickness at the higher temperature of 80-90°F over standard baseline conditions (70F/50%RH). WDS3 pipe shell thickness is also similar to Figure 13B with a flat response surface near standard humidity levels and greater build at the extremes of humidity when greater temperatures were tested. It is unclear why high and low humidity would build thicker shells (at the same middle to higher temperatures) for

WDS3. Population sizes were identical at 10 for all conditions and standard error ranges were largely very similar.

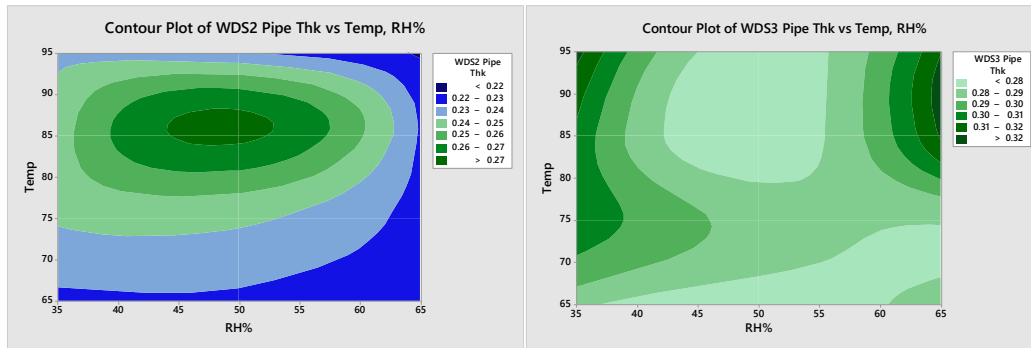


Fig. 14A and 14B. Shell Pipe Thickness for WDS2/ WDS3 (in.).

#### 4.2.2 Shell Permeability

Shell permeability is displayed in Figures 15A and 15B. Permeability of the WDS2 shell systems appears to be optimized at typical shell room conditions of 45-50%RH and 70-75°F. WDS3 shows improvements in permeability at conditions under 45%RH and over 60%RH. The traditional 50%RH in most dry rooms may be where WDS3 permeability performs the poorest, at least for the short dry times studied here.

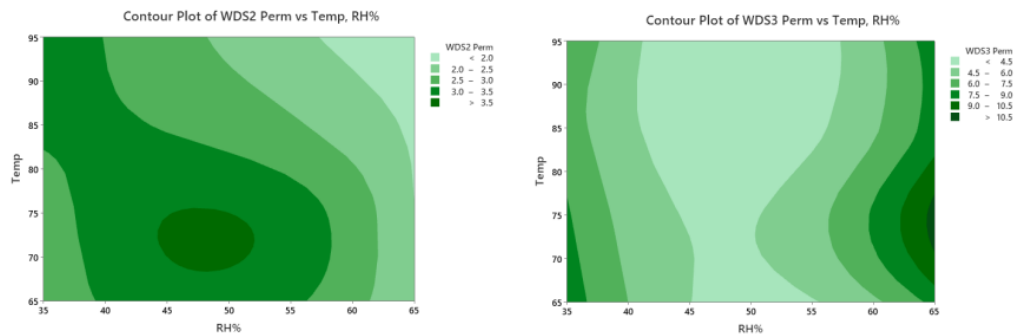


Fig. 15A and 15B. Shell Permeability for WDS2/ WDS3 ( $\times 10^{-10} \text{cm}^2$ ).

#### 4.2.3 Shell Hot/ Wet Burst Strength

After the non-destructive permeability test, shells were boiled for 10 to 15 minutes before being internally pressurized with the same boiling water. The pressure at failure is recorded and used to calculate the hoop strength which is shown in Figs. 16A and 16B for both WDS2 and WDS3 respectively. The weakest shells tested for both these shell systems were built at or near current shell room settings of 70-75°F and 45-50%RH. Increases in temperature

consistently improved burst strengths, well over two fold for WDS2 and up to four fold for WDS3. Recall that the 2.25 hour drying time for WDS3 was actually too short but was adopted to best fit the time envelope available to gather this data.. Strengths should be markedly better with longer dry times for this enhanced shell system. This short dry time was a near worst case condition. However, the trend here is indeed very interesting and worthy of study and consideration by foundries.

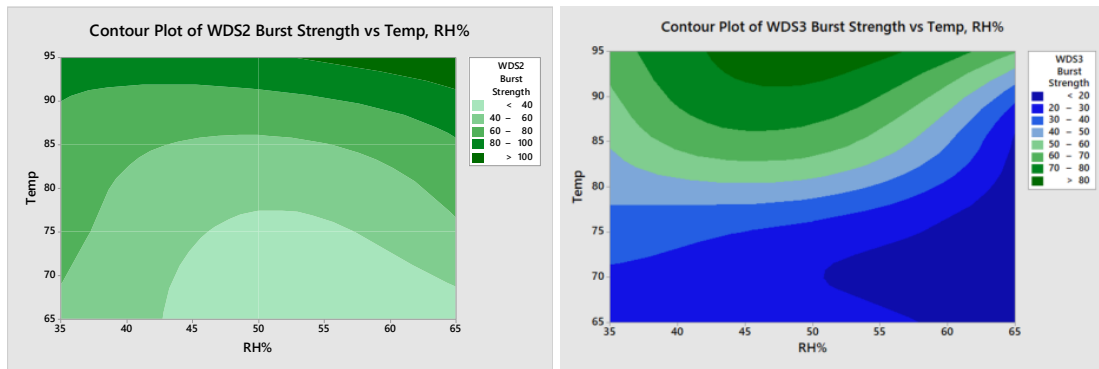


Fig. 16A and 16B. Shell Pipe Boiled Burst Strength for WDS2/ WDS3 (psi).

#### 4.2.4 Shell Green/ Dried Properties

Dried shell conditions were measured next. In Figures 17A and 17B, WDS2 and WDS3 modulus of rupture response surfaces are shown. Similar to what was seen with the hot/wet burst strength, increased temperatures resulted in a two fold increase in strength at some conditions.

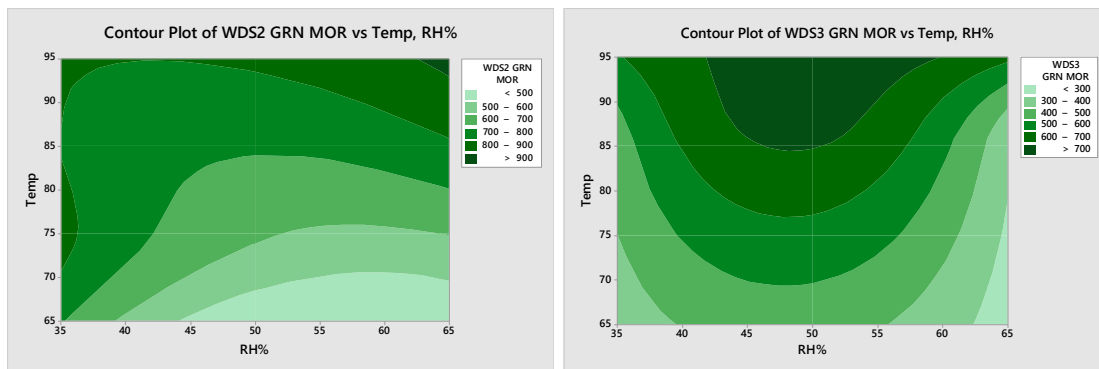


Fig. 17A and 17B. Shell Green Strength for WDS2/ WDS3 (psi).

Shell toughness, or fracture index, is shown in Figures 18A and 18B for WDS2 and WDS3. Toughness for WDS2 was relatively consistent, independent of humidity, for temperatures above 70°F. Toughness of WDS3 also appears to be somewhat insensitive to humidity. This system did demonstrate more sensitivity to temperature as 85-90°F at 45-50%RH is perhaps most optimal for toughness.

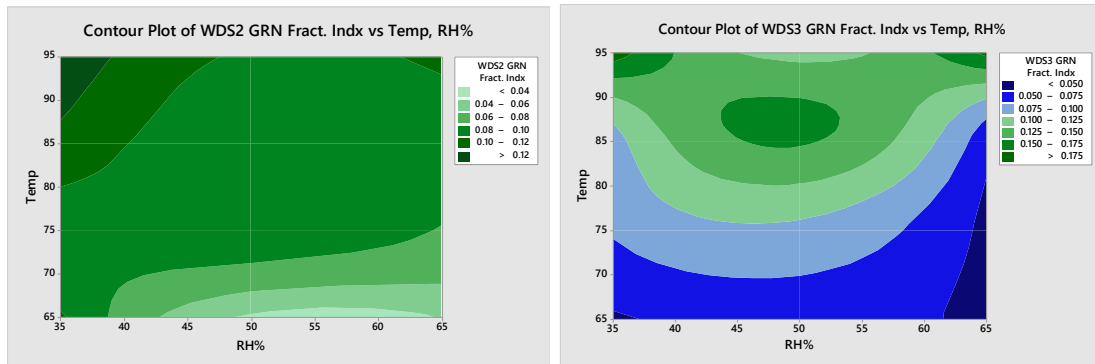


Fig. 18A and 18B. Shell Green Toughness for WDS2/ WDS3 (in-lbs.).

Failure loads are depicted in the two response surfaces in Figures 19A and 19B. Higher temperatures aid in the evaporation of water from the shell for both shell systems and result in higher failure loads at each humidity condition. The failure load for WDS2 increases more rapidly at lower humidity, clearly reinforcing the fact that dryer conditions help build shell load carrying capability. The WDS3 response surface showed that the lowest shell breaking loads occurred at the lowest drying room temperatures. This condition was where the shell system had the greatest difficulty drying. Highest failure loads were measured at 35-55%RH ad 85-95°F.

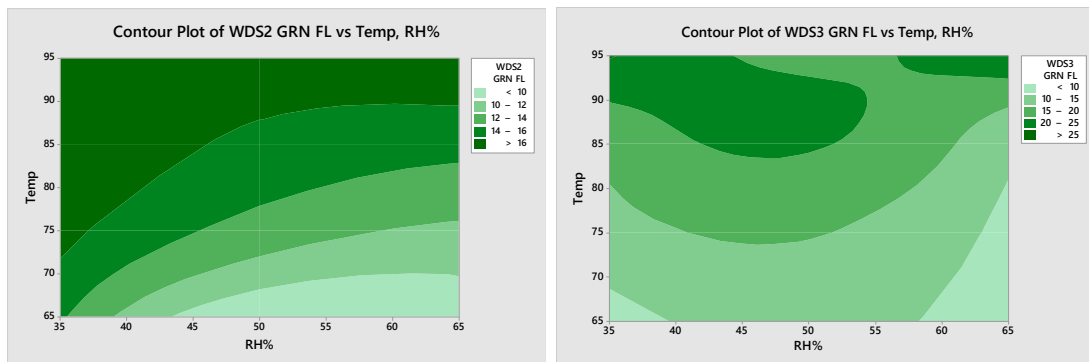


Fig. 19A and 19B. Shell Green Load of Failure for WDS2/ WDS3 (lbs.).

#### 4.2.5 Shell Hot/ Wet Boiled Properties

Next, MOR shell sections were boiled for 10-15 minutes to further assist in a replication of autoclave performance. Response surfaces are shown for both WDS2 and WDS3 in Figs. 20A and 20B. The typical ambient shell room condition of 70-75°F and 50%RH appears to be the low point for hot/boiled strength. Any movement in temperature or humidity away from these typical conditions appears to help the performance of WDS2. Ultimate strength for both shell systems was shown to be at 85-95°F and a range of different humidity values. WDS2 appears somewhat less affected by humidity whereas WDS3's best hot/wet strength may be around 50%RH and 90-95°F.

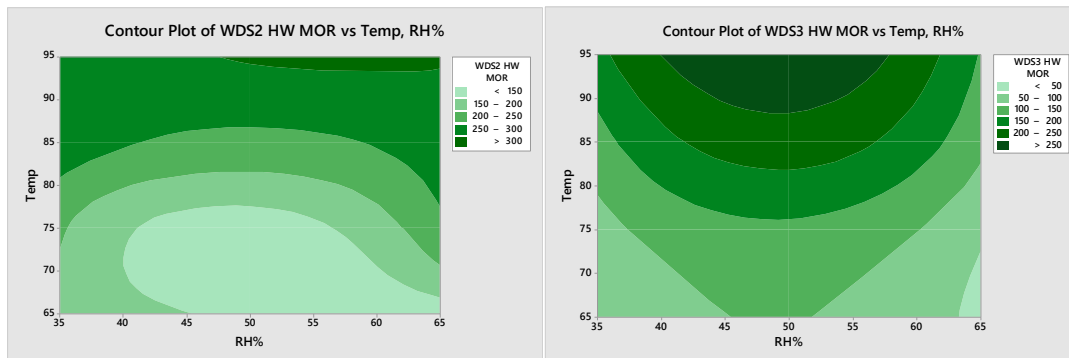


Fig. 20A and 20B. Shell Hot-Wet/ Boiled Strength for WDS2/ WDS3 (psi).

Figures 21A and 21B depict similar response surfaces to Figures 20 A& B. WDS2 may show the best values at 90-95°F at a wide range of humidity and WDS3 may perform best at over 90°F and 50%RH drying conditions. Again, current dry room conditions appear to be the low point for hot/wet toughness, with changes in temperature and humidity resulting in a three or five fold improvement for WDS2 and WDS3 respectively.

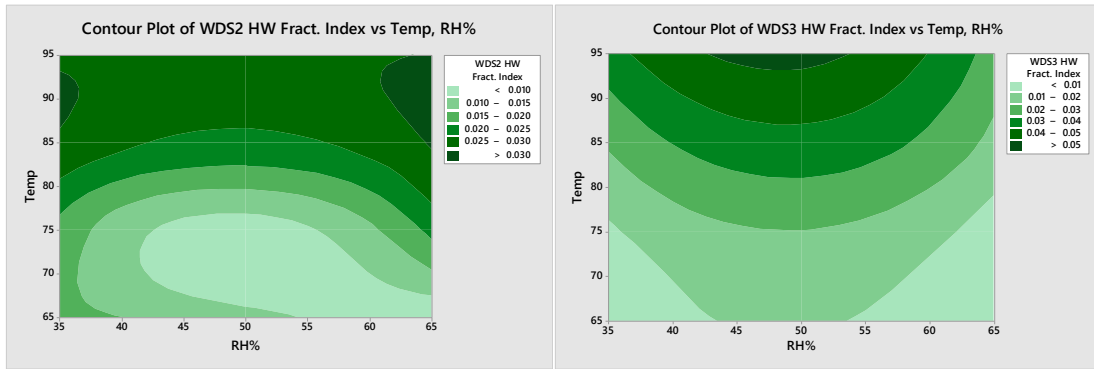


Fig. 21A and 21B. Shell Hot-Wet/ Boiled Toughness for WDS2/ WDS3 (in-lbs.)

Load of failure in the boiled and hot/wet state is shown in the two response surfaces in Figures 22A and 22B. Again the pattern of these surfaces mirrors that seen for toughness and shell hot-wet/boiled strength for both WDS2 and WDS3. WDS2 loads increased by nearly two-fold for higher temperature conditions at a wide range of humidity. WDS3 failure loads increased from 2 lbs. to nearly 8 lbs. with the increase in drying temperature and reflects the inadequate drying for this enhanced shell build system. The effect of the short drying time constraint of this study is realized here.

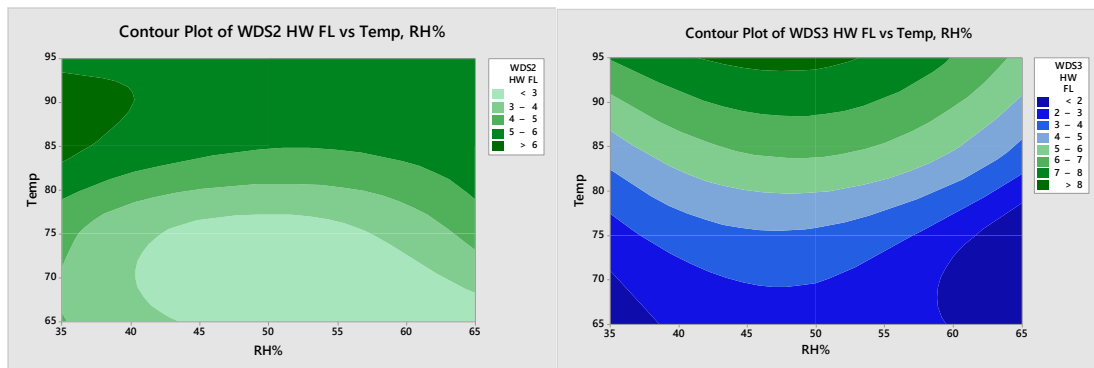


Fig. 22A and 22B. Shell Hot-Wet/ Boiled Failure Load for WDS2/ WDS3 (lbs.)

## 5.0 CONCLUSIONS

- 1- Significant shell property enhancements are possible if higher temperature drying conditions could be implemented for both shell systems.
- 2- While drying, WDS2 is less affected by humidity levels while WDS3 performance is much more sensitive to humidity levels when drying. The greater build rate of WDS3 should be matched with optimum drying conditions.

- 3- Shell thickness for WDS2 was optimized near a traditional drying room atmosphere of 50%RH while WDS3 performed best at both lower and higher humidity but only at higher temperatures.
- 4- Shell permeability may be optimal for WDS2 at traditional 50%RH and 70-75°F conditions. WDS3's best permeability was reported at either much lower or much higher humidity when these short dry times are used.
- 5- Overall shell performance enhancements of 2X may be possible with altered ambient room conditions if foundries can alter processes to take advantage of them.

## 6.0 POSSIBLE APPLICATIONS

- Numerous foundries freeze shells after drying to reduce temperatures by 40°F or so prior to autoclaving to reduce shell cracking. If new wax formulations that allow for higher ambient drying temperatures were used, a similar cooling effect could be achieved by increasing the drying room temperature to 95°F and then progressed into a 70°F autoclave room, creating a 25°F shell cooling effect with little or no additional cost.
- Costs of higher ambient temperatures in northern shell rooms might be prohibitive, but southern foundries would find this to be a cost savings with reductions in air conditioning costs which would multiply the shell cost reductions.

## 7.0 REFERENCES

1. Snow, J, Scott, D. "Shell Drying- Water Based", 46th Annual Technical Conference of the Investment Casting Institute, 1998, pp 8:1-30.
2. Brienza, et. al, "Intercoat Drying and Shell Properties", 65<sup>th</sup> Annual Technical Meeting of the Investment Casting Institute, 2018, pp 6:1-12.
3. Snyder, B., et.al, "Mold Dryness and the Impact upon Shell Strength", 66<sup>th</sup> Annual Technical Meeting of the Investment Casting Institute, 2019, pp 2:1-18.
4. Snyder, B., Snow, J. "A New Combination Shell Strength and Permeability Test", 51st Annual Technical Meeting of the Investment Castings Institute, 2003, pp 11:1- 26.

# **INVESTMENT CASTING INSTITUTE**

## **An Investigation into Misrun Defects in Investment Cast Stainless Steel Castings**

Gerald Richard  
MAGMA Foundry Technologies, Inc.

### **68<sup>TH</sup> TECHNICAL CONFERENCE & EXPO 2021**

Paper No 4

# An Investigation into Misrun Defects in Investment Cast Stainless Steel Castings

Gerald Richard  
MAGMA Foundry Technologies, Inc. Schaumburg, IL  
Anthony Geiger  
Stainless Foundry & Engineering Milwaukee, WI

## ABSTRACT

The Investment Casting industry produces complex castings to near net shape. Regularly, these precision components either have thin walls or thin features that are challenging to fill, which result in misrun defects. Producing these defects is especially problematic because they will likely result in scrap castings due to their inability to be repaired, leading to lost time and high cost. Methods used to mitigate this challenge such as increasing shell and pouring temperatures can be effective, however, changing those thermal conditions are subject to process variation or could even produce defects of their own. Understanding how the melt front cools as it flows through the investment shell cavities, analyzing the temperature and velocity profiles of the flow front while the shell is cooling, and knowing the fluidity of an alloy's impact on the length it can flow given a section thickness will provide the tools needed to gain insight as to why these defects develop and how to eliminate them. In this paper, the various parameters needed to understand and combat misrun defects will be discussed.

## Introduction

There is increasing demand from casting designers to produce lightweight, thin-walled castings which is incentivized by one major factor with a few different implications. The major factor is that thin-walled castings are

lighter weight. If the end component is going into an application where fuel consumption is used or there are loading limits are imposed, light weight become paramount. There are cost implications associated with casting weight as well. Castings are often sold on a per pound basis and so lighter castings are cheaper and use less materials to produce, and if there are shipping cost or any other cost aligned with weight, castings are better lighter. Even so, there are many complicated technical challenges involved in producing castings with smaller and smaller section sizes. Misrun and other non-fill defects can impose limits to how thin we can make a casting given a specific process. When those challenges arise in the foundry, engineers have to understand all of the relevant effects that lead to challenges with filling a casting and how to combat them. Misrun is a complex defect with physical, chemical, and thermal causes. A challenge for the foundry engineer is to determine the root cause of the defect and execute necessary measures to combat the defect while also minimizing any negative effects produced by the solution. With looming deadlines for casting shipments and incentives to find quick fixes for defects that result in scrap castings, a typical approach of steadily increasing the pouring temperature or telling the pourer to "pour it faster" becomes the strategy for many. However, understanding the cause of the defect will allow us to analyze and weigh potential solutions that are more effective and suffer less shortfalls in the long run. Before we get into

temperature, velocity and other parameters, we must begin with the physical characteristic of the material itself that will dictate flow, fluidity.

## Fluidity

In physics, fluidity is defined as the inverse of viscosity, however in casting, fluidity is described as the ability of a given material to flow a certain length given a certain section thickness. Many factors influence how far metal can flow including temperature, velocity, local air pressure, metal chemistry, among other factors. Let's first turn to the alloy composition and note the effects it plays on fluidity.

**Alloy composition** plays an important role in the fluidity of the material. Different alloys have different fluidity profiles depending on alloy makeup. Pure metals or alloys closer to the eutectic composition tend to have a higher fluidity than their larger solidification range counterparts due to the nature of their solidifying front (1). Even within a particular alloy, elemental changes can have an effect on fluidity. For example, when pouring certain steel alloys, foundries may increase their addition of silicon or in other words run silicon higher on the chemical range for silicon to increase fluidity in the alloy.

**Shell composition** and makeup will have an effect on fluidity in a few different ways. The permeability of the shell is greatly important in the efforts to fill out thin sections, which will be discussed in detail later in the paper. Another factor is the surface that makes up the internal cavity of the shell. The coarseness of the prime coat or any ash that may remain in the shell cavity are sources of friction, which by definition, resist flow. Imagine pouring water onto glass vs sandpaper and ignore any wetting effects. You intuitively know that water will flow with ease on glass but slow and laborious on sand paper. In a similar way,

albeit less drastic, the effect can be seen when pouring shells of different surface roughness.

**Viscosity** is the measure of a fluid's ability to resist deformation at a given shear rate. Put another way, it is a measure of how "thick" the material is; the classic example being water vs honey. Generally speaking, many alloys have similar viscosities when they are fully liquid, making the difference negligible in many cases. However, things change once the metal begins to solidify or if the material forms solid stable oxides. Solidification rates and the solidification morphology changes the viscosity of the material and its ability for flow through thin sections as well as oxide films on film forming alloys.

**Oxides and oxide films** also have an implication to fluidity. Aluminum for example forms a very stable oxide film on its surface which, combined with its surface tension, can have a profound influence on the flow characteristics of the material. As discussed earlier, sources of friction can restrict the flow and even "thicken up" the material. Some materials have a sludgy appearance during filling due to their interaction with the atmosphere and the formation of oxides and oxide films. Pourers will tell you that these alloys are difficult to pour and the result can be defects in the casting.

An effect not often considered is **capillary repulsion**, the opposite effect of capillary action, which becomes important due to the non-wetting effect of the shell (1). The adhesive forces, molecular attraction between unlike molecules, is less than the cohesive forces, intermolecular bonding, in casting which pulls the material into itself rather than pulling the material through a section by "gripping" the walls.

**Measuring fluidity** is not done frequently in the foundry, but there are tests that are

used and have been performed to measure fluidity. The fluidity spiral is probably the most well-known and is a mold that has a constant thickness that forms a spiral, mainly to limit the size of the mold you would need to produce, and after the metal is poured you measure the length that the metal traveled; that's your fluidity. Another test is pouring linear sections but of decreasing thicknesses. The idea that you will get to a thickness where the metal will not be able to travel very far and the information you can obtain is both your minimum thickness that you can pour and the length at which you can fill that thickness.

## Temperature

Temperature is by far the first thing that is considered when addressing misrun defects or even figuring out if you would be able to pour a given section size or not. There are however many different temperatures one must know and the first is pouring temperature. **Pouring temperature** is the temperature at which the mold begins to fill. One thing to point out here is that pouring temperature is different from tap temperature and can be different for each shell if multiple shells are poured out of a given heat. Using a lip pour or teapot ladle is an efficient way of delivering liquid metal to the shell but during the pouring process metal is rapidly losing temperature as the pourer fills the shells. Depending on how many shells are being poured at once and the pour weight, there would be losses as high as 100°F in temperature out of the ladle. Knowing what the actual initial temperature is, is important when determining the root cause of the misrun defect. Furnace pouring somewhat eliminates this issue, but presents challenges in shell handling, setup on the pouring floor, and control of the metal

delivery. Pouring practices will be different depending on how the foundry is setup, but knowing your process will be a key factor in determining what your temperatures should be. To know better what the pouring temperature should be for a given alloy and process, one must first consider other important temperatures of the material.

**The liquidus** temperature is the temperature at which the metal begins to solidify. As the metal cools below the liquidus temperature, solidification starts and solid fraction increases. Just under the liquidus temperature however a stable dendritic network hasn't been formed yet and so although there is solid phase starting to grow, the material maintains its ability to flow; albeit with increasing difficulty as solid fraction increases. A pouring temperature is usually determined by how many degrees above the liquidus temperature a particular alloy needs to be poured at to fill out the cavity. This temperature difference between the pouring temperature and the liquidus temperature is called the superheat. The superheat is sometimes determined with trial and error and is based on the experience of the foundry as well as industry guidelines. However, this doesn't mean that the accepted rules cannot be challenged. As we will see later, there may be methods to explore to lower the pouring temperature and maintain a full casting tree at the same time. As solid fraction continues to increase during the solidification process however, there will come a point where the metal no longer has the ability to flow. This point at which the flow of material essentially stops in dendritic materials is called its coherency point.

**The Coherency point** is where dendrites in a material form a coherent structure that can inhibit or eliminate the ability for the material to flow. Even though the material is not 100% solid, it can no longer flow any reasonable length to fill out a section. Flow

essentially stops and is frozen in the state that it is left in. An exception that is worth pointing out is when the pressure is sufficiently high. Similarly to a fluid passing through a porous medium, given enough pressure to overcome the pressure drop created over the small length scale of high solid fraction material, the remaining liquid metal can be forced to move. The amount of pressure needed would be dependent on the solid fraction and other external forces that may exist. As the metal continues to cool through the solidification interval it reaches its solidus temperature.

**The solidus temperature** is the temperature at which the alloy material is 100% solid. At this point, metal has no ability to flow and will remain quite literally frozen in place. Even though the coherency point is the important stop condition to consider when evaluating misrun, knowing the solidus temperature caps off the freezing range and along with solidification rate can help determine how quickly the material will transition through this temperature interval.

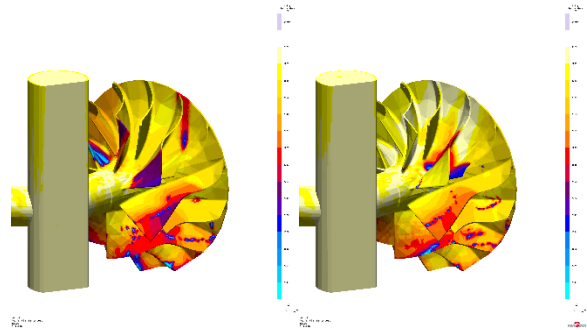


**Figure 1.** *Effects of changing pouring temperature.*

However, there are a few problems with increasing the pouring temperature that must be weighed against other factors before committing to this route. Firstly, when you increase the pouring temperature you will also need to increase the tap temperature, and further still, increase the melting temperature. Increasing the melting temperature can have a few detrimental effects such as damaging furnace lining or crucible and thus decreasing its life, increasing the damage of the liquid melt due to absorption of gases and oxidation at high furnace temperatures, among others. Secondly, when you increase the pouring temperature you can also have debilitating effects during mold transfer and mold filling. Similar to the furnace, the ladle lining and protection of the liquid melt is needed during metal transfer. Air can be entrained at a higher rate and oxidation more readily when the temperature is higher. Further, the temperature could not be the root cause of the issues. Issues with shell permeability or low velocity while filling the casting cavity could also be at play. The superheat applied to the melt must be minimized while maintaining sufficient temperature to battle heat extraction during mold filling and so other factors must be considered in addition to filling temperature must be evaluated.

**Shell temperature** works in tandem with pouring temperature because if you pour hot material into a cold shell, non-fill defects would almost be certain; not to mention cracked shells. What gives investment castings an advantage over sand casting is the ability to heat up the mold. Filling up a shell at elevated temperatures allows for thinner sections to be filled out that wouldn't be achievable in sand casting. However, there are limits to this. You may be limited by how hot your preheat furnace can operate at consistently and with limited maintenance. You may also have limits in shell transport. The shell needs to come out of the furnace and poured as quickly as possible. The longer there is a delay, the more the shell cools and can contribute to misrun defects.

## Velocity

The velocity of the melt, or how fast the metal is moving in a given direction, can determine if the casting cavity or thin features are filled. Even if the metal arrives at the gate at a sufficient temperature, metal moving through thin sections at slow speeds can aid in the heat extraction of the shell and plunge the temperature of the advancing melt front sufficiently low to labor the flow and ultimately stop it. Conversely, increasing the velocity of the advancing metal front can be an effective way of filling out casting cavities. As mentioned prior, even at temperatures below the liquidus temperature, if the metal is moving a sufficiently high velocity, momentum will move the material through thin sections, provided there isn't resistance to flow like the accumulation of local air pressure or capillary repulsions.

One way to increase the velocity leading into the casting cavity would be to angle the gates to take advantage of the increase of velocity due to the falling stream. If the

gates are horizontal the metal will need to move down and across to enter the cavity. Minimizing that 90° turn and allowing the metal to run downhill will help the metal fill out the cavity. Of course, dewaxing challenges must be considered.

Another way to increase the velocity at the gate is to decrease the cross sectional area of the gate. Given a constant flow rate decreasing the cross sectional area of a gate will increase the velocity through that gate due to continuity, which will be discussed further below.

In some cases, the speed of the moving metal front doesn't need to be changed, but the direction of the metal. Figure 2 shows metal filling an impeller casting on a 48 on tree. The image on the left is a still image of the velocity profile with vectors added to the image to show the direction of the moving metal. The image to the right shows the casting shape for clarity. In the image to the left, you can see higher velocities in the yellow and white colors as well as the lower velocities in the shades of blue. As the metal enters the casting cavity from a vertical position. It swirls in the center of the cavity until moving outwards towards the impeller vanes. The changes in direction the metal must undergo makes it difficult maintain a higher velocity as the metal reaches the impeller tips. Changing the flow pattern in the cavity will improve the ability to fill out the vanes.

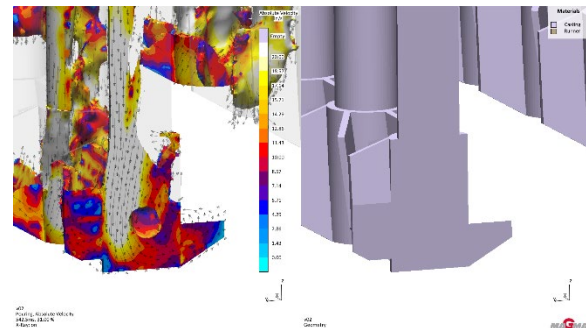


**Figure 2.** *The velocity decreases as it reaches the impeller vanes due to the flow direction of the metal in the casting cavity.*

The problem with increasing the velocity is turbulent flow. Turbulent flow, in this case referring to an erratic filling pattern, can increase the surface area of the metal in contact with air and thus cooling the metal faster. Another challenge is as you increase the surface area in contact with air, oxide forming alloys can be damaged and inclusions will become a problem. So balancing an increase in velocity to fill out a cavity vs potentially inclusion formation need to be considered. A parameter related to velocity but should be interpreted on its own is the pouring rate.

**Pouring rate**, which is the rate at which the metal is delivered to the shell cavity and is typically measured in lbs per second. Metal delivery becomes important because a relatively constant flow rate needs to be supplied during the pouring process. Any interrupted pours or drastically changing pour rates can have a substantive effect on the ability to fill all castings on the tree. Sometimes pouring rate and velocity are used interchangeably in foundry settings, which is not correct. It is possible to pour at a higher rate but achieve lower velocities if the cross sectional area you are pouring through increases. This fact is due to continuity, a fundamental physical phenomenon derived from the conservation of mass. However, when you keep the cross sectional areas the same and increase the pouring rate, you will in turn increase the velocity and so understanding those effects both with production tooling or during sampling where gate sizes and locations can change becomes important.

## Cavity Air

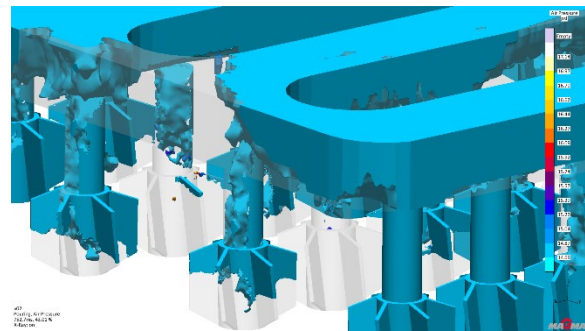


**Figure 3.** *Air must be evacuated and displaced by the advancing metal front. Failure for this to occur either restricts the metal from flow or penetrates into the melt.*

If your permeability is low, the metal can't escape out of the cavity fast enough through the shell walls causing an increase in air pressure. That increase in air pressure, if high enough, can resist the advancing melt front halting its progress, which can lead to a misrun. One way to help fill out a thin section is to increase the permeability of the shell. If the permeability is increased, the metal can displace the air out of the cavity with relative ease and the local pressure does not increase. Another method is to add vents. Venting isn't typically in investment casting, but cavities used for dewaxing can serve as vents if placed appropriately.

A negative effect of increasing the permeability of your shell could be surface

finish issues. A small sand grain structure on the surface produces a remarkable finish, but at the same time, it doesn't leave channels open for air to flow through. Changing the makeup to find an appropriate balance of surface quality and permeability is needed.

## Pressure

Pressure, usually in the form of metallostatic head in gravity casting application, is often not considered when evaluating misrun defects. As mentioned in earlier sections, increasing pressure can help fill out sections even if the metal has fallen into the solidification interval. The faster you can fill the tree before metal begins to enter the casting cavity for example, the more head you will have while filling the cavity and thus will be able to fill challenging features. At the same time, the lower the metallostatic pressure during filling, the more difficult it will be to prevent misrun.

## Conclusion

Misrun defects are complex and there are many factors that play a role in its occurrence. Evaluating temperature, velocity, air components, among other things will allow the foundry engineer to discover the root cause of the issue and find more effective solutions to increase the quality of the part but minimize any detrimental effects a solution may cause.

## References

1. John Campbell, *Complete Casting Handbook Metal Casting Processes, Metallurgy, Techniques and Design* (Oxford, UK: Elsevier Butterworth-Heinemann, 2011).



# **INVESTMENT CASTING INSTITUTE**

## **AM4IC Report Out**

Gerard Thiel  
University of Northern Iowa

## **68<sup>TH</sup> TECHNICAL CONFERENCE & EXPO 2021**

Paper № 5

**AM4IC – Report Out**  
**Gerard Thiel**  
**University of Northern Iowa**

AM4IC - A Symposium on Additive Manufacturing for Investment Casting was hosted by the University of Northern Iowa, an ICI Allied Member. AM4IC included a tour of the UNI Additive Manufacturing Center, six presentations by industry leaders and a joint meeting of the AFS and ICI committees addressing additive and pattern manufacture. Foundries and suppliers serving the investment casting industry were invited to attend. It was held on October 5, 2021, at the University of Northern Iowa.



# **INVESTMENT CASTING INSTITUTE**

## **Optimization of an Aerospace Casting: A Case Study**

Tom Mueller  
Mueller Additive Manufacturing Solutions

## **68<sup>TH</sup> TECHNICAL CONFERENCE & EXPO 2021**

Paper № 6

# Optimization of an Aerospace Casting: A Case Study

Thomas Mueller

Mueller Additive Manufacturing Solutions, New Berlin, WI

## ABSTRACT

Solidiform, an aluminum aerospace investment casting foundry in Fort Worth, Texas has been casting an aircraft instrument housing for a defense supplier customer. Solidiform's customer was looking to reduce weight on the aircraft the housing was used on with the objective of reducing fuel consumption. Using topology optimization and printed patterns, the company was able to present a design that would bring the company annual fuel savings.

## INTRODUCTION

For the past few years, Solidiform, an aluminum aerospace investment casting foundry, has been casting an aircraft instrument housing for a defense supplier, shown in Figure 1. While it was not a huge order, there was a consistent demand and when orders were down, Solidiform's VP and General Manager, Larry Andre, could work ahead on the order to fill in gaps in the foundry schedule.

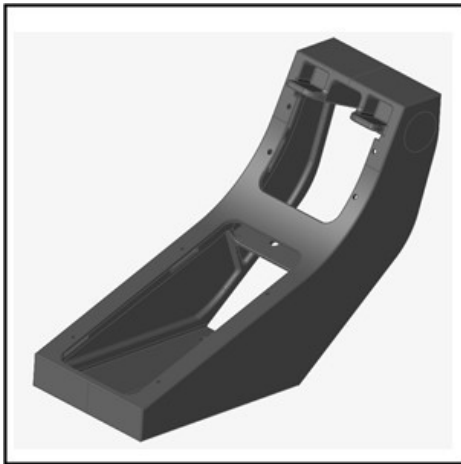


**Figure 1. The original design of the aircraft instrument housing.**

*(Note: Because the component is from a military aircraft, Solidiform was not allowed to identify either the component or the aircraft. For this paper, the analysis was repeated on a very similar but different casting.)*

The customer let Larry know that they had begun a major effort to reduce weight on the aircraft the housing was used on with the objective of reducing fuel consumption. All non-critical structural components were being reviewed for light-weighting potential and the component that Solidiform provided was a prime candidate. Sheet metal and injection molded replacements were being considered. It seemed likely that the casting would be phased out.

To prevent losing the customer, Larry decided to be proactive and look for a way to redesign the casting to reduce the weight. He had heard about topology optimization methods to reduce weight of components without compromising strength but did not know much about it. With the help of a friend, Larry pulled together a team to explore the potential project.

It became clear that there were three requirements for the project. First, an optimized design must significantly reduce weight without sacrificing functionality of the component, including strength and durability. Second, the optimized design must be manufacturable, although not necessarily by conventional means. Finally, the optimized design must provide better value than the current design. It may be more expensive than the current design but could provide benefits that outweigh the increased cost.

Three companies teamed with Solidiform in the project. First was Altair, a company with a history of experience in topology optimization with its Altair OptiStruct™ software. They agreed to assist in the optimization as well as the manufacturability objectives as a demonstration project. The second company was Ultimaker, a 3D printer company leading the development of low-cost printed patterns for investment casting. The third company was Polymaker, a supplier of additive manufacturing materials who had developed a filament specifically for investment casting. The four companies worked as a team to redesign the casting to meet the customer's requirements. The following six-step process was used for fulfilling the project.

1. Determine design stress limit
2. Optimize the design
3. Verify manufacturability
4. Create prototype casting
5. Estimate value of design change
6. Propose optimized design to customer

## PROJECT STEPS

### DETERMINE DESIGN STRESS LIMITS

One of the requirements of the optimization process is to have a stress limit that cannot be exceeded under load. This was information that the team did not have access to. Consequently, it had to be estimated. There were two load cases that needed to be considered. First was the load exerted on the housing by the instruments themselves undergoing g-forces. Design forces were estimated based on maximum g-forces expected and instrument weights. A finite element model of the current design was created, and the estimated forces were applied to the model to predict the stresses in the casting, shown in Figure 2. If the resulting stresses were well within design limits for the material, then the team could be confident that their estimate of loads was reasonable. The stress was determined to be 79MPa. The Solidiform team also learned from their contact at the company that an abuse load needed to be considered. The instrument housing was located in a position where it became a convenient footrest for pilots and early housings had failed under that load. This load was also modeled and a maximum stress of 121MPa was predicted, well under the yield stress of the E357 aluminum material. These values were assumed to be the stress limits of the component.

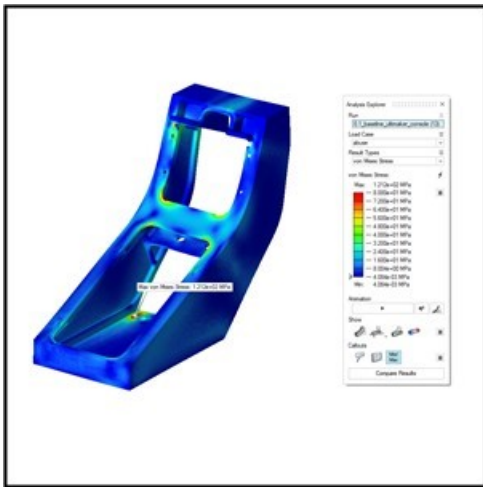


**Figure 2. The stress contour plot of the original design shows where stresses occurred in the casting.**

### OPTIMIZE THE DESIGN

The first step in optimization was to determine constraints for the optimization process. Locations for attachment points such as bolt holes were defined (illustrated in Figure 3) and became fixed features in the model. It was also necessary to define such things as minimum wall thickness, minimum fillet radii, etc. Once the constraints were defined, Altair could begin the optimization process

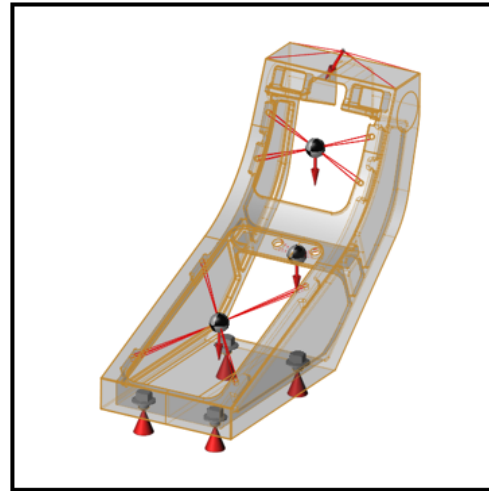


**Figure 3. The load and constraint points were defined on the model.**

Altair's Inspire™ software was used for the design optimization. This simulation-driven design tool leverages the OptiStruct™ engine for structural analysis and optimization in an intuitive, designer-oriented interface.

Optimization is an iterative process. In simple terms, loads are applied to a finite element model of the component and stresses throughout the model are predicted. Wherever stresses are low, material is removed from the model. Wherever stresses are high, material is added to the model to reduce stress levels. The analysis is then repeated on the modified model. This process is repeated dozens or even hundreds of times to reach an ideal optimized geometry, and all the calculations and iterations are completed by the tool automatically.

The optimized geometry is often organic in appearance, sometimes looking very much like a bone structure. Because there are no constraints related to being able to manufacture the geometry by conventional manufacturing methods, the optimized geometry is often not easily manufactured.

In the Inspire™ software, a user can indicate the manufacturing process that will be used to manufacture the component and the system will specify constraints for that process. For example, for investment casting, a minimum wall thickness might be specified. The software will then optimize the geometry within the constraints of the manufacturing process. Without the constraints, the optimized design might not be manufacturable by the selected process

Figure 4 shows the optimized geometry that Inspire™ software produced. The surface of the optimized model is often rough as evidenced by this model. To create a smoother surface, Inspire™ has the capability to automatically generate smooth geometry that satisfies both structural and manufacturing requirements.



**Figure 4. The original optimized geometry produced by Inspire.**

Figure 5 shows the optimized geometry after smoothing was applied to the model. Solidiform suggested that a small strut between the sides of the casting be added to minimize distortion of both the printed pattern and the casting. The strut would be removed from the finished casting. The optimized casting would weigh 1.66 pounds, a reduction of 3.06 pounds. This 65% reduction in weight far exceeded the customer's goal.



**Figure 5. The optimized geometry produced after smoothing.**

#### VERIFY MANUFACTURABILITY

Although the optimization results were successful, there were three significant issues related to casting the optimized design. First, the design was complex and not easily moldable. While it may be possible to create a tool to mold wax patterns, it would require many loose inserts to create all the undercut features of the pattern. Not only would it make the tool prohibitively expensive, the time

required to assemble all the inserts into the tool prior to wax injection and disassemble them after injection to remove the pattern would significantly increase cycle time, reducing capacity and increasing pattern cost. Consequently, it would be necessary to use printed patterns.

While Solidiform has extensive experience with printed patterns, most of the foundry's usage was for prototype castings, not production. Their customer typically ordered 500 of these castings annually or roughly 10 castings per week. Ultimaker calculated that three printers, at a cost of about \$6,000 per printer, could supply that level of production.

Second, the optimized design was challenging to cast. There were two potential casting issues: filling and shrink voids.

**Filling** - Much of the geometry was thin struts. The issue with thin struts is that unless properly gated, they will freeze off quickly and may prevent a complete fill of the mold.

**Shrink voids** - The thin struts also presented a higher probability of shrink voids than for most castings. Shrink voids are created when metal shrinks during solidification and there is no molten metal available to fill the space created by the shrinkage. There are thicker areas in the geometry where the thin struts come together. The risk is that the thin struts will solidify quickly due to their thin cross section. That may leave the thicker section still molten and isolated from any supply of molten metal to fill the volume made available due to solidification shrinkage. The resulting voids will reduce the strength of the component and create a point of potential failure.

Finally, there are demanding quality requirements for the casting and meeting these metallurgical and radiographic requirements for the casting had the potential to be challenging. The customer required the castings to meet Class 4 Grade D qualifications per AMS 2175. This requirement is typical for non-critical structural aircraft components.

The Solidiform team created a gating design, shown in Figure 6, based on their decades of experience with aerospace casting. While they were reasonably confident that the gating design would result in an acceptable casting, it was different than anything they had cast in the past. Altair offered to model the gating design and do both a filling and solidification simulation using Inspire Cast, a complete manufacturing simulation solution for all types of casting processes. Utilized early in the design process, users can visualize common casting defects such as air entrapment, shrinkage porosity, cold shuts, or mold degradation within the module. The tool allowed them to quickly determine whether the gating design would result in a casting filled completely and with no shrink voids. If

those conditions were met, they could be reasonably sure that the casting would meet radiographic and metallurgical requirements. Figure 7 shows the filling and solidification analysis at several points in a 4 second fill and subsequent 25-minute solidification. The analysis showed that the mold could be filled without excess turbulence and solidify without significant porosity or residual stress.



Figure 6. The gating design created by the Solidiform team.

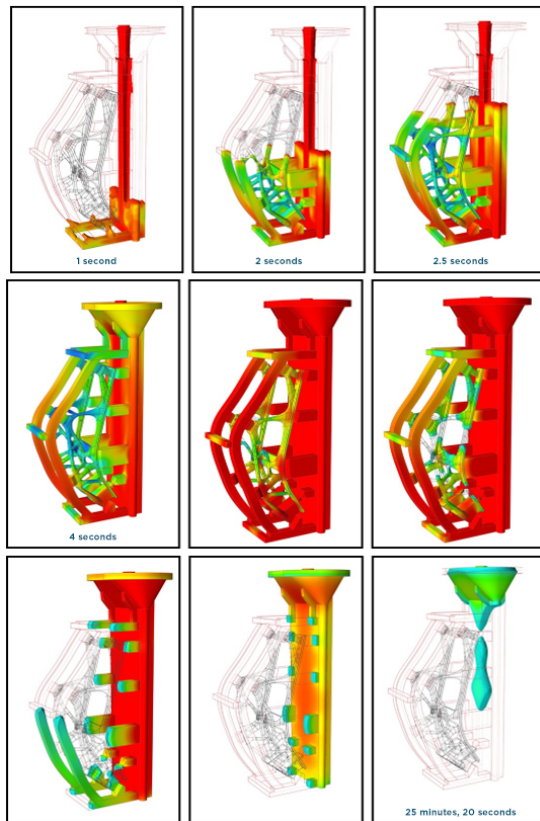


Figure 7. Altair Inspire Cast produced the filling and solidification analysis, shown here at several different points.

Figure 8 shows the volumetric shrink cavities predicted by the Inspire Cast software. The only shrink cavities predicted are in the gating, not in the casting itself.

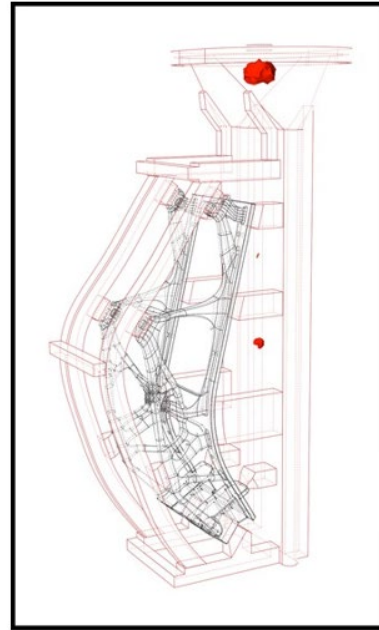
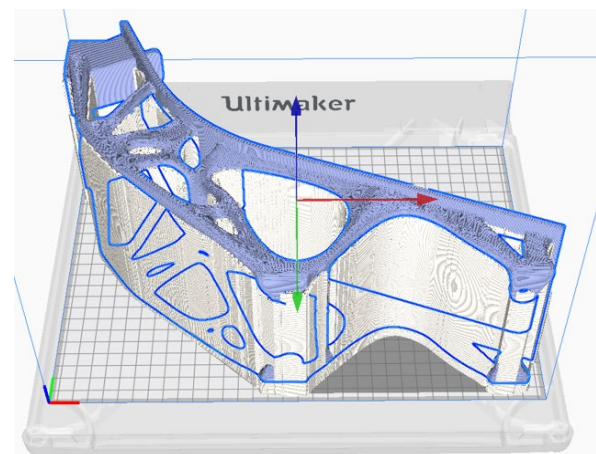


Figure 8. The predicted porosity within the gating is shown.

With the assurance that printed patterns could be made fast enough to meet production demand and that an acceptable casting could be created with the proposed gating system, the team decided to proceed to the next step.

CREATING A PROTOTYPE CASTING

Ultimaker provided patterns for the optimized casting design. They were printed using PolyCast, a filament designed specifically for investment casting. Initially, they planned to print the pattern as a single piece, illustrated in Figure 9.



**Figure 9. The print time and support material needed for the original design, shown here, was very high.**

Analysis showed, however, that because of all the supports required, building the pattern in one piece would take 66 hours and require nearly \$48 in material. If they instead built the pattern in two halves, both the build time and material required would be cut by more than half. In addition, post processing time would be cut dramatically. They decided to build the patterns in two pieces and assemble them to create the finished pattern, illustrated in Figure 10.

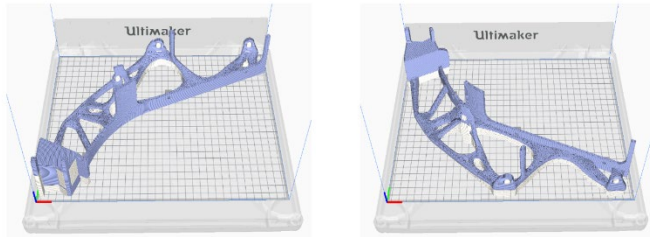


**Figure 10. The modularized design of the two printed pattern parts.**

The Solidiform team then assembled the printed pattern to a sprue using the gating design, illustrated in Figure 6. The result of the final printed pattern is illustrated in Figure 11.



**Figure 11. The printed investment pattern of the aircraft instrument housing.**

For the investment casting process, Solidiform had to take into consideration that casting printed patterns requires certain modifications to be made to the traditional process. When casting printed patterns, the company has developed a process for casting that uses a flashfire de-

wax system to both eliminate wax components of the assembly and burn out the printed pattern.

For this project, the Solidiform team first tested their process on sample Ultimaker patterns and discovered no issues. They then used their normal process to cast the optimized casting pattern supplied by Ultimaker.

When using molded wax patterns, Solidiform uses an autoclave for the de-wax step. Using some sample patterns, they tested whether they could have used an autoclave to remove the wax components of the assembly and then burned out the pattern in a pre-heat furnace. They were able to do that without damage to the shell. They concluded they could use the same casting process that they use for molded wax patterns.

Figure 12 shows the resulting casting. After radiographic testing, the Solidiform team was pleased to see that not only did the casting meet Class 4 Grade D requirements, but it also met the more stringent Grade B requirements.



**Figure 12. The the optimized casting.**

**ESTIMATE VALUE OF DESIGN CHANGE**

The question of value would be critical in the customers' decision of whether to adopt the new design. Would the fuel savings resulting from a three-pound reduction in weight offset a potential increase in production cost? It was a question the engineering team needed to be prepared to answer. They needed to determine whether there would be an increase in production cost and if so, how much. They also needed to estimate the savings in fuel costs resulting from the weight reduction.

The cost of the molded wax pattern including injection cost, the cost of wax, and allowance for scrap was \$22.79. It can be argued that the cost should also include amortization of the wax pattern mold, but in this case, the tool had been paid for at the beginning of production. If tool amortization were added to the cost, it would increase

the cost of molded patterns and thus reduce the cost of changing to the optimized design.

The estimated cost of the printed pattern including the cost of printing and the cost of both pattern and support materials was \$120.85. The printed pattern was \$98.06 more expensive than the molded wax pattern. This is partially offset by savings in metal cost. The optimized design used 3.06 less pounds of aluminum which saved \$5.36. The net increase in cost was then \$92.70.

Because it had been determined that the same process could be used to cast the printed pattern as was used for the molded wax patterns, the cost to convert the pattern to a casting is the same for the original design and the optimized design. Consequently, the difference in the manufacturing cost of the two designs is the total of the difference in the pattern cost and the material savings. The optimized casting will cost \$92.70 more than the existing design.

The next task was to estimate the savings in fuel costs from the lower weight. Larry had no information about fuel consumption of the military aircraft in question. He was, however, able to find a reference to the experience of American Airlines. American Airlines saved \$1.2 million per year by replacing 35 pounds of flight manuals with an iPad loaded with the manuals in electronic form. In that example, one pound of weight reduction yielded fuel savings of \$34,285.71 across the fleet. Wikipedia reports that American Airlines has 864 aircraft in their fleet so the savings in fuel cost for a single plane per pound of weight reduced was \$39.68 per year. Commercial aircraft fly a lot, more than most military aircraft. Larry estimated that the aircraft that used the housing flew roughly half as much as a commercial aircraft and would have half the fuel savings. Consequently, he assumed that the aircraft would save \$19.84 per year for each pound of weight eliminated. The change to the optimized design would reduce weight by 3.06 pounds for an annual savings of \$60.71.

At that level of fuel savings, the increased cost of the optimized design would be paid for in about a year and a half. Those savings continue, however, for the life of the aircraft. Assuming a 20-year life of the aircraft, the savings in fuel cost per aircraft would be \$1121.50 for just this one component. For a fleet of a thousand aircraft, the total savings would be over \$1.1 million. If the same weight reduction was achieved on as few as twenty components on the aircraft, the savings for the fleet could easily exceed \$22 million dollars.

This analysis does not include the cost of certifying the new casting. Any component needs to be certified through analysis and testing to be considered safe for the aircraft. However, that is a one-time cost and for a non-structural component like this, physical testing is unlikely to be required, lowering the cost.

The Solidiform team then wondered if it was worthwhile to replace the component on the existing aircraft. For that situation, the cost included the cost of a new casting, not just the difference between the new and existing casting. Larry estimated the total cost of the new casting including the cost of the printed pattern (\$120.85) and the cost of converting it to a casting (\$450) to be \$570.85. With an estimated annual fuel savings of \$60.71, it would take more than 9 years to break even on the cost of retrofitting existing aircraft. Clearly, replacing the component on aircraft near the end of their useful life would not be cost effective. However, it may be worthwhile for those existing aircraft with a remaining life of ten years or more.

#### PROPOSE OPTIMIZED DESIGN TO CUSTOMER

*The customer is reviewing Solidiform's findings and weighing the benefits of potential weight savings versus the change in cost if they were to proceed with the company's presented design.*

#### CONCLUSION

Although the cost of moving forward with the new design for the company would be higher than staying with the current design, the benefits of the reduced weight of the aircraft instrument housing outweigh the additional cost. Solidiform emphasized the following benefits to the customer while they considered their production decision. The results of this case study demonstrate the following:

1. Topology optimization can provide significant value in weight sensitive applications.
2. Topology optimized components can be cost-effectively manufactured using hybrid investment casting. While the cost of manufacturing may be higher, the benefits of the lighter weight more than offset the higher cost.
3. High quality optimized components can be produced in volumes and speed required for mass production using hybrid investment casting.

#### OBSERVATIONS

Larry made some key observations after the study was complete:

1. There are no viable competitors for production of components this large. They would be prohibitively expensive to create using metal AM. High speed machining would not be possible without geometry changes that would significantly increase weight.
2. Topology optimized configurations represent a potentially meaningful market segment for the investment casting industry.

# **INVESTMENT CASTING INSTITUTE**

## **Rapid, Low-Cost Tooling for Small Engine Castings**

Dan Z. Sokol  
Renaissance Services – PERFECT – 3D

## **68<sup>TH</sup> TECHNICAL CONFERENCE & EXPO 2021**

Paper № 7

## Rapid, Low Cost Tooling for Small Engine Castings

Dan Sokol

Renaissance Services – PERFECT-3D Division

[dzsokol@ren-services.com](mailto:dzsokol@ren-services.com)

A historical challenge for the U.S. Air Force is rapid development and deployment of new systems to meet evolving and emerging threats. In recent years, a critical element in the new systems equation has focused on expendable and attritable aircraft. Investment castings are critical to the cost and performance of the small and medium-sized engines for these systems. Essential turbine engine components, produced from castings, impact cost, lead time, and performance. A key driver for these castings is the tooling used to produce them.

A growing need exists for engine component parts that can be delivered rapidly, affordably, and in both small and variable quantities. This presents a challenge for not only essential castings, but for the tooling required to produce them, as considerations such as tooling durability and life, non-recurring and recurring costs, design and delivery lead times all become important variables in the decision process. For example, conventional wax die injection tooling is proven to be durable for thousands of applications, but the lead time and non-recurring cost are prohibitive for a program that needs 250 or fewer castings to be delivered in a few months.

To address this need, Renaissance Services is leading a U.S. Air Force-sponsored program for *Low Cost Tooling for Castings*; specific focus is on castings for small turbine engines. The team consists of foundries (Bimac, HTCI, Nucor, and PCC) and small engine programs/OEMs (Air Force Research Lab Responsive Open Source Engine, FTT, UAV Turbines). Included are castings for rotating and non-rotating components (rotors, impellers, stators) as well as structural components (casings, housings). Materials range from nickel-based alloys to steel and aluminum. The program focuses on multiple tooling options for the optimal solution to address overall cost, lead time, and tooling life to meet specific engine program needs. Tooling concepts combine 3D-printing of ceramic molds, spacers, wax patterns, and limited life injection dies. The initial tooling concepts are:

- **3D-Printed Ceramic Molds.** These molds have been demonstrated for selected castings; application is being expanded for integrally bladed rotors and stators.
- **3D-Printed Wax Patterns.** Cost and lead time for printed wax patterns, relative to conventional injection dies, is under consideration for selected applications.
- **3D-Printed Injection Dies and Ceramic Spacers.** High strength printed wax injection and printed ceramics can offer durability for limited production.
- **3D-Printed Injection Dies and Wax Assembly.** An injected die for a rotor hub, with printed airfoils assembled to the hub offers a rapid solution for complex rotating parts.
- **Hybrid Injection Dies and 3D-Printed Shape Inserts.** A solution that includes a conventionally machined die from alternative materials, accompanied by printed shaped inserts. Each tooling approach, using component designs from the OEMs, is being applied by the participating foundries to produce castings. The tooling approaches are then being evaluated by Renaissance engineers, the OEMs, and the foundries to determine the viability for each to address specific product development, performance, and production requirements.

The Renaissance Services PERFECT-3D Division will provide an overview presentation of the program, as well as results from the participating OEMs and foundries.



# **INVESTMENT CASTING INSTITUTE**

## **Automated Methods of Slurry Testing, Monitoring & Control**

Lee Chamberlain  
VA Technology Ltd.

## **68<sup>TH</sup> TECHNICAL CONFERENCE & EXPO 2021**

Paper No. 8

**Automated Methods of Slurry Testing, Monitoring and Control.**

ICI 68<sup>th</sup> International Conference

November 7<sup>th</sup> - 10<sup>th</sup> 2021

Grand Rapids, Michigan

Mr Lee Chamberlain,

Engineering Director, VA Technology Ltd.

&

Mr Mark Windmill,

Group Facilities Manager, Tritech Group

Automation is developing beyond the physical manipulation of items to become one of data capture, analysis and response. This paper covers factors defining one aspect of this development; the measurement of viscosity in slurries, and discusses the parameters and methods to allow us to easily capture and record this data in real-time. It suggests ways to use this data to identify issues in slurry quality or provide triggers for intervention. The aim of expanding this automation to slurry testing is to reduce the need for manual action, reduce the risk of human error, and to remove subjectivity from decision making on this one aspect of material control. The paper will also indicate how this may provide some reduction in overall production time and provides a description of how these could be integrated into shellmaking systems.

As a critical component, any issues with the slurry will impact on the efficiency and effectiveness of the shell manufacturing process. If slurry is not at the correct consistency it can prevent coating of fine detail in the wax moulds leading to poor geometry, surface finish or even scrap of the cast parts. It can cause slurry coatings to be too thick, leading to increased drying times and can affect the consistency in the cast part metallurgical properties. Since the use of robots in shell production, the possibility of automated slurry control has been brought into focus and provides the potential to conveniently make adjustments for changes in slurry rheology.

With this in mind, this paper identifies a number of approaches to improve the monitoring of slurry viscosity and thixotropy. It reviews current common manual practices, identifies new automated methods of replicating those methods and compares the use of these automated techniques as a direct replacement of those practices. There are typically two methods of testing commonly used in foundries; flow cup and plate weight testing and it is these methods this paper predominantly focuses on replicating.

The paper also reviews the direct measurement of viscosity, interprets the results from the sensor and provides a comparison to the other methods.

The methods were developed in conjunction with an established investment casting foundry that offer expertise on integrated manufacturing solutions for Aerospace, Defence and related industries. The trials were conducted during standard production manufacture of investment shells and the results presented are representative of a production setting.

## Resonant viscosity sensor

Trials utilised a modern resonator viscosity sensor; these sensor types overcome the limitations of traditional measurement methods and earlier vibrational probes and are not affected by tank sizes and slurry flow. Resonant viscometers work by creating shear waves within the liquid being measured; a solid stainless steel sensor element is submerged in the slurry and made to move back and forth microscopically at a high frequency, as the surface of the sensor shears through the liquid, energy is lost to the fluid due to its viscosity. The dissipated energy is measured and then equated back to viscosity. Higher viscosity causes a greater loss of energy and hence a higher reading.

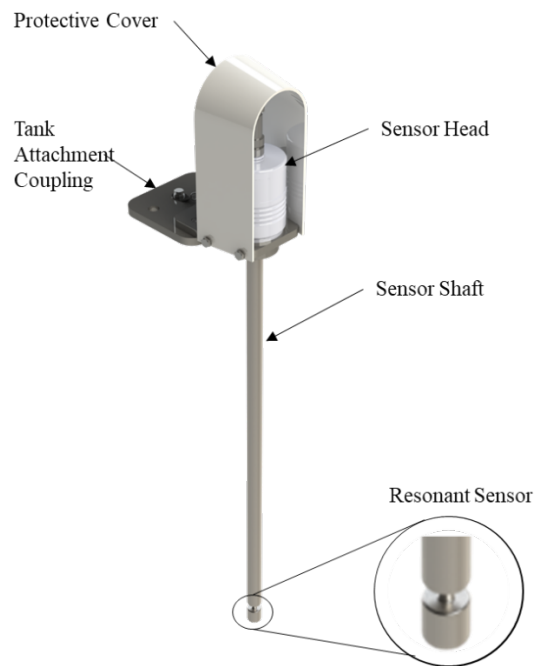


Figure 1 – Viscometer

The sensors are rugged in construction and do not require guards to protect the sensor during use and requires minimal maintenance (see figure 1). Manufactures calibration is preserved regardless of installation and there are no adjustments required once installed. The aim is to automatically monitor changes in viscosity over time within a much narrower band compared to manual techniques.

### Viscometer Data

Two slurry were measured using the viscometer; a Prime slurry using a Zircon flour and dosed using a Primecoat Plus <sup>TM</sup> binder and de-ionised water and a Back-up slurry using a Rancho-Sil <sup>TM</sup> # 4 (200 Mesh) Fused Silica flour, MXC Excel X2 blend <sup>TM</sup> and dosed using a with Matrixsol 30 <sup>TM</sup> Colloidal Silica – Binder and de-ionised water. It was observed that visually the Prime mix was more viscous and less translucent than the Back-up mix.

The viscometer was situated into the slurry tank so that, as a minimum, the sensing head was fully immersed in the slurry (see figure 2a and 2b). The sensor is located in front of the slurry tank paddle, relative to the tank rotation, in a position that provided a constant and uniform flow across the sensor.



*Figure 2a - Viscometer Positioning within Slurry Tank*



*Figure 2b – Viscometer Sensing Head*

Note: the viscometer was positioned using an external mounting frame for flexibility during the trials, production solutions would have the sensor mounted to a removable plate which locates directly to the top of the slurry tank.

The viscometer has a configurable sampling range; for these trials the sampling range was kept high at a reading every 5 seconds to allow interrogation of raw data with the application of averaging applied external from the sensor. The sensor outputs data in centipoise (cP).

A typical output from the viscometer is shown in figure 3; the graph shows two aspects of the measured viscosity: the measured range or the minimum and maximum band of measurements (shown as a gold serrated band), for the example shown this max-min range is 70cP. The second aspect of the curve is a rolling average range (shown as an orange line) which tracks the change of viscosity over a longer period of time. A 15 minute rolling average was utilised for these trials. The sudden change in viscosity starting at 14:45:00 is a slurry dosing event (the application of 15L of water added to the slurry). This changed the viscosity from an average of 590cP to 450cP which takes around 20 minutes, the slurry viscosity exhibits an initial overshoot indicating areas where the water was not fully mixed; with full mixing not complete for another hour.

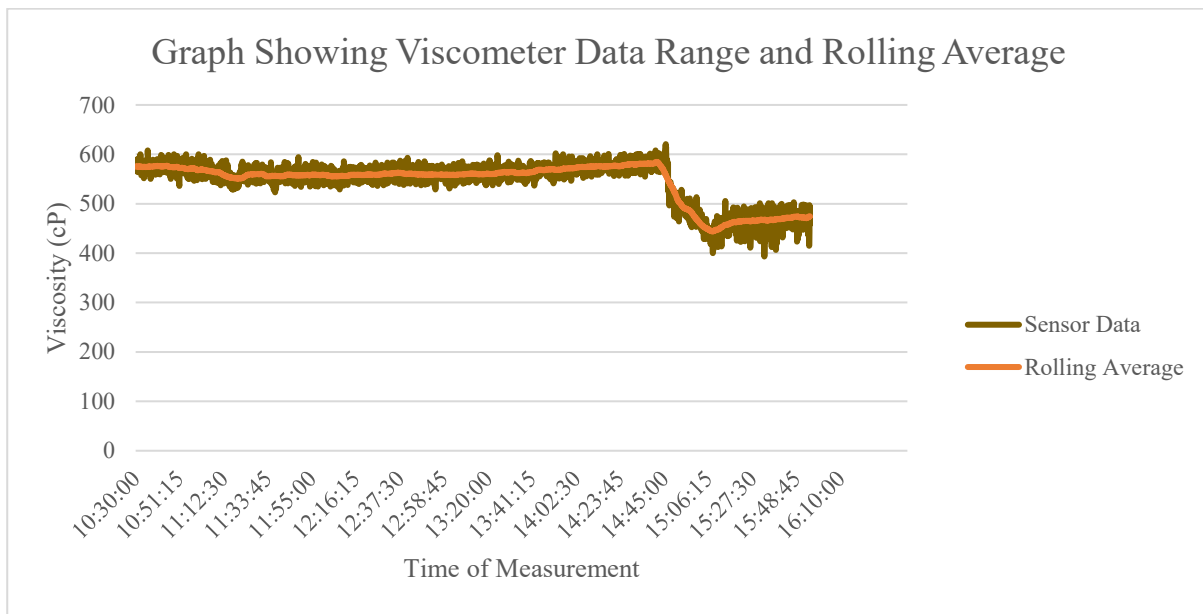


Figure 3 - Typical Viscometer output

Both the direct sensor reading and the rolling average reading track this sudden change, and maintain the relationship between the results once the new viscosity has been reached.

Away from the dosing event the change in viscosity through evaporation is slow with an average increase of 0.14cP / minute. Temperature was constant at 26 °C for the trial.

### Comparison of Viscometer against Flow Cup

Flow cup testing was conducted in accordance with standard ASTM - D4212 utilising a number 4 cup. Daily density measurements were also taken utilising a standard pycnometer. Flow cup measurements were conducted hourly over a number of days and drain time values (efflux) measured and converted to cP utilising the following:

*The calculation required for converting the Zahn cup seconds into Kinematic viscosity ( $m^2/s$ ) is as follows;*

$$V = \text{Kinematic Viscosity (mm}^2/\text{s)}$$

$$K = \text{Means Constant}$$

$$t = \text{Flow Time (result value)}$$

$$c = \text{Means Constant}$$

$$K \text{ value for Zahn Cup 4} = 14.8$$

$$C \text{ Value for Zahn Cup 4} = 5$$

$$V = K \cdot (t - c)$$

The calculation required for converting from Kinematic Viscosity to Dynamic Viscosity is as follows;

$$V = \text{Kinematic Viscosity (m}^2\text{/s)}$$

$$\rho = \text{Slurry Density (Kg/m}^3\text{)}$$

$$\mu = \text{Dynamic Viscosity (Pa-s)}$$

$$\mu \cdot 1000 \text{ converts Pa - s into cP}$$

$$\mu = V \cdot \rho$$

These flow cup viscosity measurements were compared with viscometer data for the same time. Measurement range values for both flow cup and viscometer were calculated; table 1 shows a typical daily viscosity table and the corresponding graph is shown in figure 4.

Date	Time of Test	Efflux Time	Cup cP	Sensor cP	Efflux Time Range	cP Range	Sensor cP Range	Zine cP - Sensor cP
Day 1	10:40:00	20.94	736.00	565.14	0.03	1.60	0.33	170.86
	10:50:00	20.97	734.40	564.81				169.59
	11:40:00	20.87	732.80	581.38	0.59	27.20	1.37	151.42
	11:50:00	20.28	705.60	580.01				125.59
	12:40:00	20.85	731.90	592.64	0.07	3.20	1.19	139.26
	12:50:00	20.78	728.70	591.45				137.25
	13:40:00	20.72	725.90	595.69	0.06	2.80	1.69	130.21
	13:50:00	20.66	723.10	597.39				125.71
	14:40:00	21.69	770.70	608.59	0.21	9.70	0.29	162.11
	14:50:00	21.90	780.40	608.88				171.52
	15:40:00	20.93	735.60	624.85	0.41	18.90	1.52	110.75
	15:50:00	21.34	754.50	623.33				131.17

Table 1 - Flow Cup and Viscometer Data Capture Table

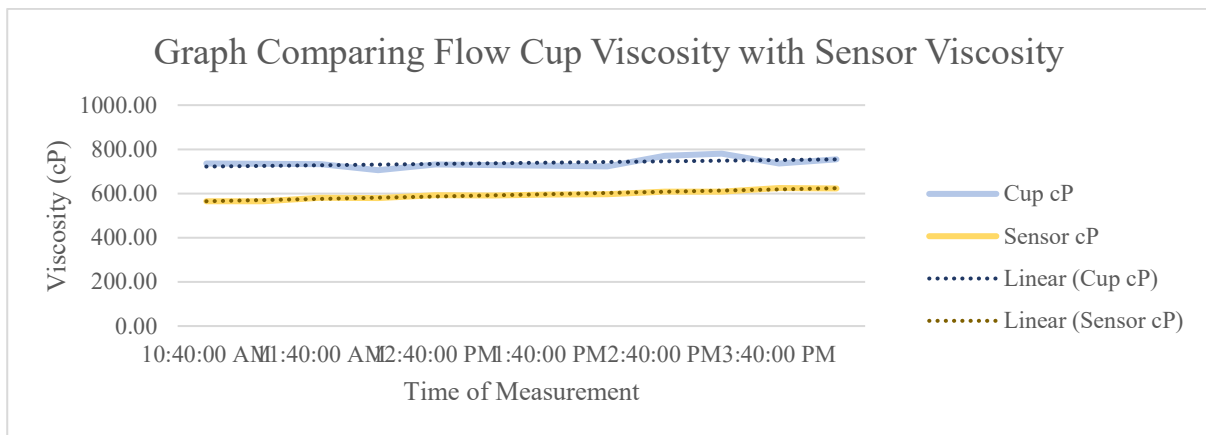


Figure 4 - Graph Comparing Measured Viscosity Using Flow Cup and Viscometer

Linear trend lines have been added to the graph in figure 4; these trend lines exhibit similar increases in viscosity rate over the day with the flow cup indicating an average increase of 0.24cP / minute and the sensor calculating an average increase of 0.2cP / minute representative of a reasonable correlation between the viscometer and the manual flow cup method.

The fit of viscometer data to the trend line is much closer than for the flow cup with a  $R^2$  value of 0.9558 compared with a  $R^2$  value of 0.2632 for the flow cup. It is also important to note that changes in viscosity do not always fit to a linear trend line; slurry temperature and the surrounding environment temperature and humidity, and the frequency of intervening processes effect viscosity. It has also been observed reductions in viscosity over shorter time frames of two to three hours. Taken over a longer time frame, over 8 hours or so, these short term reductions will change back to an overall upward trend and conform to what would be expected.

### **Using data Range as an Indicator of Slurry Quality**

It was observed that the measured range or the minimum and maximum band of measurements may be utilised to indicate the quality (or cleanliness) of a slurry. Undissolved powder, solids and small partials of debris left within the slurry from shell dipping changes the local viscosity which the sensor measures, these randomised particulates increase the spread of results while keeping the viscosity rolling average generally reflective of the actual viscosity. Note: rolling average trend was verified with use of flow cup.

The same prime slurry was measured, on separate days, and their viscosity range compared. The set of measurements shown in figure 5 and shows the spread of results of slurry after continuous production. The slurry was then filtered to remove undissolved solids and retested (figure 6). A view of the filtered slurry is showing in figure 7 and shows particles of stucco and wax within the slurry.

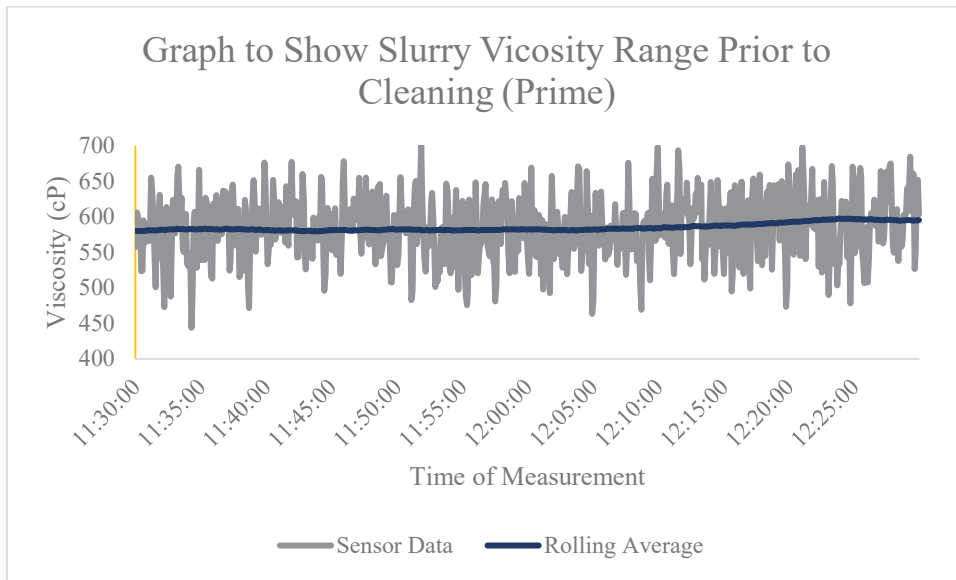


Figure 5 - Viscosity Range of Slurry Prior to Cleaning

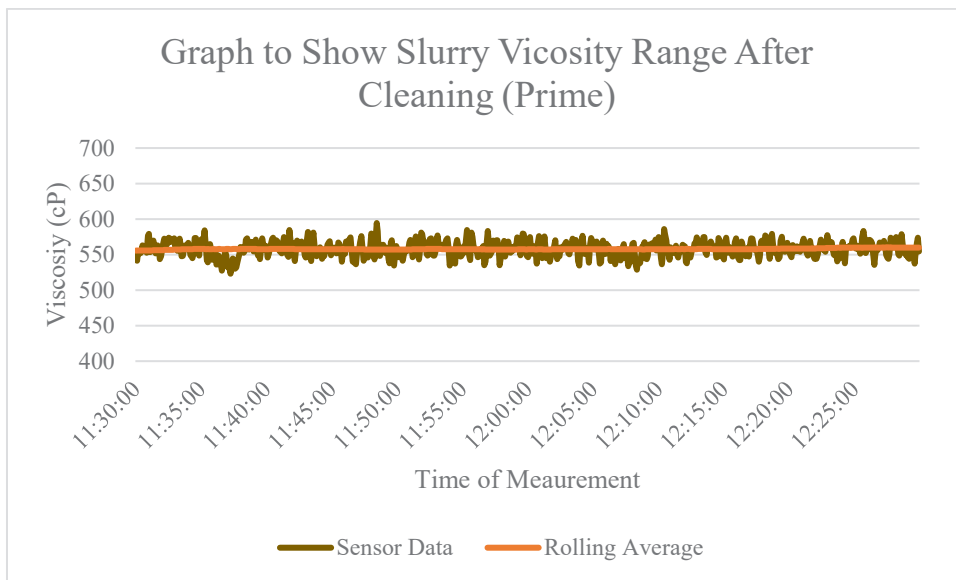


Figure 6 - Viscosity Range of Slurry After Cleaning

The rolling average viscosity for the two sets of results are similar at around 560cP, however the range variation was significantly different with the pre-filtered slurry having a range of 250cP compared with 70cP for the filtered slurry. The variation in the rolling average viscosity remained modest at 18cP and 4.5cP respectively.



Figure 7 - Filtered Slurry with Particulates

Each slurry type will have their own characteristic data range, with thicker slurries exhibiting a wider range than the thinner mixes. The thinner mixes are also less susceptible to this data volatility and more tolerant to interviewing processes. A typical min and max measurement band for the thinner Back-up slurry, with processing, is shown in figure 8 and has a range of 60cP, slightly less than the filtered Prime slurry.

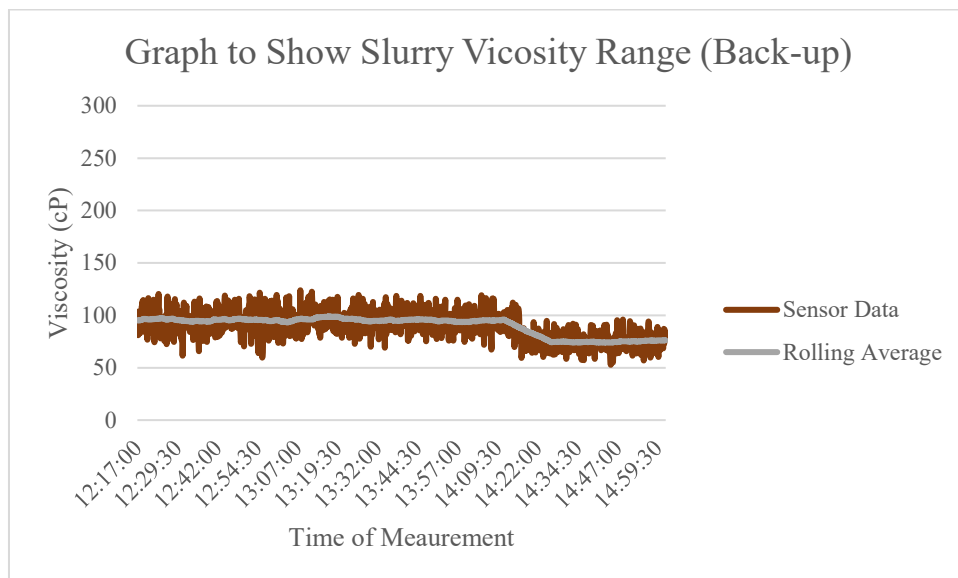


Figure 8 - Typical Viscometer output - Back-up Slurry

It is important to initially set-up the viscometer using newly mixed slurry to obtain a typical viscosity range before setting the quality limits. These limits will need to be individually set for each slurry and reflect their relative process frequency.

### Comparing Viscometer and Flow Cup Measurement Variation.

A range of three sequential flow cup and viscometer measurements were taken each hour over one week period and the variation recorded (constituting one test on table 2). Production processing in the slurry tank, slurry dosing and slurry filtering activities were conducted during this time. The results are thus normalised to record the variation in the tests rather than viscosity, as this varied considerably throughout the weeks measurement. Table 2 shows the results with the corresponding graph shown in figure 9.

Test Number	Efflux Time Range	Flow Cup cP Range	Sensor cP Range
1.00	0.71	33.20	2.06
2.00	0.13	6.10	2.28
3.00	0.28	13.10	1.63
4.00	0.34	15.90	2.37
5.00	0.15	7.00	1.03
6.00	0.53	24.80	2.27
7.00	0.03	1.60	0.33
8.00	0.59	27.20	1.37
9.00	0.07	3.20	1.19
10.00	0.06	2.80	1.69
11.00	0.21	9.70	0.29
12.00	0.41	18.90	1.52
13.00	0.69	32.80	1.22
14.00	0.16	7.40	0.54
15.00	0.90	41.70	0.15
16.00	0.40	18.50	1.59
17.00	1.37	63.40	0.94
18.00	1.25	59.50	0.28
19.00	0.51	24.10	0.82
20.00	0.26	12.20	0.29
21.00	0.56	26.40	0.94
22.00	1.10	51.90	2.81
23.00	1.29	60.90	0.38
24.00	0.50	23.60	7.49
25.00	0.65	30.70	0.25
26.00	0.43	20.30	0.37
27.00	0.03	1.40	1.22
28.00	0.16	7.60	0.64

*Table 2 - Measurement Variation*

The additional variation in the manual flow cup method reflect a number of factors; ASTM - D4212 states that repeatability should be in the region of 11% of the mean value and relates to reproducibility of the data collection (timing differences). Other factors include slurry temperature differences at the time of testing and slurry quality.

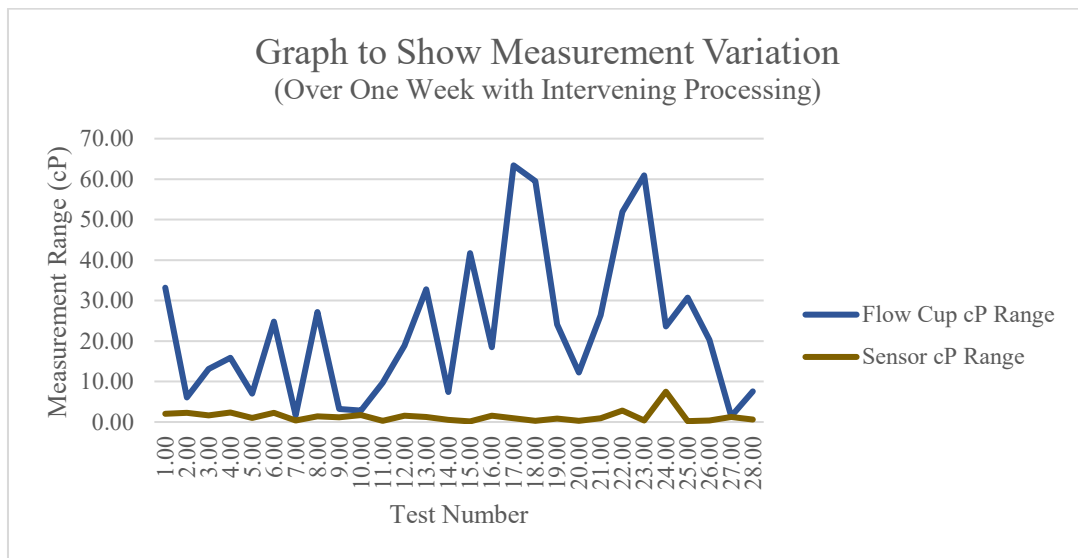


Figure 9 - Graph Showing Measurement Variation of Flow Cup and Viscometer

Over the week period the slurry temperature varied between 24 °C and 26 °C. It is known (ASTM - D4212) that measurement variation for standard oils over a two degree range could be as high as of 11% of the mean value. These variations can be compensated for by testing the slurry viscosity over a range of temperatures and calculating an efflux time / viscosity curve, however these curves would be unique to each slurry and, as with these test above, not practical to generate in a production setting. This is unlike the viscometer where the sensor automatically compensates for temperature changes prior to publishing the data point.

As shown previously; pre and post cleaning can also show variation of a slurries viscosity, at a particular point of measurement; small changes in the amount of suspended solids can have an effect on both viscometer measured range and flow cup measurements.

It is impractical to try to pick apart and attribute these factors for each method of measurement and it is likely the differences in actual value between the sensor and flow cup testing seen in figure 4 is a combination of the variations discussed above and the disparate way of calculating viscosity for each method. It is important to note that the viscosity trend of the two methods are similar though the values differ (an average of 130 cP separation). In the same way that foundries do not convert flow cup efflux times into cP, but set time limits for the quality of the slurry, then the values from the viscometer should be used on its own terms, and limits set accordingly to that method.

### Comparison of Viscometer with Plate Weight

The use of plate weight testing for slurry viscosity assessment is common across foundries, however the methods of use vary; foundries may measure the weight of the slurry remaining on the plate weight after a set drain time or when fully dried, or measure the time taken for the slurry stream to break (drip time). Daily measurements were taken utilising two of these methods; slurry weight after two minutes drain time and the time taken for the slurry stream to break.

These plate measurements were compared with viscometer data at the same time of measurement and values for both collected. The daily plate weight record is shown in table 3 and the corresponding graphs shown in figure 10. Production processing in the slurry tank, slurry dosing and slurry cleaning activities were conducted during this time and account for the large variations in measurements.

Time	Drip Time	Plate Weight	Weight After 2 Mins	Slurry Weight	Viscometer (cP)
1	02:23.6	375.3	387.4	12.1	656
2	02:39.4	375.3	386.7	11.4	655
3	02:38.6	375.3	386.5	11.2	690
4	02:46.1	375.3	386.2	10.9	706
5	02:40.1	375.3	386.3	11	710
6	02:12.7	375.3	387.5	12.2	656
7	02:34.5	375.3	387.5	12.2	690
8	02:34.5	375.3	387.3	12	704
9	02:38.5	375.3	385.1	9.8	573
10	02:35.1	375.3	385	9.7	557
11	02:39.0	375.3	385	9.7	560
12	02:32.9	375.3	384.9	9.6	572
13	02:45.5	375.3	384.9	9.6	580

Table 3 – Plate Weight and Viscometer Data Capture Table

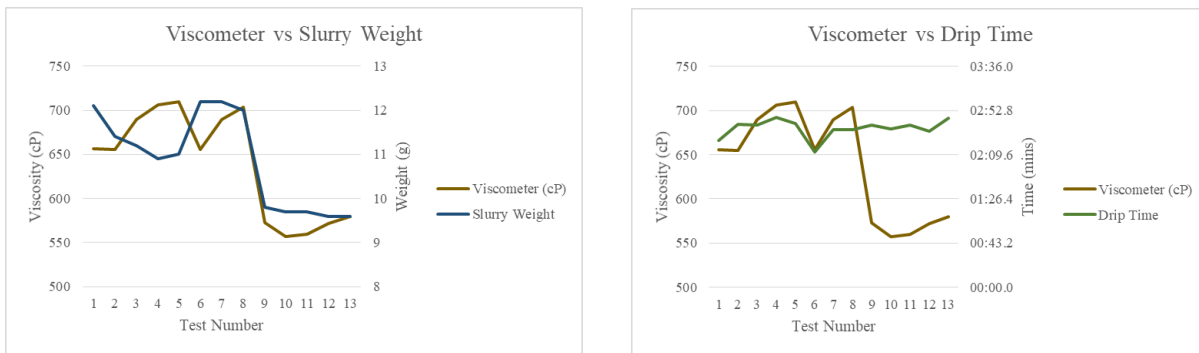


Figure 10- Graph Comparing Measured Viscosity Using Flow Cup Methods and Viscometer

Of the two approaches, measuring the slurry weight after two minutes drain time provided a more reliable match to the viscometer data and indicated that the differences between the two methods would equate to a 60cP measurement range.

The 'drip time' method provided consistent results, however did not identify the change in viscosity unlike the final slurry weight method. The error indicated would equate to a minimum of a 150cp measurement band and suggests that this method would be unreliable as a measurement of viscosity.

### Effect of slurry build-up on Viscometer Readings

Like slurry tank paddles, any stationary equipment mounted into the slurry from the side of the tank will be subject to slurry build up at the surface, and though slurry build-up on the sensor is away from the active part of the viscometer it is important to understand that the sensor will not be damaged or its results affected due to the build-up. The degree to which this build-up occurs is also dependent on the slurry type; figure 11 shows the development of slurry build-up on the sensor for the Prime slurry and figure 12 shows it for the Back-up slurry.

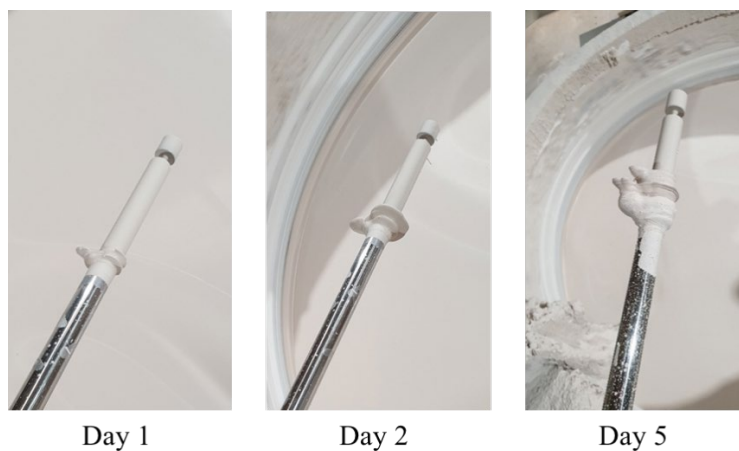


*Figure 11 - Prime Slurry Build-up on Viscometer*

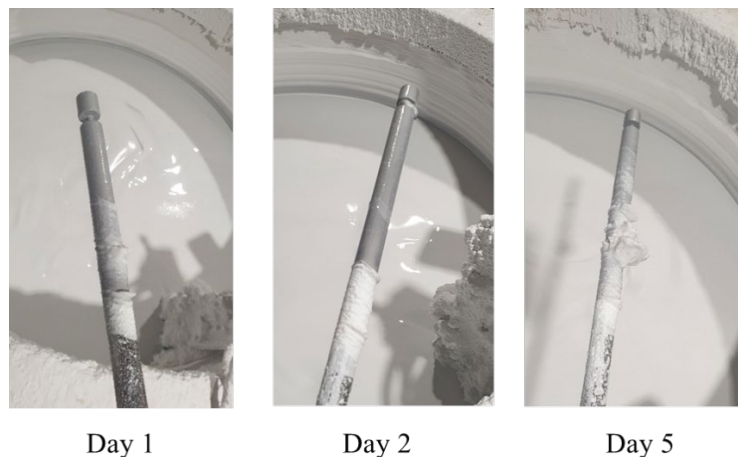


*Figure 12- Prime Slurry Build-up on Viscometer*

up accumulated on the side of the tank and as such did not deposit any abraded dried slurry back into the slurry mix. The slurry was easily cleaned from the sensor using a soft PTFE spatula to remove the large deposits, Scotch-Brite™ and a soft, damp cloth to remove the residue. The sensor showed no sign of wear or damage.

Sensor data readings were taken at the end of a five days immersion and compared with readings taken after the sensor was cleaned and relocated in the slurry. Note the results shown in figure 13 are for the Back-up slurry.

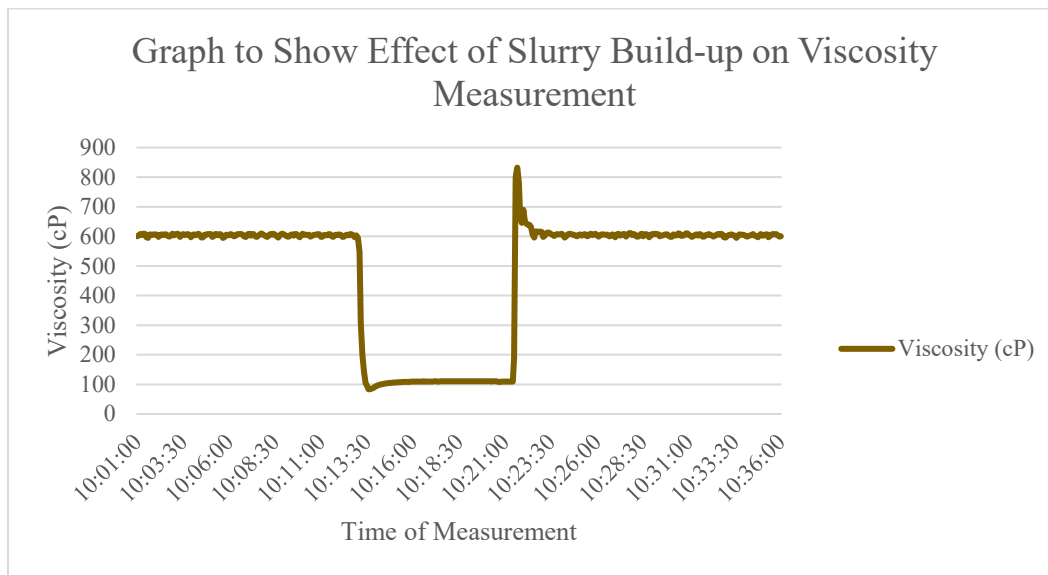


Figure 13- Effect of Slurry Build-up on Viscosity Measurement

The average viscosity before cleaning was 604.27cP and after 605.53cP providing a difference of 1.2cP between the results. The recorded range was 22cP which equated to 6% of the data range and 0.2% of the average recorded mean. It was observed that a settling time of 1 minute was necessary for the readings to reach a consistent recording once placed back into the slurry.

### Effect of Debris on Viscometer results.

During a two week period one incidence of debris accumulation occurred. This accumulation is shown in figure 14 and shows undissolved flour lodged between the sensor head and shaft affecting the sensor readings (see figure 15). This incidence immediately followed topping up the tank with slurry and the addition flour and binder to the slurry tank.



Large accumulation of this sort will show a spike in viscosity; in this instance the sensor reading rose to the full sensor scale (1000cP) and remained high until the debris was detached.

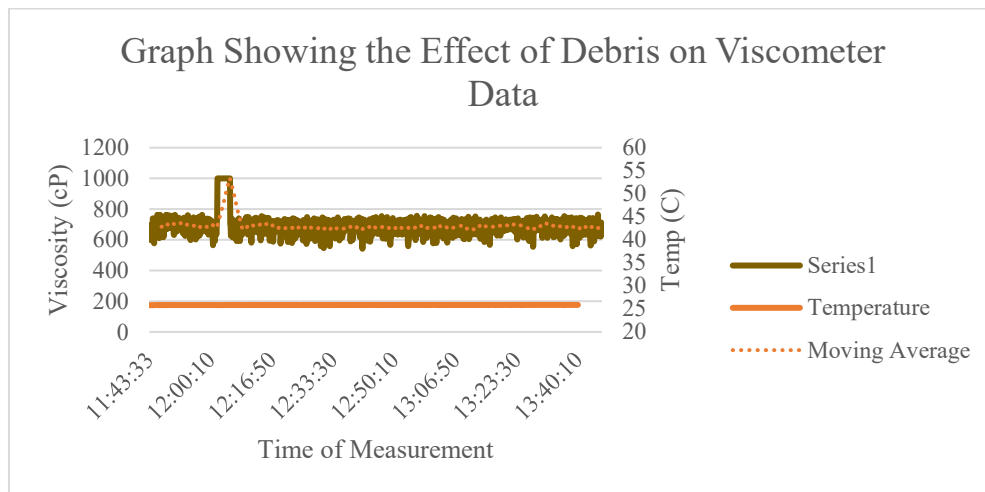


Figure 15 - Graph Showing Effect of Debris on Viscometer Data

It is recommended that the sensor be removed from the tank for slurry level filling. It is not necessary to remove the sensor for dosing events, however reading during this time may become erratic until fully mixed.

## Load Cell Sensor

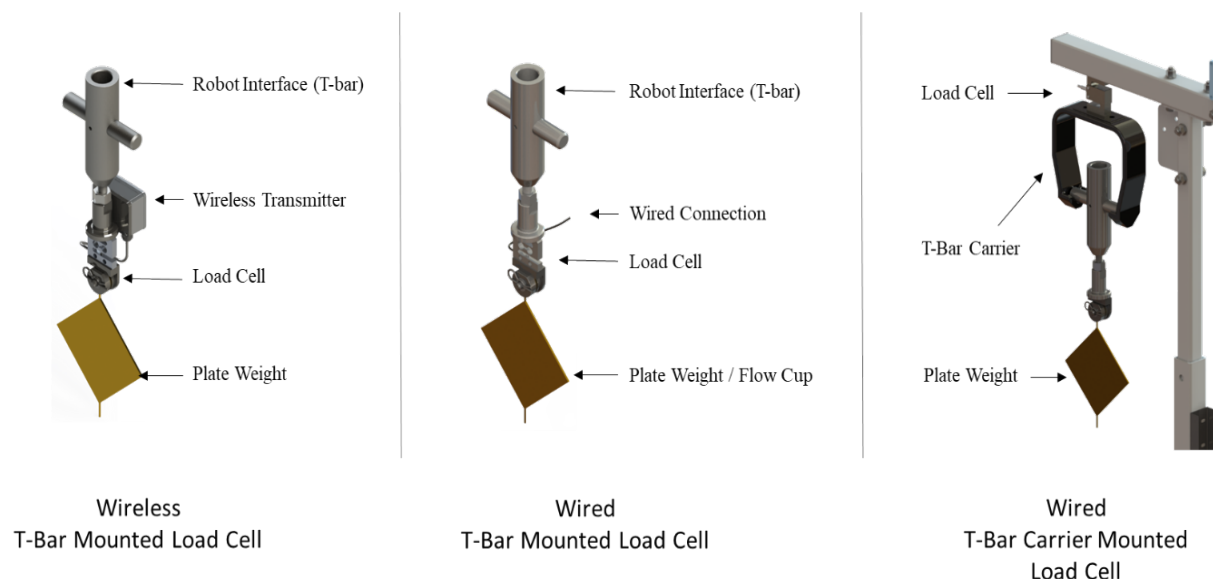
The idea is to replace operator testing and utilise the cell robot to dip either the flow cup or plate weight into the slurry; the slurry removal rate and start and finish weights are then automatically captured by the software. To conduct a sampling the system would run a dedicated ‘slurry weighing’ robot program; the robot interface adaptor would be picked from a dedicated station in the cell, and a weigh programme executed. The data collated would be processed and their values compared to acceptable limits.

Three approaches were investigated; a T-bar (robot interface adaptor) mounted load cell with wireless communication, a T-bar mounted load cell with wired communication and a static, carrier mounted load cell with wired communication, see figure 16 for each arrangement. Attached to these devices is a coupling that will accommodate the use of both a flow cup and a plate weight.

The wireless T-bar mounted load cell has a battery powered transmitter which also powers the load cell and automatically transmits data to a receiver located within the shell management processing software system. This requires minimal interaction from the operator in its set-up and requires no special modification to the robot or the robot gripper (manipulator).

The wired version is similar in construction, but utilises power taken from the robot and utilises direct communications to the load cell control. This system requires more operator interaction in its use and modification to the robot for cable integration.

Both these methods work best when integrated with a slurry level sensor which modifies the robot position to ensure a constant dip depth and that the test equipment is always positioned in the same place in the tank and for the same amount of time.



The last method is a static, remote system that can be positioned in the cell. This is also a wired solution and provides direct communication to the load cell control.

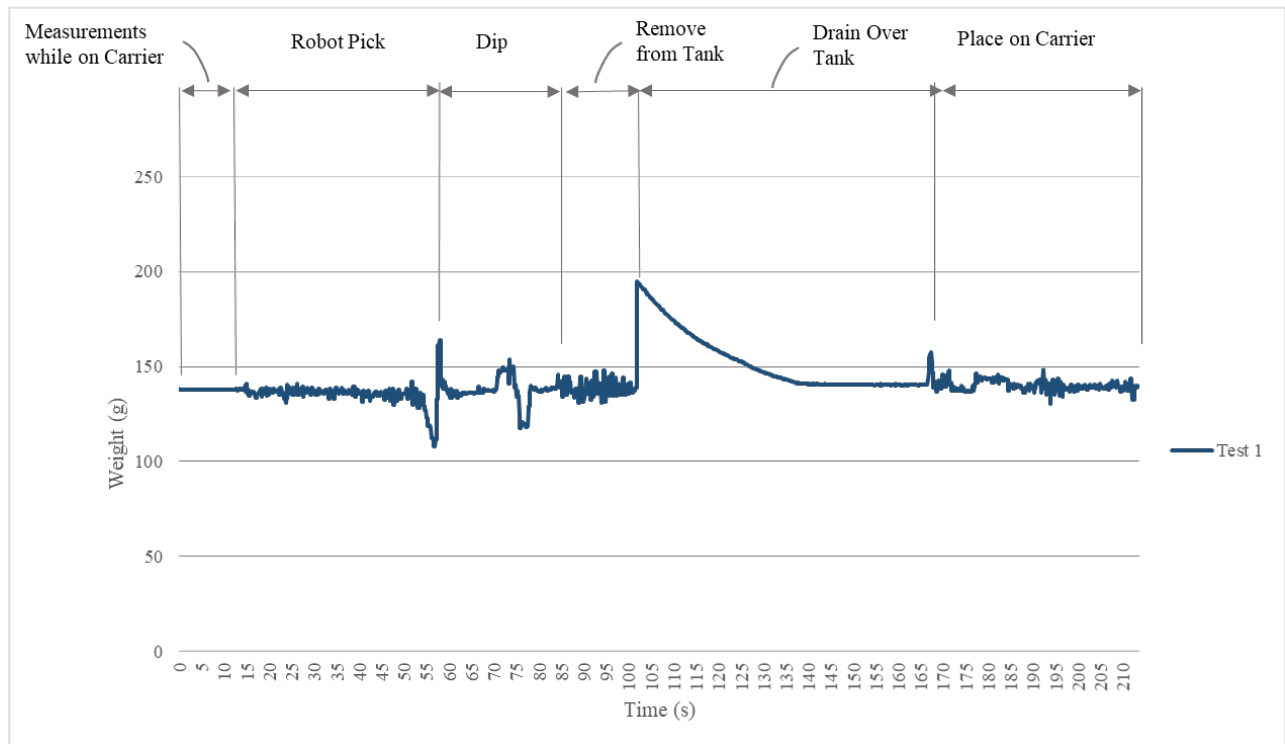
All the three methods utilised a 2kg load cell which provides a 0.1g resolution and is comparable with the resolution found in industrial scales used in foundries.

### **Robot Interface Adaptor (T-bar) Mounted Load Cell Data**

The same robot program was utilised for all tests; the robot initiates the data gathering from the load cell prior to picking the T-bar and captures a baseline weight, it then picks the T-bar interface and conducts a plate weight / flow cup dip in the slurry tank. The robot retracts out of the tank and holds for two minutes and 30 seconds until the slurry is completely drained from the device (figure 17). It is then plated back on the load station, the data collection stopped and the weigh cycle completed.



The load cell has a configurable sampling rate; for these trails the sampling rate was kept at 100 milliseconds to allow interrogation of raw data. The sensor outputs data is in grams (g). A typical output from the load cell for a flow cup test is shown in figure 18.

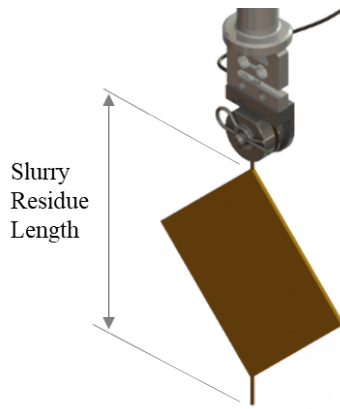


The graph shows the discreet output areas from the sensor, with the key areas for analysis being the weight at the start of the process and a weight measurement taken along the drain curve.

### Robot Dip Depth Repeatability

Remarkable constancy can be achieved when dipping a plate or flow cup into slurry, the average human can compensate for the changing slurry depth in a tank with ease and without much thought; not so for robotic processes where active compensation is required. Dip too deep and you could be covering measuring equipment with slurry; dip too shallow and you could be measuring much less accumulated slurry or none at all. Understanding the repeatability of the dip process and its effect on the final weight is an important factor in the viability of the automated process.

To compensate for the changing slurry levels in the tank a robot mounted laser measuring device was used, prior to each dip the robot would activate the laser and take a measurement from the known position of the laser mounted on the robot and the top of the slurry liquid. This measurement would be utilised as an offset within the robot program to compensate for the variation in slurry depth.



The length of slurry residue remaining on the plate weight was used as the measurement method (see figure 19). Sequential plate weight dips, with intervening shell processing, were conducted to measure the baseline slurry level compensation repeatability (figure 20). Manual plate dipping was also conducted immediately after the robot dipping to provide a comparison.

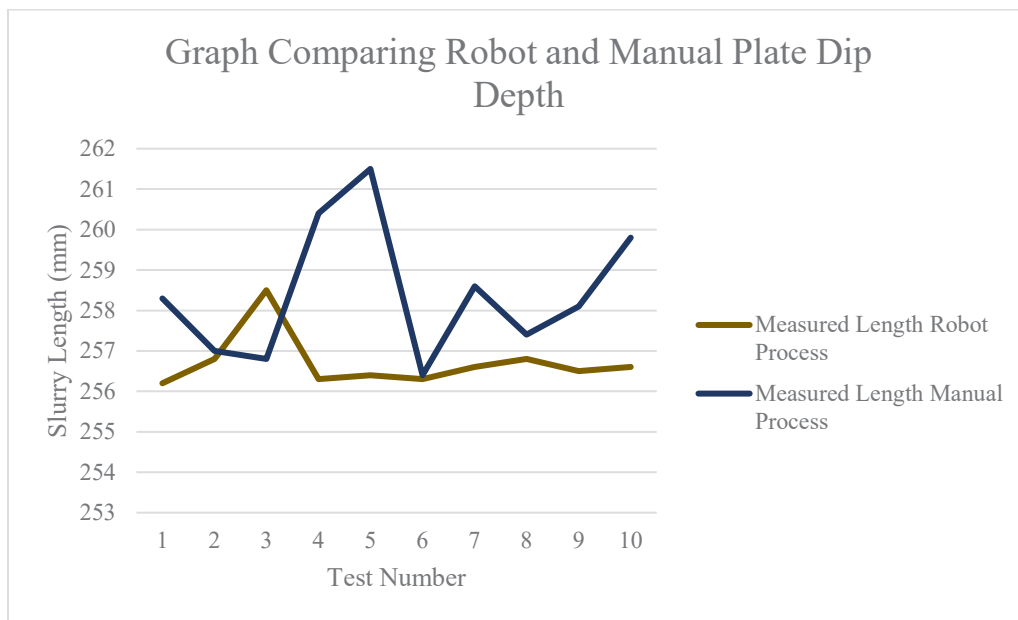


Figure 20 - Graph Comparing Plate Weight Immersion Depth for Robotic and Manual Process

Robot dip depth range was 2.3mm compared with the manual process of 5.1mm, both methods were acceptable for the Plate weight assessment and had insignificant effect on the final measured weight. The data indicates the manual process tended towards over dipping into the slurry.

## Variation in Wireless Automated Plate Weight Measurement

Plate weight tests were conducted using the wireless load cell; start weight (plate only) and finish weight (plate and slurry) were recorded and compared to manual measurement of the same plate and slurry using standard industrial scales.

The results are shown in Table 4 and indicate a large variation between the two methods. The load cell showed a 0.54g variation for the starting, clean plate, weight and a maximum 1.17g for the final slurry weight.

A similar variation was present when comparing the final plate weight between the two methods with a maximum variation of 1.39g between the readings from the load cell and industrial scales.

Plate Weight clean (g)	Load Cell Start Weight (g)	Load Cell Weight after 2min (g)	Diff Start - Finish (g)	Diff Manual Test (g)
375.30	374.61	381.67	7.07	6.9
375.30	374.10	380.93	6.83	7.2
375.30	374.64	380.65	6.01	7.4
375.30	374.26	381.13	6.87	-
375.30	374.47	381.65	7.18	-
375.30	374.49	381.47	6.98	-

The data logs from the wireless sensors showed a variation in constancy with approximately 60% of the data from the sensor exhibiting a data characteristic typical of that shown in figure 21.

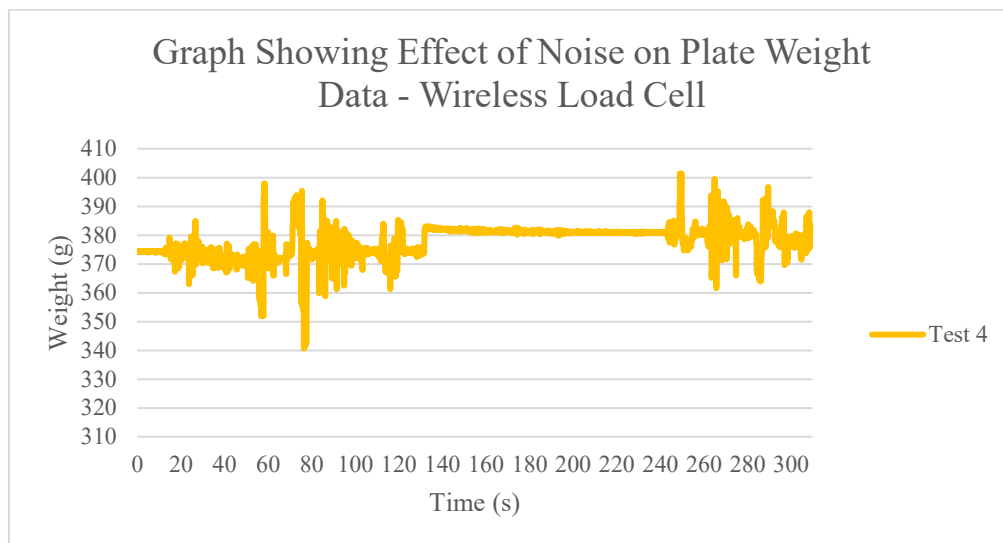


Figure 21 - Effect of EM Noise on Automated Plate Weight Data

A correlation was observed between the quality of the data and the operation of surrounding equipment, use of wireless devices by operators and position of the wireless receiver. Improvement in

the constancy of the data was shown by re-housing the wireless receiver, however the noise from the surrounding equipment could not be eliminated.

These results differ significantly from those previously conducted in the test environment where impact from electrical noise was not a factor; therefore the use of this device, in a foundry setting, is not recommended.

### Assessing Break in Slurry Stream from Sensor Data

A number of automated flow cup trails were conducted and their slurry stream break point manually timed and recorded. A typical weight decay graph is shown in figure 22. Overlaid on this graph was the manually measured slurry stream break point; this break point occurs approximately three quarters the way down the decay curve at 21.5 seconds after removal from tank and 124.1 seconds into the overall process.

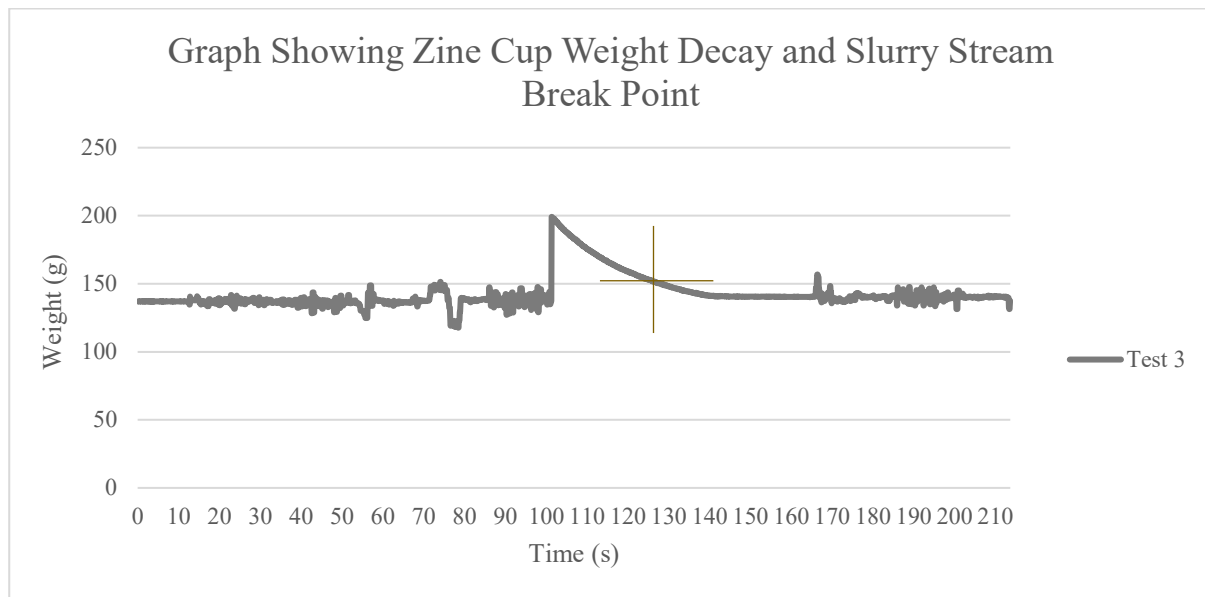


Figure 22 - Automated Flow Cup Weight Decay Graph with Slurry Stream Point

The decay curve shows no discernible indication that this event has taken place with the weight loss curve uninterrupted and smooth. Without the ability to detect the flow cup break point any correlation or replication of the manual flow cup method isn't feasible. And therefore the use of load cells for replication of flow cup testing is not recommended.

### Variation in Wired Automated Plate Weight Measurement

Plate weight tests were conducted using the back-up slurry and start weight (plate only) and finish weight (plate and slurry) were recorded and compared to manual measurement of the same plate and slurry using standard industrial scales. A typical load cell plate weight data is shown in figure 23, and is similar in form to that for the flow cup in figure 18.

The results for the wired load cell are shown in Table 5 and indicate a consistent final slurry weight left on the plate. This was constant between each trial and when compared to the manually weighed plate weight, with a finished slurry weight of 6.4g for each method. A 63g variation was observed for the initial plate weight reading.

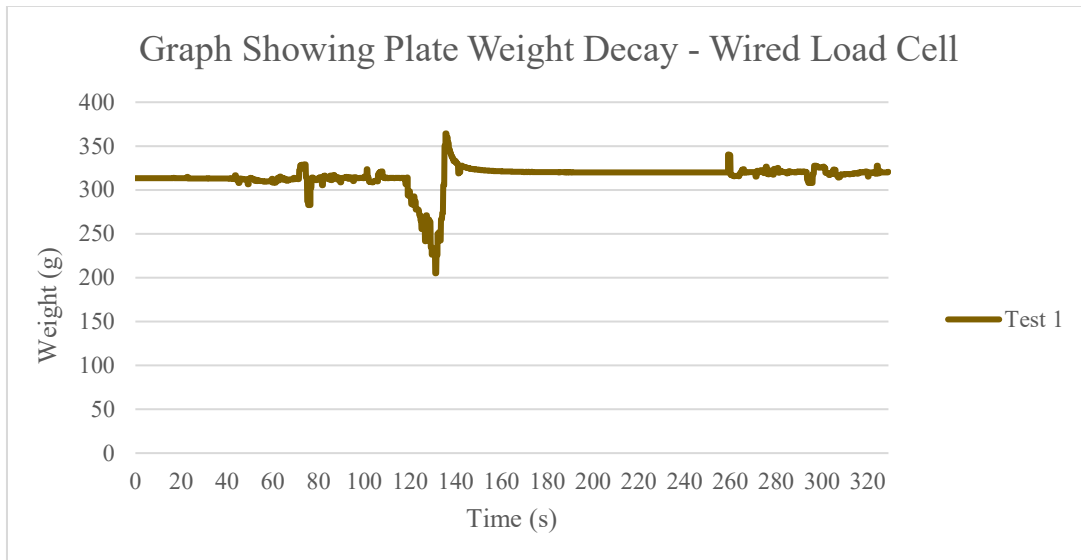


Figure 23 - Graph Showing Plate Weight Decay - Wired Load Cell

Load Cell Start Weight (g)	Load Cell Weight after 2min (g)	Diff Start - Finish (g)	Diff Manual Test (g)
313.50	319.9	6.40	6.4
314.20	320.6	6.40	6.4
336.20	342.6	6.40	6.4
380.00	386.4	6.40	6.4
378.50	384.9	6.40	6.4

Table 5 - Auto and Manual Plate Weight - Weights

To compensate for this variation in starting weight an initial tare weight at the start of the process can be taken and the resulting weight data offset by the difference. A representation of this offset is shown in figure 24.

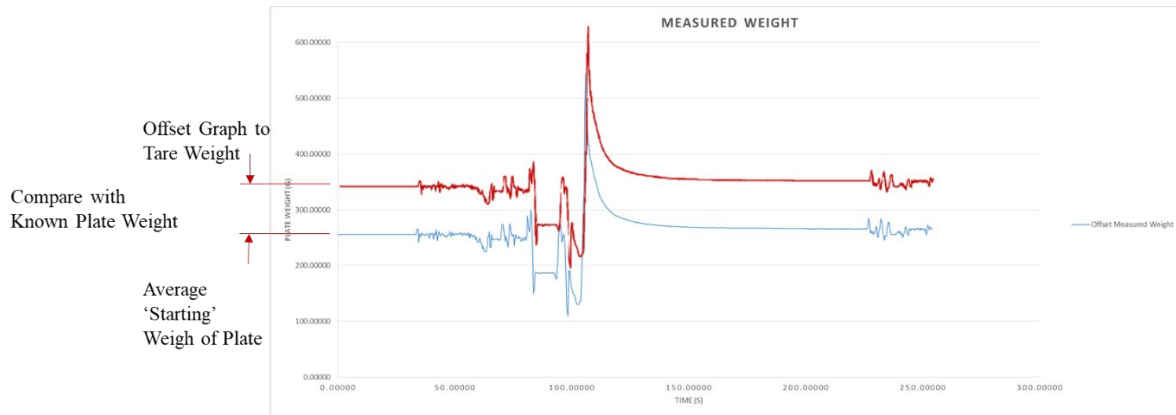


Figure 24 - Representation of Load Cell Data Translation by Tare Weight

Mounting the load cell on a static carrier removes this variation as seen from the results in table 6 where consistent start weights were observed. These constant start weights had no detriment to the finished measured weight and were comparable to manual plate weights conducted at the same time.

Plate Weight clean (g)	Load Cell Start Weight (g)	Load Cell Weight after 2min (g)	Diff Start - Finish (g)
375.30	375.30	381.6	6.30
375.30	375.30	381.6	6.30
375.30	375.30	381.6	6.30
375.30	375.30	381.6	6.30

Table 6 - Auto Plate Weight - Weights - Static Load Cell

Potential reason for the variation on the T-bar mounted load cell is out of plane distortion of the load cell when dipping into the slurry. This movement could be restrained using a housing to reduce the flex seen in the load cell and reduce the variation.

## System Integration

Systems utilising the viscometer and include PLC devices for equipment control and status messaging can utilise serial communication (RS485) direct from the viscometer to I/O modules within the PLC. The PLC is programmed such that it takes the raw viscometer data and conducts the required averaging and rate of change calculations prior to sending to the system process control PC and software via the system Ethernet / Modbus TCP network. The sampling rate can be changed from configuration settings within the system process software and communicated back to the PLC via the system network. Systems with auto-dosing equipment will also provide dosing rates, from the PLC, to the dosing pump based on calculated viscosity rates of change.

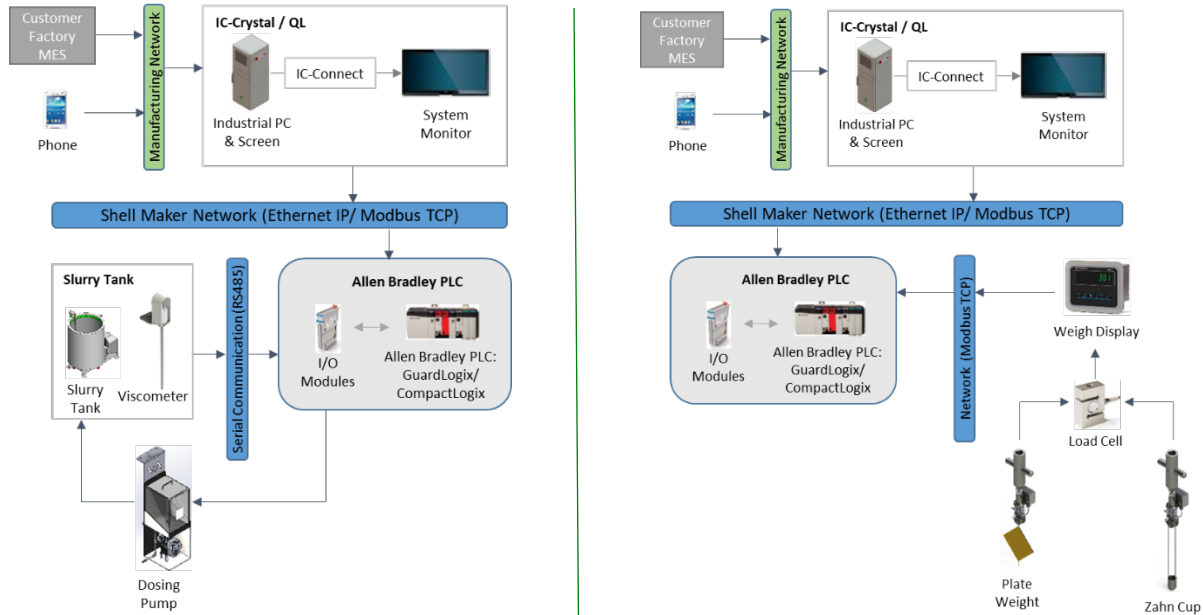


Figure 25 - Viscometer & Load Cell System Integration Diagram

Systems utilising the plate weight / load cell measuring device will use Modbus TCP to communicate load cell data to the PLC rather than a RS485 link. The data and calculation will remain in the PLC and be outputted to the process software through the Ethernet IP network per the viscometer arrangement (see figure 25).

Legacy systems that do not include a PLC control device can read directly from the viscometer to the system process control PC with the additional calculations for averaging conducted by the software. Dosing systems can also be managed by the process PC in a similar manner to the PLC with

calculated rate of change data communicated directly via the network. This option is less favoured as it is reliant on the process software running and would not have independent control of the recording or the outputs to other devices such as the auto dosing equipment. In the situation where the PC or the process software has stopped, data recording and auto dosing would also stop for the duration the process software isn't running.

Standalone software for both the viscometer and load cell is available. The software will require a local PC in the Shellroom to host and provides basic data collection and history reporting facility, however using the data for interaction with system equipment would not be possible without additional PLC controls being added.

## Process Control Software

Viscosity data logs can be accessed via Key Process Variables (KPVs) defined within system process system. The current manually recoded viscosity KPVs are replaced with auto generating history plots. The upper graph detailed in figure 26 shows a typical representation of how this data is presented with each point a discrete reading from with the viscometer or the load cell. Data displayed from the viscometer would be the rolling average as described previously and shown in figure 3. The sample range and frequency can be configured by the process engineer depending on the sensitivity required.

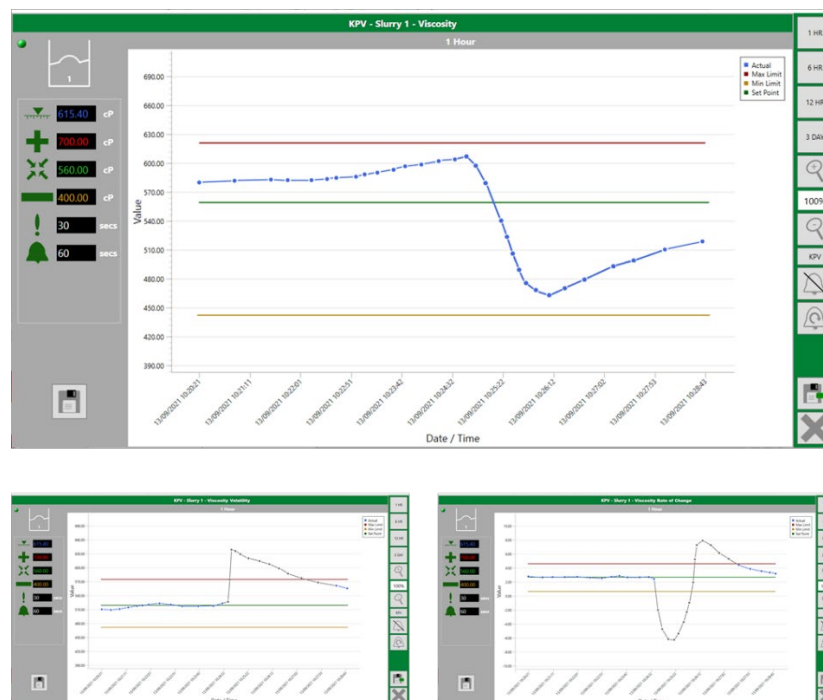


Figure 26 - Typical KPV Viscometer Plots

A second KPV is available for both the viscometer and load cell which calculates and plots a moving rate of change in the slurries viscosity and a third KPV, viscosity volatility, is available for the viscometer and relates to the total maximum - minimum variation of viscosity readings as an indication of the slurries quality.

Limits for each KPV are defined by the process engineer, and exceeding these limits trigger alarms providing warnings to the operator for further investigation. Each KPV set is related to a slurry tank which allows viscosity limits to be individual to the slurry type.

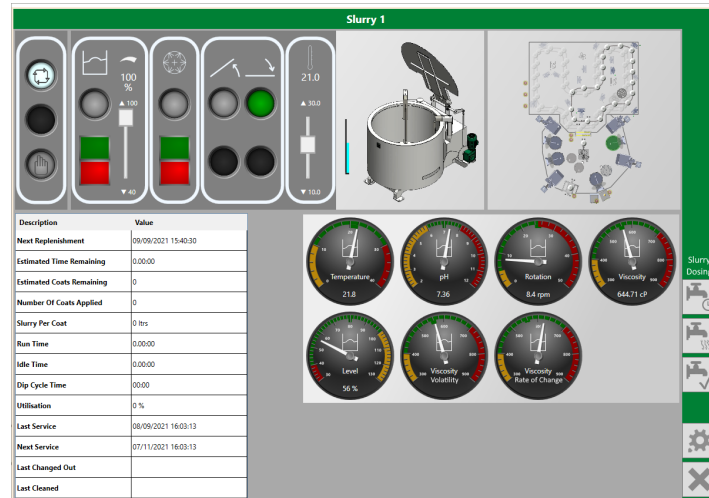


Figure 27 - System Process Software - Viscometer KPV

Manual dosing or slurry filling events are recorded via each slurry tank KPV main page (figure 27). During these events both the moving rate of change and viscosity volatility is likely to exceed predefined limits, in this event the KPV will continue to plot the data, however the alarm will be suspended and the data on screen coloured grey to indicated an external event. The length of time which the alarms are disabled is configurable and individual to the slurry.

### Initial Set-up and Defining Limits

Modification of existing systems to add the viscometer or load cell devices can be relatively quick with the additional network cable, hardware, software upgrade and additional robot programmes taking around half a day to complete, once installed the systems can immediately start logging viscosity.

The viscometer will require correlation back to the limits set from the manual testing; starting from newly mixed slurry would provide the quickest way of defining these limits. The manual testing regime will need to continue alongside the viscometer logging and when the slurry reaches the upper viscosity range the upper limit in the KPV can be set. It is also expected that during processing the

data band will also increase and at a slurry cleaning event the volatility upper limit set. Modification to these limits can be completed at any time.

The load cell / plate weight method can utilise existing manual viscosity limits and have these directly set into the KPV limits. Additional robot programmes would need to be generated and any external load / unload equipment installed.

## **Review of Benefits**

Areas studied included direct measurement of viscosity and replication of the manual thixotropy measurement utilising robot manipulation and wired load cells. These methods have been shown to have a practical use in a foundry setting and afford the easy capture and recording of data in real-time, and opens up the possibility of generating system for the automatic compensation of changes in viscosity within a much narrower band.

The viscometer offers the less invasive solution to viscosity monitoring and requires minimal intervention once set-up, however the plate weight capture method is directly relatable to current manual methods found in foundries and could provide a direct replacement for that technique.

Depending on the method use, between 65% to 75% reduction in the time to conduct slurry tests has been observed this equates up to 2,500 additional cell processes over a year's production. The possibility of further automation also promises a more reliable, tightly controlled variation of slurry viscosity which may lead to a more predictable process and consistent end product.



# **INVESTMENT CASTING INSTITUTE**

## **Development of Investment Casting Shells Based on Calcia Stabilised Zirconia for Ti-6Al-4V**

Angelika Priese  
Imerys Fused Minerals Murg GmbH

## **68<sup>TH</sup> TECHNICAL CONFERENCE & EXPO 2021**

Paper No. 9

## Development of investment casting shells based on calcia stabilised zirconia for Ti-6Al-4V

Michael Weissenbacher\*<sup>1</sup>, Angelika Prieße\*<sup>2</sup>, John W. Kight\*<sup>3</sup>

\*1) Imerys Technology Center Austria, Seebacher Allee 64, 9524 Villach, Austria

\*2) Imerys Fused Minerals Murg GmbH, Ferroweg 1, 79725 Laufenburg, Germany

\*3) Worldsource Inc., 530 Alpha Drive, Pittsburgh, PA 15238, USA

### Abstract

This study describes the development of an investment casting mould with calcia stabilised zirconia / ammonium zirconium carbonate as a face coat for Ti-6Al-4V. The slurry stability was evaluated by aging studies measuring the pH, Zahn cup viscosity and plate weight. Full investment casting shells were built up and tested for MOR and with dilatometry for the softening point. Finally, casting trials were made and alpha case formation was assessed by measuring the hardness and chemical composition with ICP-OES and hot gas extraction. The study provides recommendations on the preparation of the zirconia slurry to improve quality and reduce alpha case formation.

### 1. Introduction

Compared to standard titanium alloy, titanium aluminium alloys have a lighter weight and a higher heat resistance and therefore are often used for casting of turbocharger wheels or for medical implant, but also in sporting goods as golf club heads, bicycling or in motorcycle parts [1]. The casting of titanium aluminides is a very demanding process mainly due to the low fluidity of the TiAl alloy around its melting temperature. Due to the high affinity of certain elements, like oxygen, titanium and its alloys can easily interact with the materials used for the shell (moulding process), including the binders [2]. This results in the formation of a hardened layer at the interface of the metal with the shell, the so-called alpha case layer [3]. This layer contains certain amounts of dissolved oxygen and is feared for its brittle behaviour and susceptibility to crack generation and propagation. To keep the alpha case formation as low as possible, special raw materials are required which have a more negative standard Gibbs free energy charge than  $TiO_2$ , for instance  $ZrO_2$ ,  $ZrSiO_4$ ,  $CaZrO_3$ ,  $CaO$  or  $Y_2O_3$  [4, 5]. This has to be taken into consideration by choosing the right raw materials for the shell system coming into contact with the alloy during the casting process, which includes the flour, the stucco as well as the binder used for the front and also for the intermediate layer.

### 2. Materials and slurry preparation

Investment casting moulds were prepared in the standard way of preparation, i.e. dipping wax models into ceramic slurries, followed by application of coarser grits ("stucco") with rainfall-technique, resulting in layered ceramic parts. The following materials that were used in the different layers are described in the following paragraphs.

#### 2.1 Materials used in slurry preparation

T-Power Prime<sup>®</sup> 60, i.e. ammonium zirconium carbonate binder supplied by Worldsource, Pittsburgh, OH, was used in the face coat and intermediate layer. A standard colloidal silica (24wt%, 8nm) was used as binder in the face coat and intermediate layer of the comparison shell, as well as in the back up and seal coatings of both types of shells.

Calcium stabilised zirconia (Zionic® 95ZC, produced by Imerys, Greeneville, TN) was used as ceramic flour in the face coat and intermediate coat slurries of both shell types. For the back up and seal coatings we used Teco-Sil® Hybrid+ (made by Imerys in Greeneville, TN) which is an aluminosilicate-amorphous silica blend with a very broad particle size distribution enabling an extremely high filler load. This product allows to reduce the number of layers to speed up the shell building process and facilitates the shell removal versus aluminosilicate-based systems.

### 2.3 Stucco materials

Calcium stabilised zirconia (Zionic® 95ZC -100+200#) was used in the first stucco layer, followed by fused alumina (Alodur® ZWSK60, produced by Imerys in Zschornowitz, Germany) and calcined alumina silicate (Mulgrain® Mulcoa M47 S22, produced by Imerys in Andersonville, GA). The same stucco materials were used for both different shells.

### 2.4 Preparation of the slurries and evaluation of slurry stability

The following three different slurries were prepared for mould build-up:

- **AZC binder system with 95ZC flour (used in shell A)**

The slurry was made by dispersing 95ZC -325# and 95ZC-100# in T-Power Prime 60 binder using a rotating drum. Since adding all powder directly into the binder led to the formation of a very viscous slurry, it was decided to take time for the slurry preparation and to add the ceramic powder in small additions - this also helped to obtain a good dispersion of the zirconia powder. We started with 50wt% 95ZC. After 6 hours homogenization time the filler load was increased to 70 wt.-% and the pH level was adjusted between 9-9.5 by adding ammonium in a concentration of 30%. The preparation worked perfectly and the slurry was running at a very stable level. Finally, it was possible to adjust the slurry at a flour level of 81 wt.-% which led to a viscosity around 13-14 seconds measured with a Zahn 5 cup. As a wetting agent 0.5wt% of T-Power Prime Wet 200, supplied by Worldsource, Pittsburgh, OH was added at the beginning of the slurry preparation.

- **CS binder system with 95ZC flour (used in shell B)**

95ZC -325# and -100# were added to the colloidal silica binder with a rotating drum. The solid concentration realised was 86wt% - no pH adjustment was necessary. The observation of lower viscosity when using colloidal silica as a binder for calcium stabilised zirconia powders and therefore the achievement of higher solid concentrations (at constant viscosity) was already reported in literature [6]. As a wetting agent we used Victawet 12.

- **CS binder system with Hybrid# flour (used in both shells for back-up and seal layers)**

Hybrid+ flour was directly dispersed in the colloidal silica binder with a rotating drum. The solid concentration was set to 72% and the viscosity was measured to be 11-12 seconds with Zahn 5 cup. No pH correction was required. The preparation and characterization of Hybrid+ slurries have been reported in literature [7].

The slurry stability of the 95ZC slurries (with AZC and colloidal silica binder) are shown in figure 1. To maintain the pH of the AZC slurry at constant level it was necessary to periodically add ammonia in small amounts. By doing so the slurry could easily be controlled and kept at a good viscosity. The colloidal silica based slurry was lower in the pH compared to the AZC based one. The slurry was very constant over the time without the need to correct the pH value.

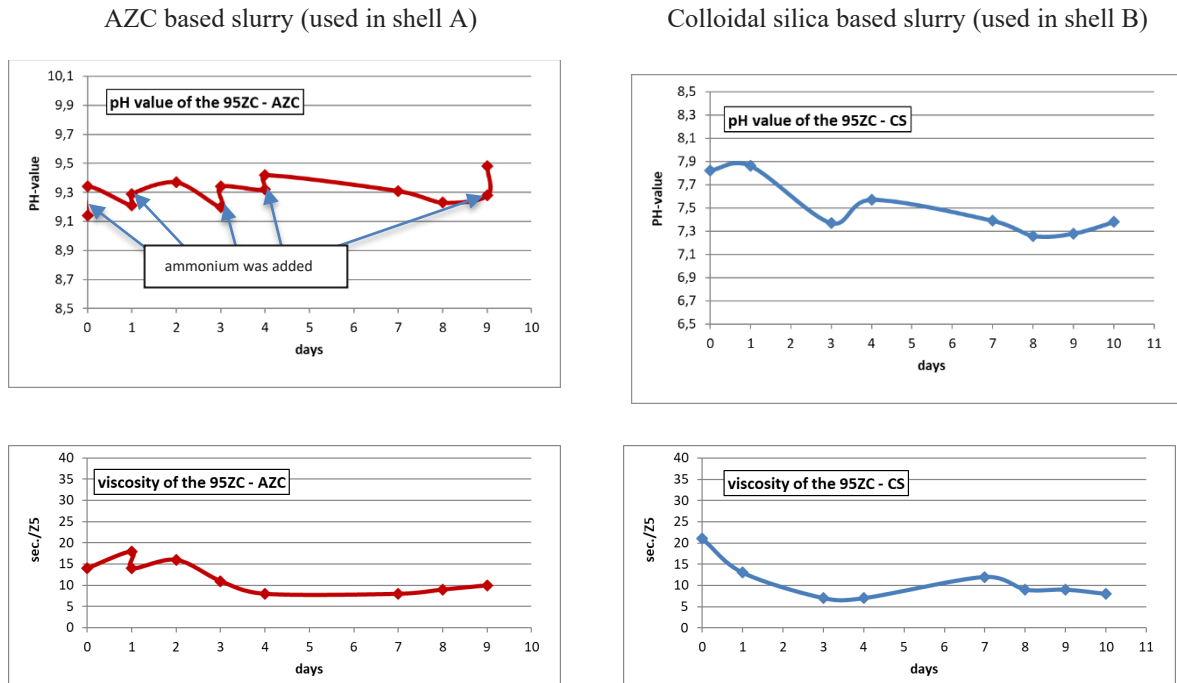


Fig.1: pH and viscosity evolution for the AZC based slurry system and the colloidal silica based one

The plate weights of the 2 slurries were determined and are shown in figure 2. The viscosity of the slurries was adjusted to 13-14 seconds measured with a Zahn 5 cup. The filler load was 81% for the AZC slurry and 86% for the colloidal silica one. These differences led to a slurry density difference of 3,48 g/cm<sup>3</sup> for the AZC and 3,63 g/cm<sup>3</sup> for the colloidal silica which explains the slightly higher final plate weight of the colloidal silica based slurry, which was around ~5g, respectively ~4g for the AZC based one.

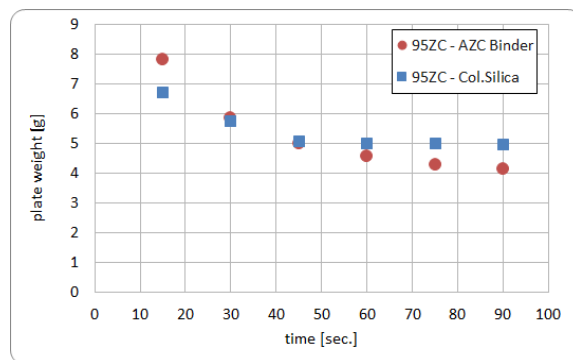


Fig.2: Comparison of the plate weight of the AZC and the colloidal silica based slurry

### 3. Preparation of investment casting moulds and characterisation

Two different shell formations were prepared for this study and characterized. Each test shell was made with 5 layers (1 front layer, 1 intermediate layer, 3 backup layers) and a seal coat. For each formulation 4 shells were built. The shell formulations are shown in table 1.

Tab.1: composition of the different test shells

	AZC based Shell		CS based Shell	
	Slurry	Stucco	Slurry	Stucco
<b>Layer 1 (face)</b>	95ZC - AZC	95ZC	95ZC - CS	95ZC
<b>Layer 2 (Int.)</b>	95ZC - AZC	ZWSK60	95ZC - CS	ZWSK60
<b>Layer 3 - 5 (backup)</b>	Hybrid+ - CS	M47	Hybrid+ - CS	M47
<b>Seal coat</b>	Hybrid+ -CS	-	Hybrid+ - CS	-

The wax pattern used to prepare those shells was dimensioned 6cm x 8cm x 0.5cm. Prior to the to the preparation of investment casting moulds used in the casting trials several different particle size distributions of 95ZC flours were evaluated - when only using -325# powder it was found that after dipping the wax pattern and application of the stucco of the first layer, the coating was sliding off the wax pattern (see fig.3). Therefore, the particle size distribution was optimised by adding a higher percentage of coarse (-100#) zirconia particles so that the distribution was broadened and the finer particles could fit the matrix of the coarser ones. The solid concentration given in paragraph 2.4 was achieved with the optimised particle size distribution. The coated wax plate of the optimised slurry is shown in figure 4 - here we found a perfectly coating behaviour.



Fig.3: First layer was running down the wax pattern due to a too fine flour material with a too narrow particle size distribution.



Fig.4: Optimized particle size distribution, the finer part was reduced. The first layer could be applied perfectly.

The shells were dewaxed, pre-fired at different temperatures, which were 800°C and 1100°C, respectively and finally test pieces were cut out of them.

- **Mechanical strength of the shells**

Afterwards the cold modulus of rupture (CMOR) of the two different shells were determined. Figure 5 shows the CMOR as a function of the sintering temperature. The shells based on colloidal silica were slightly higher in the bending strength compared to the AZC based ones. The lower bending strength at higher temperature could lead to an easier shell removal of the shell after the casting process.

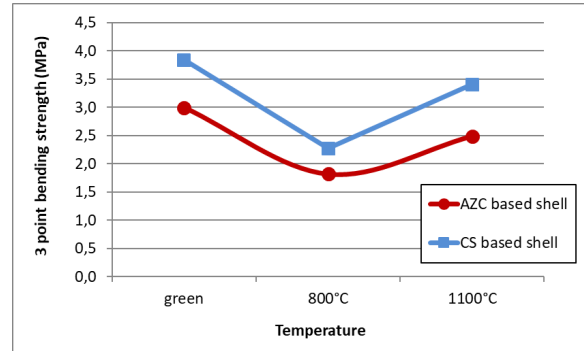


Fig.5: cold modulus of rupture of the different shells

- **Thermal expansion of the shells**

In the next step the thermal properties of the shells were investigated by using dilatometry. Figure 6 shows the thermal expansion curves of the shells. Due to the fact that the thermal expansion is mainly influenced by the thicker backup layer the curves were overall quite similar. The thermal expansion curves of both shells are not significantly different from each other - this is as expected since the only difference is in the binder in the first two layers (which would account to a very small difference in regard to total weight percentage).

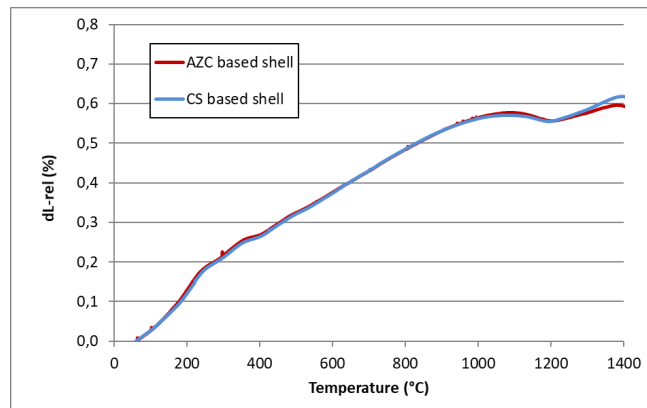


Fig.6: thermal expansion of the shells

- **Cold and hot permeability of the shells**

The permeability of the shells was determined by using some standard ping pong balls in which an aluminium oxide tube was inserted and then those balls were shelled. Due to the fact that also the hot permeability should be tested, glass tubes could not be used for the test build up, since the heat transfer of those would be too high. After the shelling was finished a controlled burn out of the ping pong balls was done, so that a cracking could be avoided. The ceramic balls were then pre-fired at 1050°C and were then measured at room temperature, 400°C, 800°C and 1050°C, respectively. During the test compressed air was pressed at 300 mbar through the aluminium oxide tube and the volume of air going through the shell per minute was measured. A specially designed furnace with a hole in the bottom was used to insert the shells inside the furnace and to measure the hot permeability of those.

The results of this investigation are shown in figure 7. As one can see the colloidal silica binder based shell was lower in the permeability compared to the AZC based shell. The higher permeability of shell made with the AZC binder could help for the dewaxing process and for removing free gas through the shell during the casting process. The difference was probably due to the packing density of the first two layers - which again results from the solid concentration of the slurry: the higher solid concentration of the colloidal silica-based shell closed the finer pores and therefore decreased the shell permeability.

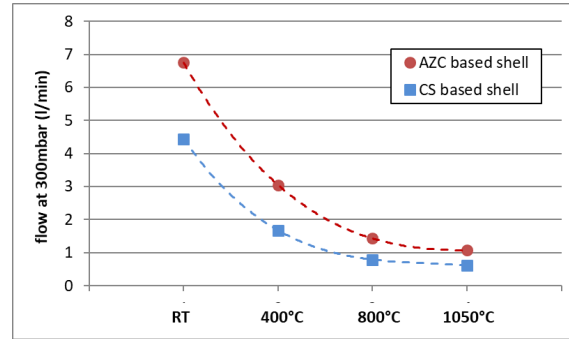


Fig.7: permeability of the tested shells at different temperatures

#### 4. Casting trials with Ti-6Al-4V

In the next step of this study we compared the performance of the different shells made from different binders in a casting trial done at the Forschungsinstitut Edelmetalle + Metallchemie (FEM) located in Schwäbisch Gmünd in Germany. The shell formulations are shown in table 3 - the only difference was in the face coat and intermediate layer, which had been prepared with AZC or CS. We increased the amount of backup layers from 3 to 6 to increase the mechanical strength of the shells to sustain the casting process. The shell formulations are shown in table 2.

Tab.2: shell build up for the casting trials

##### Shell A – AZC based shell

Shell build up		Binder	Flour	Stucco	Viscosity
Layer 1	Face Coat	AZC	95ZC	95ZC	14-15 / Z5
Layer 2	Intermediate	AZC	95ZC	ZWSK60	7-8 / Z5
Layer 3-8	Backup	CS	Hybrid+	M47	11-12 / Z5
Layer 9	Seal Coat	CS	Hybrid+	-	11-12 / Z5

##### Shell B – Colloidal silica based shell

Shell build up		Binder	Flour	Stucco	Viscosity
Layer 1	Face Coat	CS	95ZC	95ZC	14-15 / Z5
Layer 2	Intermediate	CS	95ZC	ZWSK60	7-8 / Z5
Layer 3-8	Backup	CS	Hybrid+	M47	11-12 / Z5
Layer 9	Seal Coat	CS	Hybrid+	-	11-12 / Z5

The casting was done by melting Ti-6Al-4V (Titan Grade 5) alloy in calcium zirconate ( $\text{CaZrO}_3$ ) based crucibles. Afterwards the cast pieces were analysed by hot gas extraction and ICP-OES and the cross sections were metallurgically evaluated.

The figure 8 shows the shell A before dewaxing. The shells were dewaxed in an autoclave (shell A after de-waxing is shown in figure 9) and afterwards sintered at  $1100^\circ\text{C}$  for 2 hours. For the casting itself the shell was preheated to  $800^\circ\text{C}$ .



Fig.8: build up shell A

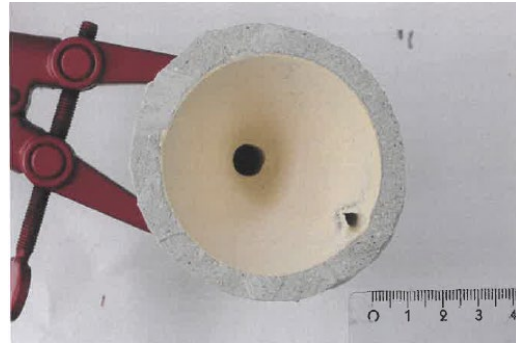


Fig.9: shell A after the dewaxing process

Figure 10 and 11 show the cast metal parts after demoulding (“knock-out”). The demoulding could more easily be achieved from shell A; we also found a better surface finish (smoother, glossier surface) for the parts made from shell A. Parts recovered after casting shell B seemed to have suffered from a reaction with the ceramic shell, so that knock-out was more difficult and the surface finish was not that good.

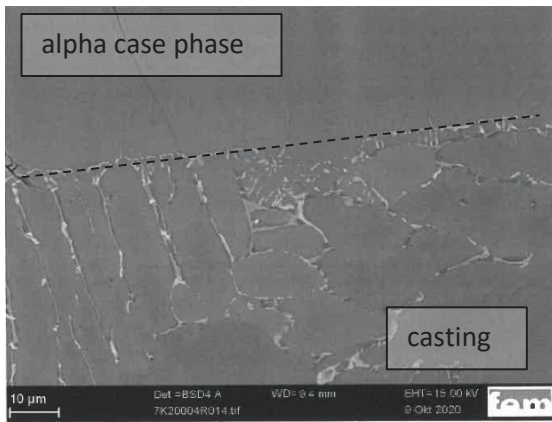


Fig. 10: shell A after the casting and demoulding process, which showed a good shell removal and good casting surface

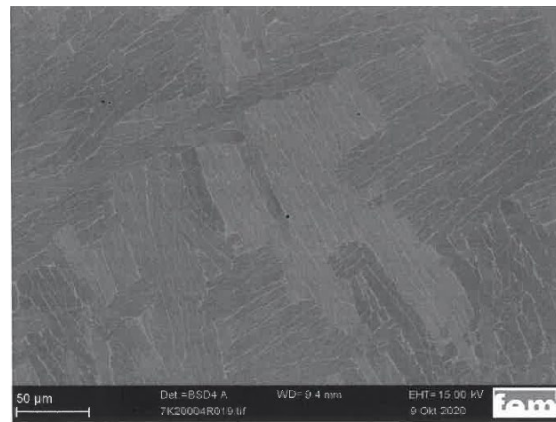


Fig. 11: shell B after the casting and demoulding process, which showed more reaction between the casting surface and the ceramic

Polished cross sections of parts cast in shell B are shown in figure 12. The alpha case formation on the surface of the cast part is clearly visible and the boundary between the hardened oxygen enriched phase (alpha case) and the undisturbed cast part can be identified. Figure 13 shows the alpha beta structure of the Ti-6Al-4V casting in the centre of the cast part.



**Fig.12:** border between the hardened alpha case and the residual Ti-6Al-4V casting part (shell B)



**Fig.13:** alpha beta structure of the Ti-6Al-4V casting part (shell B)

Figure 14 and 15 display the Vickers microhardness profiles of the Ti-6Al-4V casting produced in a colloidal silica binder based mould (shell B) as well as the AZC binder facecoat based mould (shell A). As one can clearly see, the hardness of the surface region, which is a clear indication for the alpha case phase formation, could be significantly reduced by using the AZC binder for the face coat. The increase in hardness was 114% for the shell B (within a depth of 600μm to the surface) whereas we only found an increase in hardness of 48% for the cast part from shell A. This demonstrates that the alpha case formation could be reduced by nearly 60% using the AZC binder system in the front layers.

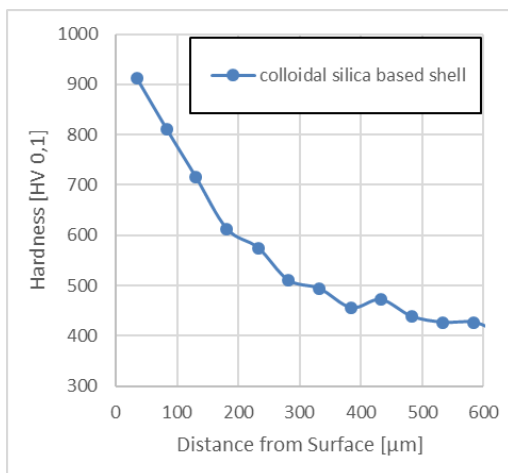


**Fig.14:** Vickers microhardness profile of a Ti-6Al-4V casting produced in a colloidal silica binder based mould (shell B)

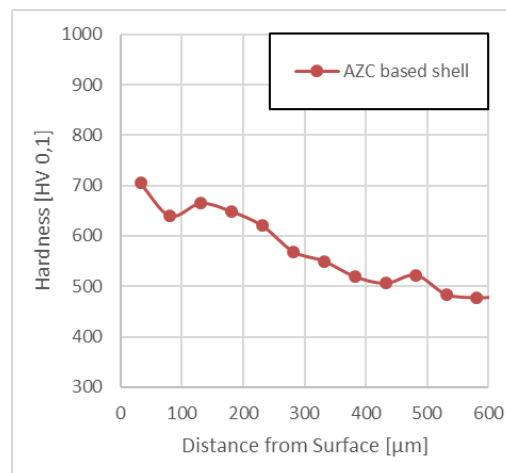


**Fig.15:** Vickers microhardness profile of a Ti-6Al-4V casting produced in an AZC binder facecoat based mould (shell A)

The chemical surface composition of the 2 shells was determined by using inductively coupled plasma optical emission spectrometry (ICP-OES), the results are shown in table 3.

Parts made from shell B were found to contain increased oxygen concentrations, which could be an indicator for the presence of oxygen enriched alpha case surface layers. Parts made with shell A showed a higher amount of zirconium in the surface layers, which could probably be a result from a reaction with the ammonium zirconium carbonate binder.

**Tab.3:** ICP-OES analysis of the 2 shells (results in wt.%)

	Shell A	Shell B
Al	6.00	6.42
Cr	0.008	0.009
Fe	0.16	0.17
Ni	0.014	0.014
V	4.0	4.2
Y	0.0003	0.0002
Zr	0.69	0.33
N	0.027	0.028
O	0.58	0.65
Ti	88.52	88.18

## 5. Conclusion

- (1) The stability of slurries made with AZC binder was proven to work well with the calcia stabilized zirconia flour.
- (2) Shells were built up with the AZC binder and compared to a traditional colloidal silica based shell, and it could be shown that there was a significant improvement during the casting trials using the AZC binder.
- (3) The amount of alpha case could be significantly reduced by nearly 60% using ammonium zirconium carbonate binder on the first layers of the shell.
- (4) The surface quality of the Ti-6Al-4V casting could be improved by using the AZC binder together with the 95ZC system.

## 6. References

- [1] M.Takahashi., The investment casting technology of Ti products, 13th World Conference on Investment Casting (2012), Kyoto
- [2] Myoung-Gyun Kim et al, Effect of Mold Material and Binder on Metal-Mold Interfacial Reaction for Investment Castings of Titanium Alloys, Materials Transactions 43 (2002) pp. 745-750
- [3] Si-Young Sung and Young-Jig Kim, Alpha-case formation mechanism on titanium investment castings. Mater. Sci. Eng. A 405 (2005) pp 173-177.
- [4] S.-Y. Sung et al., Formation of Alpha Case Mechanism on Titanium Investment Cast Parts, Titanium Alloys – Towards Achieving Enhanced Properties for Diversified Applications, InTech (2012), 228p.
- [5] R. Sharon Uwanyuze et al, A review on alpha case formation and modeling of mass transfer during investment casting of titanium alloys, J. Alloys Comp. 865 (2021), 158558
- [6] Z.Ertuan et al., Characterization of zirconia-based slurries with different binders for titanium investment casting, China Foundry Vol.9 No.2 (2012), pp.125-130
- [7] Krumrei et al, Engineered Ceramic Solutions based on Fused and Sintered Mineral Products, 14<sup>th</sup> World Conference in Investment Casting, April 17-20 (2016), Paris (F)



# **INVESTMENT CASTING INSTITUTE**

## **Process Control Standards for Investment Castings**

Nip Singh – S&A Consulting Group, LLP  
Brian Ferg – Consolidated Precision Products  
Joseph Fritz – Investment Casting Institute  
Craig Lanham – Member Emeritus  
Thad Nykiel – BESCOAST, Inc.  
Tom Planz – Kovatch Castings, Inc.

## **68<sup>TH</sup> TECHNICAL CONFERENCE & EXPO 2021**

Paper № 10

## 1. Process Control Standards (PCS) for Investment Castings:

**Nipendra (Nip) P. Singh,**  
**Chair, ICI Process control Standards Core Team**  
**S&A Consulting Group LLP, USA**  
[nsingh@sa-consultinggroup.com](mailto:nsingh@sa-consultinggroup.com)  
**216-593-0050**

### PANEL DISCUSSION

#### Abstract

As Process Control is very critical to our manufacturing of Investment Castings (IC) worldwide, we would like to involve all sectors of IC in all countries. This panel will present the current status of the Process Control Standards (PCS) and also will detail how casters can start using this ICI benefit.

The task force on PCS, a subgroup under Education Committee has made considerable strides since our last presentation at ICI 66th conference in 2020.

Training program for surveyors (internal/external) certification was developed by the core team, tested, and now being uploaded on Tune'Em platform for certification. This training program was considered very crucial and necessary for the success of PCS acceptance from foundries.

A survey operating team was split out from core PCS team for streamlining of day-to-day operation of PCS. The details of operating and continued core team functions will be detailed by the panel.

It is expected that some foundries will share their experience with PCS so far, and PCS core team members are expected to join the panel to answer any questions.



# **INVESTMENT CASTING INSTITUTE**

## **Steel Performance Initiative (SPI) and Digital Innovative Design (DID)**

Raymond Monroe  
Steel Founders' Society of America

## **68<sup>TH</sup> TECHNICAL CONFERENCE & EXPO 2021**

Paper № 11

## Steel Performance Initiative and Digital Innovative Design

Raymond Monroe, (CK?, DP?, HB?,...)

Our manufacturing economy and in particular our national security systems relies fundamentally on the most advanced steel technology. Globalization with the accompanying trade policy, tax policy, regulatory burdens, cultural misunderstandings, etc., have led to decades of underinvestment in steel technology. The lack of support from federal research dollars and the burdens shrinking the industry have also led universities to move away from steel as a core area of research and expertise. Kent Peaslee saw this and persuaded NUCOR to endow a professorship at MS&T to institutionalize steel research at that university. There are only a few universities that are involved with industry to move steel technology forward.

There has been a generational change in industry in the past 10 year where the baby boomer experts have retired and in the military services, new steel experts have been hired but they have limited budgets and influence. As a part of wider trends in research with the move from analytical methods to numerical methods, new alloys and technologies are incremental improvements on existing technology that are done on a case-by-case basis. At the same time universities continue to develop in ICME basic atomic level understanding of how steel works. This university level work is fundamental but often not well placed to provide industrial advances.

Steel Founders' Society of America (SFSA) has been a partner with the Defense Logistics Agency (DLA) for more than 30 years in developing casting technology. SFSA was able ten year ago in partnership with DLA to expand the casting program in steel to begin to enable domestic producers to have the competitive advantage and leading technology to support DoD requirements. The first expanded program was the Digital Innovative Design (DID) program to support steel casting design using process modeling to support performance modeling. This program was fully funded and was succeeded by the Steel Performance initiative (SPI) that broadened the emphasis to the whole range of specialty steel products required in DoD equipment including mill products, forgings and castings. SFSA wants to partner with ICI and the investment casting community to advance the key technologies to provide the highest quality investment castings. Both DID and SPI aims to connect the principal investigators (PIs) at the university to the steel producers to support the equipment manufacturers that supply the services to provide the most capable equipment to the warfighter.

DID identified three objectives to provide the design engineer with tools to allow them to use castings more capably. The aim to equip them with tools and information to allow them to full exploit the steel casting process for their requirements.

The first area was to demonstrate and support the use of an ASME BPVC approach to the design of structural castings. In the Boiler Code, casting designers do not need to determine

the strength properties or the non-destructive test (NDT) requirements because they are embedded in the Code. This led to ironic situation where the designer of a frame for equipment that wants to use a casting for a corner must make these decisions that are outside of his expertise while the designer of a steel fitting for a nuclear power plant does not. SFSA is working with the American Institute of Steel Construction (AISC) and the American Welding Society (AWS) to incorporate steel casting grades into AWS D1.1 and the AISC building codes. An ASTM standard is being developed that emulates common mill grades to reduce the uncertainty designer may face using castings.

The second area for high and reliable performance is to utilize the process solidification and heat treat modeling to determine lower bound design allowable properties in each location of a proposed casting design to be imported into the Finite Element Analysis (FEA). This will allow a dialog between the designer and the producer to optimize the design for the requirements. It also will provide the benefit of locating the critical design features that determine the reliability of performance.

The third area uses the ability to identify this critical region and provided quantitative non-destructive testing (QNDT) that can be correlated with performance. The current commercial NDT standards are workmanship standards that are unrelated to performance. Aerospace industries already have customized NDT for critical parts based on a fitness-for-service design methodology. The efforts in DID in modeling and QNDT will move the DoD and commercial designers to higher performance fitness-for-service designs.

The challenges that exist though are bigger and more systemic than just equipping designers. This led to the proposed SPI program. While it will not deal with the cultural or public policy problems, the goal is to develop the steel technology required to have the most advanced steel performance in the world. This means addressing strategic challenges and opportunities. The areas identified by the steel community in DoD at their steel summits include:

- Robust Advanced High Strength Steels (RAHSS)
- Integrated Computational Materials Engineering (ICME) and Model-Based Process & Product Design (MP<sup>2</sup>D)
- Hybrid Manufacturing Technology (Hybrid ManTech)
- Quantitative Non-Destructive Testing (QNDT) and Non-Destructive Evaluation (NDE)
- Next Gen Job Shop Manufacturing (Smart JSM)

Robust Advanced High Strength Steels (RAHSS)- SFSA through the long term involvement with DLA has been involved from the start in initiatives to develop RAHSS. Three areas of interest are currently under development. A traditionally alloyed martensitic steel, AF96 is a candidate to provide a high strength affordable steel from defense requirements. Producing HY grades for the Navy is problematic and improved alloys are needed. Other advanced steels like an austenitic FeMnAl or multi-principal entropy alloys (MEPA) should be explored.

Integrated Computational Materials Engineering (ICME) and Model-Based Process & Product Design (MP<sup>2</sup>D)- This effort extends the DID work to include alloy design for unique service requirements and to continue to develop the engineering information needed for users to exploit the steel technology. The use of numerical methods to do case study type work has resulted in a failure to develop engineering handbook like properties that provide the infrastructure for design and manufacturing. This would include the combination of processes to gain the benefits of these process technologies. Work has been initiated to use forging as a processing step in casting to get forging properties in critical sections.

Hybrid Manufacturing Technology (Hybrid ManTech)- This area looks to innovative ways to use steel in hybrid casting. Two areas are currently of interest, casting ceramics into steel and casting steel around steel to get properties in heavy sections of unique combinations and properties and cast structures.

Quantitative Non-Destructive Testing (QNDT) and Non-Destructive Evaluation (NDE)- The use of current workmanship standards for quality is problematic. SFSA work has shown that they are poor in their Gage R&R with little agreement on evaluating any particular component. Most of the standards are qualitative comparing images and without a criteria for evaluation subjectively rating a part image against a standard image. Even if this image type standard could be done objectively, it is unrelated to performance. QNDT continues in SPI to develop quantitative NDT relatable to performance.

Next Gen Job Shop Manufacturing (Smart JSM)- Workforce for future production is a challenge. Improving the situation requires both improve job-shop automation and better training and development tools. SPI is sponsoring projects to develop artisan training and robotic systems for single piece automation.

SPI's goal is to include the entire specialty high performance steel industry in this effort and as a part of this community. We are delighted to invite ICI and the members to participate. SPI is initiating investment casting programs with the guidance of key PIs and industrial leaders in the ICI community. We look forward to a constructive and profitable collaboration.



# **INVESTMENT CASTING INSTITUTE**

## **Implementing Best Practices & Reducing Process Costs for Refractory Use in Investment Casting & Alloy Production Foundries**

Phil Geers  
Blasch Precision Ceramics

## **68<sup>TH</sup> TECHNICAL CONFERENCE & EXPO 2021**

Paper No. 12

**BLASCH**  
PRECISION CERAMICS



Where your ideas take  
**SHAPE** in **CERAMIC**

*“Implementing Best Practices and  
Reducing Process Costs for Refractory Use  
in Investment Casting and Alloy  
Production Foundries ”*

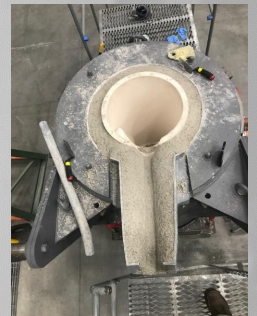
Phil Geers – Sr. Market Manager

ICI Technical Conference 2021



## Agenda:

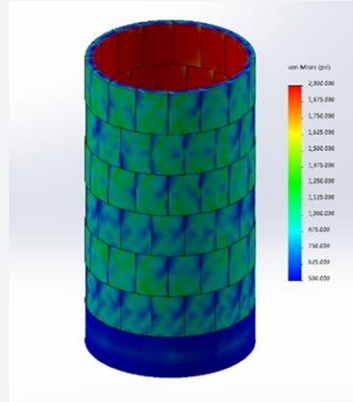
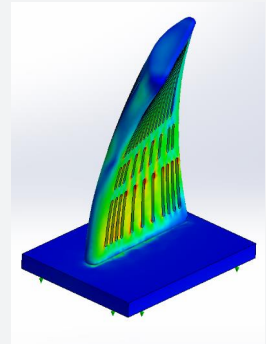
- Introduction of Blasch Ceramics
- Refractory Installation & Use Procedure Document
- Induction Furnace function and how it affects the refractory
- Evaluate Best Foundry Practices for Refractory Installation
- Explore Furnace / Melt operation: Practices and Procedures
- Metallurgy, Refractory and Process compatibility





## Blasch Precision Ceramics

- Founded in 1979 (Over 40 years in business)
- Employee-owned manufacturer of engineered industrial ceramic shapes and systems
- Headquarters in Albany, NY with production, sales and representation world wide
- ISO 9001 Certified since 1999
- Provide products for the Specialty Alloy, Investment Casting, Chemical / Petrochemical, Process Heating, Power Generation and Mining Markets.
- Manufacturer with significant engineering, design and research & development capability, and systems design experience



© 2021 Blasch Precision Ceramics



## Blasch Precision Ceramics:

### Products for Specialty Alloys (Investment Casting/Super Alloy Production)



InterLok™ Segmented Linings



ProCaster™ Crucibles



Back up Ram, Plastic and Slip Plane



Core Setters



Launders and Tundishes



Sample Cups



Setters and Kiln Furniture for cores and core setters



Atomization Nozzles

© 2021 Blasch Precision Ceramics

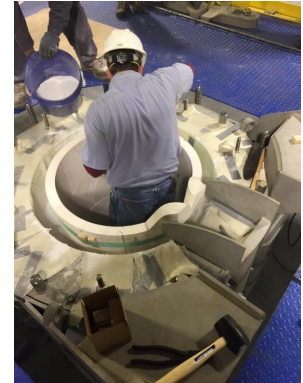


## Best Refractory Practices

### Refractory Installation & Use Procedure Document:

A document that explains the complete process of preparing, lining and removing the lining for an induction furnace.

- Do you have one?
- Is it current & representative of the products you use?
- Does it include the variants you might have in process?
- Does your team understand it & are there good explanations?
- Does your team know what to do if something is not normal? What changes if you have a freeze off, an over temperature event, an extended melt “hold”?



#### MONOLITHIC CRUCIBLE INSTALLATION AND OPERATIONS MANUAL

Prepared by:  
Blasch Precision Ceramics, Inc.  
580 Broadway  
Albany, NY USA 12204  
Tel (518) 436-1263  
Fax (518) 436-0098

	Rev. 10/19
I. CRUCIBLE PRE-INSTALLATION MATERIALS CHECKLIST .....	I-1
II. MONOLITHIC CRUCIBLE INSTALLATION PROCEDURE .....	II-3
A. UNPACKING .....	II-3
B. REMOVAL OF PRODUCT .....	II-3

© 2021 Blasch Precision Ceramics

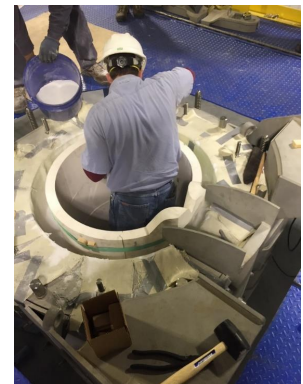


## Best Refractory Practices

### Refractory Installation & Use Procedure Document:

A document that explains the complete process of preparing, lining and removing the lining for an induction furnace.

- Do you have one?
- Is it current & representative of the products you use?
- Does it include the variants you might have in process?
- Does your team understand it & are there good explanations?
- Does your team know what to do if something is not normal?
- Continuously updated and part of the standard foundry documents.  
Make it part of the quality / document standard you have for your foundry. What ways can consistency of the process and understanding be improved?



#### MONOLITHIC CRUCIBLE INSTALLATION AND OPERATIONS MANUAL

Prepared by:  
Blasch Precision Ceramics, Inc.  
580 Broadway  
Albany, NY USA 12204  
Tel (518) 436-1263  
Fax (518) 436-0098

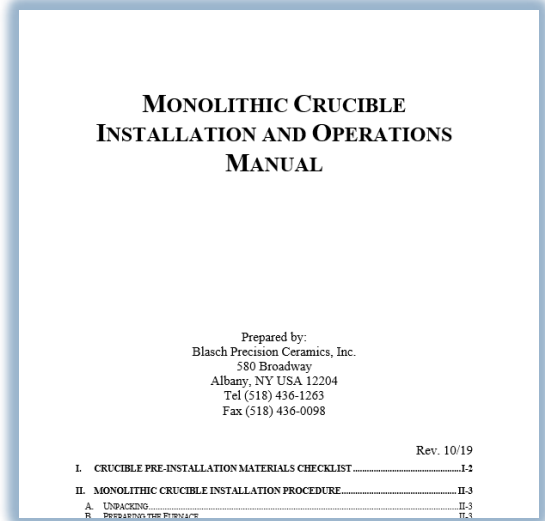
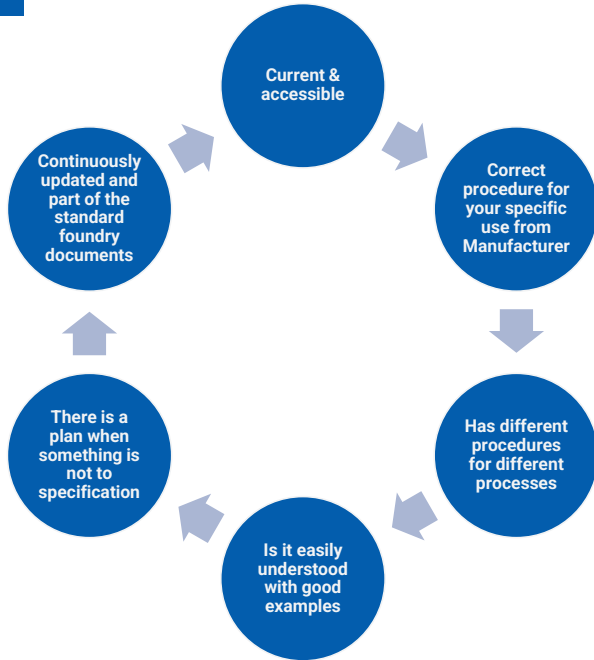
	Rev. 10/19
I. CRUCIBLE PRE-INSTALLATION MATERIALS CHECKLIST .....	I-1
II. MONOLITHIC CRUCIBLE INSTALLATION PROCEDURE .....	II-3
A. UNPACKING .....	II-3
B. REMOVAL OF PRODUCT .....	II-3

© 2021 Blasch Precision Ceramics



# Best Refractory Practices

## Refractory Installation & Use Procedure Document:



© 2021 Blasch Precision Ceramics



Now a ....



**With your  
Procedures:**

- Do you know what you know?
- Does everyone have the same understanding?
- Someone can provide you wrong information unwillingly



© 2021 Blasch Precision Ceramics



## Best Refractory Practices

### Refractory Installation Practices & Procedures:

- Safety & Ergonomics
- Make sure the furnace coil grout (bare furnace lining) is in good shape.
- Follow your furnace manufactures instructions for the leak detector system.
- When done with the installation, leave time for drying of the refractory.
- Short cuts in best practices may save time now, but they will add more time and issues later.

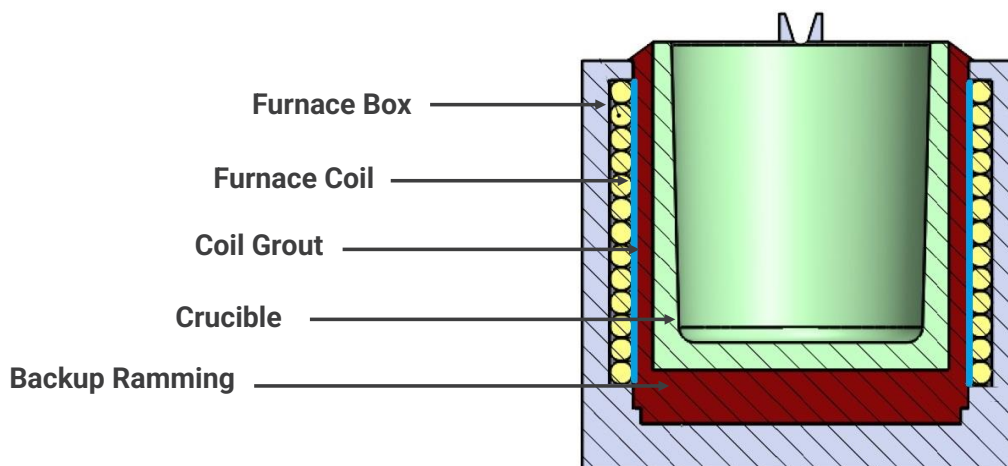


© 2021 Blasch Precision Ceramics



## Best Refractory Practices

### Refractory Installation Practices & Procedures: Induction Furnace Diagram

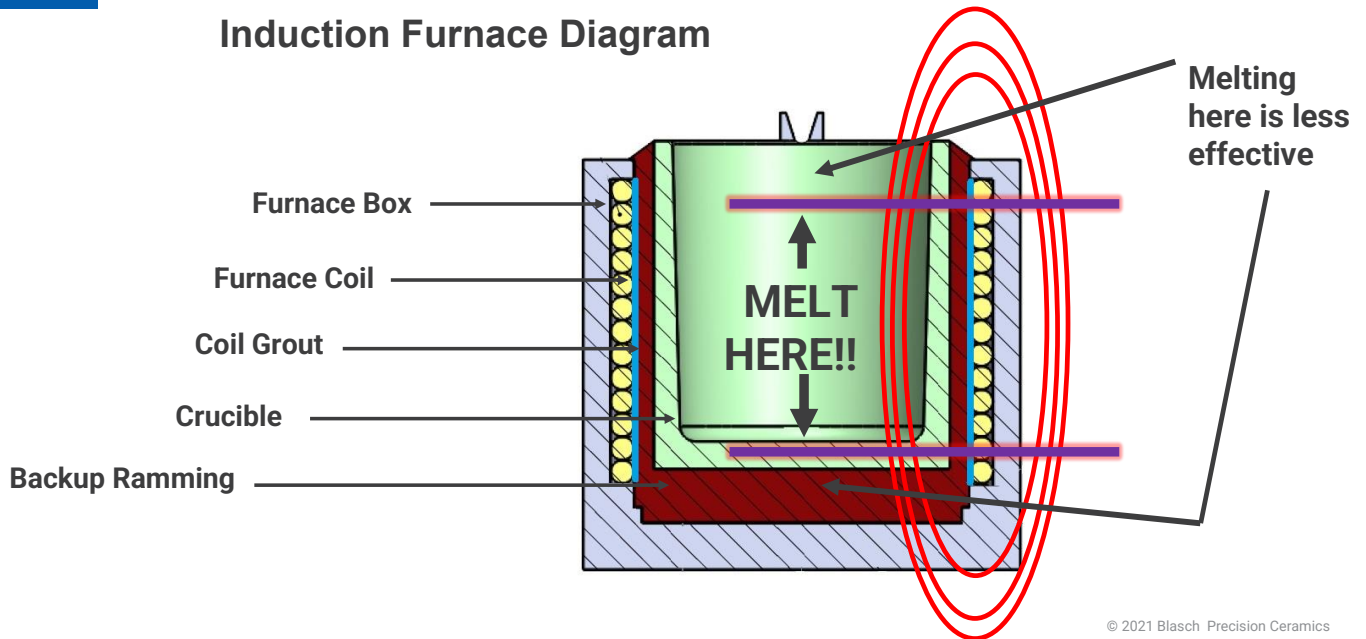


© 2021 Blasch Precision Ceramics



## Best Refractory Practices

### Refractory Installation Practices & Procedures: Induction Furnace Diagram

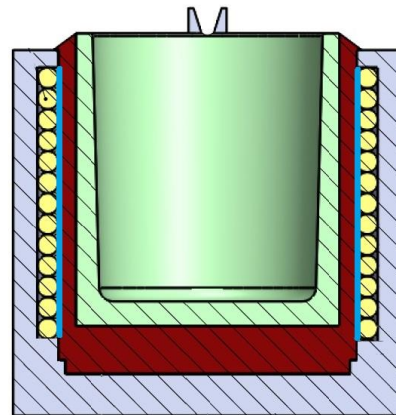


## Best Refractory Practices

### Refractory Installation Practices & Procedures:

- When using either a fired crucible or a sintered lining, follow the manufacturers directions for installation.

*This includes the methods of ramming, temperatures to sinter and drying methods*

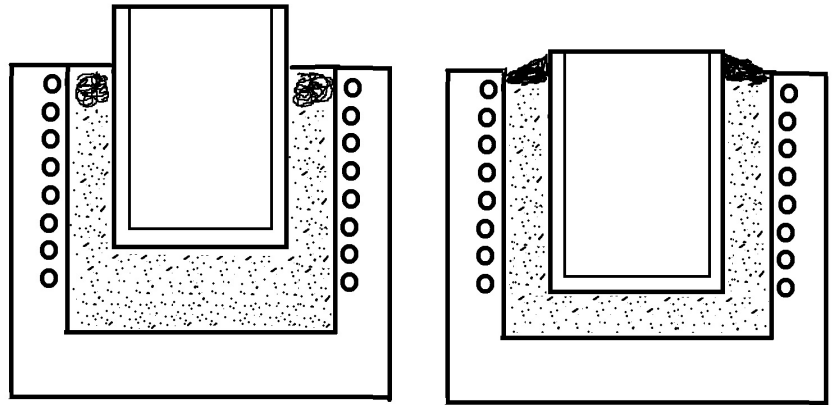




## Best Refractory Practices

### Refractory Installation Practices & Procedures:

- Size and position the Crucible or the Sintered Lining Form correctly.



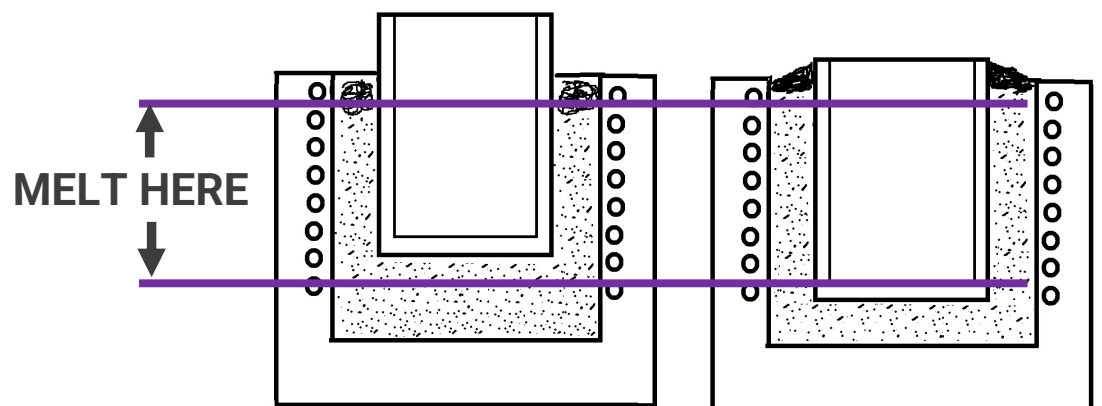
© 2021 Blasch Precision Ceramics



## Best Refractory Practices

### Refractory Installation Practices & Procedures:

- Size and position the Crucible or the Sintered Lining Form correctly.



© 2021 Blasch Precision Ceramics



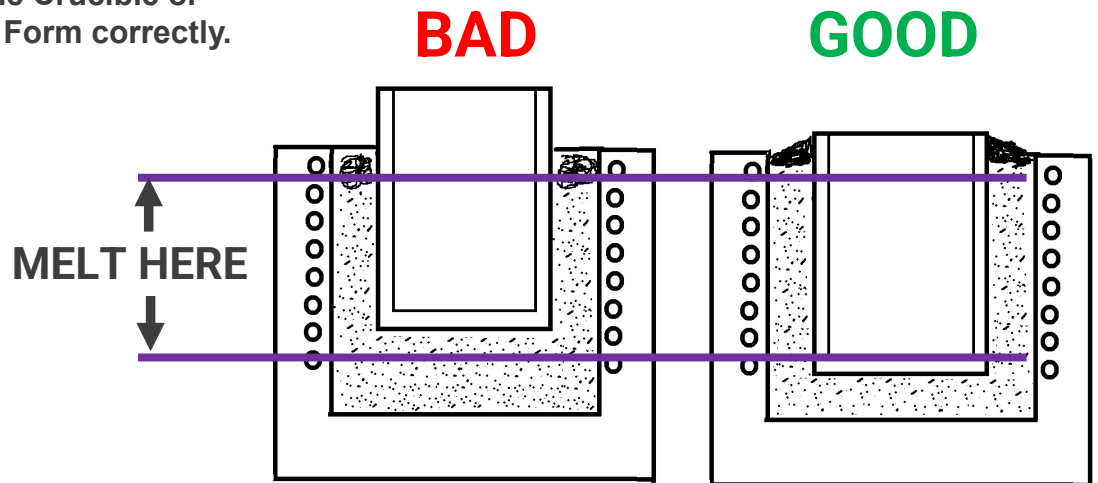
## Best Refractory Practices

### Refractory Installation Practices & Procedures:

- Size and position the Crucible or the Sintered Lining Form correctly.

What happens when we melt out of the induction focus?

- Potential freeze offs (bridging)
- Inefficient melting (hot spots)
- Over heating to hold temperature- stirring (refractory corrosion)



© 2021 Blasch Precision Ceramics



## Best Refractory Practices

### Refractory Installation Practices & Procedures:

- Follow the manufactures directions for installation.
- Size and position the Crucible or the Sintered Lining Form correctly
- Use the correct Ramming tools and methods
- If you perform the Backing Ram or Sintered ramming process *Thoroughly, Effectively, and Consistently* many of your refractory issues will reduce.



© 2021 Blasch Precision Ceramics

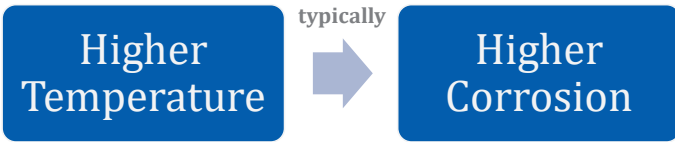


# Best Refractory Practices

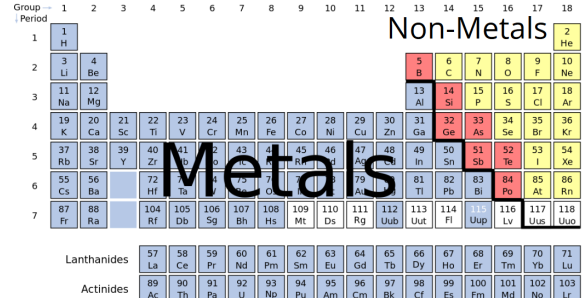
## Metallurgy, Refractory and Process Compatibility

- There are many different types of Refractory, and many different types of Metals
- Refractory needs to match the molten metal process requirement in all aspects:

Temperature – Maximum use: 1500C, 1720C?



© 2021 Blasch Precision Ceramics



# Best Refractory Practices

## Metallurgy, Refractory and Process Compatibility

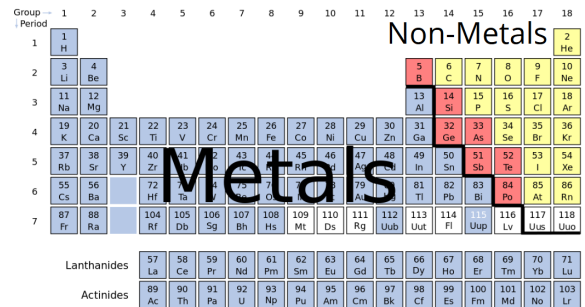
- There are many different types of Refractory, and many different types of Metals
- Refractory needs to match the molten metal process requirement in all aspects:

Temperature – Maximum use: 1500C, 1720C?

Material pH (H = hydrogen) needs to match as close as possible for the Melt and the Refractory



© 2021 Blasch Precision Ceramics





# Best Refractory Practices

## Metallurgy, Refractory and Process Compatibility

- There are many different types of Refractory, and many different types of Metals
- Refractory needs to match the molten metal process requirement in all aspects:

Temperature – Maximum use: 1500C, 1720C?

Material pH (potential hydrogen) needs to match as close as possible for the Melt and the Refractory

- If you have not run an alloy before in your current refractory, consult someone before you try it. The results could be drastic!

The periodic table shows elements grouped into 'Non-Metals' (yellow) and 'Metals' (blue). The 'Non-Metals' group includes elements from Boron (5) to Xenon (54). The 'Metals' group includes elements from Lithium (3) to Francium (87), excluding the noble gases and non-metals.



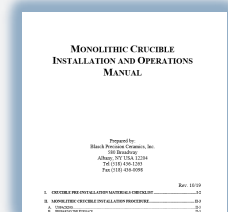
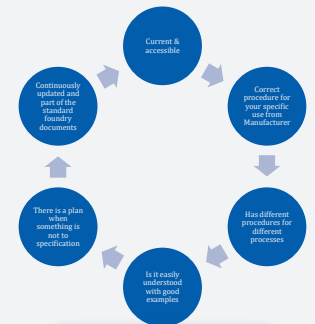
© 2021 Blasch Precision Ceramics



# Best Refractory Practices

## Summary:

- Have a current Refractory Installation & Use Procedure Document
- Have an Ergonomic and Safe area to perform your installations
- Orientate your lining correctly in the furnace
- Do not short cut your installation procedure
- Follow your refractory manufacturers recommendations for installation, use and operation



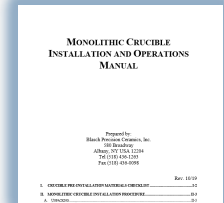
© 2021 Blasch Precision Ceramics



# Best Refractory Practices

## Summary:

- Have a current Refractory Installation & Use Procedure Document
- Have an Ergonomic and Safe area to perform your installations
- Orientate your lining correctly in the furnace
- Do not short cut your installation procedure
- Follow your refractory manufactures recommendations for installation, use and operation
- Match your refractory to your melt (for each different metal)



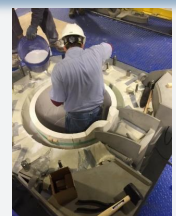
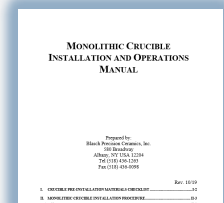
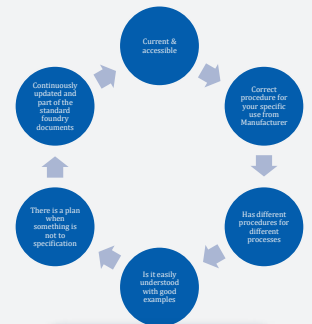
© 2021 Blasch Precision Ceramics



# Best Refractory Practices

## Summary:

- Have a current Refractory Installation & Use Procedure Document
- Have an Ergonomic and Safe area to perform your installations
- Orientate your lining correctly in the furnace
- Do not short cut your installation procedure
- Follow your refractory manufactures recommendations for installation, use and operation
- Match your refractory to your melt (for each different type)



© 2021 Blasch Precision Ceramics

Doing this will result in: Longer Refractory Life  
 More consistent melts = more uptime  
 Reduced furnace maintenance  
 Safer work environment





# Thank You

Visit [www.blaschceramics.com](http://www.blaschceramics.com)  
for more product & industry information.



© 2021 Blasch Precision Ceramics

# **INVESTMENT CASTING INSTITUTE**

## **The Effect of Firing Temperature & Time on Silica Based Investment Shells Strength**

Samuel Holt  
Georgia Southern University

### **68<sup>TH</sup> TECHNICAL CONFERENCE & EXPO 2021**

Paper № 13

# The Effect of Firing Temperature and Time on Silica Based Investment Shell Strength at Ambient and Elevated Temperatures

Samuel L Holt

Georgia Southern University, Statesboro, GA, USA

Jingjing Qing

Georgia Southern University, Statesboro, GA, USA

Mingzhi Xu

Georgia Southern University, Statesboro, GA, USA

## ABSTRACT

Shell flexural strength is an important variable for investment casting. Pre-firing is commonly utilized to increase strength, and each investment manufacture uses their own pre-firing temperature and time. Previous research has studied ambient and hot flexural strength of silica investment shells, but not over various pre-firing temperatures and times.

This research involved ambient and hot flexural strength testing of silica-based shells pre-fired at 1112F (600C), 1472F (800C), and 1832F (1000C) for 20, 60, 180, and 540 minutes. Cristobalite formation was quantified using powder x-ray diffraction from 5° to 70° with a copper target and an alumina standard. Samples were examined under microscope to identify the change in grain size. Archimedes method was used to find open porosity and bulk density, and an He pycnometer for closed porosity and true density. It was found that the strength is significantly altered by varying pre-firing temperatures and times.

**Keywords:** fused silica, investment casting, flexural strength, x-ray diffraction (XRD), cristobalite, density, porosity, grain growth

## INTRODUCTION

Investment shells are pre-fired before casting for a few reasons. The first reason for pre-firing is pattern removal. When the shells are heated the pattern is either burned or melted out. Another goal for pre-firing is to heat the shells close to pouring temperature. This is important because it allows better metal flow throughout the mold, which decreases casting defects. This study focuses on pre-firing for the purpose of increasing shell strength. It was found that sintering and coarsening of the grains increases the shell strength [1], [2]. However, there is a change in shell strength due to other factors, which are affected by pre-firing temperatures and times. The factors analyzed in this study include cristobalite formation, density, porosity, and grain size.

Generally, the grain size of a material has a direct effect on its strength. As grains get bigger the material gets weaker. This relationship is represented in the Hall-Petch equation (Eqn. 1). Where  $\sigma_y$  is the yield stress,  $d$  is the grain size diameter,  $\sigma_o$  is the stress constant for large grain size, and  $k_y$  is a material constant. Due to the other factors that affect silica-based shell strength, there is not a direct relationship with grain size and strength. The grain size of the flour particles in the binder should be measured to understand the changes in strength caused by grain growth. This is because the flour particles are the particles that undergo the most dramatic grain growth from sintering.

$$\sigma_y = \sigma_o + k_y/\sqrt{d} \quad \text{Eqn. 1}$$

When fused silica-based shells reach temperatures greater than 1832F (1000C) some amorphous silica begins to devitrify and form beta-cristobalite. Once the shell has cooled below 518F (270C) the beta-cristobalite stabilizes into alpha-cristobalite. The beta to alpha transformation is associated with a 7% volume expansion. [3] This volume change causes cracking in the shell. The cracks reduce the flexural strength of the shells. The amount of cristobalite formed in the shell after pre-firing can be found by looking at the crystallinity of the shell sample using x-ray diffraction with an alumina standard.

Porosity is inherently high in investment shells due to the manufacturing process. Porosities are formed when small air bubbles are trapped between the layers of the shell. The air bubbles are scattered throughout the shell, and the amount of porosity varies between shells. Porosities are necessary because they give investment shells permeability, which is necessary to let the mold vent during casting. However, the amount of porosity also affects the shell properties such as strength and thermal conductivity [4]. Therefore, density must be known so that porosity can be referenced when investigating changes in shell strength. A He-pycnometer and the Archimedes method can be used to find the bulk density,

true density, open porosity, closed porosity, and total porosity of the shells.

## METHODOLOGY

### SHELL BUILDING

Making shells is the first step of the experiment. Foam patterns were cut to 9in x 5in x 1in, the foam patterns were dipped in slurry and then coated with stucco. The slurry was made of one-part colloidal silica binder (.02  $\mu\text{m}$ ) and two-parts fused silica flour () (1:2 weight ratio). The binder and flour were mixed, and water was added to control viscosity. Viscosity was measured with a USS-DVT4 digital rotary viscometer using the number 3 rotor at 60 RPM. The slurry had a viscosity of  $1100\pm 100\text{cP}$  and fine stucco mesh (50/100) was used for the first coating of the shells. The shells were air dried for 4 hours between coats and the process was repeated to add backup layers for support. The slurry had a viscosity of  $600\pm 50\text{cP}$  and coarse stucco mesh (30/50) was used for the backup layers. The shells were given one prime coat, nine backup coats, and one seal coat with no stucco. The shell composition is given in table 1.

**Table 1. Composition of Investment Shells**

Coat (Number of Layers)	Slurry Composition and Viscosity	Stucco Particle Size
Prime Coat (one)	Colloidal silica (.02 $\mu\text{m}$ ) + fused silica flour () (1:2 weight ratio) Viscosity $1100\pm 100\text{cP}$	0.15-0.3 mm
Backup Coat (nine)	Colloidal silica (.02 $\mu\text{m}$ ) + fused silica flour () (1:2 weight ratio) Viscosity $600\pm 50\text{cP}$	0.3-0.6 mm
Seal Coat (one)	Colloidal silica (.02 $\mu\text{m}$ ) + fused silica flour () (1:2 weight ratio) Viscosity $600\pm 50\text{cP}$	N/A

Once the shells had all 10 coats, they were air dried for 24 hours. Then the foam patterns were burned out of the shells with a propane torch under a vent. After the foam patterns were removed the shells were pre-fired.

### PRE-FIRING

Pre-firing of the shells was performed in a heat treatment oven. The shells were pre-fired at 1112F (600C), 1562F (850C), and 1832F (1000C) for 20, 60, 180, and 540

minutes. These pre-firing temperatures and times were selected to give the shells varying strengths due to changes in porosity, crystallinity, and grain size. Table 2 shows the pre-firing temperatures and times used in this study.

**Table 2. Pre-firing Temperatures and Times**

Pre-firing Temperature	Pre-firing Time (minutes)
1112F (600C)	20
	60
	180
	540
1472F (800C)	20
	60
	180
	540
1832F (1000C)	20
	60
	180
	540

### FLEXURAL STRENGTH

Generally, four-point flexural tests are used for accurate characterization of materials. This is because four-point test configurations evenly distribute the loading. The three-point test configuration only exposes a small portion of the sample to maximum stress, so the material will appear to have a higher strength. The purpose of this experiment is to identify the effects of various pre-firing temperatures and times. Accurate characterization of the flexural strength is not necessary, so long as the testing procedures are consistent for all shell samples. Also, four-point bending tests are suitable for perfectly flat and straight samples. If there is variation in the sample, the four-point configuration would cause a twisting effect, this will not give accurate results. The three-point configuration is better suited for varying samples. The samples in this project will be tested as fabricated. Therefore, the three-point configuration will be used.

Ambient flexural strength of ceramic shells was determined by three-point flexural test according to ASTM C1161 [5]. Three samples from each pre-firing temperature and time were tested. The shell samples had dimensions of 6mm x 8mm x 90mm. The flexural strength of a beam is calculated from (Eqn.2). Where P is the force, L is the length, b is the width, d is the depth, and S is the strength.

$$S = 3PL/2bd^2 \quad \text{Eqn. 2}$$

Hot flexural strength of ceramic shells was determined by three-point bending test inside of a furnace at 2012F (1100C) according to ASTM C1211 [6]. The same sample size, dimensions, and testing equipment was used from the ambient testing. The furnace was heated at a constant rate and never allowed to go 10F(5C) over the target temperature. During the test the furnace maintained a

temperature  $\pm 4F(2C)$  and the furnace has a readout of 1C. Also, it was ensured that the sample did not have a gradient of more than 10F(5C) from end to end. The samples were placed in the furnace and given five minutes of hold time to ensure they were at temperature. The hot flexural strength is also calculated from (Eqn.2).

The flexural strength testing was conducted using a Mark-10 ESM303 motorized test stand attached to a Mark-10 series 5 force gauge model M5-300. The equipment is capable of 300 LBF (1334.5 N) and has an accuracy of 0.1 LBF (.44 N). A stainless-steel rod was attached to the bottom of the force gauge and a section of stainless-steel half round was welded to the bottom of the rod for the force bearing. The support bearings were half round alumina tubing seated in refractory brick. The support bearings and refractory brick were placed in the testing furnace for the hot flexural testing. A hole was cut in the lid of the testing furnace for the force bearing to be inserted.

### X-RAY DIFFRACTION

X-ray diffraction was performed on shell samples using an Empyrean Alpha 1 by Malvern Panalytical. The machine was run at 45kV and 40mA with a copper target emitting K alpha radiation. X-ray diffraction was performed from 5 to 70 degrees with the sample in a rotating holder. Samples were crushed to approximately 200 mesh. Shell samples pre-fired at 1832F (1000C) for 20, 60, 180, and 540 minutes were tested with an alumina standard to quantify the cristobalite formation. A shell sample pre-fired at 1472F (800C) for 540 minutes was examined without alumina standard to see if any cristobalite had formed. The analysis was performed on the HighScore software by Malvern Panalytical. The software can be used to merge scans and to identify the materials present

### DENSITY AND POROSITY

Open porosity and bulk density of ceramic shells were determined by the Archimedes method according to ASTM C20 [7]. A scale with accuracy of .01 grams was used to weigh the samples. First the samples were saturated by boiling in water for 2 hours and leaving them submerged for another 12 hours. Then the suspended weight S was found by looping the sample with wire attached to a frame on a scale and suspending the sample in water. The wire and frame weights were subtracted to give the suspended weight. Next the saturated weight W was determined by blotting the sample with a moist cloth to remove excess water from the surface, then the sample was placed on the scale and weighed to the nearest .01 gram. Once the saturated and submerged weights had been found the dry weight D of the samples was determined. The samples were dried in an oven at 230F (110C) and then weighed to the nearest .01 gram. Exterior volume V was found using (Eqn. 3). The bulk density B of the samples was found using (Eqn. 4). Open porosity P was found using (Eqn. 5).

$$V = W - S \quad \text{Eqn. 3}$$

$$B = D/V \quad \text{Eqn. 4}$$

$$P = \left( \frac{W-D}{V} \right) * 100 \quad \text{Eqn. 5}$$

An AccuPyc II 1340 gas displacement pycnometer by micromeritics was used to find true density of the shell samples. The true density was used with the bulk density and open porosity from the Archimedes testing to calculate closed and total porosity. Samples were crushed to approximately 100 mesh before testing. The samples were weighed in the sample chamber with an accuracy of .0001 grams and then placed in the He-pycnometer. The measurement process was fully automated, and three cycles were performed per sample. The pycnometer measures to the nearest .0001 g/cm<sup>3</sup>.

### METALLOGRAPHY

Shell samples were mounted in epoxy and polished, so they could be examined under microscope. Pictures were taken at 100X zoom and used to measure grain size of the flour particles in the binder of the samples. Then the grain sizes were compared to determine how much grain growth is associated with each pre-firing temperature and time.

## RESULTS

### AMBIENT FLEXURAL STRENGTH

A graph of the ambient flexural strength of green shell and of shells fired at 1112F (600C), 1562F (850C), and 1832F (1000C) for 20, 60, 180, and 540 minutes can be seen in figure 1.

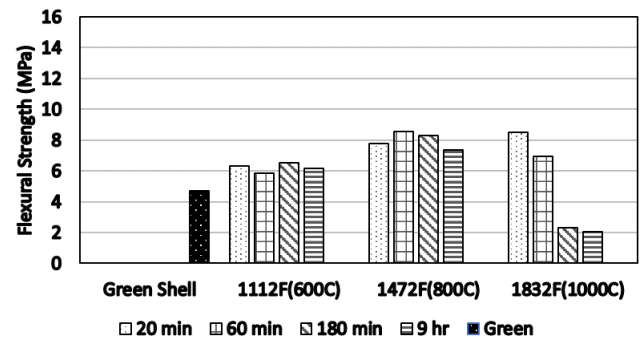


Figure 1. The ambient flexural strength of shells after various pre-firing conditions.

### HOT FLEXURAL STRENGTH

Figure 2 shows a graph of the hot flexural strength at 2012F (1100C) of green shell and of shells fired at 1112F (600C), 1562F (850C), and 1832F (1000C) for 20, 60, 180, and 540 minutes.

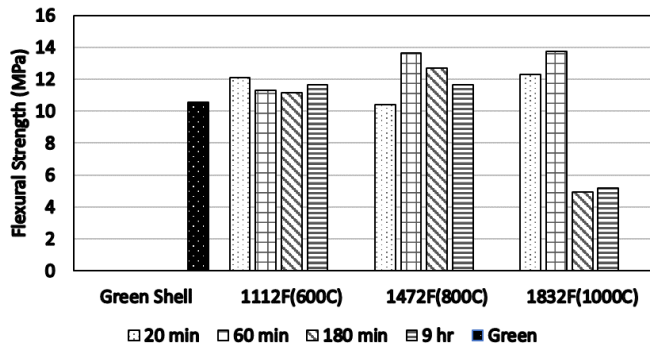


Figure 2. The hot flexural strength at 2012F (1100C) of shells after various pre-firing conditions.

DENSITY AND POROSITY

Table 3 includes the bulk density, true density, open porosity, and closed porosity of green shell and of shells fired at 1112F (600C), 1562F (850C), and 1832F (1000C) for 20, 60, 180, and 540 minutes.

Table 3. Density and Porosity of Shells

Pre-firing Process		Bulk Density (g/cm <sup>3</sup> )	True Density (g/cm <sup>3</sup> )	Open Pores %	Total Pores %
Green Shell		1.74	2.2198	20.6	21.6
1112F (600C)	20 min	1.75	2.2233	19.9	21.3
	60 min	1.76	2.2461	19.3	21.6
	180 min	1.73	2.1950	20.4	21.2
	540 min	1.72	2.2519	20.3	23.6
1472F (800C)	20 min	1.71	2.2233	23.6	24.1
	60 min	1.74	2.2587	22.0	23.0
	180 min	1.73	2.2160	21.6	21.9
	540 min	1.72	2.2481	22.4	23.5
1832F (1000C)	20 min	1.75	2.2900	20.8	23.6
	60 min	1.73	2.2830	21.6	24.2
	180 min	1.76	2.2613	22.0	22.2
	540 min	1.74	2.2729	22.5	23.4

CRYSTALLINITY

Figure 3 contains the x-ray diffraction results for a shell pre-fired at 1472F (800C) for 9 hours. It is noted that there is no intensity peak present due to the lack of long-range crystal structure in the sample.

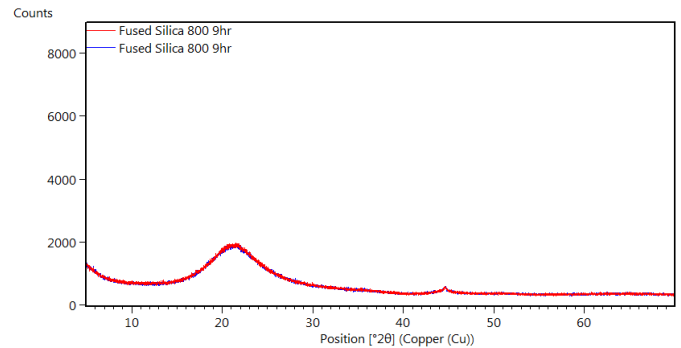


Figure 3. XRD results of silica shell pre-fired at 1472F (800C) for 9hr

Figure 4 contains the x-ray diffraction results for a shell pre-fired at 1832F (1000C) for 20 minutes and an alumina standard that was used for quantification of the cristobalite formation. There is a minute amount of cristobalite formed in the sample, and it creates a small but noticeable peak.

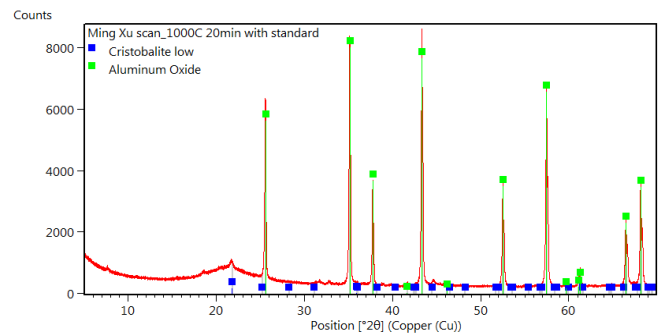


Figure 4. XRD results of silica shell pre-fired at 1832F (1000C) for 20 minutes and alumina standard

Figure 5 contains the x-ray diffraction results for a shell pre-fired at 1832F (1000C) for 9 hours and an alumina standard that was used for quantification of the cristobalite formation. There is a significant amount of cristobalite formed in the sample, and it creates a large intensity peak.

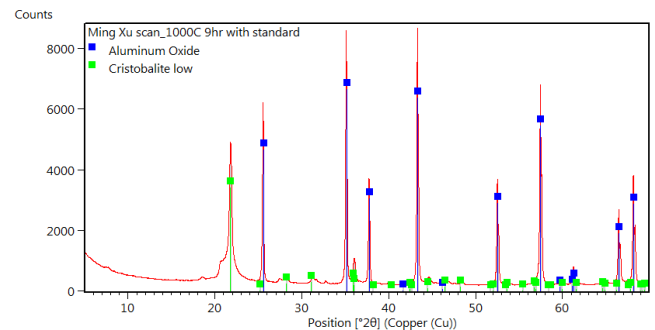


Figure 5. XRD results of silica shell pre-fired at 1832F (1000C) for 9hrs and alumina standard

Table 4 contains the amount of cristobalite formed in shells fired at 1112F (600C) and 1472F (800C) for 9 hours and of shells fired at 1832F (1000C) for 20, 60, 180, and 540 minutes.

**Table 4. Cristobalite Formation**

Pre-firing Process		Percentage Cristobalite
1112F (600C) 540 mins		0%
1472F (800C) 540 mins		0%
1832F (1000C)	20 mins	<1%
	60 mins	2%
	180 mins	6%
	540 mins	9%

**DISCUSSION**

**AMBIENT FLEXURAL STRENGTH**

The ambient flexural strength of green shell and shells pre-fired at 1112F (600C) can be seen in figure 6. All shells pre-fired at 1112F (600C) are stronger than the green shell that was not pre-fired. The average flexural strength of the shells pre-fired at 1112F (600C) is 32% higher than the average of the green shell. Between the shells fired at 1112F (600C) for different times, there is no significant difference in flexural strength.

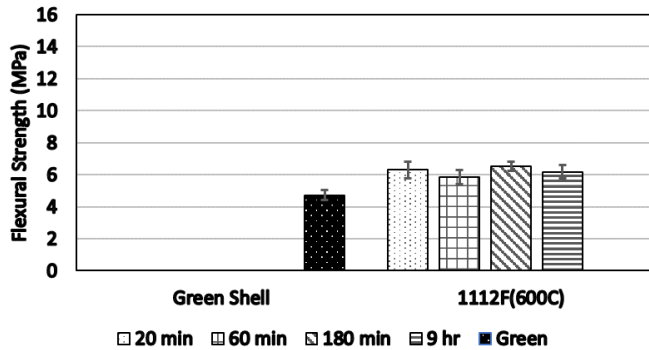


**Figure 6. Ambient green shell flexural strength compared to strength of shells pre-fired at 1112F (600C)**

From figures 6 and 7 all shells pre-fired at 1472F (800C) are stronger than the shells pre-fired at 1112F(600C). The average flexural strength of the shells pre-fired at 1472F (800C) is 29% higher than the average of the shells pre-fired at 1112F (600C). The shell fired at 1472F (800C) for 60 minutes has 10.1% more flexural strength than the shell fired for 20 minutes. The shells pre-fired at 1472F (800C) for 180 and longer have decreasing strength compared to the shell pre-fired for 60 minutes. At first there is an increase in shell flexural strength as firing time increases for shells fired at 1472F (800C), but then strength starts to decrease after firing for more than 60 minutes.

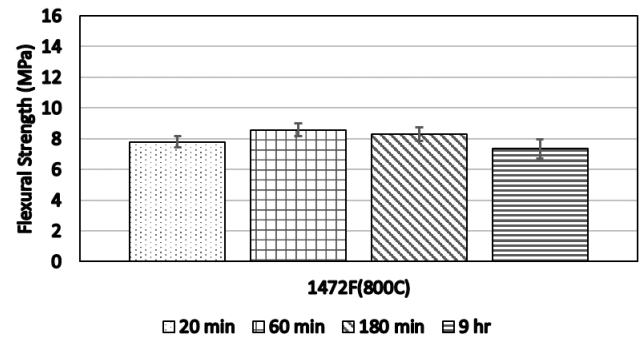


**Figure 7. Ambient flexural strength of shells pre-fired at 1472F(800C)**

From figures 7 and 8 the shell fired at 1832F (1000C) for 20 minutes has a flexural strength very close to the shell fired at 1472F (800C) for 60 minutes. The flexural strength decreases for the shells fired at 1832F (1000C) for over 20 minutes.

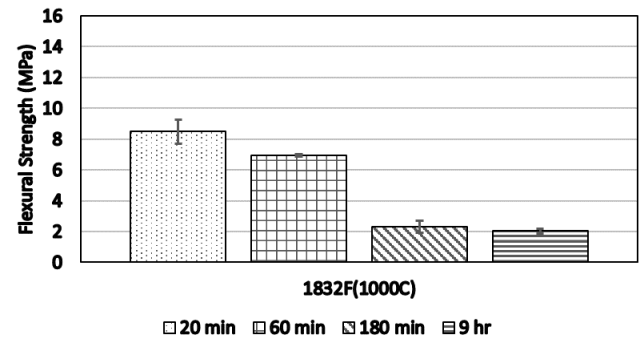


**Figure 8. Ambient flexural strength of shells pre-fired at 1832F(1000C)**

**HOT FLEXURAL STRENGTH**

The hot flexural strength of green shell and shells pre-fired at 1112F (600C) can be seen in figure 9. All shells pre-fired at 1112F (600C) are stronger than the green shell. The average flexural strength of the shells pre-fired at 1112F(600C) is 9.4% higher than the average of the green shell. Between the shells fired at 1112F (600C) for different times there is no significant difference in flexural strength.

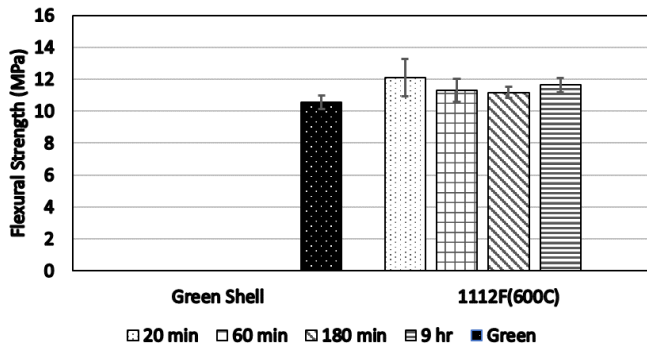


**Figure 9. Hot green shell flexural strength at 2012F (1100C) compared to strength of shells pre-fired at 1112F(600C)**

From figures 9 and 10 the shell fired at 1472F(800C) for 20 minutes has less strength than all the shells fired at 1112F (600C). The average flexural strength of the shells pre-fired at 1112F (600C) is 10.8% higher than the average of the shell fired at 1472F (800C) for 20 minutes, but shell strength increases until firing time is more than 60 minutes. The shell fired at 1472F (800C) for 60 minutes has 18% more flexural strength than the average of the shells fired at 1112F (600C). The shells pre-fired at 1472F (800C) for 180 and longer have decreasing strength compared to the shell pre-fired for 60 minutes.

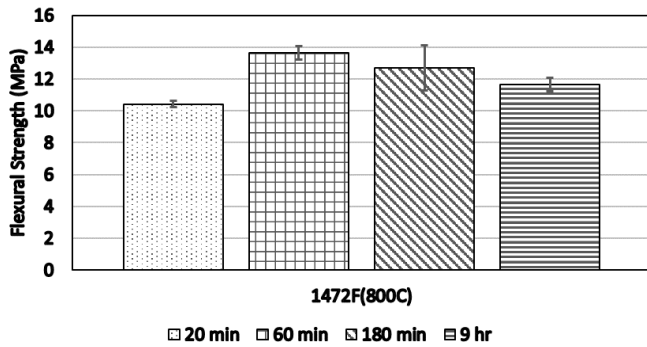


**Figure 10. Hot flexural strength at 2012F (1100C) of shells pre-fired at 1472F(800C)**

From figure 11 it can be seen that the shell fired at 1832F (1000C) for 60 minutes has 11.6% more strength than the shell fired for 20 minutes. The shells fired at 1832F (1000C) for 180 and 560 minutes have decreasing strength compared to the shell fired for 60 minutes. Looking at figures 10 and 11 the strength of the shell fired at 1832F (1000C) for 60 minutes is comparable to the strength of the shell fired at 1472F (800C) for 60 minutes.

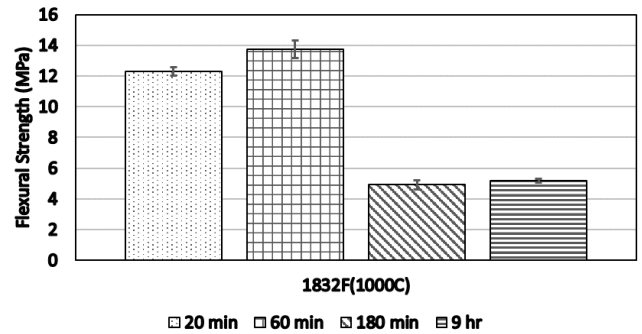


**Figure 11. Hot flexural strength at 2012F (1100C) of shells pre-fired at 1832F (1000C)**

**EFFECTS OF DENSITY AND POROSITY**

Total porosity should be referenced when explaining strength variations in investment shells. Increased porosity decreases the flexural strength by lowering the force required to fracture the sample. Table 3 contains the total porosity of the shells. There is less than 5% variation in total porosity between the shells. This means major changes in strength amongst these samples are likely not due to differences in total porosity percentage. While lower strengths may not be due to a higher amount of porosity it may be due to a concentration of porosity around the fracture surface.

The difference between total porosity and open porosity is the closed porosity. The amount of closed porosity in these shell samples is small with a maximum of 3.3%. The amount of closed porosity is small due to the size of the shell samples. With the shells being approximately .24in. (6mm) thick, there is not much volume in the shell where closed porosity can exist.

**EFFECTS OF CRISTOBALITE FORMATION**

No cristobalite is detected in the XRD results displayed in figure 3. This means the effects of cristobalite formation on shell strength will not need to be investigated for shells pre-fired at 1472F(800C) or lower. It can be seen from table 4 that the shells fired at 1832F (1000C) for 20, 60, 180, and 540 minutes had increasing amounts of cristobalite formed the longer they were fired. This means the cristobalite formation must be considered when investigating the changes in strength of the shells fired at 1832F (1000C).

The shells fired for 20 and 60 minutes had a smaller amount of cristobalite formation compared to the shells fired for 180 and 540 minutes. This would cause only minor cracking from volume expansion. The effect is shown in the results of the ambient flexural tests in figure 1. The shell pre-fired at 1832F (1000C) for 20 minutes had comparable strength to the shell pre-fired at 1472F (800C) for 60 minutes. The shell pre-fired at 1832F (1000C) for 60 minutes had lower strength than the shell fired for 20 minutes, but its strength was still higher than the average of the shells fired at 1112F (600C).

The effect is also shown in the results of the hot flexural tests in figure 2. The shell pre-fired at 1832F (1000C) for 60 minutes had comparable strength to the shell pre-fired at 1472F (800C) for 60 minutes. The shell pre-fired at 1832F (1000C) for 20 minutes had lower strength than the shell fired for 60 minutes, but its strength was still higher than the average of the shells fired at 1112F (600C). These results prove that a slight amount of cristobalite formation does not completely remove the strength of a shell.

The shells fired for 180 minutes and over have more cracking from volume expansion. The effect this has on shell strength can be seen in both the ambient and hot flexural tests. In both tests the shells pre-fired at 1832F (1000C) for 180 minutes and over had the least amount of strength of the samples tested. The difference in strength between the samples was minor, approximately 5%. The amount of cristobalite formation is dependent on the firing temperature and duration. It is likely there will be a downward trend in strength as the firing time or firing temperature increases from 1832F (1000C).

## EFFECTS OF GRAIN GROWTH

microscope pictures

Table of grain size vs pre-firing conditions

## CONCLUSION

There appears to be no trend between the pre-firing process and total porosity. The variation in amount of porosity between the shells was less than 5%. This means amongst these samples there is not a likely connection between major changes in shell strength and total porosity percentage. However, there may be reduced shell strength due to concentration of porosity at the fracture surfaces.

It was found that there is a relationship between cristobalite formation and flexural strength. A small amount of cristobalite formation (<5%) does not cause enough cracking from the volume expansion to significantly weaken the shell strength. Larger amounts of cristobalite formation (>5%) cause enough cracking from the volume expansion to significantly weaken the shell strength.

Shell strength increases for shells pre-fired at 800C for up to 60 minutes. After 60 minutes the shell strength starts to decrease as firing time increases.

## REFERENCES

- [1] J. Q. Mingzhi Xu, "Effect of Firing Temperature and Duration on Fused Silica Investment Shell Strength at Room Temperature," *International Journal of Metal Casting*, 2019.
- [2] S. L. V. R. Mingzhi Xu, "Impact of Firing Temperature on Phase Transformations and Properties of Silica-Based Investment Shell Molds," *American Foundry Society*, 2017.
- [3] S. Z. M. D. Beals, "Volume Change Attending Low-to-High Inversion of Cristobalite," *Journal of the American Ceramic Society*, 2006.
- [4] S. L. C. M. V. R. S. D. Mingzhi Xu, "Measurements and Confirmation of Thermal Properties of Investment Ceramic Shell by Multiple Methods," 2015.
- [5] "Standard Test Method for Flexural Strength of Advanced Ceramics at Ambient Temperature," *ASTM C1211*.
- [6] "Standard Test Method for Flexural Strength of Advanced Ceramics at Elevated Temperatures," *ASTM C1211*.
- [7] "Standard Test Methods for Apparent Porosity, Water Absorption, Apparent Specific Gravity, and Bulk Density of Burned Refractory Brick and Shapes by Boiling Water," *ASTM C20 - 00*.



# **INVESTMENT CASTING INSTITUTE**

## **Process Cycle Time Analysis & Optimisation for Efficient Vacuum Precision Investment Casting Furnaces**

Iñaki Vicario  
Consarc Engineering Ltd.

### **68<sup>TH</sup> TECHNICAL CONFERENCE & EXPO 2021**

Paper No 14

## **Process cycle time analysis and optimisation for efficient vacuum precision investment casting furnaces**

### Abstract

The production of advanced superalloy components for applications in aerospace, power generation, automotive etc industries is accomplished in Vacuum Precision Investment Casting (VPIC) furnaces. Consarc recognises the technical and commercial importance involved in optimising modern VPIC operation efficiency, and apply these to their state of art VPIC furnace technologies.

The Vacuum Precision Investment Casting process includes many activities to perform a complete casting cycle. There are many sensitive and complex operations, including: mould loading into the furnace, mould pump down stage, mould raise to heating/pouring position, mould heating (DSSX process), liner and ingot loading, alloy melting, mould pouring, casted mould unloading and used liner removal. Among each of these operations, there are many subtasks that should be identified, analysed and optimised.

Proper cycle process time analysis enables a view of the time consumption of each process stage, and the best synchronisation strategies to avoid wasted time and ensure the fastest cycle time is achieved.

This work will show how furnace design principles can permit the operator to achieve the fastest, most productive, most efficient, and reliable casting process. It is a work focused on the equiaxial casting process.

Iñaki Vicario

Consarc Corporation

October 2021

# 1. Introduction to Cycle Time Analysis

## 1.1 Definition of Cycle Time

Cycle time is the time required to complete a given process and also including many sub-processes. Then, the total cycle time of all of the sub-processes determines when you can finish the complete process.

It is also important to say that cycle time should not be confused with Lead Time. [1], [4].

The following figure shows an example of a process cycle time analysis chart, explaining cycle times and lead times:

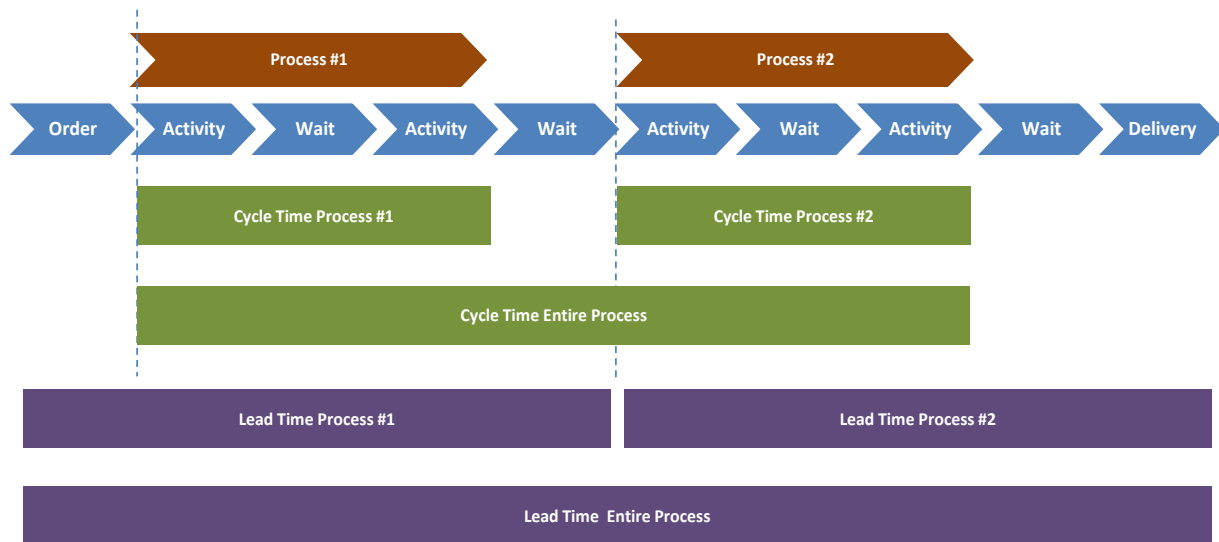


Figure 1. Picture showing Cycle Time

## 1.2 Cycle Time Reduction

Generally speaking, the cycle time reduction strategy consists on identifying and implementing more efficient and effective ways to do things in any process.

In order to achieve that goal, this strategy requires eliminating or reducing non-value-added tasks and activities, which do not provide any real value. This consists on:

- Reducing/eliminating tasks where machine waits for human.
- It also requires faster completion of activities.
- Examples of non-value-added activities: waste, wait, movement of materials, duplication, unnecessary movement, over-supply of inventory, rework, machine time set-up, etc. [1]

### 1.3 Most Common Wait Examples on the Foundry

There are many typical reasons why foundry waits, here are some examples:

- Wait for preheater because molds loaded inside that furnace are not ready yet. They might be under the normal preheating time, or waiting for a new preheating temperature different to the one that the furnace has, or any other reason.
- Wait for materials that are not ready at the furnace, for example alloy, liners, etc.
- Wait for the operator because he is not at the furnace when the process is ready to start.
- Wait for casting furnace operation because it is heating up, making the initial vacuum inside the melt/mold chambers, or any other reason.
- Wait for the change backup crucible or coil because the casting campaign required another charge size different than the current one.
- Wait for leak up rate test, or any other process test completion that VPIC furnace needs to conduct in the frequency needed.
- Wait for any maintenance operation that would be scheduled on the furnace.

In order to avoid these waiting times, there are some rules to be followed:

- Organize optimised casting campaigns, as large as possible, and also trying to organize preheating temperatures from lower to higher temperatures. Maximise the number and flexibility of the preheating furnaces.
- Try to adjust and minimise the backup or coil changes trying to synchronize them with preheating wait times, or any other furnace stops.
- Schedule preventive maintenance works when the furnace is not being used.
- Try to synchronize leak up rate tests and other tests when the furnace is not being used or when the preheating wait times are happening.

### 1.4 Strategy for Cycle Time Reduction

The strategy for cycle time reduction should follow some scheduled steps:

#### Step n.1: Process Mapping

- It is a technique that highlights the inputs, actions and outputs of a process graphically by a flowchart.
- It should be done from the most macro perspective, to the level of detail required to identify opportunities for improvement.
- As a result of it, it reveals constraints and bottlenecks in an operation, which is a great information to be known.
- There are many types: Activity/Detailed Process Map, Value-Added Chain Diagram, Value Stream Map, Work Flow Diagram, etc. [1], [2], [3]



## 2. VPIC furnace

The following two pictures show the main features of the VPIC furnace that are important to understand the process that is carried out:

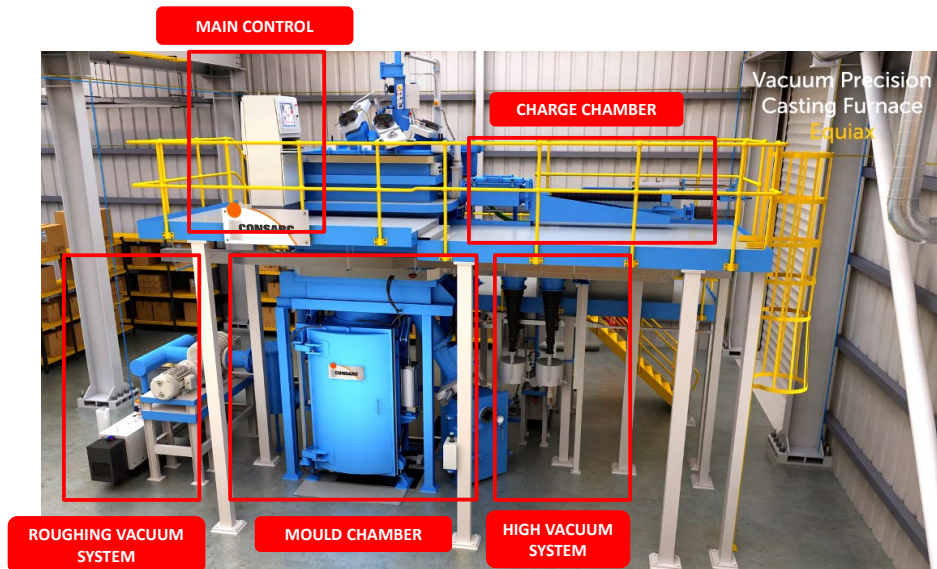


Figure 4. Front picture of an equiaxial vertical VPIC furnace.

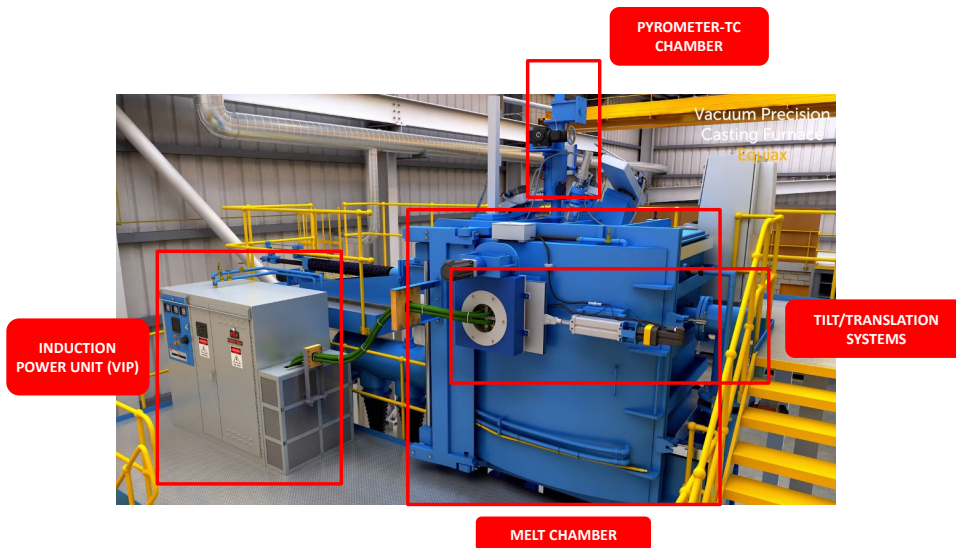


Figure 5. Back picture taken from the melting chamber platform of an equiaxial vertical VPIC furnace.

### 3. Understanding the VPIC process

There are two basic VPIC processes. They are explained very briefly:

- Equiaxial castings: are crystals that have axes of approximately the same length.
- DSSX castings: columnar grains are long, thin, coarse grains created when a metal solidifies with a certain temperature gradient and cooling speeds. If there is a grain selector feature that is capable of filtering just one grain, then single crystal castings are made.

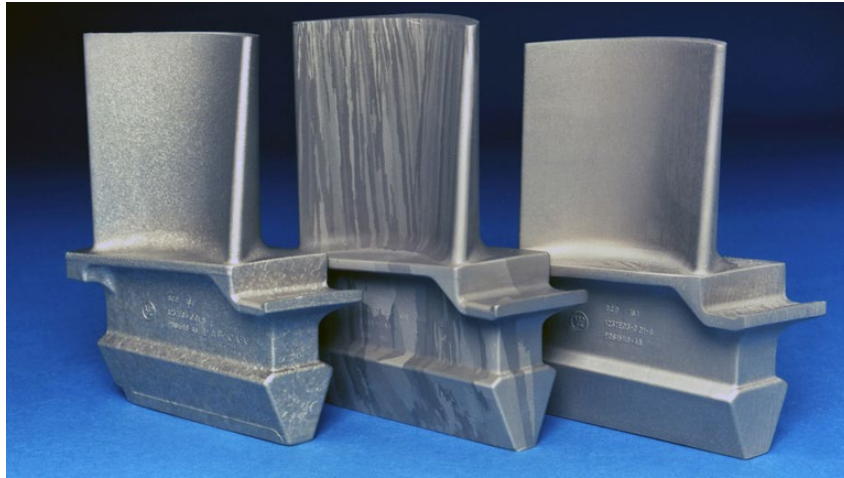


Figure 6. Pictures of a blade manufactured by Equiaxial (left) DS-Columnar (centre) and DS-Single Crystal/SX (right) technologies. [5]

As it has been said before, this works is focused on an equiaxial casting process.

The following flowchart shows equiaxial process (showing also the preheating process just before VPIC furnace)

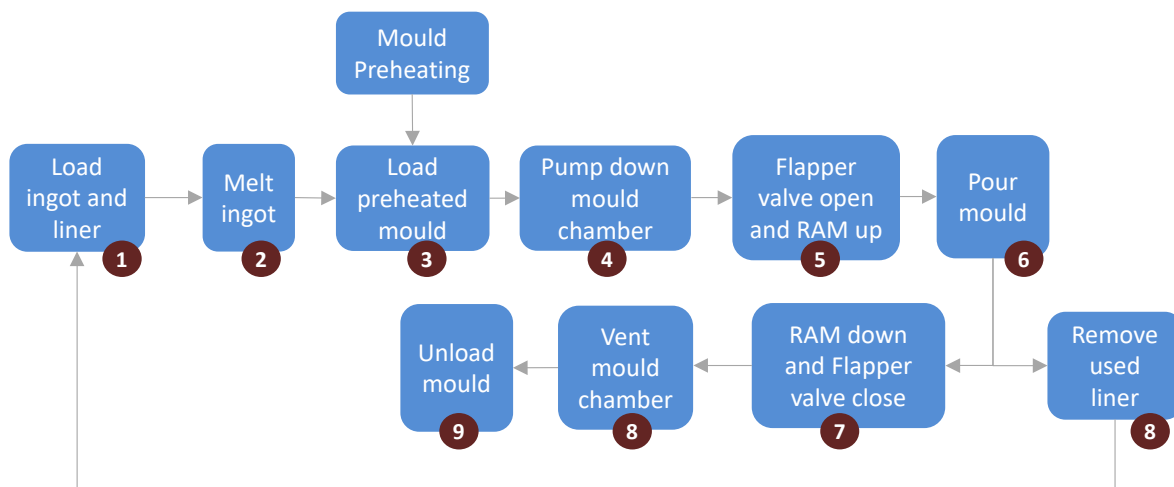


Figure 7. Equiaxial process flowchart.

- Step 1: the process starts when the ingot and liner are loaded.

- Step 2: the melting stage is conducted.
- Step 3: once the alloy is melted and ready to be poured, the shell mold is loaded into the VPIC furnace coming from the preheating furnace.
- Step 4: when the shell mold is loaded, the mold chamber door is closed and pump down stage of that chamber starts.
- Step 5: once mold chamber vacuum reaches the flapper valve opening set point, that valve opens and mold is raised to the pouring position.
- Step 6: when the mold reaches the pour position and pouring time is reached, the pouring stage is carried out.
- Step 7: once shell mold is poured, the ram moves the casted mold to the mold chamber and flapper valve closes, In the meantime, the used liner removal may start.
- Step 8: mold chamber is air admitted.
- Step 9: casted mold is taken out from the VPIC mold chamber.



Then, the initial time consumption of this process is shown in the following pie chart:

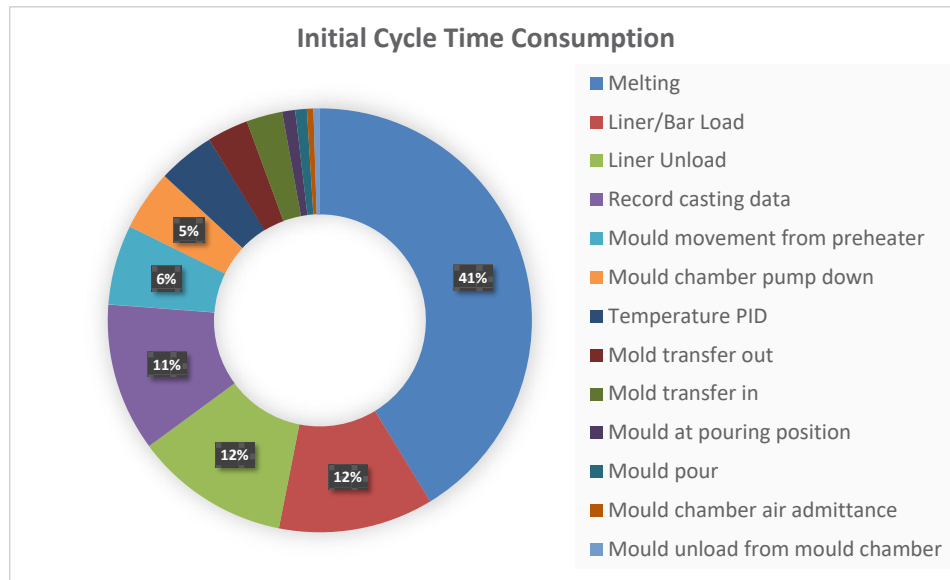


Figure 9. Initial Time Consumption (Case Study - Equiax Process)

These are some conclusions that can be made from the previous pie chart:

- Melting stage is the most time consuming. It represents 43% of the total cycle time. This is a fact in the equiaxial process, the melting stage is the “heart” subprocess or stage, and the rest of subprocesses are linked to it,
- Liner/alloy loading and liner unloading are the second most time consuming. They are 12% each from the total time.
- Then, some extra operations like casting data recording, etc, are the following time consumers.

## 5. Actions for cycle time reductions

Based on the initial process shown before, there are some specific actions that are made in order to reduce the total cycle time. The following 5 points summarize all of them:

### 5.1 Actions for Cycle Time Reduction

These are the general actions to be carried out to produce the cycle time reduction on this specific example:

- Identify which are machine and which are human times, this consists of 2 actions:
  - Identify machine and human times.
  - Quantify those machine and human times.
- Make sure that machine does not wait for human, so for the operator:
  - Overlap the stages, if possible, for example the final melt report task with the beginning of the following cycle.
  - Stages from the machine needed always ready when they should, so for example, vacuum/liner/ingot/mould ready/available when needed.
- Make all tasks as short as possible, so faster. There are 2 stages that have been improved as follows:
  - Faster melting stage: this is very critical as it is the most time consuming one. In this case, the melting speed has been increased to 2kg/min.
  - Reduced liner removal time: this reduction has been done from the VPIC furnace design point of view during the engineering phase of the equipment, so at the design stage of the project. To reduce liner disposal time, a liner disposal system has been created to allow a safe and super-fast removal of the used liner after pouring.
- Remove all not needed tasks of the process. A couple of targets has been chased on this specific task:
  - Remove time at pouring position after pouring, which has been demonstrated that was not needed on this specific casting process (although for any other case, it might be).
  - Automate melt report creation task avoiding further manual records, so allowing fast and automatic stage.
- Reduce all possible wait times, which are a waste on the process. There are two specific wait times that has been improved:
  - Reduce the wait time that always exists between two consecutive cycles, so since one finishes, until the following one starts.
  - Automate the cycle to produce a smoother process without any or minimum wait time between any two consecutive tasks of the process.
- Reduce machine down times. This is not a direct and short-term action, but the strategy for maintenance related tasks is an essential objective to chase on the cycle time reduction final aim.
  - Optimised charge-liner-backup setup: this means a previous overall production analysis focussing on the pareto of the most produced part numbers, having the data of the charge and liner/backup needed for each one of them. Once this information is available, an optimised definition of the needed liner for each charge shall be done. This definition shall look for the minimum amount of backup changes. For that, there are available special stilted liner designs that share the same backup size.

- Preventive-predictive maintenance schedule to reduce the time that the equipment is down: this is a medium/long term action that shall be carried out after analysing needed preventive maintenance tasks on the VPIC furnace, and also available resources for that on the company. Then, the main target is scheduling those activities, trying to find the right times to perform them when the VPIC furnace is not being used, or during any process wait time.

After listing all needed actions to try to reduce cycle time, the following points will explain in more detail them:

## 5.2 Faster and More Reliable Melting Stage

Melting faster is not just increasing the kW in the VIP® power unit, it is much more than that. If a simple power increase is done, there are risks of suffering process/machine problems. There are some clues to be considered in order to design a faster melting stage:

- VIP® power unit and coil designs: this means that it is needed to find the right and optimised induction melting coil design, together with a specific VIP® power unit, in order to match and accommodate all the melting requirements, so in order to obtain the right induction coupling of the ingot to be melted. If this is not done like this, there is a high chance of witnessing issues with the refractory being used for melting, or not conducting a smooth and fast melting stage.
- Ingot preparation and sizing: ingot shall be chamfered to prevent any scratching with the refractory. Besides, ingot diameter shall be maximised and length minimised to get the best induction coupling during melting stage, trying to have the alloy as close as possible to induction field, and trying to minimise the part of the ingot that might be out of that field.
- Liner/Crucible material and shape selection: if the refractory used is not the right one, there is a chance of having not the right melt-refractory reactions, so, there is a chance of having a fast-melting stage, but with a bad quality melt that might produce defects on the casting.
- Melting witnessing/controlling: by means of viewports/cameras to have a clear view of the melting stage. Also, good and reliable pyro dip-TC systems, in order to have a process control that will permit to have the melt at the right pouring temperature required.
- Appropriate melting procedure/automation/logging/control: this is essential for an accurate, fast and consistent melting process control.

With all these specific details known, the following chart shows the original melting recipe and the new one:

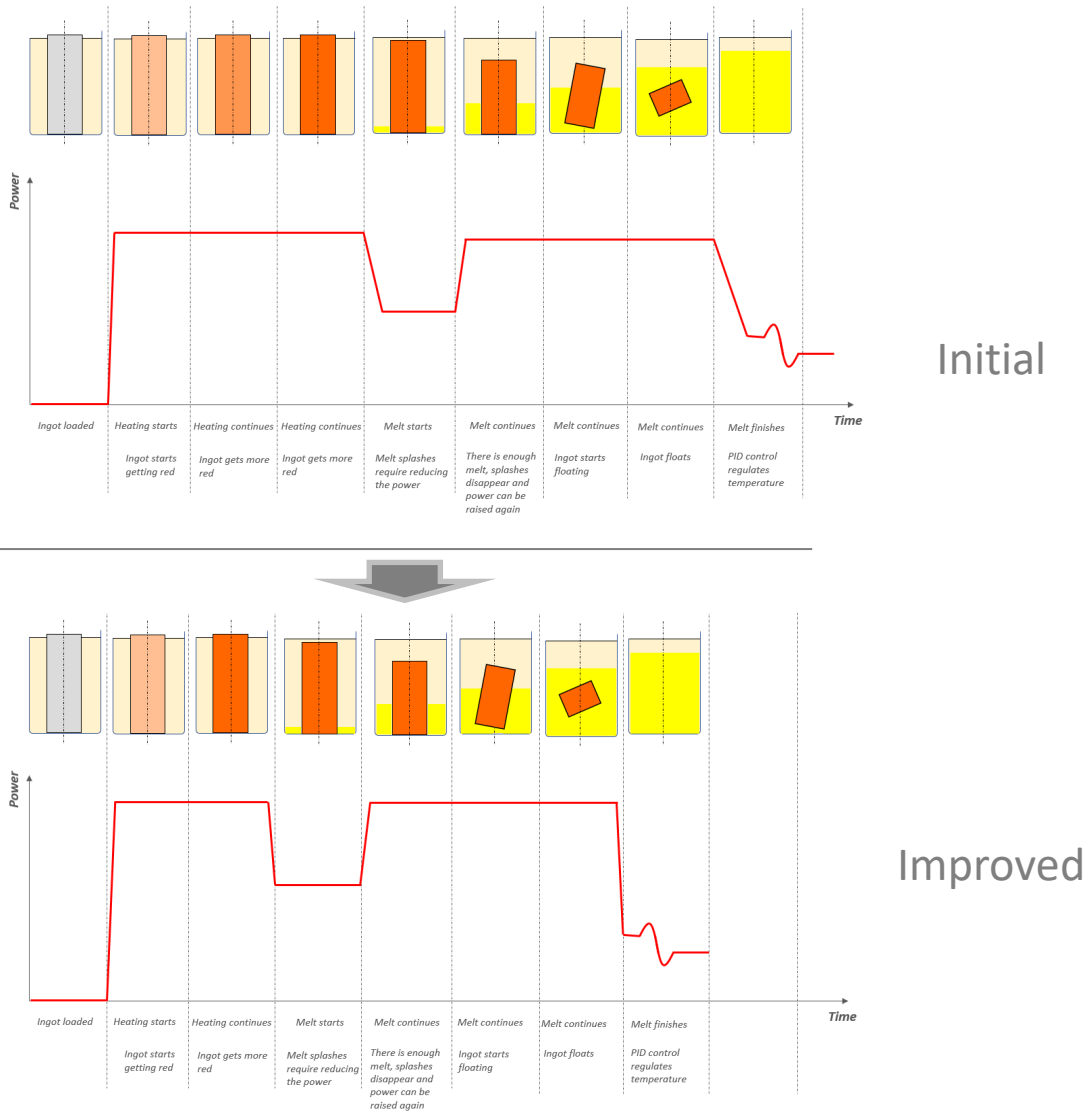


Figure 10. Initial and improved melting recipes.

The previous figure shows the melting dynamics since the ingot is solid until the melt is ready to be poured. The top figure shows the original recipe, and the one at the bottom, the improved final one.

### 5.3 Faster Liner Unloading

As explained before, there is a design feature given by Consarc that consists on a separate chamber for liner disposal system. This feature consists of tilting the coil fast until a certain angle is reached where liner goes out of the backup crucible into that liner separated liner chamber.

For that purpose, the melting chamber has a port through which liner is disposed, transferred to that liner chamber.

There are two benefits from this separate fast liner unloading system:

- It means a significant time saving on this stage. Approximately 66% of time required is saved compared to the traditional liner removal system by means of grippers and similar tools used in the charging chamber.
- Safety is also improved: by the use of this system, very hot used liner is stored in a bin inside the liner disposal chamber. This means that there is no need to handle them, so that potential safety risk is absolutely avoided.



Figure 11. Liner Disposal/Dumping System

#### 5.4 Improved Pyrometer Performance

Having a reliable, accurate and consistent melt temperature measurement system is a very important thing to also obtain a fast cycle.

The main points to be considered are the following shown below:

- Dual Pyrometer System (or three): this enables a continuous reliable multiple temperature reading of the melt. Then, a fast and accurate pouring temperature regulation is possible by means of an improved confidence on the optical pyrometer performance.
- Moreover, as a result of this, there is a clear reduced need of testing of the pyrometer against immersion thermocouple.

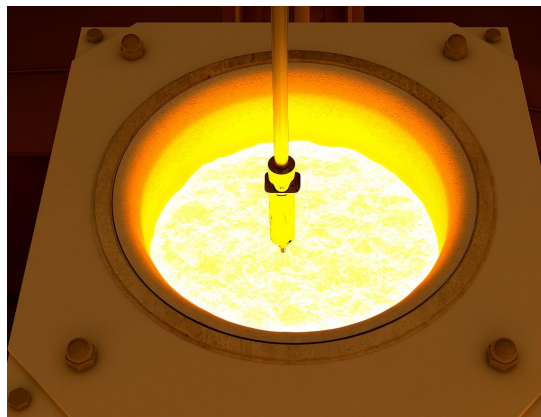


Figure 12. Immersion TC going into the melt



### 5.7 Optimised Cycle Time (Case Study - Equiax Process)

As a result of the previous actions and strategies, a new cycle time analysis was performed to check how it improves.

The following chart shows the new and improved cycle time analysis:

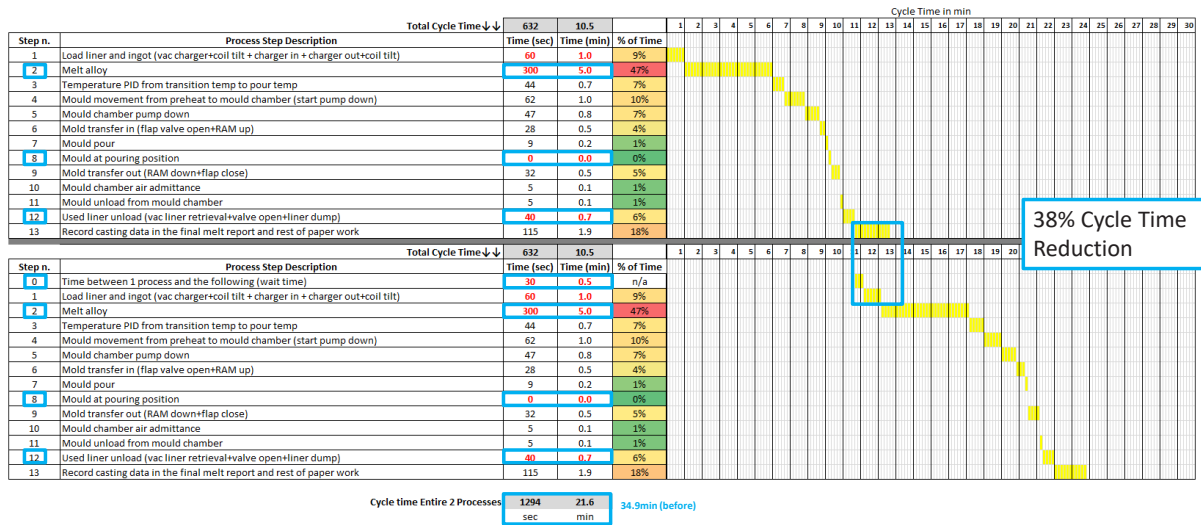


Figure 15. New and improved cycle time analysis chart.

The new two consecutive cycles last 21.6 minutes, while this time was 34.9 minutes at the initial condition, so there is a 38% cycle time reduction.

The following pie chart explains the share of the obtained reduction of time:

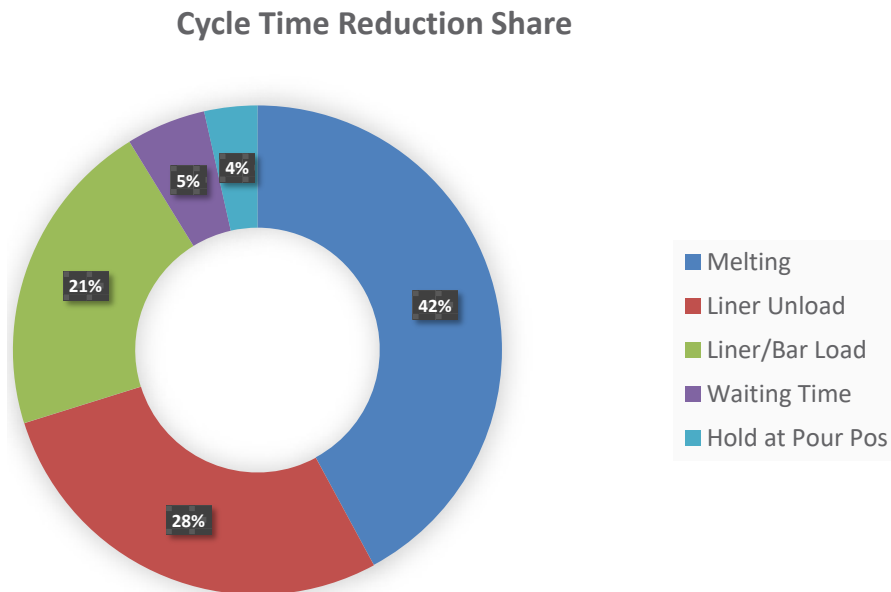


Figure 16. Cycle time reduction share.

There are some conclusions to be made from the previous pie chart:

- Melting stage is the stage that produces the greatest time reduction (42%).
- The liner unloading stage is the next most significant (28%).
- Then the liner and alloy loading stage (21%).
- The rest are much less significant

## 6. Final conclusions

The cycle time reduction strategy consists of identifying and implementing more efficient and effective ways to do things, but also making a consistent new process.

This work has shown how some process and furnace design principles can permit achieving the fastest, most productive, most efficient, and reliable casting process.

In summary, the following items have been highlighted:

- Procedures to improve cycle time analysis.
- Basic features around vacuum precision casting.
- Equipment specific components and critical devices.
- Understanding and analysis of a real equiaxial casting cycle example.
- Developing of ideas to improve the total cycle time.
- Creating a new and improved process.
- Measuring and evaluating of the new process.
- Showing the final improved time results.

## 7. Cross References

- [1] Workplace One. <http://www.wp1.ca/>.
- [2] Process Mapping. Performance Technology and Training. Margaret L. Bailey, PhD Uni Northern Illinois.
- [3] Lucid. <https://lucid.co/>.
- [4] Presentationeze. <https://www.presentationeze.com/>.
- [5] Foundrymag. <https://www.foundrymag.com/>.
- [6] <https://sixsigmastudyguide.com/process-mapping/>.

# **INVESTMENT CASTING INSTITUTE**

## **Pattern Cleaning & Study of Pattern Formulation Effects on Surface Energy Measurements**

Mark Oles - Pine Tree Castings  
Alfred Kaulius - Paramelt

## **68<sup>TH</sup> TECHNICAL CONFERENCE & EXPO 2021**

Paper № 15

## PATTERN CLEANING

Mark Oles, Normal Lowden III, Pine Tree Castings

### ABSTRACT

Why clean a wax assembly prior to the application of the prime coat? A pattern cleaning operation involves labor, materials and disposal costs that can be significant. This operation would not be performed unless there was some benefit in casting quality. The most common reason is to improve prime coat wax adhesion to prevent shell buckle.

The adhesion of a prime coat to a wax pattern is dependent on the ability of the prime coat to wet the wax. For successful bonding to occur, the surface tension of the prime coat must be lower than the surface energy of the wax pattern.

This collaborative paper will demonstrate several methods of measuring the surface energy of wax patterns and show the relationship between surface energy and prime coat bond strength.

A wax supplier will present data collected using direct surface energy measurements, as well as traditional wet analysis, to show how wax chemistry, choice of release agent and cleaning regime can impact prime coat integrity.

From a foundry perspective, measurement of the bond between the prime coat and wax pattern is not simple or easy. Many tests have been used over the years with the most of the industry settling on the “button pull” test as the standard. Unfortunately, this test is time consuming to perform and requires a large number of replications to obtain meaningful statistics. Pine Tree Castings developed a modified version of the tape peel test that quickly and accurately measures the prime coat bond strength. This paper will show how the tape peel test was used to determine the influence various pattern-cleaning variables have on prime coat bonding.

It has been postulated there is an ideal level of prime coat adhesion; one where there the bond is strong enough to resist shell buckle and yet not so high as to promote spall. This paper will also attempt to determine the relationship between wax cleaning technique and spall severity.

## INTRODUCTION

It ain't so much the things we don't know that get us in trouble. It's the things we know that ain't so." **Artemus Ward**

"The more I learn, the less I know" **Jeff Rasley**

I used to think I knew a lot about pattern cleaning. I have read all of the ICI technical papers related to the subject and used the button pull test to find the optimal conditions for our pattern cleaning process. I even created a Pine Tree Castings training document specific for pattern cleaning. All this confidence evaporated when we starting finding a very small percentage of castings with shell buckle.

After verifying the solution concentration and percent active ingredients were in-specification and the as-cleaned patterns were tacky, we were still unsure if the effectiveness of the cleaning process had changed.

We considered using the button pull test to measure the prime coat bond strength but did not feel it would be effective in revealing any potential shift in our process. Fortunately, the percentage of rejected castings were low, allowing time to improve the adhesion test, and using the results, better understand the cleaning process.

## PROJECT GOALS

Pine Tree Castings decided to collaborate with Paramelt in attempt to understand critical aspects of pattern cleaning. We formulated the following goals:

1. Improve the adhesion test.
2. Determine how residual silicone release affects adhesion and wetting.
3. Determine how pattern cleaning affects adhesion and wetting.
4. Determine the relationship between pattern cleanliness and mold quality.
5. Understand how wax formulations affect adhesion and wetting.
6. Produce a cleaning process that provides consistent and uniform adhesion and wetting.
7. Produce a method for monitoring the effectiveness of the cleaning process

## ADHESION TEST

Many prime coat adhesion tests have been used over the years. In 1990, Argueso, Kovach and Schiefelbein<sup>1</sup> introduced four different prime coat adhesion measurement methods; a knife test, bend fracture test, cantilever adhesion test and large surface area test.

In 1999, Snow and Scott<sup>5</sup> presented the button pull test that Minco had been using for many years.

The ICI Ceramics Testing Guidebook<sup>9</sup> references the button pull test as a method for determining prime coat adhesion. The guidebook states a reasonable adherence is essential to avoid shell buckle however, if the adherence is too strong shell scabbing can occur.

The painting and coating industries use two methods for measuring adhesion, ASTM D3359 and ASTM D4541-17. In the ASTM D3359 method, a series of parallel cuts are made through the coating. Tape is applied to the coating surface and then slowly removed. The severity of flaking is compared to a reference standard. In the ASTM D4541-17 method, a test dolly is glued to the coated surface and allowed to cure. A hole saw is used to cut through the coating surrounding the dolly. The force to pull the coating from the substrate is measured.

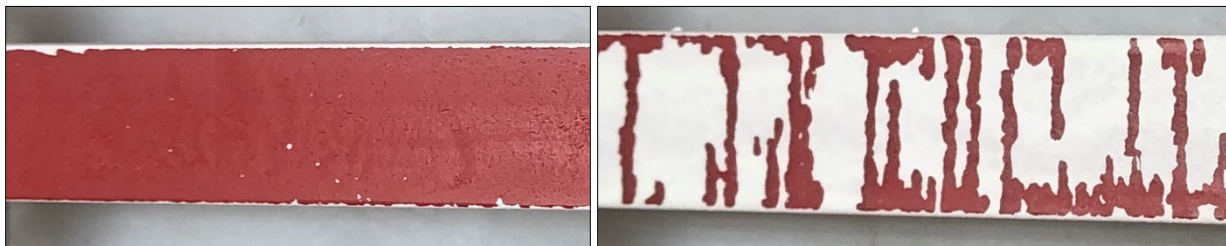
Bhattacharja, Doles, Romba and Wang<sup>2</sup> used two methods of adhesion testing, crosscut (similar to ASTM D3359 but without tape) and a tape peel test. In the tape peel test, tape is applied to the prime coated surface and then peeled off. The amount of prime coat removed by the tape is an indication of adhesion.

D.C. Holek and Z. Feffer<sup>13</sup> further improved the button pull test by modifying the dolly design to minimize lateral forces.

Many use pattern tackiness as an indication of cleaning. Others judge cleaner efficiency by the time to remove permanent marker from the pattern. Another test measures the time for the cleaner to dissolve through a Styrofoam cup.

We decided we needed a different approach. Our goal was to create a test that was easy to perform, did not require expensive instruments and would provide repeatable results. After reviewing the all of the different test methods and consulting with a few industry colleagues, we decided a modified version of the tape peel test might be a good method for measuring adhesion.

In the tape peel test, tape is applied to a prime coated surface and slowly peeled off. Prime coat still attached to the wax after the test is interpreted as having a higher bond strength to the wax than the tape, providing visual indication of high and low areas of adhesion (Figures 1 and 2). By using tapes with different adhesive strength, a better indication of prime coat bonding is obtained.



*Figures 1 and 2, wax samples after tape peel test. Low adhesion (left) and high adhesion (right)*

To improve the tape peel test we needed to control the speed of tape removal and capture the force required to remove the tape. This was done using a force gage mounted to a test stand (Figures 3 and 4). To perform the test, a piece of tape is applied to the prime coated surface of the sample. A hole in the tape is looped over the hook on the force gage and the test stand is raised, starting the removal of the tape from the sample. When removal point reaches the test area, the memory mode on the force gage is started. When the removal point reaches the end of the test area, the memory is stopped.

Testing was standardized at a tape removal speed of 10 inches per minute with a test distance of 4 inches. Under these conditions, the force gage records around 70 readings. After each test, the gage calculates the minimum, maximum and average values.



Figures 3 and 4, wax adhesion test (left) prime coat adhesion test (right)

An important consideration with this test method is the sensitivity and load capacity of the force gage. With a 1-inch sample width, we found the peak load of many tests to be below 1000 grams with some less than 10 grams. We chose an instrument that had a 1-gram resolution with a load capacity of 1650 grams.

Another consideration is the width of the tape. The tape should be as wide or wider than the sample, insuring the prime coat will consistently fail at the edge of the sample.

We use our five-finger sprue as our wax sample. This sprue is always in stock and provides up to 10 tests per sample. Samples are dipped in prime slurry and statically drained until dripping is complete. No stucco is applied to the prime coat. After drying, a high strength, highly adhesive tape is pressed onto the prime coat surface. The tape is applied to the sample a minimum of 12 hours prior to testing to insure maximum bonding to the prime coat.

In addition to measuring prime coat bond strength, we also use this approach to measure the bond strength of tape directly to the wax pattern. We refer to this the *wax adhesion test*. This test provides an indication on the cleanliness of the wax pattern.

## RESIDUAL SILICONE

A release agent is typically applied to the wax injection tool to prevent sticking. One of the most common release agents is silicone (polydimethylsiloxane or PDMS). Silicone oil has a very low surface tension, reported to be  $19.8 \text{ mN/m}^{32}$ .

Petrie<sup>25</sup> stated “However, the problem occurs once the silicone is on the substrate surface. Since it has a low surface energy, other adhesives, sealants or coatings will not wet or bond to the silicone surface.” “If unwanted silicone attaches to the substrate, the result is the formation of a *weak boundary layer*. The silicone contamination prevents the direct contact between the adhesive and the adherend.”

We wanted to understand the effect residual silicone release played in adhesion. The five-finger wax injection tool was sprayed with a silicone release agent and 10 consecutive injections were made without re-spraying. Wax adhesion testing was performed on fingers 1, 3, 5, 7, 9 using 3M 401+ high performance masking tape (Figure 5).

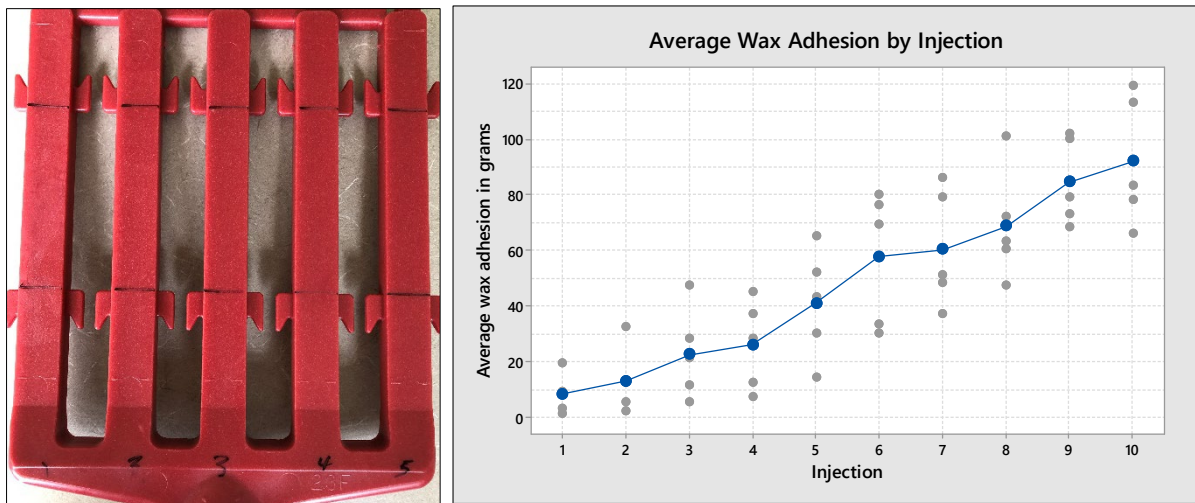


Figure 5 wax sprue identified by finger number. Lines designate the approximate start and end of the test area (left). Figure 6 average wax adhesion (right)

As expected, wax adhesion incrementally increases after each injection (Figure 6). After spraying with release agent, the tool is covered in silicone oil. The wax pattern from each injection removes some of this oil, leaving less remaining in the tool. In this test, the average

adhesion progressively increased from 8 grams to 92 grams over the course of 10 injections. This simple test demonstrates the profound effect residual silicone oil has on adhesion.

## SUCCESSIVE WAX ADHESION TESTS

Because the amount of residual silicone oil dramatically affects adhesive strength, and because it is difficult to consistently apply the same amount silicone to the tool, we wanted to be able to test the same wax sample before and after cleaning in order to verify any improvement. By knowing wax adhesion prior to cleaning (and therefore the amount of residual silicone), the effectiveness of the cleaning process could be better understood.

First, we had to understand if the wax adhesion test alters the surface of the sample, either by leaving a tacky residue or by removing some of the silicone.

Two randomly selected five-finger sprues were measured for adhesion in the as-injected condition. The average adhesion values were recorded for each finger. The wax adhesion test was repeated and the results recorded.

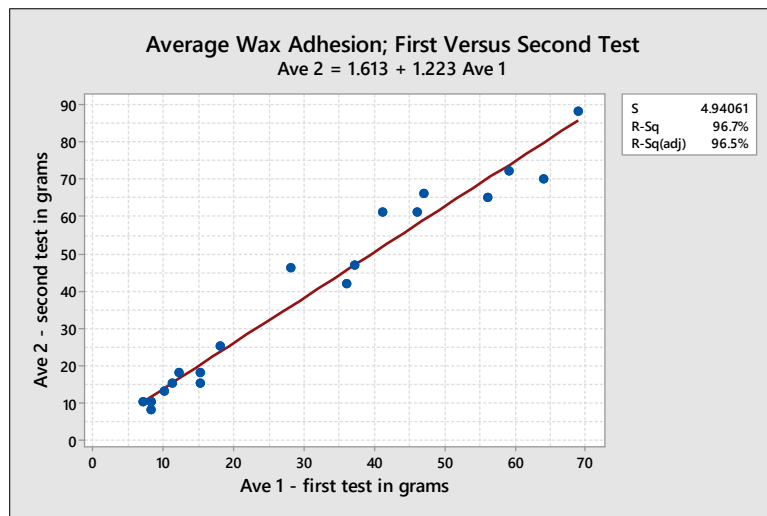


Figure 7, average wax adhesion regression plot; first versus second test

The regression plot shows good correlation between the tests with the second test having approximately 22% higher average bond strength than the first (Figure 7). The adhesion test either removes some of the silicone oil or leaves a slight residue.

We concluded that the value of knowing the as-injected condition of the sample outweighs the negligible change to the sample due to testing.

## PATTERN CLEANING AGENTS AND PATTERN CLEANING

Cleaners are used to remove contaminants from the pattern surface, promoting wetting and adhesion of the prime coat. There are many different pattern cleaners used in the investment casting industry. Most claim they remove silicone oil and other release agents, etch the wax surface, and promote increased prime coat adhesion. How should they be compared? A partial list of important characteristics might include:

- Flash point
- VOC's
- Odor
- Rinse water treatment
- Removal of silicone oil from the pattern
- As-cleaned wax texture
- Usage
- Compatibility with prime coat binder
- Rinsability; ease of cleaner removal

Argueso, Kovach and Schiefelbein<sup>1</sup> stated, “immersion time to remove silicone was measured and recorded.... The immersion time required to remove silicone from the wax ranged from 10 seconds to 120 seconds.”

Snow and Scott<sup>5</sup> “It proved nearly impossible to get the standard silicone mold release off using cleaners that do not dissolve the wax.” “The extent that the silicone can be removed is the main determinate of wax/shell adherence and hence buckle.”

Mills<sup>4</sup> “Since wax injection usually results in non-wetting release agent left on the patterns some sort of wax wash is required. This can be a simple detergent wash or an etch using a suitable solvent system.”

Niles and Bozzo<sup>16</sup> “Wetting agents are a necessary ingredient in primary slurries to lower their surface tension. This is especially important in today’s world where more environmentally safe pattern cleaners are used. Previous pattern cleaners like Freon, 1, 1, 1, trichloroethane, etc. were used and they etched or modified the surface of the wax. In essence, the surface tension of the wax was increased and provided a surface that the primary slurry could adhere to.”

Many pattern cleaning processes use the terms “etching” and cleaning interchangeably. What is etching? Etching is the process of corroding or dissolving the material’s surface. In the case of pattern cleaning, changing the surface from a semi-gloss finish to a matte finish may be an indication of etching (Figure 8). Not all pattern cleaners will etch the wax surface.

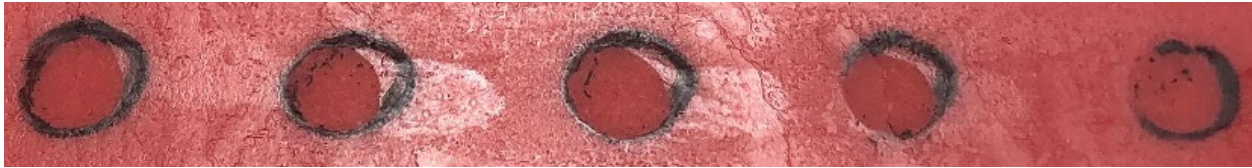


Figure 8, wax surface after droplet test. Note the etched appearance where cleaner was in contact with wax.

## DROPLET TEST

We use the droplet test to determine if a cleaner will remove a heavy coating of silicone oil from a wax sample.

A light coating of silicone oil is directly applied to the sample. Each finger is checked for adhesion after spraying to confirm that tape will not stick. Drops of cleaner of varying concentrations are placed on the fingers for times ranging from 5 seconds to 4 minutes (Figure 9). After rinsing and drying, the cleaned areas are checked for adherence (Figure 10).

We used this test to compare three different cleaners; identified as A, B and C. Cleaners A and B are dilutable, Cleaner C is non-dilutable.



Figure 9, cleaner A sample at 20%, 50% and 100% concentration (left to right). Figure 10, after rinse and dry. Contact time, 15 seconds to 4 minutes (furthest to closest)

Cleaners A and B, when diluted, did not remove enough silicone oil to produce measurable adhesion, regardless of contact time. When used straight, all cleaners removed the silicone oil and etched the surface.

## INJECTIONS AFTER SPRAYING AND CLEANER

One of the goals in the cleaning process is to produce consistent adhesion regardless of residual silicone level. We ran a test to compare wax and prime coat adhesion relative to residual silicone and cleaner type. To produce a gradient in residual silicone, the five-finger sprue wax injection tool was sprayed with a silicone release agent and 10 consecutive injections were made without re-spraying. Wax adhesion testing was performed on all fingers prior to cleaning.

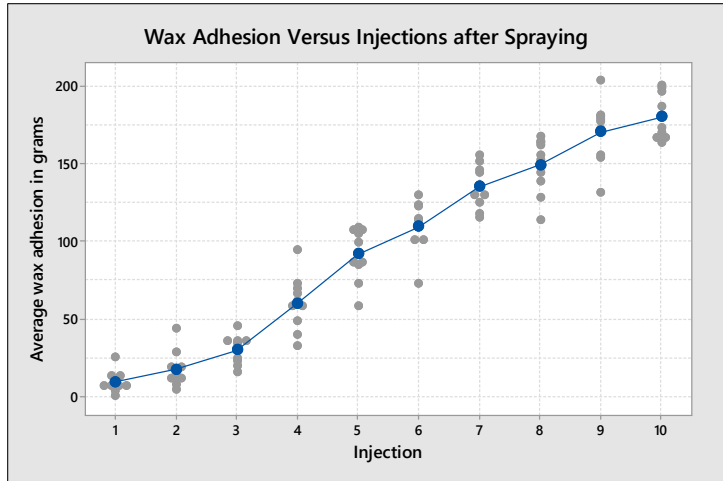


Figure 11, wax adhesion versus injections after spraying

As was found in previous testing, wax adhesion increased after each injection (Figure 11).

As-Cleaned Wax Testing

The odd numbered sprues were immersed in 100% cleaner C for 30 seconds. The even number sprues were immersed 20% cleaner A for 30 seconds.

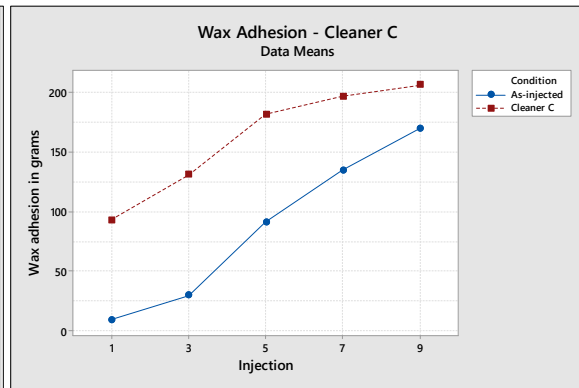
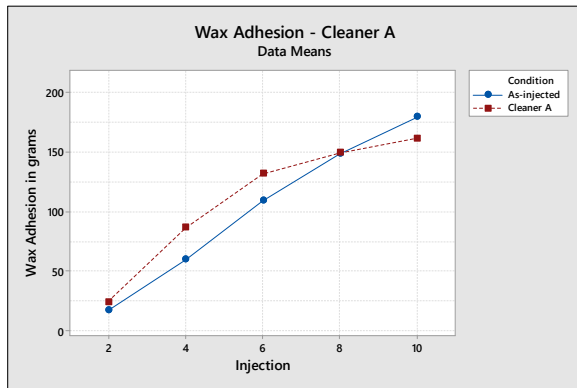


Figure 12, cleaner A adhesion before and after cleaning (left). Figure 13, cleaner C adhesion before and after cleaning (right)

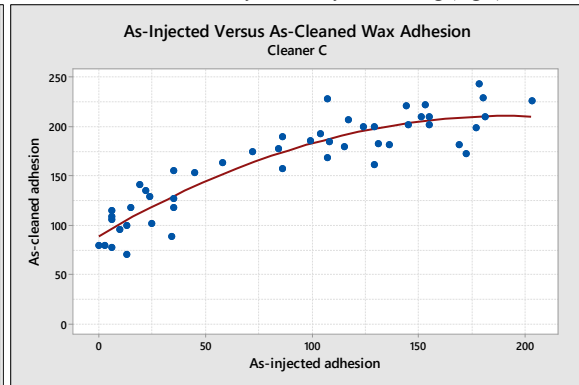
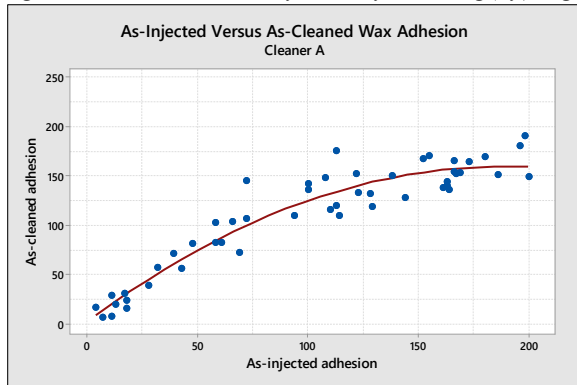


Figure 14, cleaner A as-injected versus as-cleaned regression (left). Figure 15, cleaner C as-injected versus as-cleaned regression (right)

Injections after spraying and cleaner type significantly affected as-cleaned adhesion. There was little improvement in adhesion with cleaner A (Figure 12). There was a large improvement in adhesion with cleaner C (Figure 13).

Prime Coat Testing

All of the test sprues were prime coated and dried. Tape was applied to the prime coat and allowed to sit overnight prior to testing.

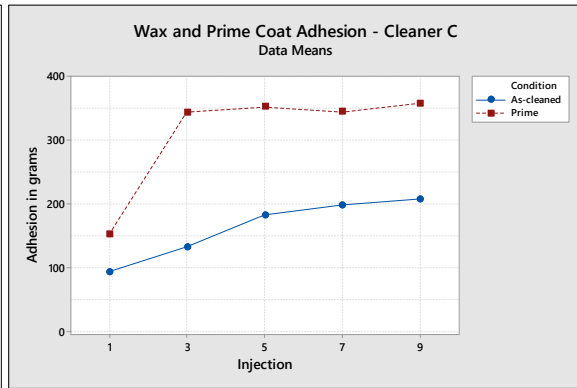
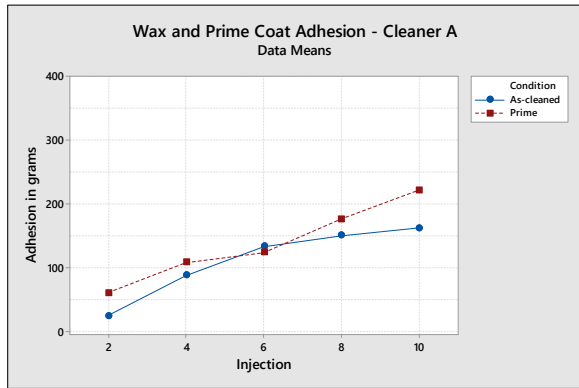


Figure 16, Cleaner A as-cleaned and prime coat adhesion (left). Figure 17, cleaner C as-cleaned and prime coat adhesion (right)

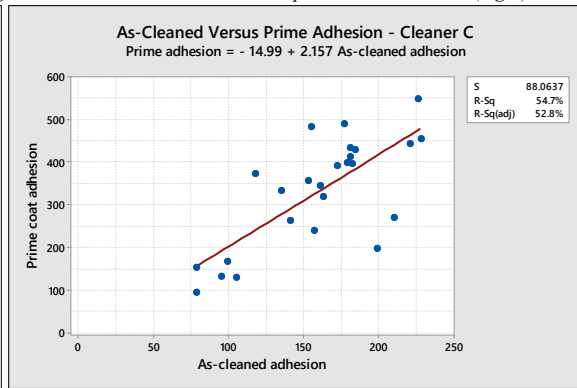
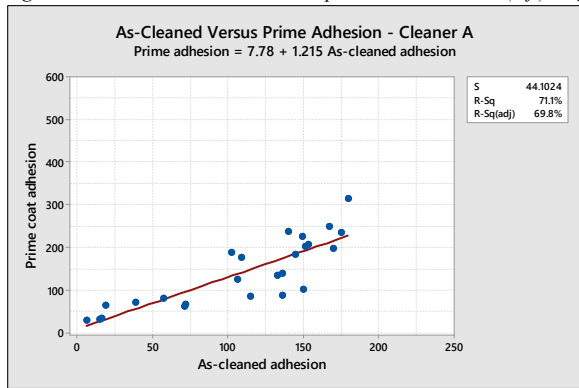


Figure 18, cleaner A as-cleaned to prime coat regression (left). Figure 19, cleaner C as-cleaned to prime coat adhesion (right)

There was little difference between wax and prime coat adhesion for cleaner A up until six injections, after which prime coat adhesion progressively improved (Figure 16). Prime coat adhesion progressively increased relative to injections after spraying.

There was a large difference between wax and prime coat adhesion for cleaner C, indicating a secondary mode of bonding (mechanical). (Figure 17). This plot shows consistent prime coat adhesion starting at three injections after spraying. It appears the improved mechanical bonding due to the etched wax surface, negates any silicone remaining after cleaning.

The regression plot of cleaner A shows the prime coat adhesion is 120% higher than wax adhesion (Figure 18).

The regression plot of cleaner C shows the prime coat adhesion is 210% higher than wax adhesion (Figure 19).

## RELEASE AGENT, CLEANING AND ADHESION

This test had several goals:

- Determine wax and prime coat adherence to a wax free of release agents.
- Measure the improvement of prime coat adhesion due to etching.
- Compare wax and prime adhesion when using a non-silicone release agent.

Paramelt provided wax samples using a tool that did not require a release agent. A total of 12 samples were tested per condition.

- Heavy coating of silicone release
- Light coating of silicone release
- No release
- Light coating of non-silicone release

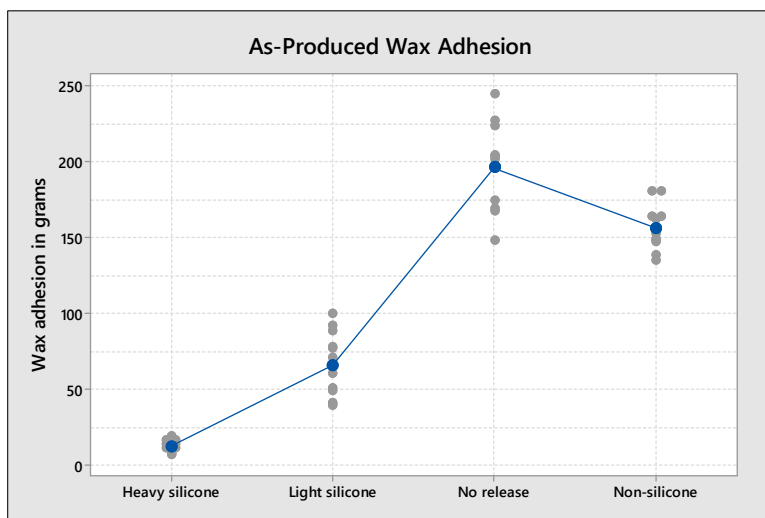


Figure 20, as-produced adhesion by release agent

Wax adhesion on samples with light and heavy coating of silicone were similar to those found in previous tests. Adhesion to wax with no release was very high. Adhesion to wax with non-silicone release was also high but less than no release (Figure 20).

### As-Cleaned Wax Adhesion Testing

Half of the samples of each group were cleaned for 30 seconds using Cleaner C. The other half were not cleaned. Adhesion was measured 45 minutes after cleaning.

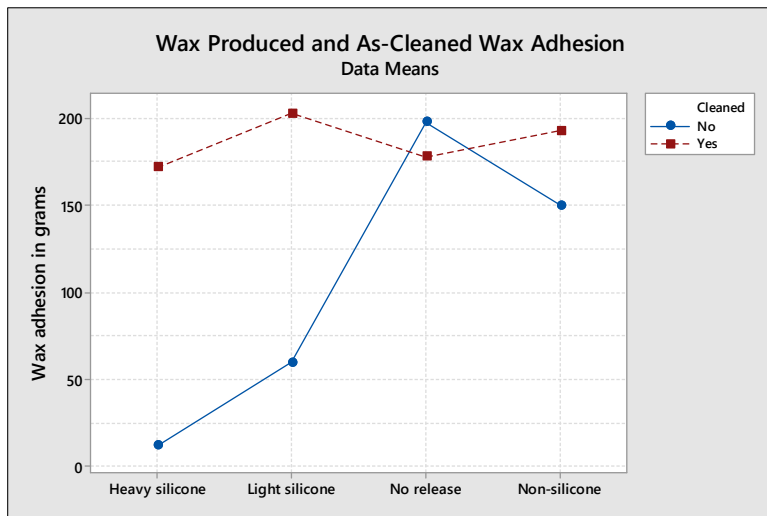


Figure 21, as-produced and as-cleaned wax adhesion by release agent (right)

As was found in previous trials, cleaning patterns coated in silicone oil dramatically improved adhesion. Cleaning patterns without release did not produce a statistical improvement. Cleaning patterns with non-silicone release only produced a moderate improvement (Figure 21).

All as-cleaned samples had similar wax adhesion, regardless of release agent type or amount.

### Prime Coat Testing

All of the samples were prime coated. The prime coat was allowed to dry overnight prior to applying tape. The tape was allowed to bond to prime coat for 14 hours prior to testing.

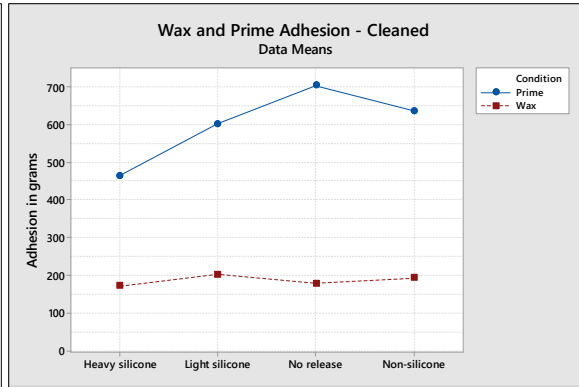
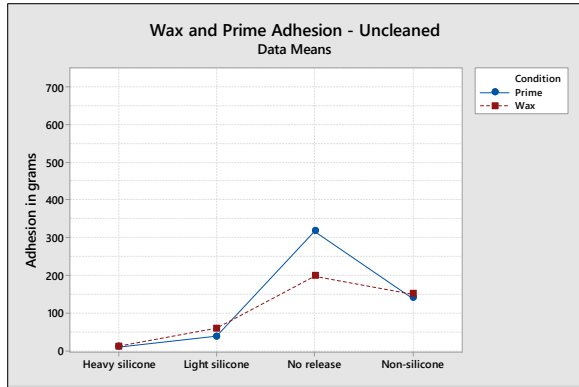


Figure 22, un-cleaned wax and prime adhesion by release (left). Figure 23, cleaned wax and prime adhesion by release (right)

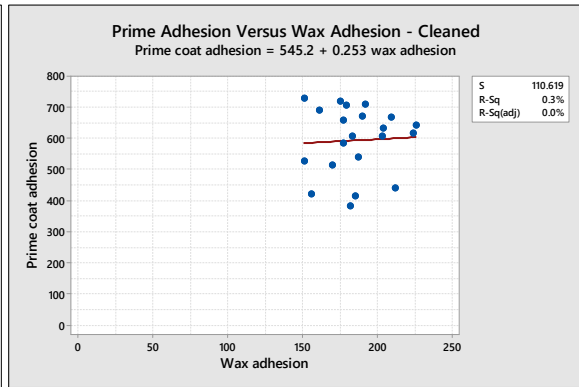
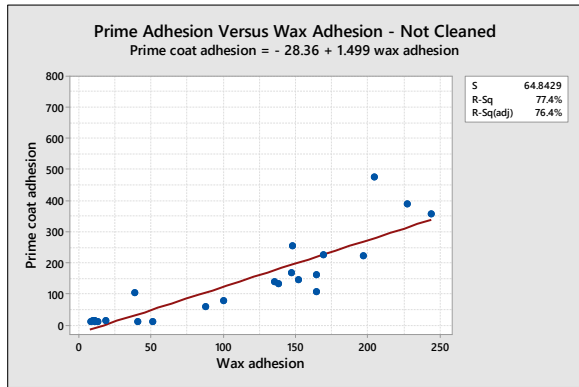


Figure 24, regression plot of uncleaned wax and prime adhesion (left). Figure 25, cleaned wax and prime adhesion (right)

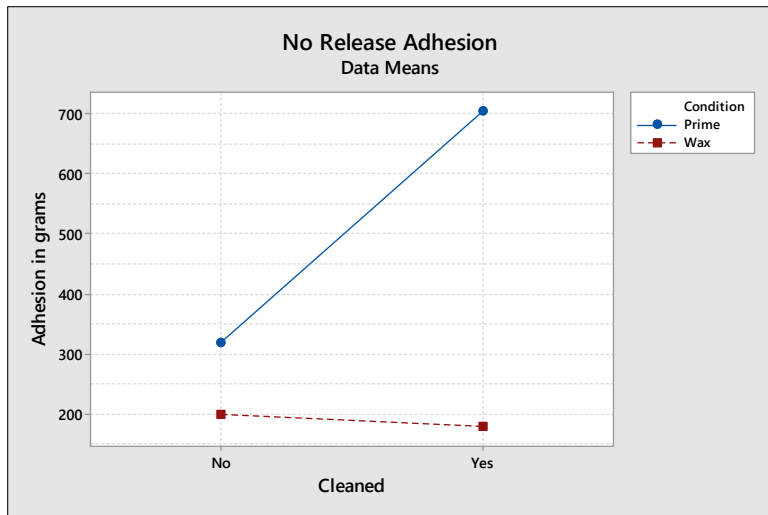


Figure 26, interaction plot for cleaning and test condition for no release wax samples

We see the dramatic improvement in prime coat adhesion due to pattern cleaning when comparing figures 22 and 23. Figure 23 also shows *no release* samples having the highest prime adhesion even though wax adhesion was the similar to other conditions.

Wax to prime coat regression plots are shown in figures 24 and 25. The difference in the regression lines highlight the effect of etching.

The etching effect is also shown in figure 26. Wax adhesion for *no release* samples were virtually the same whether cleaned or uncleaned yet prime adhesion doubled. This difference is visually apparent when comparing figures 27 and 28.

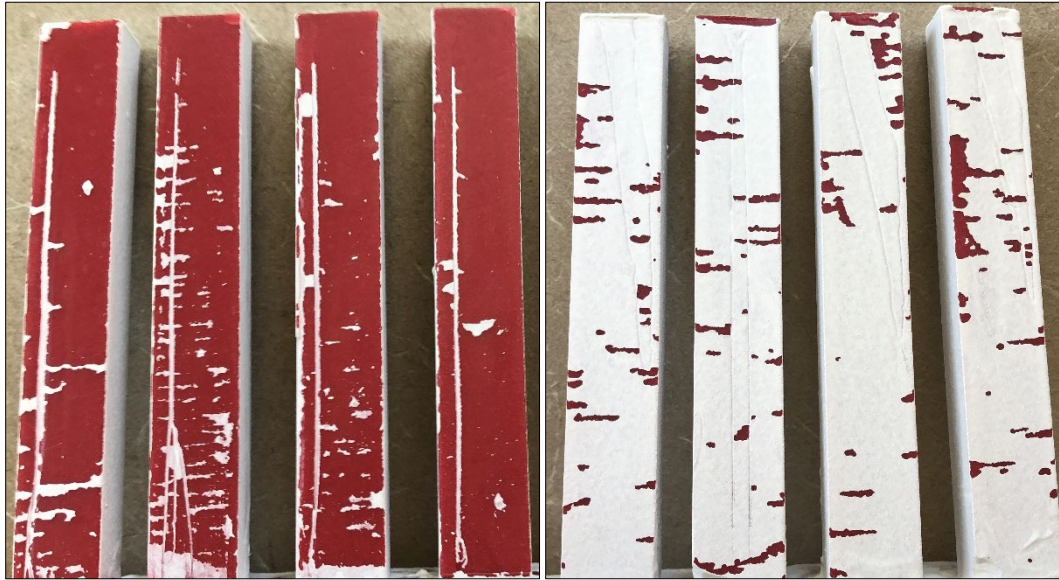


Figure 27, no release samples after prime coat adhesion testing, not cleaned (left). Figure 28, cleaned (right)

## TACKINESS AND CLEANING TIME

We wanted to understand the role tackiness and cleaning time played in prime coat adhesion. A total of four wax samples were made with a heavy coating of silicone release. This was done by spraying the five-finger sprue die prior to each injection. The wax samples were processed according to the matrix below (Figure 28). Wax tackiness was adjusted by varying the delay between cleaning and prime coat application. A five-minute delay produces high tack and 24 hour delay produces no tack. All samples were cleaned in cleaner C at 100% concentration.

Sample	Delay time	Immersion time
1	1440 minutes	120 seconds
2	1440 minutes	30 seconds
3	5 minutes	30 seconds
4	5 minutes	120 seconds

Figure 28

The prime coat was allowed to dry overnight prior to applying the tape. The tape was applied 24 hours prior to testing. As-cleaned wax adhesion was not measured. A total of ten readings were obtained per sample.

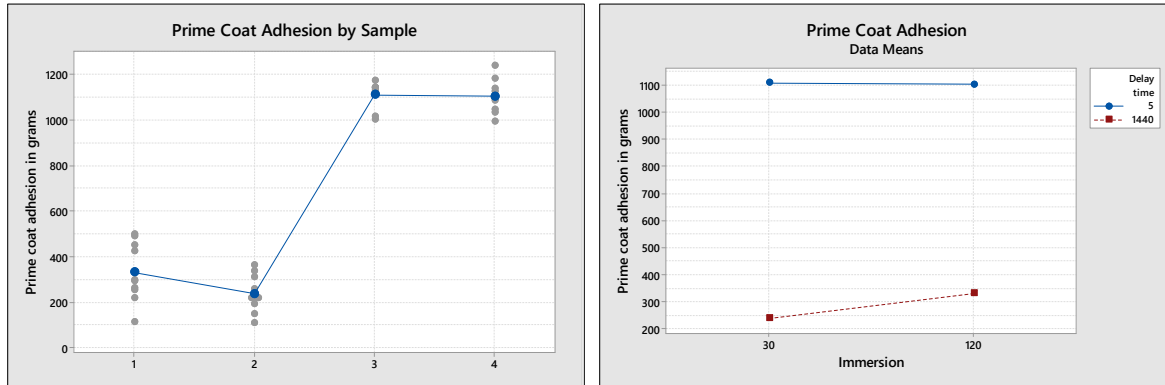
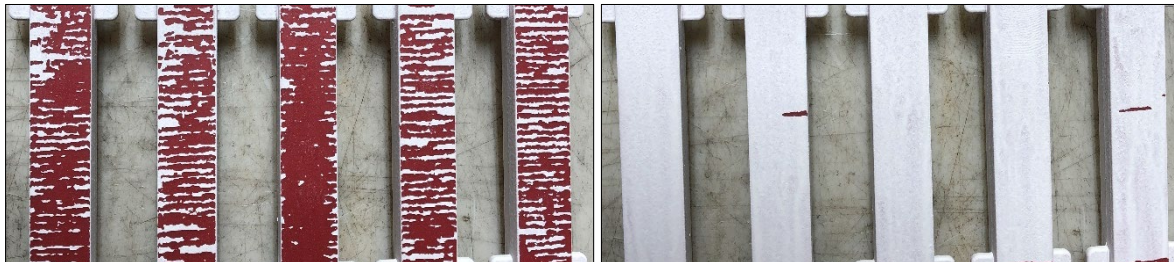


Figure 29 prime adhesion by sample (left) Figure 30 interaction plot of adhesion by delay and immersion time.

Figure 30 shows the dramatic impact delay time has on prime coat adhesion. Applying the prime coat when the wax is still very tacky increased adhesion by over 300%. It is important to note the tape did not remove the prime coat from samples 3 and 4. This means the actual adhesion was higher than measured.



## PRIME COAT ADHESION AND SPALL

Previous researchers have stated there is an ideal level of prime coat adhesion; high enough to prevent prime coat lifting yet not so high as to cause delamination or spalling.

Hendricks and Wang<sup>14</sup> stated “Another important area concerning the primary slurry is the adhesion strength of the slurry to the bare wax as well as the subsequent coat. If the adhesion to the wax pattern is not sufficient, the first primary coat might crack or lift after the second dip. If adhesion of the first coat to the wax pattern is too strong and stronger than the adhesion to the

subsequent coat, the primary coats might come off the shell during autoclave dewaxing and resulting in delamination or spalling.”

For purposes of this paper, we will use the following definition for spall:

Spall is the failure of the prime coat layer in a highly detailed feature of the mold. This failure can be between prime and 2<sup>nd</sup> shell layer or within the prime layer. Highly detailed features that retain a thick layer of prime slurry such as depressed lettering, sharp internal corners and golf club score lines are prone to spall.

Pine Tree Castings has been developing a test to measure spall severity. This test uses a wax specimen with features that are particularly difficult to produce without spall: four pyramids with ridgeline angles ranging from 30 to 75 degrees (Figure 33).

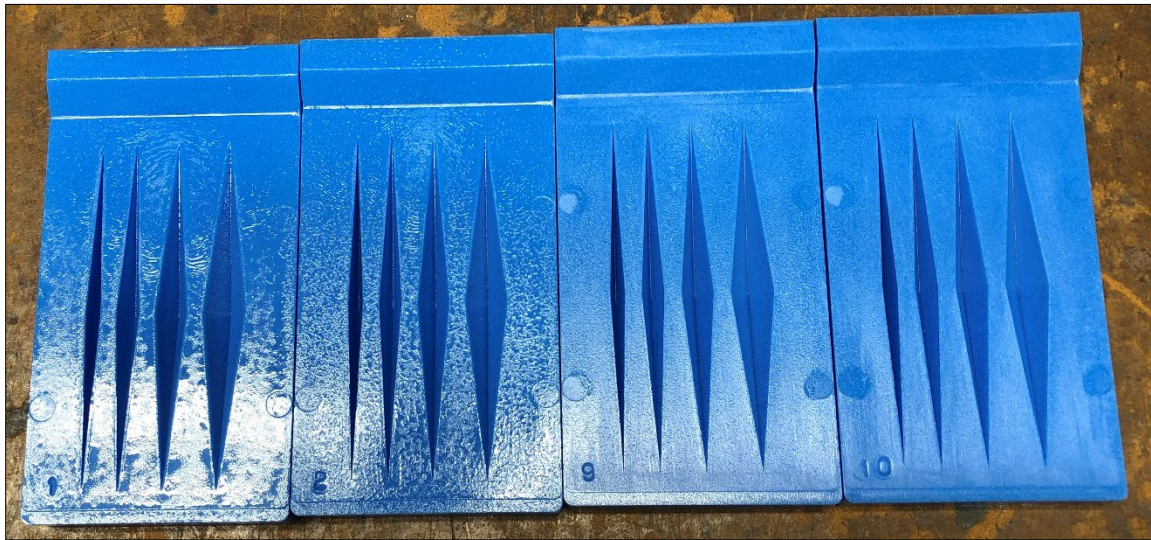


Figure 33, spall severity patterns; 1<sup>st</sup>, 2<sup>nd</sup>, 9<sup>th</sup> and 10<sup>th</sup> injections after spraying (left to right)

Samples are shell built, flashfire dewaxed and allowed to cool. Each mold cavity is removed from the sprue and the back face pried off. The ridgeline of each of the pyramids is graded for spall severity (Figures 34 and 35).



Figure 34, spall severity test: 30 degree to 75 degree pyramid (closest to furthest). Low spall level



Figure 35, high spall

In this test, we wanted to determine if silicone level or cleaning condition affect spall severity.

- Injection after spraying; 1, 2, (high residual silicone) 9 and 10 (low residual silicone)
- Cleaning; None, Cleaner A, Cleaner C (20%)

A total of three molds were tested per cleaning condition. Each mold had eight patterns with two patterns from each injection condition. Pattern cleaning time was 30 seconds.

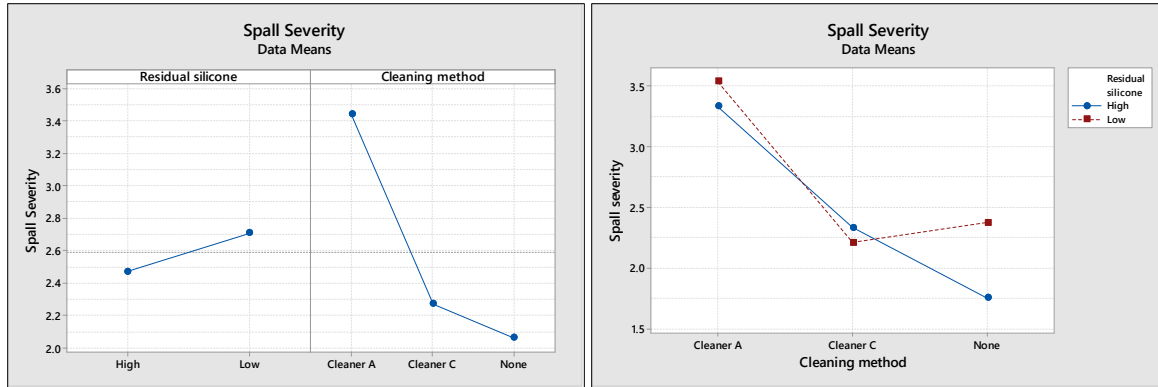


Figure 36, Spall severity by residual silicone and cleaner (left). Figure 37, interaction plot of silicone and cleaner (right)

The results showed the least amount of spall occurred when the patterns were not cleaned and had a high level of residual silicone. Cleaner C, which would produce the most adhesion, had less severe spalling than cleaner A.

## WETTING, SURFACE TENSION AND SURFACE ENERGY

Wetting is the ability of a liquid to maintain contact with a solid surface. Wetting is typically measured by the contact angle of a liquid droplet on the solid surface. A system is considered wetting when the contact angle is less than 90 degrees and non-wetting when the contact angle is greater than 90 degrees (Figure 38). However, wetting is not simply yes or no result.

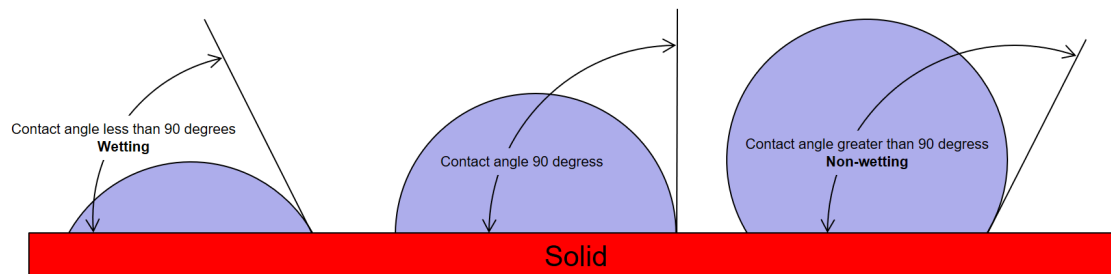


Figure 38, comparison of contact angles

Hendricks and Wang<sup>14</sup> stated, “The surface tension (or energy) difference between the slurry and the substrate dictates the entire wetting behavior and a good portion of the adhesion strength. The rule of thumb of making a perfect condition is that the surface tension of the coating agent should be lower than that of the substrate. Waxes are known to have a surface tension lower than most of the material used in the ceramic shell process. To make a good coat on the bare wax, the surface tension of the primary binder must be reduced to a level that makes coating possible.”

Dooley, Spence, Guerra and Juhari<sup>17</sup> stated, “The surface energy of materials used within the Investment Casting sector is currently not well understood and rarely investigated within the industry.”

This statement adequately summarized my knowledge of the subject. I thought that as long as the prime coat slurry wet the wax pattern everything was fine. I had no knowledge of the complex forces that determine the degree of wetting and adhesion. The paper by Dooley et al<sup>17</sup> was my introduction into the intricacies of this subject.

A simplistic view of wetting only considers the surface tension of the liquid and the surface energy of the substrate. This approach predicts a liquid will wet a substrate when the surface tension of the liquid is less than the surface energy of the substrate. However, we wanted to predict how well a liquid would wet a substrate. We had to learn more about the forces of wetting.

We start with some of the terminology.

Surface Tension is the excess energy at the surface of a liquid relative to the core. It is an attractive force that pulls the liquid molecules inward.<sup>15</sup> A low surface tension liquid will form a lower contact angle with a substrate than high surface tension liquid. Surface tension will be abbreviated as **LV (Liquid to Vapor surface energy)** in equations in this paper.

Surface Energy is the excess energy that exists at the surface of a solid. This excess or “free” energy exists because the molecules at the surface cannot interact with as many like neighbors as molecules in the bulk.<sup>18</sup> Surface energy of a solid is analogous to surface tension in a liquid. It indicates the maximum surface tension of a liquid that will wet a solid under ideal conditions.<sup>23</sup> A high surface energy solid is easier to wet than a lower surface energy solid. Surface energy will be abbreviated as **SV (Solid to Vapor surface energy)** in equations in this paper.

Interfacial Tension is the adhesive force between the liquid phase of one substance to the substrate of another. “It is the minimum amount of work required to create that interface.”<sup>15</sup> As

interfacial tension is reduced, the contact angle is reduced and adhesion is improved. Interfacial tension will be abbreviated as **SL (Solid to Liquid surface energy)** in equations in this paper.

Dispersive and Polar Components of Surface Energy/Tension. The forces that make up surface energy/tension are generally divided into two main components; **dispersive** and **polar**.<sup>30</sup>

“Comparing the ratio of between the dispersive and polar part of surface energy for two phases allows for a prediction of the adhesion between these two phases. The closer the ratios match the more interactions are possible between the phases and the higher the adhesion. A high potential for interaction between two phases also leads to small interfacial energy.”<sup>22</sup>

Surface tension/energy is typically reported in dynes/cm, mN/m or mJ/m<sup>2</sup>.

The relationship between surface tension, surface energy, interfacial energy and contact angle is described by Young’s equation. To predict the contact angle of a liquid on a substrate, the surface energy of these three forces must be known (Figure 39).

#### Young’s equation

$$LV \cos \theta = SV - SL$$

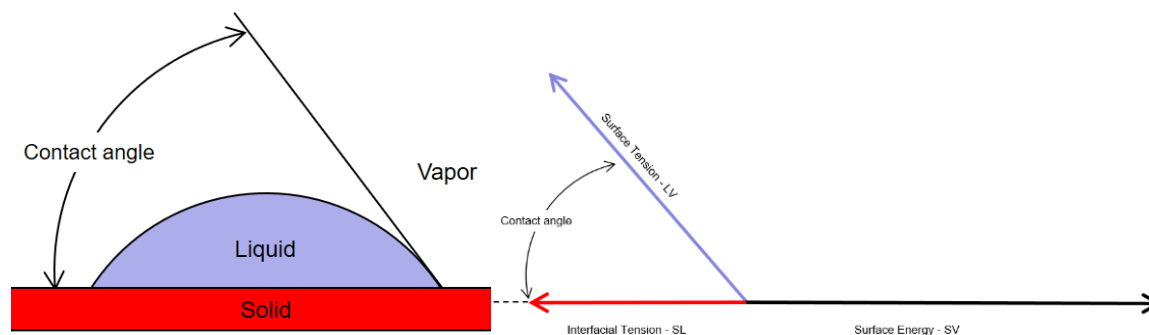
Where:

*LV* = surface tension of liquid

*SV* = Surface energy of solid

*SL* = Interfacial tension of liquid to substrate

$\theta$  = contact angle



The interfacial tension between a liquid and solid can be calculated using Fowkes equation if the dispersive and polar components of the surface energy/tension are known.

Fowkes equation

$$SL = LV^t + SV^t - 2(\sqrt{LV^d SV^d} + \sqrt{LV^p SV^p})$$

Where:

$t$  = total surface tension

$d$  = dispersive energy

$p$  = polar energy

Once interfacial tension has been determined (SL), the contact angle can be calculated by rearranging Young's equation.

$$\cos \theta = \frac{SV - SL}{LV}$$

From this equation, we see:

- The contact angle will be less than 90 degrees when the surface energy of the solid (SV) is greater than the interfacial tension (SL) (figure 40).
- The contact angle will be greater than 90 degrees when the surface energy of the solid (SV) is less than the interfacial tension (SL) (figure 41).

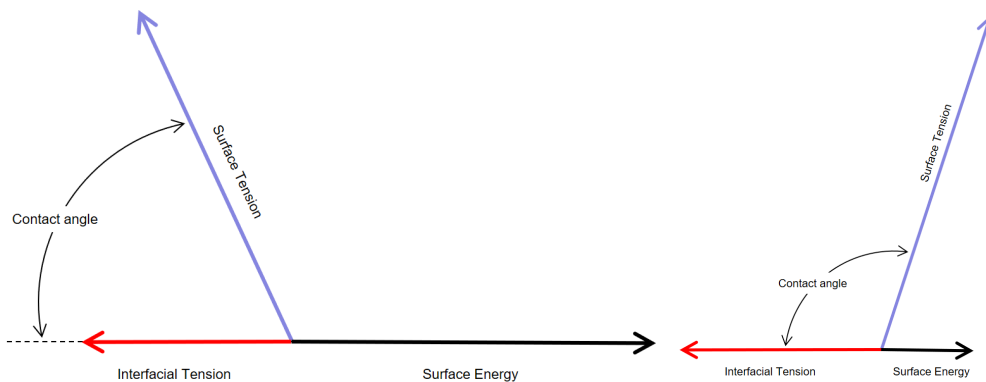


Figure 40, wetting condition; interfacial tension < surface energy (left). Figure 41, non-wetting condition; interfacial tension > surface energy (right)

The adhesion of the liquid to the substrate is known as the *Work of Adhesion*. Work of Adhesion is defined as the energy required to separate a liquid from a solid surface. The higher the work of adhesion, the better the bonding. It is calculated using a formula that is similar to Fowkes equation.

$$W_{\text{adhesion}} = 2(\sqrt{LV^d SV^d} + \sqrt{LV^p SV^p})$$

### *Spread Wetting*

In spread wetting, a liquid in contact with a substrate will spread over the substrate and displace the air from the surface.<sup>15</sup> For spread wetting to occur, the surface energy of the system must decrease during the spreading process.

$$SV > (LV + SL)$$

Shown in the force diagram below, the surface energy of the solid is greater than the surface tension of the liquid + interfacial tension (Figure 42). When spread wetting occurs, the contact angle will be 0.

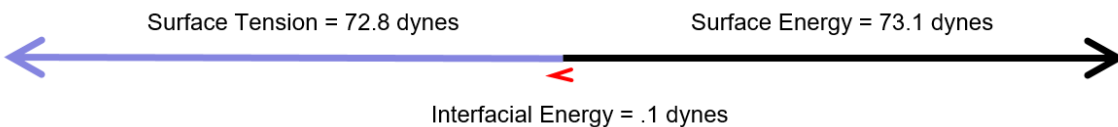


Figure 42, spread wetting force diagram for water on glass.

### *Spreading Coefficient*

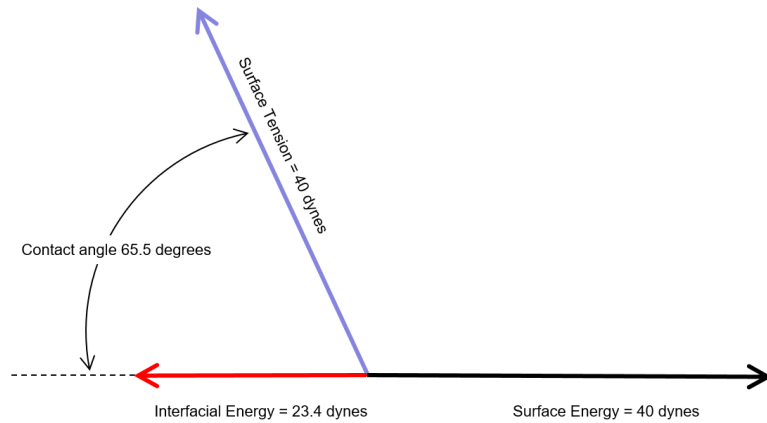
The spreading coefficient defines the degree of spread wetting. If the coefficient is negative, spread wetting will not occur. If the spreading coefficient is positive, spread wetting will occur.

$$\text{Spreading coefficient} = W_{adhesion} - (2 \times LV)$$

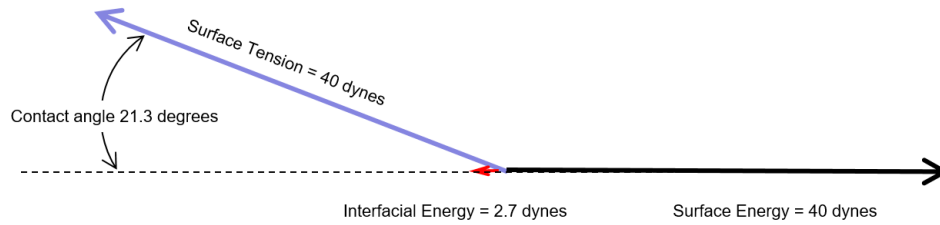
### *Wetting Example*

As an example of the importance in balancing dispersive and polar forces, a comparison was made between substrates of different polar ratios. In this example, a droplet of 40 mN/m liquid with 20 mN/m dispersive and 20 mN/m polar energy is placed on different substrates. The wetting characteristics were calculated.

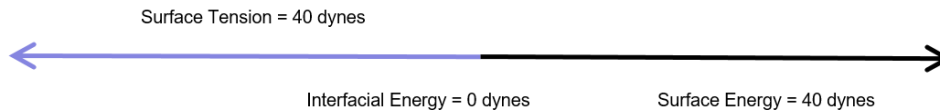
- Substrate 1; 40 mN/m total, 40 mN/m dispersive and 0 polar.
  - Calculated contact angle; 65 degrees
  - Spreading coefficient; -23.4



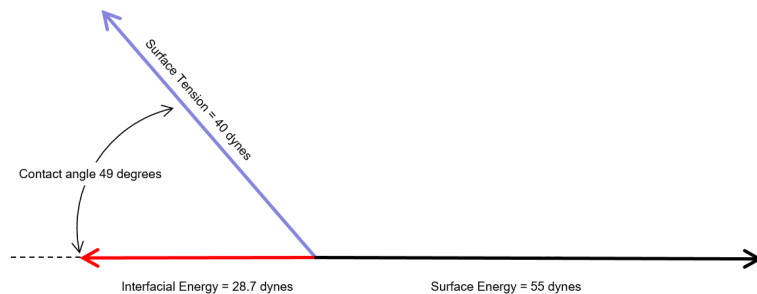
- Substrate 2; 40 mN/m total, 30 mN/m dispersive and 10 polar.
  - Calculated contact angle; 21 degrees
  - Spreading coefficient; -2.7



- Substrate 3; 40 mN/m total, 20 mN/m dispersive and 20 polar.
  - Calculated contact angle; 0 degrees
  - Spreading coefficient; 0.



- Calculated contact angle; 49 degrees
- Spreading coefficient; -13.7



As can be seen from these examples, minimizing the interfacial energy by matching dispersive and polar forces is more critical to wetting and adhesion than increasing the surface energy of the substrate.

## WAX SURFACE ENERGY MEASUREMENT

Paramelt performed surface energy testing on various pattern conditions: no release, light silicone release and heavy silicone. The same pattern wax was used for all conditions.

Group	Total Surface Free Energy	Dispersive	Polar
No mold release	28.0	27.7	.3
Light silicone release	28.7	28.7	0
Heavy silicone release	32.4	31.8	.6

These results are similar to those presented by Dooley, Spence, Guerra and Juhari<sup>17</sup>. They found

- 22.9 to 27.8 for pattern waxes without release.
- 39.0 to 41.4 for pattern waxes with silicone release

It is interesting to note that silicone on the wax pattern increases surface energy, making it easier to wet than bare wax.

## BINDER SOLUTION SURFACE TENSION MEASUREMENT

In order to predict the wetting characteristics of the prime coat slurry on a wax pattern, we needed to measure surface tension of the prime coat binder.

A typical prime coat binder solution comprised of colloidal silica, deionized water, latex polymer, surfactant and antifoam was tested for surface tension by Dataphysics-Instruments. The surface tension measured 25.48 mN/m with 25.37 dispersive and .11 polar.

## WAX WETTING

Using the surface tension data for the binder solution, the predicted wetting characteristics of various pattern conditions were calculated.

Predicted Work of Adhesion, Spreading Coefficient and Contact Angle				
Substrate	Total surface energy (solid)	Work of adhesion	Spreading coefficient	Contact angle
Pattern Wax "A", no silicone	22.5	47.83	-3.13	28.7
Pattern Wax "B", no silicone	22.6	48.01	-2.95	27.8
Pattern wax "C", no silicone	28.0	53.38	2.42	0
Pattern wax "C", light silicone	28.7	53.97	3.01	0
Pattern wax "C", heavy silicone	32.4	57.32	6.36	0
Cleaned pattern wax*	38.8	62.93	11.97	0

\* Dooley, Spence, Guerra and Juhari<sup>17</sup>

## SUMMARY

The wax injection operation produces patterns with a wide range of residual silicone release. The amount of residual silicone is one of the determinants in prime coat adhesion. Effective pattern cleaning can remove this silicone, allowing for consistent wetting and adhesion of the prime coat.

To date, it has not been easy to determine if the cleaning process is removing the silicone. Many methods were either subjective, difficult to perform or did not provide a definitive result. The modified tape peel test, as demonstrated in this paper, can quickly and accurately determine the effectiveness of the pattern cleaning process.

It is not easy to remove silicone from a wax pattern. Of the cleaners tested, only un-diluted cleaners were able to remove a heavy coating of silicone.

Etching the wax surface significantly increases prime coat adhesion. In this study, adhesion more than doubled when the pattern was etched. It is not known if all this adhesion is necessary but we were unable to remove the silicone without etching the wax.

Applying the prime coat to a highly tacky wax can increase adhesion by over 300%. Most cleaners leave the wax surface tacky immediately after cleaning even if the residual silicone is not completely removed. However, this condition is only temporary as tackiness is significantly diminished after 45 minutes and completely gone after 24 hours. Targeting and controlling the time from cleaning and prime coat application is critical.

- If the process requires a tacky wax, prime coating too late could increase buckle.
- If the process requires no tack, prime coating too soon could increase spall or delamination.

The severity of prime coat spall appears to be influenced by the surface condition of the wax.

- When covered with silicone, spall severity was minimized. It is believed the weak bond with the wax allows the ceramic to slide during wax expansion and contraction, minimizing stress.
- When effectively cleaned, spall severity increased. The theory is that uniform adhesion distributes stresses across the entire interface, minimizing peak stresses. However, this stress is higher than with uncleaned waxes.
- When poorly cleaned, spall severity was very high. It is believed the non-uniform adhesion concentrates stresses at the sites where bonding occurs, maximizing peak stress.

## FUTURE WORK

Continue to explore the role tackiness plays in adhesion and spall. Even though dilute cleaners do not remove a heavy coating of residual silicone, they do tackify the wax and should increase prime coat adhesion (if applied when tacky). We would like to be able to answer the following:

- How quickly does tackiness change?
- Is tackiness dependent on cleaner concentration or cleaning time?
- Is tackiness dependent on residual silicone amount?
- Is tackiness dependent on wax formulation?
- Does tackiness affect spall severity?

Work by Dooley, Spence, Guerra and Juhari<sup>17</sup> showed that the surface energy of the wax was increased by cleaning. It is believed this improvement is due to wax etching. To verify this hypothesis, we planned on comparing the surface energy of waxes cleaning with straight and dilute pattern washes. This work was not completed due to time constraints.

## ACKNOWLEDGEMENTS

Thanks to Alfred Kaulius, Harvey Fielder, Tim Wolff, Conrad Holek and Bill Fricker at Paramelt for their valuable contribution to this study.

## SURFACE TENSION AND SURFACE ENERGY

Surface tension of various liquids in dynes			
Material	Dispersive component	Polar component	Total
Water	26.4	46.4	72.8
Ethanol	18.4	4	22.4
Ethylene glycol	28.6	19.7	48.3
Diiodomethane	51	0	51
Colloidal silica, latex polymer, surfactant and antifoam	25.37	.11	25.48
PDMS silicone mold release <sup>32</sup>	19	.8	19.8

Surface free energy of various solids in dynes			
Material	Dispersive component	Polar component	Total
Glass	29.4	43.9	73.3
Untreated (PTFE)	18	0	18
Paraffin wax	25.5	0	25.5
Pattern wax "A" no silicone - Paramelt	22.16	.32	22.5
Pattern wax "B" no silicone - Paramelt	22.43	.24	22.6
Pattern wax "C" no silicone - Paramelt	27.7	.3	28.0
Cleaned pattern wax*	32.44	.35	32.8
Cleaned pattern wax*	38.82	.06	38.88
Pattern wax with silicone release*	39.2	.09	39.29
Pattern wax with light silicone release - Paramelt	28.7	0	28.7
Pattern wax with heavy silicone release - Paramelt	31.8	.6	32.4
Pattern wax with non-silicone release*	37.13	21.48	58.61

\* Dooley, Spence, Guerra and Juhari<sup>17</sup>

## REFERENCES

1. Innovative Pattern Waxes to Satisfy Modern Casting Needs, J. Argueso, C. Kovach, G Schiefelbein, 22<sup>nd</sup> European Conference on Investment Casting, 1990
2. The Evolution of Pattern Wax Cleaners, S. Bhattacharja, R. Doles, M. Romba, X. Wang, 61<sup>st</sup> Technical Conference and Equipment Expo, 2014
3. A Robust Solvency Power Test for Determining End Life of Pattern Washes, J. Stanco, C. Fillmore, D. Jones, 59<sup>th</sup> Technical Conference and Expo, 2012
4. The Role of the Investment Shell Mould in Determining the Quality of Castings for the Aerospace Industry, D. Mills 17<sup>th</sup> BICTA Conference, 1984
5. Prime Slurries for Investment Casting, J. Snow, D. Scott, 47<sup>th</sup> Annual Technical Meeting, 1999.
6. Wax Characterization, J. Niles, M. Anibarro, H. Fielder, 50<sup>th</sup> Technical Conference and Expo 2002.
7. Revolution in Pattern Wax, J. Argueso, P. Solomon, 45<sup>th</sup> Annual Technical Meeting, 1997
8. Pre-Wetting Effects on Shell Strength and Structure, W. Roberts, 38<sup>th</sup> Annual Technical Meeting, 1990.
9. The ICI Ceramics Testing Guidebook, Test 7.26, Shell Mold to Wax Adhesion Button Pull Test
10. An Evaluation of Green and Fired Strength Additives for Precision Investment Casting, J. Beyer, 28<sup>th</sup> Annual Meeting of the Investment Casting Institute
11. Ceramic Shell Investment Casting with Ludox, DuPont Production Information
12. Unexpected Binder Particle Size Effects in Ludox SK Slurries, W. Roberts, 46<sup>th</sup> Annual Technical Meeting, 1998.
13. Evaluating Spalling Factors Through Measuring Intercoat Adhesion, D.C. Holek, Z. Feffer, 61<sup>st</sup> Technical Conference and Expo, 2014
14. Advancements in Polymer-Enhanced Water-based Primary Binders and Slurries, M. Hendricks, P. Wang, April 2002 Incast
15. Surfactants, Wetting and Foams, A. Bozzo, 37<sup>th</sup> Annual Technical Meeting, 1989

16. Ceramic Shell and Slurry Characterization, J. Niles, A. Bozzo, 51<sup>st</sup> Technical Conference and Expo, 2003.
17. Analysis of Surface Tension of Materials to Improve Coating Performance of Wax Coating, G. Dooley, A. Spence, M. Guerra, A. Juhari, 66<sup>th</sup> Technical Conference and Expo, 2019
18. Innovations in Bonding to Low Surface Energy Surface, 3M Technical paper
19. Fluorochemical Surfactants, 3M Chemical Division
20. [industrialcommunity.3M.com/blog/surface-energy](http://industrialcommunity.3M.com/blog/surface-energy)
21. Optimization of Prime Coats for Investment Casting, Tom Branscomb, 2007
22. Dispersive and polar parts of the surface energy and surface tension, Dataphysics-instrument.com,
23. Surface Energy Heterogeneity for Coating and Adhesion Applications Surface Measurement Systems, Dr. Daniel Burnett
24. Surface Energy (Surface Wetting Capability), NDT Resource Center [nde-ed.org](http://nde-ed.org)
25. Addressing Silicone Contamination Issues, E Petrie, Techsil White Paper, March 2013
26. [nanoscience.com/techniques/tensiometry/surface-tension-surface-free-energy-and-wettability](http://nanoscience.com/techniques/tensiometry/surface-tension-surface-free-energy-and-wettability)
27. Cleaning of Silicone Contaminations: Development of Test Methods and Cleaning Efficiency, V. Liedtke, B.D. Dunn, C. Macho, E. Semerad, Austrian Institute of Technology
28. ISO 8296, Plastics – Film and Sheeting – Determination of Wetting Tension
29. Two-Component Surface Energy Characterization As a Predictor of Wettability and Dispersability, Application note #213, C.R. Ruilison, Kruss GmbH
30. Slip and Leveling Agent, March 2010
31. Measuring the Transport of Siloxane-Based Mold Release Agents in an Encapsulation Mold, J. Ohlhausen, M. Stavig, M. Chavez, K. Archuleta, M. Brumbach, A. Grillet, T. Ordonez, A. Roach, C. Brooks, Materials Characterization and Performance Laboratories, Sandia National Laboratories
32. [Surface.tension.de](http://Surface.tension.de)
33. Atlas of Casting Defects, An Investment Casting Institute Publication

## **Study of Pattern Formulation Effects on Surface Energy Measurements**

Alfred Kaulius & Harvey Fielder, Paramelt

### **Abstract**

A designed experiment was conducted to determine formulation factors influencing the surface free energy (total, polar, and dispersive) of investment casting pattern materials. Factors investigated included various base wax components (paraffin, microcrystalline, resin, etc.) and filler factors. Results indicated the potential to vary the total surface free energy from 19.3 dynes/cm to 31.6 dynes/cm by altering the formulation. Typical production pattern materials are typically measured in the 20.3 to 26.5 dyne/cm range, indicating the potential to achieve greater spread in surface energy results than typically observed. Subsequent testing with mold release materials indicated these materials, and subsequent processing may have the greatest influence on the final surface energy of the pattern materials.

### **Experimental Approach**

A fully saturated orthogonal array L18 designed experiment was carried out examining a total of eight factors at multiple levels each. An L18 array was chosen since it allows for examination of the main effects without convoluting first order interaction effects with any of the results of the main effects. It allows for relatively “clean” analysis of the main effects. The factors examined included examination of the amounts of typical pattern material ingredients as paraffin content, microcrystalline wax content, hydrocarbon resin content, and filler amount. Additionally, the types of amounts of commonly used polymers and additives were also examined. The effect of different types of fillers and amounts were examined, as well.

These factors resulted in 18 separate test formulations. These formulations were produced in small laboratory batches and tested for typical pattern material properties (softening point, drop melt point, penetration, viscosity, etc.). All 18 batches were tested for surface energy measurement at Paramelt's Heerhugowaard facility using a Kruss Mobile Surface Analyzer measuring the contact angles of water and diiodomethane. These two contact angles are used to determine the total surface free energy, as well as the polar and dispersive (non-polar) components.

Previous testing of surface energy by this method for various Paramelt production materials yielded results in the following ranges;

Total Surface Free Energy (dyne / cm): 20.3 – 26.5

Dispersive Component (dyne / cm): 19.9 – 26.2

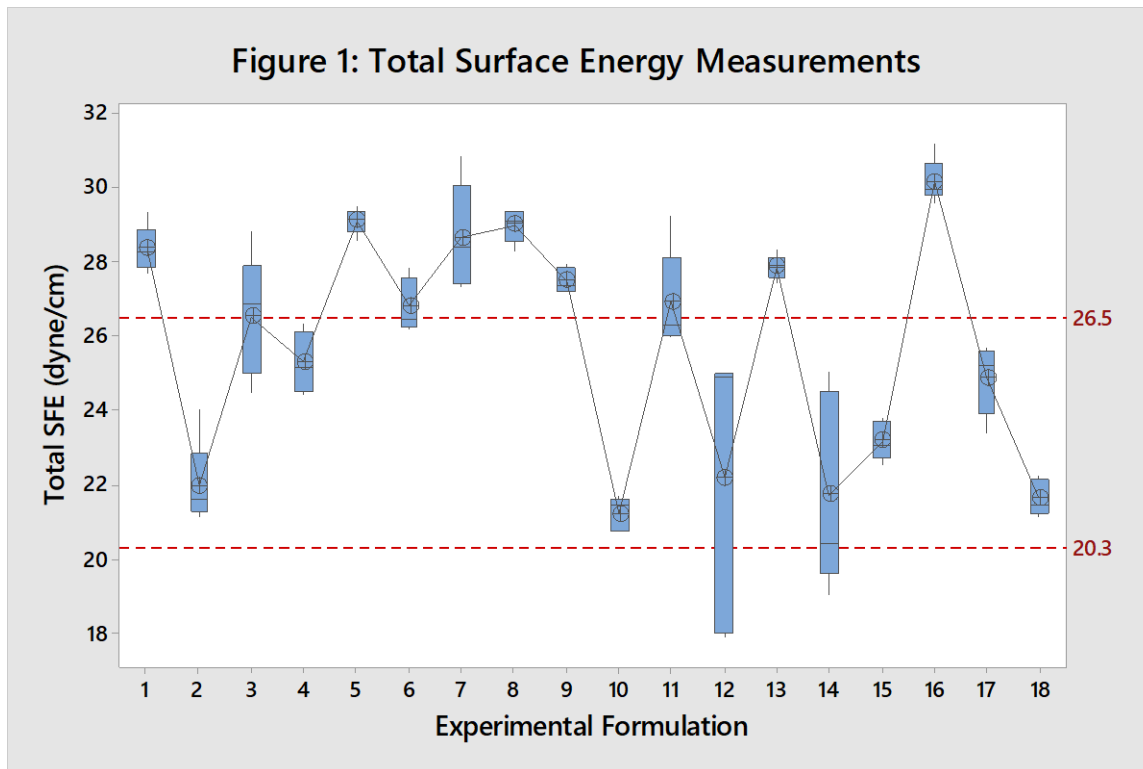
Polar Component (dyne / cm): 0.0 – 1.0

As shown, the vast majority of the surface energy component in the investment casting pattern materials come from the dispersive components. These are generally the van der Waals effects associated with fluctuations in charge distributions across the surface. The polar components are from the permanent dipoles associated with molecular structure.

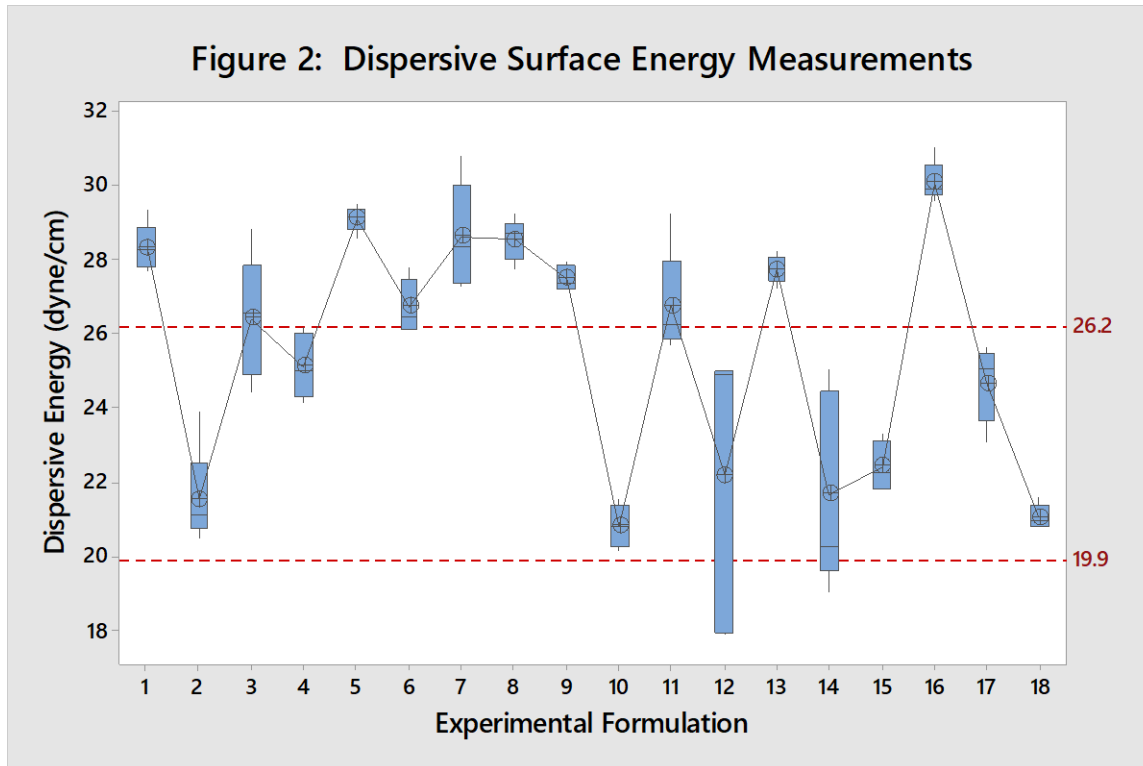
## **Experimental Results**

The focus of this paper is on the surface energy results of the experiment. Although standard physical and rheological properties were measured, these will not be discussed. The focus is purely on the effect of formulation factors on the surface energy measurements.

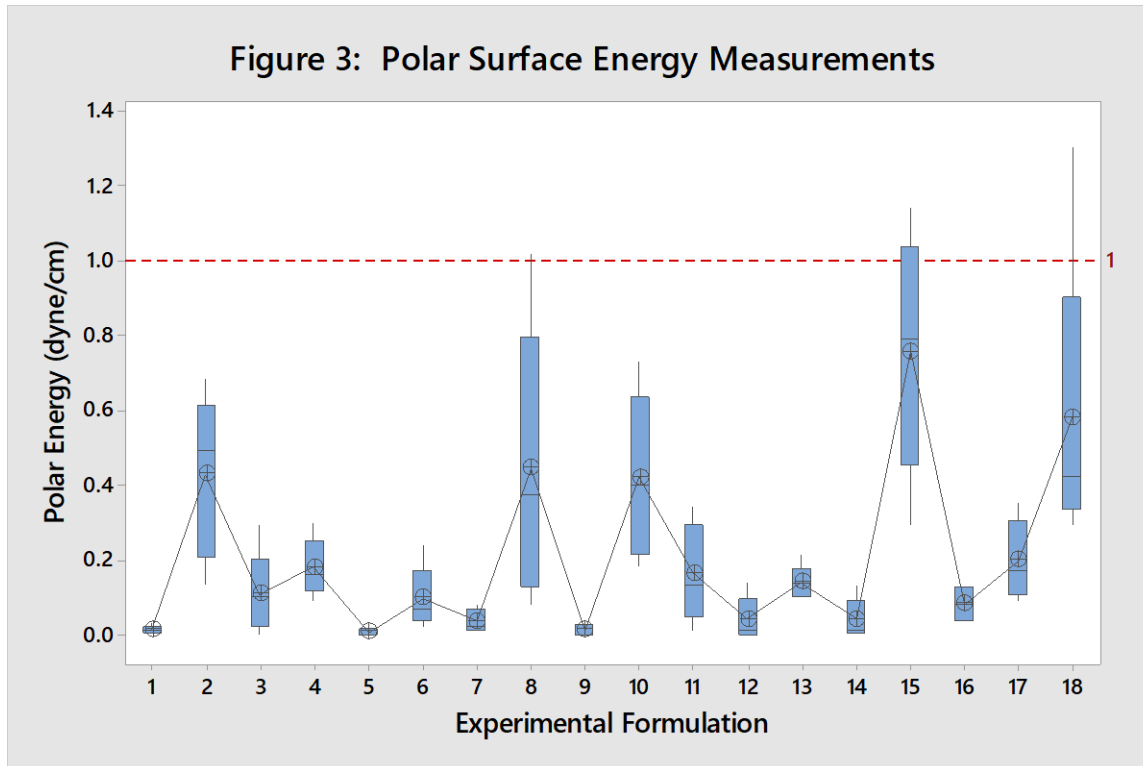
Figure 1 shows the total surface energy measurement for each experimental formulation versus the range observed with standard production materials.



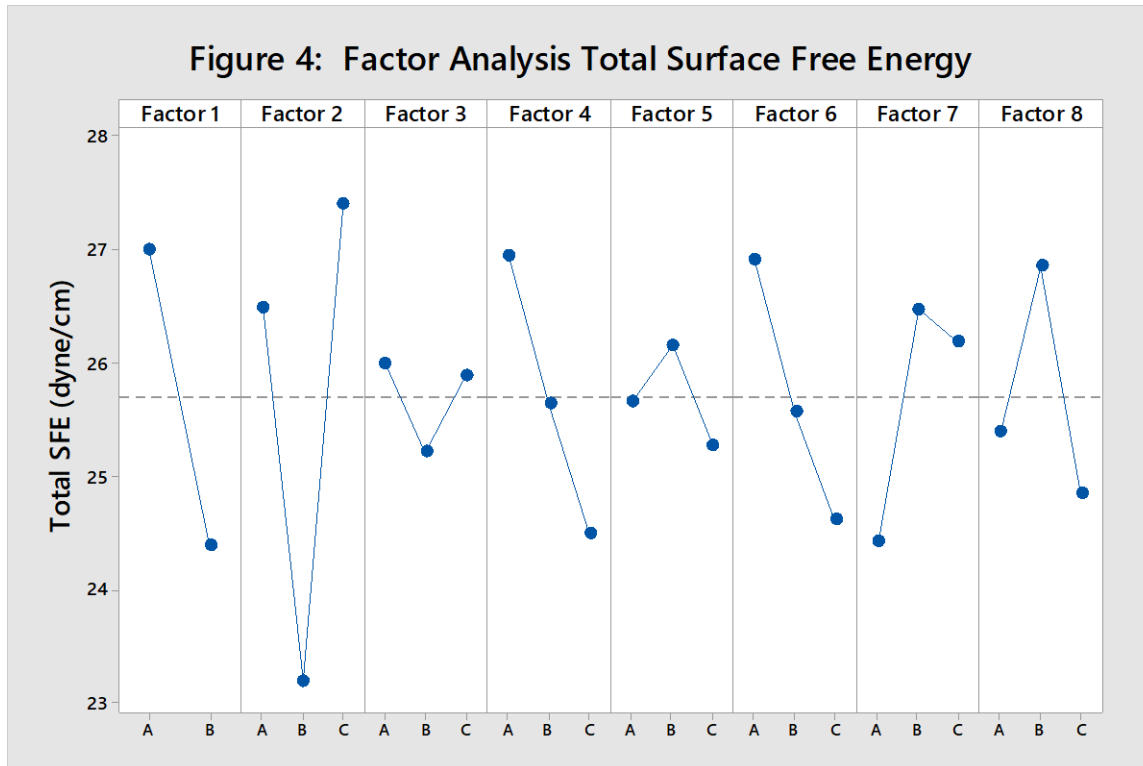
The data showed the likelihood of producing pattern materials with significantly higher surface energy than typically seen in production. Lowering the surface energy appeared to be more challenging from this data. Likewise, Figure 2 shows a similar effect with the dispersive surface energy results.



Surprisingly, the polar component of the total surface energy measurement proved difficult to move in any meaningful way, as shown in Figure 3. This is despite efforts to purposely introduce more polar components to the system.

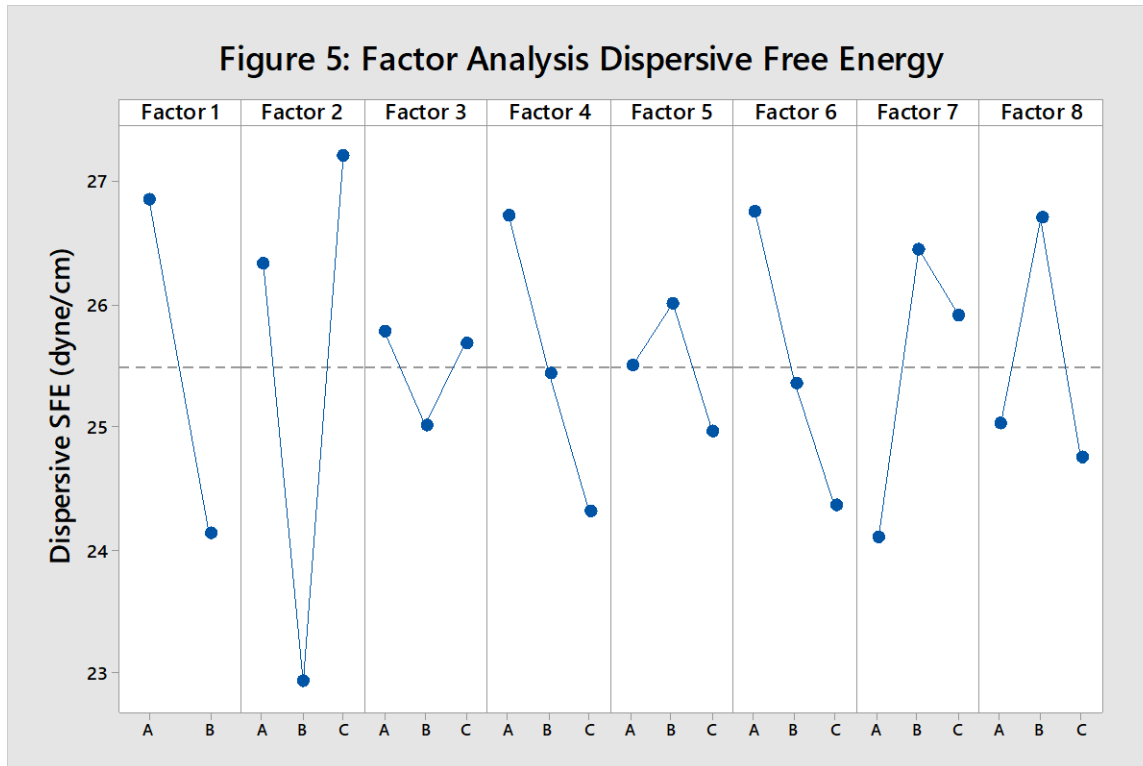


Factorial analysis of the total surface energy of the 18 experimental factors showed the following effects, Figure 4. The actual factor (i.e. resin type, filler type, etc.) were removed to protect proprietary information.



The total surface energy was most affected by Factors 1, 2, 4, 6, and 7. Interestingly, Factor 4 was previously found to be an important factor in an investigation with a customer regarding prime coat wetting and surface energy measurements.

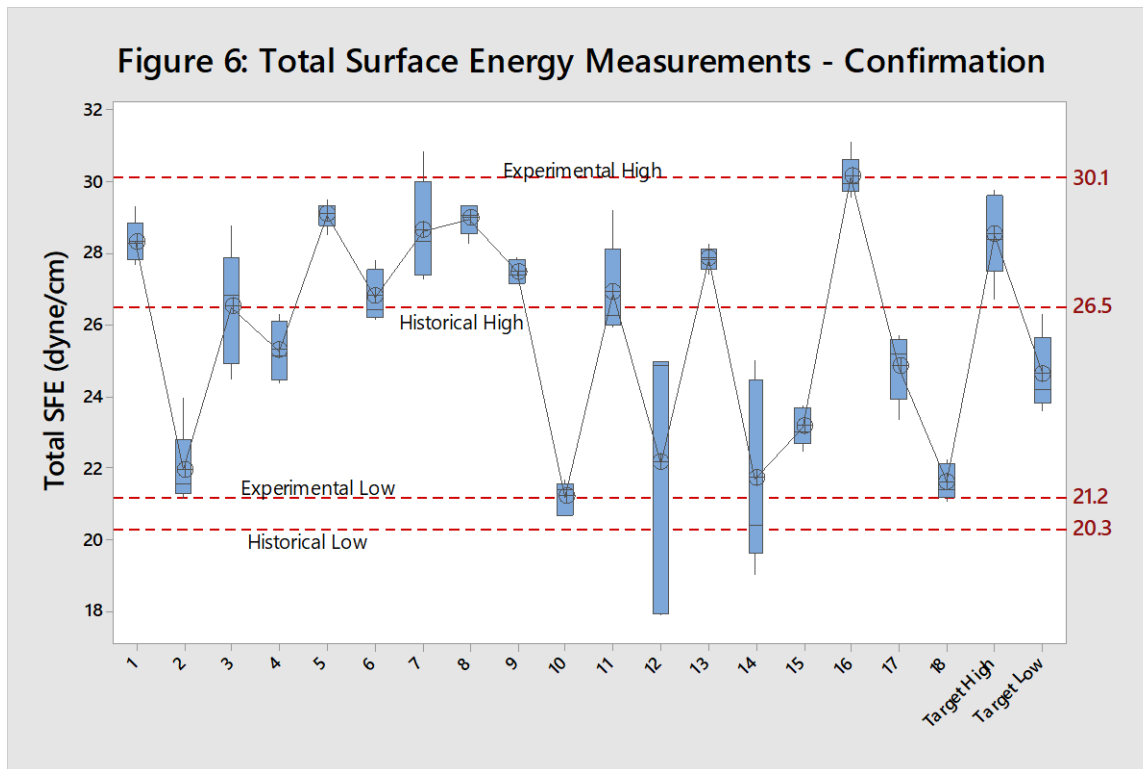
Not surprisingly, the results for the dispersive energy analysis closely mimicked that of the total surface energy, Figure 5. Again, the most influential factors were Factors 1, 2, 4, 6, and 7.



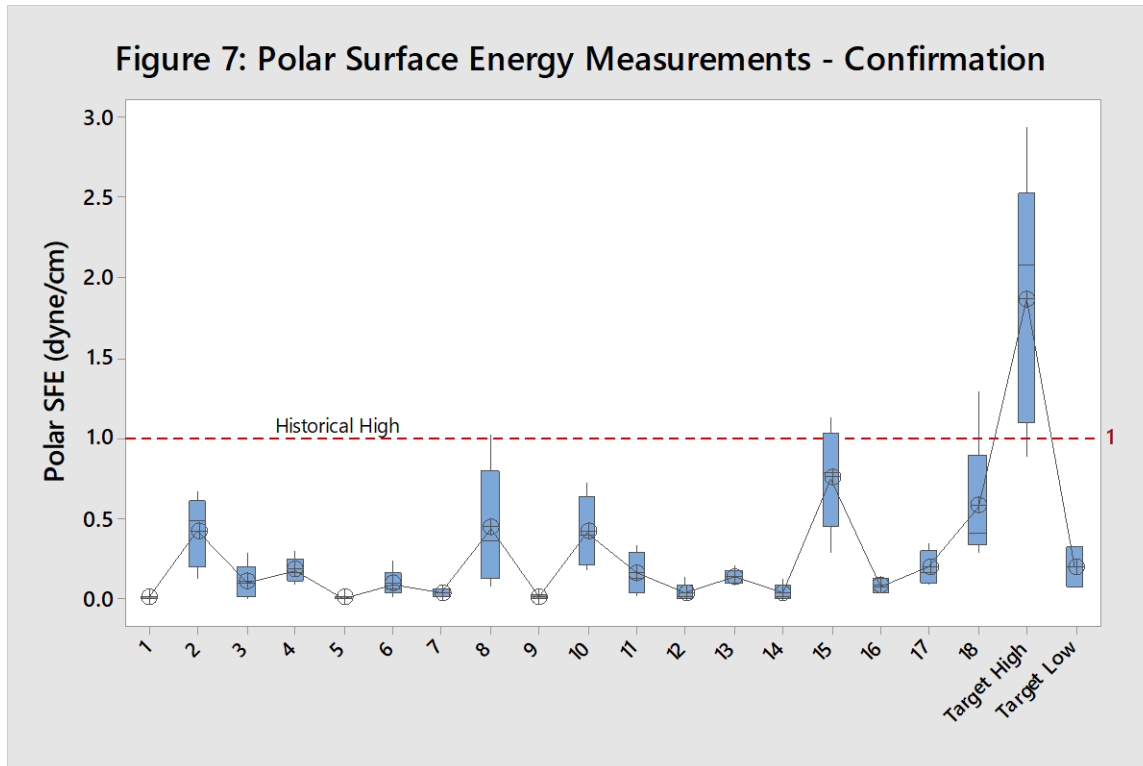
Examining the results for the polar component of surface energy revealed quite different results, Figure 6. As expected, the magnitude of the output was two order of magnitude less than that observed for the dispersive energy. The factors that influenced the polar results appeared different from those affecting the dispersive results, with Factors 2, 5, 7, and 8 being the most influential. As can be seen, Factors 2 and 7 were impactful across both measurements. Interestingly, factors specifically chosen for their polar effects did not result in significant shifts in the polar surface energy measurements.

### **Confirmation Study**

Some of the 18 experimental batches resulted in blends with properties not conducive to pattern making or the investment casting process. Therefore, the surface energy results were analyzed in conjunction with other typical investment casting pattern material characteristics to produce usable pattern materials with targeted high and low total surface energy measurements.



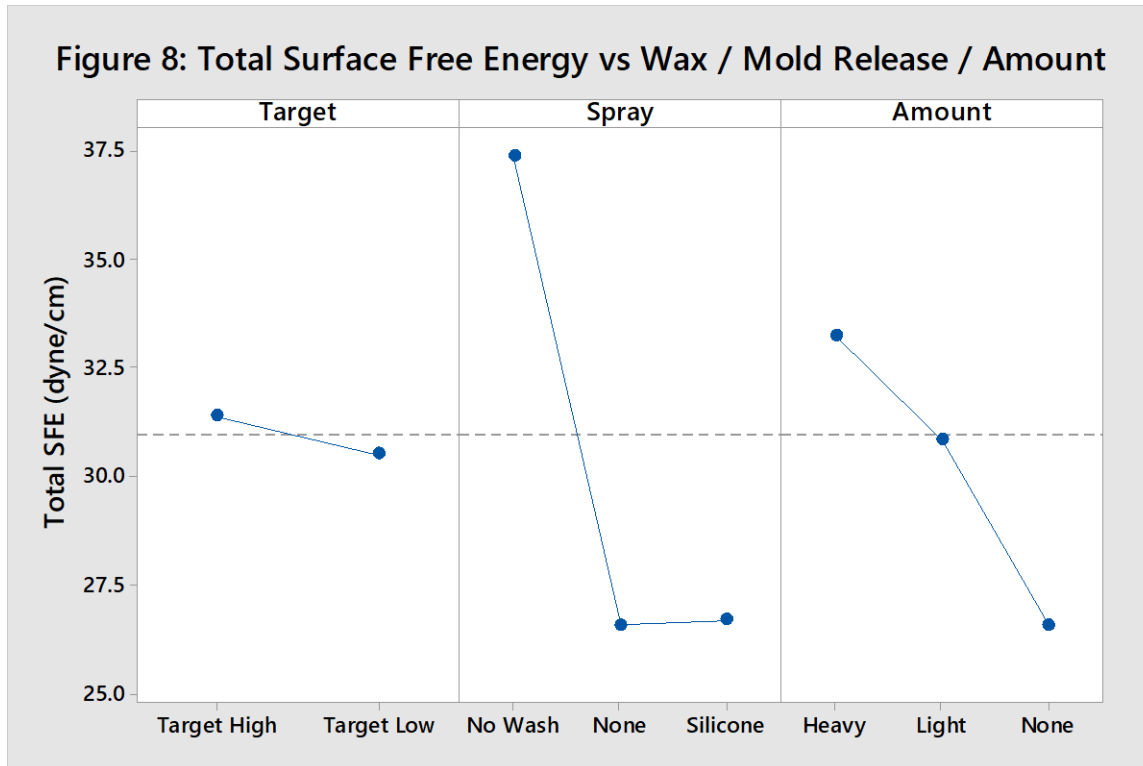
The formulation targeting a total surface energy was predicted to have a total surface energy value of 31.1 dyne/cm. The measured value was 28.5 dyne/cm; higher than seen in traditional pattern materials, but just short of prediction, Figure 6. Surprisingly, the polar component of the surface energy was the portion much higher than observed previously, Figure 7.



The targeted low surface energy also did not come in as low as predicted. The predicted value was 19.5 dyne/cm, with a measured result of 24.6 dyne/cm. These results indicate needed improvement in the reliability of the measurement system to improve the predictability of the results. The experimentation was suspended on multiple occasions due to mechanical issues and/or lack of test material (diiodomethane).

### **Mold Release Study**

A subsequent study with the targeted high and low surface energy formulations included the use of mold release agents in the sample preparation. This included silicone and silicone-free release agents and amount of release agent used. The results were quite surprising, Figure 8. The use of a non-silicone, “No Wash”, mold release agent significantly increased the surface free energy of the samples.



The No-Wash mold release showed a dramatic effect on the surface energy of the samples. The use of a common silicone-based release showed almost no effect.

Figure 9: Dispersive Surface Energy vs Wax / Mold Release / Amount

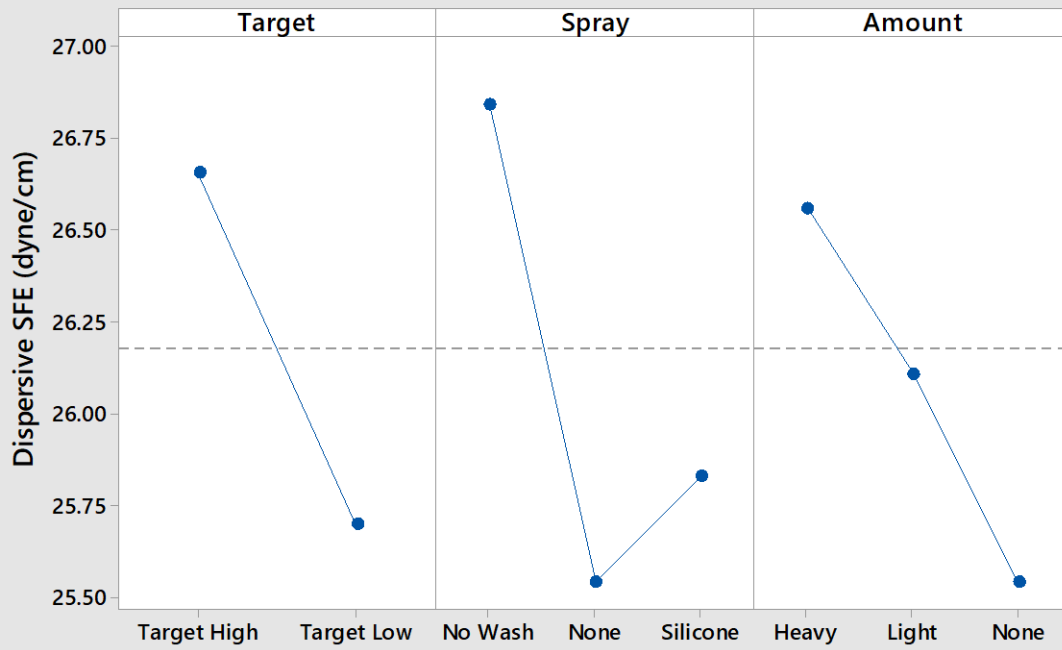
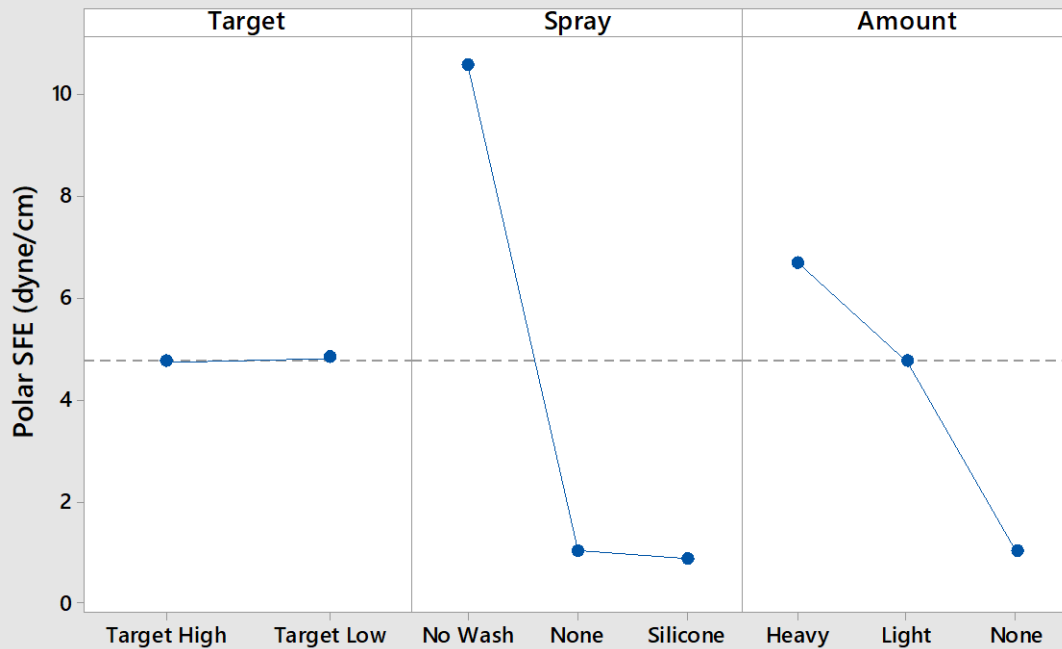
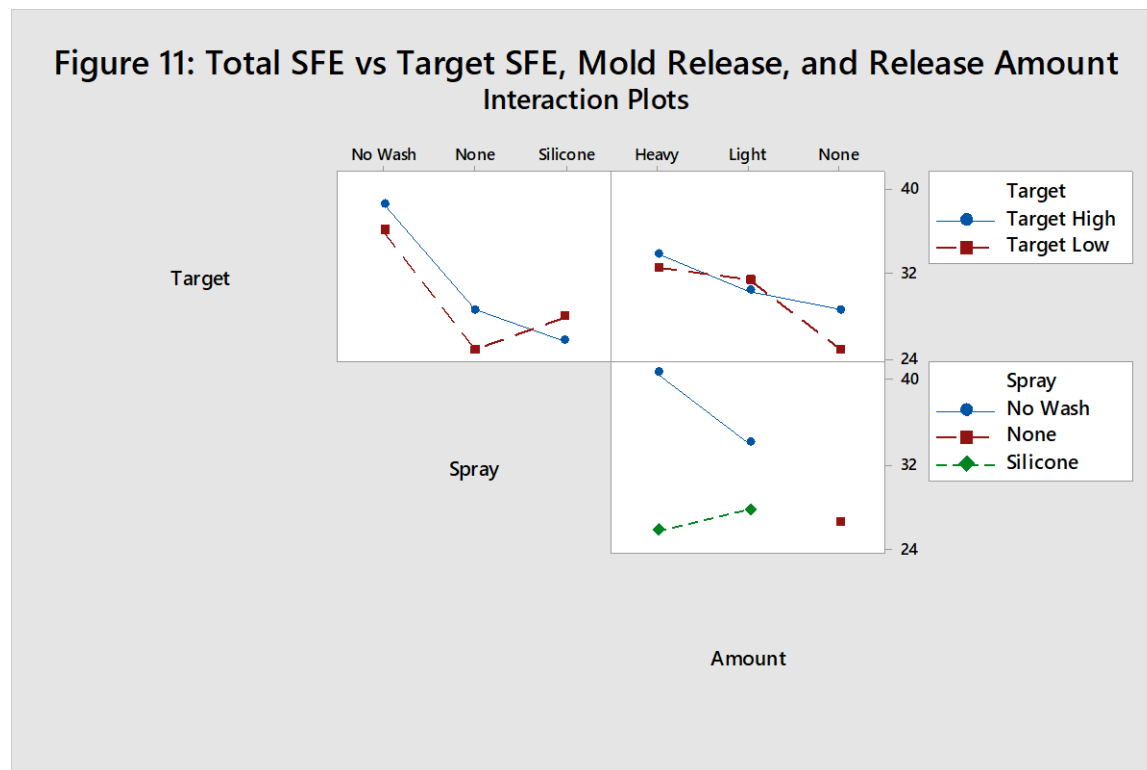


Figure 10: Polar Surface Energy vs Wax / Mold Release / Amount



Examining the effects of the mold release on the dispersive and polar components, Figures 9 & 10, provided some additional insight. The No Wash treatment increase was largely due to the effect it has on the polar component. This, perhaps, provides insight into the chemical make-up of the material. The silicone, conversely mainly influenced the dispersive, van der Waals, effects. This may explain the difference in the reaction with the wax substrate.

Figure 11 attempts to cover the interactions between the wax substrate material, the mold release material, and the amount of release.



## Conclusions and Ongoing Work

The L18 designed experiment indicated the surface free energy of the blended wax can be moved within a limited range with common pattern material ingredients. However, the methodology and practice of the test needs to be improved to increase the precision of the test and the ability to predict the result.

The potential of mold release and other materials introduced post molding appear to have a profound effect on the resultant surface energy, and potential interaction with the prime coat. This is the focus of the work being done by Ruger Pinetree castings.

Paramelt will continue to improve on the surface energy testing and the extent possible to influence the pattern material properties and subsequent investment processing.

#### Acknowledgements:

Thanks to Mark Oles and Ruger Pinetree Castings for assistance and guidance in this work and allowing Paramelt to join his study.

Thanks to the Mark van Gelder and the Paramelt Heerhugowaard for assistance in sample preparation and completing the surface energy measurements.

Thanks to the Paramelt Muskegon laboratory team for producing and testing all the experimental batches in a timely manner.



# **INVESTMENT CASTING INSTITUTE**

## **Investment Castings with Unique Levitation Melting Technology FastCast**

Dr. Sergejs Spitans  
ALD Vacuum Technologies

## **68<sup>TH</sup> TECHNICAL CONFERENCE & EXPO 2021**

Paper № 16

# Investment Castings with Unique Levitation Melting Technology FastCast

*Sergejs Spitans<sup>1</sup>, Christian Bauer<sup>1</sup>, Henrik Franz<sup>1</sup>, Björn Sehring<sup>1</sup>, Egbert Baake<sup>2</sup>*

<sup>1</sup>ALD Vacuum Technologies GmbH, Otto-von-Guericke-Platz 1, 63457 Hanau, Germany

<sup>2</sup> Institute of Electrotechnology at Leibniz University Hannover, Wilhelm-Busch-Straße 4, 30167 Hannover, Germany

## Abstract

A novel method for the large-scale crucible-less levitation melting of metals is developed. Numerical simulation has been used to verify the new method and to design ALD's pilot investment casting furnace – called *FastCast*. It allows levitation melting of various reactive metals and alloys up to 500 g with high purity, short cycle times and large adjustable superheating up to 250 C followed by single-batch defect-free casting with >98% of material landing in the mould.

This report gives an update on features and recent technical achievements of the *FastCast* demonstrator which is in operation at ALD.

## Introduction

Crucible-less levitation melting and single-batch casting of Ti- or Ni-based alloys (e. g. for turbocharger impellers or turbine blades up to 500 g) has many advantages over multi-batch castings obtained with ceramic- or cold-crucible induction furnaces.

First of all, electromagnetic (EM) levitation prevents contamination of the melt with the crucible material and results in a superior and predefined quality of alloy. Heat losses from the liquid metal are reduced and limited to radiation and evaporation that permits fast melting and much higher overheating. Due to the small melt-cast cycle time the process retains productivity comparable with conventional multi-batch investment castings, while simpler design of the crucible-less furnace and utilization of smaller single-batch molds have economic benefits. Apart from that, single-batch casting breaks down the statistical nature of a single product quality in case of a multi-piece casting, advances production to the “one-piece-flow” concept and meets requirements for process digitalization.

However, in conventional axisymmetric levitation melting (Figure 1, a), already known since 1920's [1], [2] the Lorentz force vanishes on the symmetry axis (Figure 1, b) and the melt leakage is counteracted only by the melt surface tension. Therefore, only small molten metal samples up to 50 g can be levitated in conventional way and industrial needs for the scale-up remain unsatisfied [3].

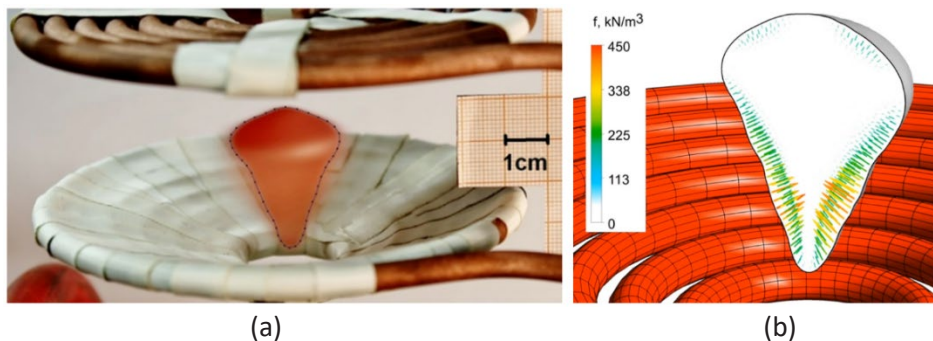


**Figure 1.** Classical levitation melting of Aluminum sample (20 g) in experiment (a) and simulation illustrating the lack of Lorentz forces at the axis of the sample (b) [4]

A novel method for the levitation melting of metals is developed to transfer the advantages of levitation melting from laboratory/R&D applications into industrial field. Numerical simulation has been used to verify the new method and to design a pilot investment casting furnace – called

*FastCast* – capable of contact-less melting and single-batch casting of Ti- and Ni-based alloys up to 500 g.

This report gives an update on features and recent technical achievements of the *FastCast* demonstrator which is in operation at ALD.

### The novel method for the large-scale levitation melting

The new method applies two EM fields of different AC frequencies, whose field lines in the absence of a charge are horizontal and orthogonal in order to exert Lorentz forces also at the axis of the levitated sample. Therefore, the charge weight can be increased and the charge can be drip- and leakage-free melted. The method for EM levitation melting in horizontal fields has been validated by a series of experiments with small samples up to 40 g [5].

Today, numerical modelling is undisputedly a very powerful tool that can lead the development of new products from idea to final implementation in a significantly shorter time and cost-effectively way. For the further development and scale-up of the novel levitation melting method a numerical model for simulation of turbulent flow and free surface dynamics of liquid metal in EM fields has been developed and extensively verified [6].

Computation of EM induced flow and free surface dynamics is ensured by means of coupling between:

- EM field and Lorentz force recalculation in *ANSYS*,
- Volume of Fluid (VOF) Large Eddy Simulation (LES) of a two-phase turbulent flow in *FLUENT* and
- a free surface shape filtering and reconstruction in *CFD-Post*.

At first, using the developed numerical model, the two-frequency EM levitation melting furnace has been designed to meet conditions for the levitation melting of 500 g of Aluminum. Following the simulation-aided design the melting unit has been built. Experiments revealed excellent agreement with modelling results and proved the potential of the scale-up of the novel method [7].

ALD has decided to apply the “state-of-the-art” levitation melting system and advantages of the novel method for real investment castings with ceramic moulds and launched the *FastCast* project. Using numerical modelling the melting unit was further optimised (Figure 2) since the levitation melting of Ti- and Ni-alloys faced advanced requirements.

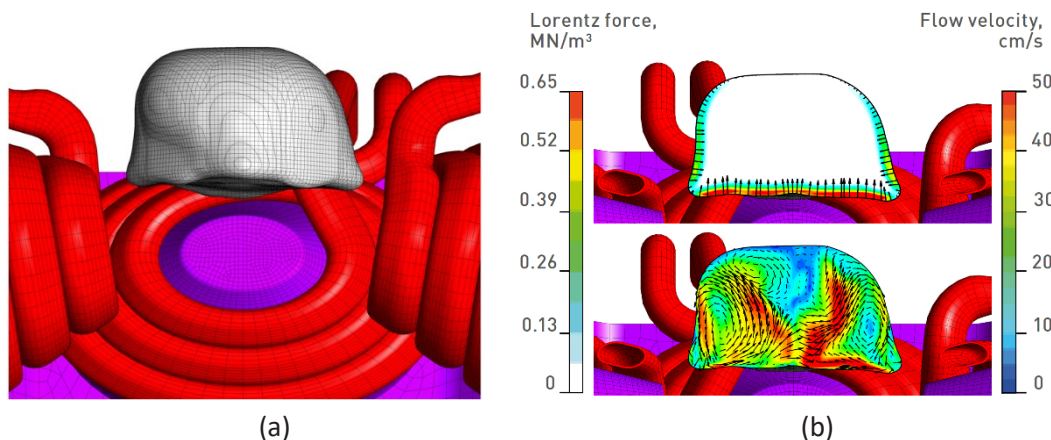


**Figure 2.** Optimized design of the novel two-frequency levitation melting unit (side view) based on modelling of the free surface shape of molten TiAl (500 g) levitating in the gap between coil pairs (a). Enhanced Lorentz force confinement and turbulent flow on the vertical cross-section of the melt (b)

Combining all gathered simulation results and ALD’s expertise in investment casting, a demonstrator furnace has been designed and manufactured (Figure 3). *FastCast* overcomes boundaries of conventional casting methods with ceramic or copper crucibles. Levitating in a magnetic field, the metal has no contact with or contamination from other materials during heating up to the moment when the melt enters the mold. No crucible or other refractories are used.



**Figure 3.** The *FastCast* levitation melting and casting furnace in operation at ALD

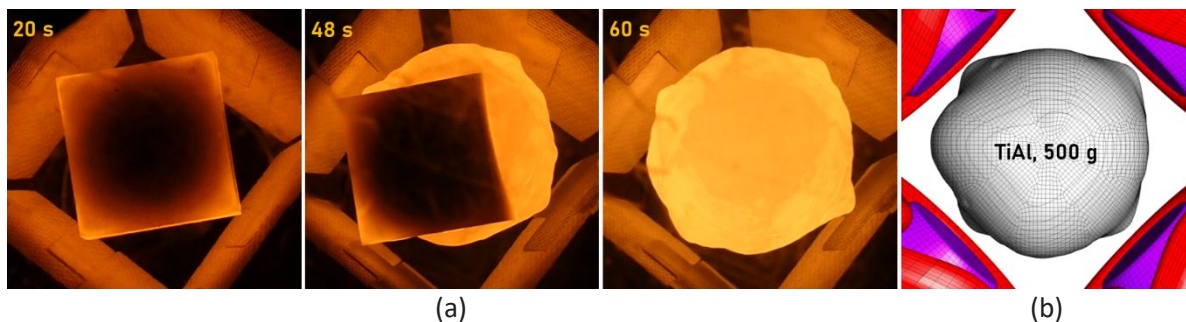


**Figure 4.** Top view of the levitation melting of a single TiAl sample (500 g/1.1 lbs) in experiment (a) and the free surface shape of fully molten sample predicted by the 3D numerical model (b)

#### **New investment casting furnace - *FastCast***

The *FastCast* furnace consists of three chambers for melting, casting and mould preheating (Figure 3). The melting chamber contains the “heart” of the plant - a levitation melting unit. The melting unit has two pairs of induction coils that generate horizontal and orthogonal EM fields of two different frequencies required for sample levitation in the gap between the coils. The EM field is enhanced by the water-cooled ferrite poles and looped through the outer ferrite ring.

The casting chamber is located right below the melting chamber and contains a mould manipulator arm, a mould table and a melt position sensor that synchronizes downward movement of the mould with the free-falling molten metal charge.

And the mould preheating furnace, in which up to 10 shell moulds can be stored and brought to temperature up to 1200 C.

The *FastCast* prototype has been assembled at the ALD in the beginning of 2019 and has been used for research and optimization of the process parameters. It is designed for demonstration of 10 consecutive casting cycles.

#### **Levitation melting and casting cycle**

The cycle starts as the mould manipulator arm takes an empty preheated mould from the mould preheating chamber and places it on the mould table. The table locks the mould and drives it up in the „ready for casting” position right below the melting unit.

Shortly after the melting starts as the lower end of the vertically oriented electrode (or a single sample) is immersed in the region of two-frequency horizontal and orthogonal EM fields by the electrode feeder. EM fields rapidly melt up to 500 g/1.1 lbs of material from the tip of the electrode and simultaneously confine the liquid metal in a levitation condition. Meanwhile, Lorentz forces contribute to intensive stirring and a great level of melt homogenization. The electrode is moved up and detached levitated melt is rapidly superheated (Figure 4). After that the EM field below the melt is reduced and the melt falls down under gravity in the awaiting preheated mould.

Synchronized with the free-falling melt position, the mould is accelerated vertically down following the pre-programmed recipe to catch the melt and full-stop at the bottom of the casting chamber. Such mould movement reduces relative velocity between the falling melt and the mould at the moment of the contact, avoids splashing and ensures smooth filling. On top of that, the mould table allows for the centrifugal casting at <800 rpm.

As the filling process is accomplished, the manipulator arm stores the filled mould and takes the next preheated mould for repeating of the cycle.

For instance, TiAl investment casting of different turbocharger wheels revealed good surface quality and defect-free filling of thin (0.5 mm) and detailed sections (Figure 5).

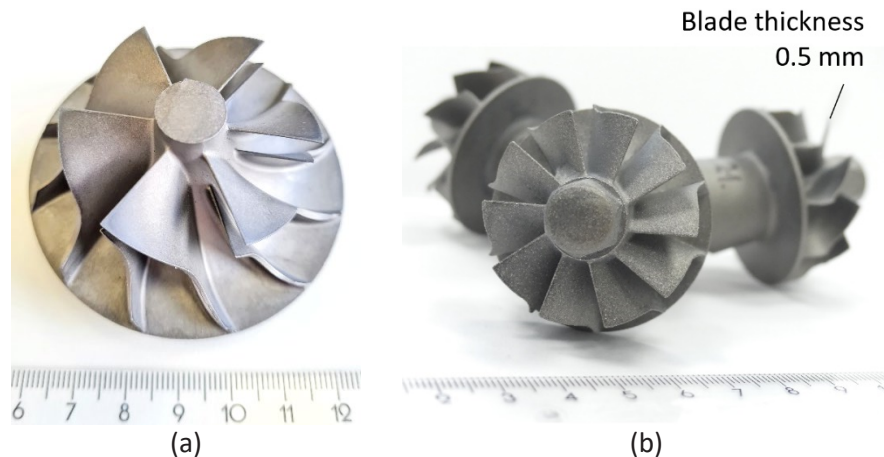


**Figure 5.** TiAl turbocharger wheels (<500 g) casted using the *FastCast* furnace

All degrees of freedom are fully programmable to ensure the perfect tuning and optimization of the melting & casting cycle. On top of that, protection measures were thoroughly engineered to keep the production conditions safe and stable.

Melting and casting system design and process features are fully protected by 5 issued international patents.

#### **The *FastCast* furnace highlights**

- Levitation melting and casting process scaled-up for industrial applications → up to 500 g/1.1 lbs of Ti-alloys and up to 400 g/0.9 lbs of Ni-base alloys for mass production of turbocharger wheels, turbine blades and other castings
  - Crucible-less contact-free melting → excellent purity and no material loss in the skull
  - Adjustable and reproducible superheat up to 250 C → no cold-runners and superb filling of the complex mould geometries even at lower mould preheating temperatures
  - Short melting time of 60 ... 100 s → high productivity
  - Advanced casting system: free-falling melt is caught by the downward accelerated mould → smooth filling, no splashing and >98% of material yield
  - Pre-alloyed electrodes or single samples as melting material
  - Melting at inert gas (Ar) atmosphere (down to 30 mbar) → no gas entrapment
  - Melting power up to 180 kW
  - High reproducibility of castings

- The furnace concept can be integrated into production lines with fully automated and continuous material flow

### Conclusions

*FastCast* overcomes boundaries of conventional casting methods with ceramic or copper crucibles. Fully levitating in magnetic field, the metal has no contact with or contamination from other materials during heating up to the moment when the melt enters the mold. No crucible or other refractories are used.

In this way, the melt achieves much higher superheat (compared to copper crucibles) that improves mold filling, especially for parts with fine and complex shapes. Moreover, much higher superheat of the melt can compensate the reduced preheating temperature of the mold.

Main applications are parts up to 500 g/1.1 lbs made of Ti-based alloys (or other reactive materials) or superalloys for automotive, aviation or general industries.

The *FastCast* concept is designed for short cycle times. The furnace can be integrated into fully automated production system – in terms of material flow and production management – to establish an inline casting route from shell making to a final cast part.

### Literature

- [1] O. Muck, German Patent 422004. (October 30, 1923).
- [2] E. Okress et al., "Electromagnetic Levitation of Solid and Molten Metals" J. Appl. Phys., 23 (1952), 545-552.
- [3] V. Bojarevics et al., "Magnetic levitation of large liquid volume" Magnetohydrodynamics, 46/4 (2010), 317-329.
- [4] S. Spitans et al., "Numerical modelling of free surface dynamics of melt in an alternate electromagnetic field. Part II: conventional electromagnetic levitation" Metall. Mater. Trans. B, 47/1 (2015), 522-536.
- [5] O. Pesteanu et al., "Two-frequency method and devices for drip- and leakage-free electromagnetic levitation melting" Heat processing, vol. 2, (2012), 96-100.
- [6] S. Spitans et al., "Numerical Modelling of Free Surface Dynamics of Melt in an Alternate Electromagnetic Field. Part I. Implementation and verification of model" Met. Mat. Trans. B, 44/3, (2013), 593-605.
- [7] S. Spitans et al., "Large scale levitation melting and casting of Titanium alloys" Magnetohydrodynamics, 53/4, (2017), 633-641.



# **INVESTMENT CASTING INSTITUTE**

## **Analysis of Thermal Distortion Data to Detect Issues in Investment Shell Materials**

Dr. Sam Ramrattan  
Western Michigan University

### **68<sup>TH</sup> TECHNICAL CONFERENCE & EXPO 2021**

Paper № 17

# Analysis of Thermal Distortion Data to Detect Issues in Investment Shell Materials

S. Ramrattan

Western Michigan University  
Department of Engineering Design, Manufacturing and Management Systems  
Kalamazoo, MI 49008

## ABSTRACT

The investment casting industry has been using shell molding materials to produce complex near-net-shape parts for centuries. Over this time period, significant process advancements have been made to increase overall quality, especially in the areas of melt and fill. Despite these advancements, the investment casting industry still suffers from high scrap/rejection rates due to shell quality. A key contributor to these less than ideal yield levels is the inability to effectively monitor and/or evaluate the quality of incoming shell molding materials.

Research has shown that measurements from a disc-shaped specimen tests are better able to discriminate between investment shell materials. The tests that were considered in this recent research were thermal distortion test (TDT) and retained strength. The results suggest that measurement taken from these tests may provide the means to effectively monitor incoming shell materials.

This paper investigates the capability of monitoring investment shell materials using TDT data. TDT is considered for this purpose because it provides coupled thermal-mechanical investment shell behavior at head pressures and temperatures that can be adjusted to represent actual casting scenarios. TDT produces a high-dimensional dataset, as it produces multiple time-series profiles, referred to as thermal distortion curves (TDCs). In order to effectively use this dataset, this paper will incorporate multivariate statistical analysis for process monitoring. The proposed monitoring scheme will be demonstrated through a case-study. The ability of the proposed monitoring scheme to detect the shift from one investment shell system to another will be determined.

## INTRODUCTION

This paper follows up on the paper “Thermal Distortion Testing of an Investment Shell Material” presented at 62nd ICI Technical Conference & Expo.<sup>1</sup> The current work deals with the newly adopted AFS standardize thermal distortion testing (TDT) technique that can detect subtle shifts in investment casting shell materials.<sup>1,2</sup>

In order to produce near-net shape investment castings, there is a need to produce investment shells of consistent dimensional accuracy, and hence an investment casting satisfying the increasingly tighter tolerances of the customer.<sup>1</sup> Investing shell materials might undergo dimensional changes when subjected to heat and mechanical stresses from molten metal. The thermal expansion, distortion, and pyrolysis, which occur during casting, are directly related to the type of materials being used. If the shell material, for example, is not stable there is a tendency for the wall to dilate when molten metal is poured into a shell.<sup>1</sup>

The dimensional accuracy, strength, and hardness of cores and shells at room temperature bear little or no relationship to performance during casting. To produce castings of consistent quality, it is therefore important to know the thermo-mechanical properties of refractory materials used in manufacturing molds/shells and cores.<sup>3</sup>

The purpose of this research was to identify an improved process control tool for measuring possible thermal distortion in investment shell materials. The tool is called a Thermal Distortion Tester (TDT) that was developed at Western Michigan University (WMU). The TDT was used to heat and load a disc-shaped specimen allowing longitudinal and radial displacements as well as thermal gradients to be measured in real time. An intent of this paper is to present and discuss the basic functions of the TDT, along with actual test results and the reasoning behind some its features.

### Need and Purpose

In today's market, with changing requirements for investment castings, tolerances have been constantly shrinking. More emphasis is placed on reducing shell distortion during pouring of castings. Investment casting wall dimension are continually being reduced for weight reduction. This increases the need for consistent dimensional integrity in shell and core materials. To adhere to these standards, it is important to be able to predict the general characteristics of the shell-making process.<sup>1</sup>

The use of refractory ceramic media for investment shells, all have one common goal: near-net shape investment castings. The goal is to produce shells of consistent dimensional accuracy, and hence a casting satisfying the increasingly tighter tolerances of the customer. This is true where a complex thin wall investment casting must mate in close tolerance with various other manufactured components and sub-assemblies. Investment cast components are designed to assuage in close tolerance. A goal of the investment casting engineer is to produce shells of consistent dimensional accuracy, and hence a casting satisfying the ever tighter tolerances of industry.

Today, the investment shell production achieves this aim successfully through de-waxing. Investment shells undergo considerable dimensional changes when subjected to heat and mechanical stresses from molten metal. The thermal expansion and distortion, which the core and shell undergoes during casting is directly related to the quality of shell wall material in use. If the shell metal interface is not stable there is a tendency for the shell wall to dilate when molten metal is poured into a shell. The expansion of the shell and potential defect can happen even before the alloy is at the interface. Regrettably,

A TDT developed at WMU for examining the thermo-mechanical properties of foundry mold and core material can be used for testing investment materials.<sup>4</sup> It is simple to operate and the test piece is a “disc-shape” specimen. The tester can be used for process control to establish a materials control program and for dimensional control of investment shell materials. The tester is another tool that would aid in identifying correct amounts of investment matrix and stucco, and for predicting the behavior of the investment casting shell material in thermo-mechanical application.

### **Thermal Distortion Testing (TDT)**

The AFS standardized TDT device was designed and built to study the effects of heat and pressure on foundry sand binder systems.<sup>2,3</sup> The TDT uses disc-shaped specimens to compare mold/shell composite materials. In this study 50 mm dia. by 8 mm thick disc-shaped investment shell specimens will be investigated. The temperature is variable and can be set to represent molten metal superheat temperatures for the specific alloy for which the investment shell material experience.<sup>2,3</sup> TDT also has the capability to reproduce the pressures that the mold or shell, will experience from molten metal filling and solidification in a mold. The duration of the test is set to mimic the time it takes for the metal skin to form at the shell mold wall interface.

After thermal exposure, the test specimen is still intact allowing determination of additional valuable information that can be gained after thermal exposure. Apart from the measurement of retained strength

in the shell, a visual analysis for cracks can be performed. In the casting process loss in strength and cracks in the shell could result in defects. Further, a weight loss measurement that relates to the presence of moisture and organics in the shell is determined. The TDT was designed with the intent of obtaining deformation data for any refractory molding system (natural or synthetic).

Operating conditions of the TDT device are like those where a mass of molten metal is pressing against the mold wall in a pseudo-static state. The load (metallostatic head pressure) on the specimen is held constant, and the specimen can only move into or out of the face of the hot surface depending on whether the specimen is expanding or plastically deforming. Holding the temperature of the hot surface constant during testing simulates the mass of molten metal. The description and functionality of the device is accomplished through the use of several instruments, controllers, mechanical devices, and a computer that is used to record data. Details are provide in standards and technical publications.<sup>1-3</sup> Ultimately, the output data from the TDT is a pair of thermal distortion curves (TDC) showing the longitudinal (axial) and radial displacements of the specimens.

## **METHODOLOGY**

The testing procedure consisted of four major steps: 1) specimen production, 2) TDT, 3) casting trial, and 4) observation and data analysis.

Note: All specimens were prepared and tested in laboratory conditions. Ambient conditions were controlled: temperature at  $20 \pm 1^\circ\text{C}$  and relative humidity at  $50 \pm 2\%$ .

### **Specimen Production**

Disc-shaped specimens 50 mm dia. by 8 mm thick were hole-sawed and ground from cured investment shell materials obtained from industry (Fig. 1). Specimens were fabricated from two investment shell materials identifies as X and Y (8 each). The first coat materials used in the investment shell development were the only differences between the specimens studied.

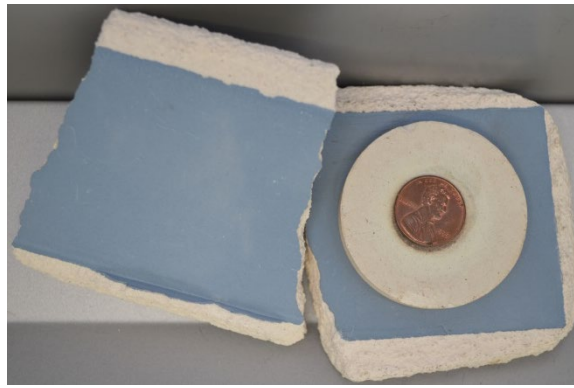


**Figure 1: Disc-shaped specimen from investment shell**

## TDT

**Procedure:** Standardized procedure AFS 3350-18-S was followed in operating the TDT (Fig. 2). Prior to running a test electrical power was switched on and test load was set to 4.5 N to represent head pressure. The temperature control was adjusted to 1000°C (1832°F) which represented the metal/investment shell mold interfacial temperature.<sup>1,2</sup>

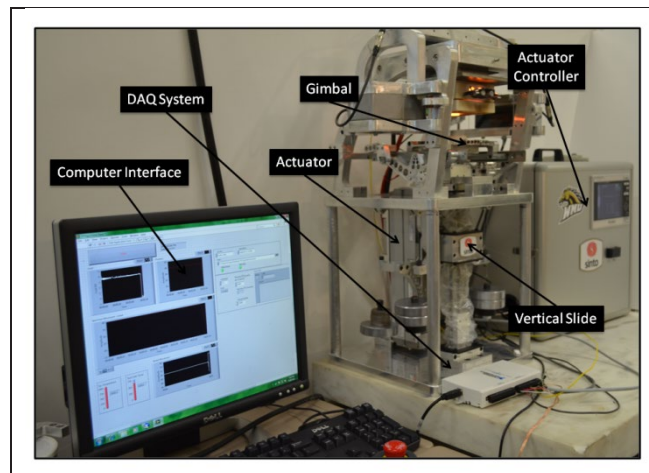


**Figure 2: TDT**

**Change in mass:** Prior to TDT each specimen was weighed. Following TDT the surface of the specimen was blown with 0.07 MPa (10 psi) air pressure to remove any loose particles. The specimens were then again weighed, and the percent change in mass was recorded. Next, the specimens were visually examined for signs of discolorations and thermally induced cracking where contact was made with the hot surface. Losses at this heat-affected-zone (HAZ) may be indicative of the tendency to produce defects. The percent change in mass was calculated based upon the difference between the weight before and after as a percent of the weight before. All percent changes in mass values represent the percentage of weight lost.

## Casting Trial

The casting trial used a 3D printed furan mold that was fabricated at University of Iowa (UNI) Metal Casting Center and shipped to WMU Metal Casting Laboratory. This was followed by mold preparation, melting, pouring, and shakeout.

**Preparation Molds:** A model of the gating system of the mold is shown in Fig. 3. The procedure consisted of the following steps:

- i. The 3D printed furan mold was fitted with a 23 cm (9 in.) diameter steel pouring sleeve and a filter for constant head-pressure and fill velocity.
- ii. The doughnut-mold gating cavities were refractory coated to protect specimen interface from loose sand and to prevent them from cracking.
- iii. Each mold contained core-prints where no positional effects exist in the casting. This approach allows possible variation in casting quality to be attributed to only disc-shaped specimens.

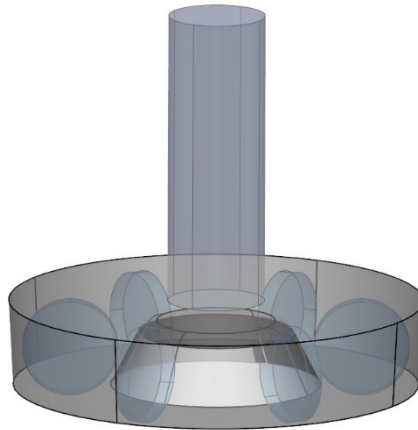


**Figure 3. Transparent view of doughnut-shaped model with disc-shaped specimens.**

**Melting and Pouring:** The mold was poured with the locations of disc-shaped specimens being randomized. The disc-shaped specimens were arranged symmetrically in the mold so that no positional effects on the casting should be present. This approach allowed possible variations in as-cast surface quality to be attributed to just the specimens. A 36 kg heat of 4130 was melted using a 3 kHz induction furnace. Initial charge consisted of 1010 punchings, FeCr, and FeMo. Once the melt achieved 1650°C, FeSi, FeMn, and graphite were added. A final addition of Al shot occurred in the ladle for full deoxidation. The tap temperature was 1730°C. The mold was manually poured at 1600°C where the average pouring time was ~12 sec. The steel was delivered through a direct pouring sleeve fitted with a ceramic foam filter. The mold was poured to a 23 cm (9 in.) head-height. The metal chemistry is shown in Table 1.

**Table 1. Steel chemistry (% mass)**

C	Si	Mn	P	S	Cr	Mo	Al
0.296	0.225	0.456	0.007	0.011	0.847	0.213	0.102

**Observations:**

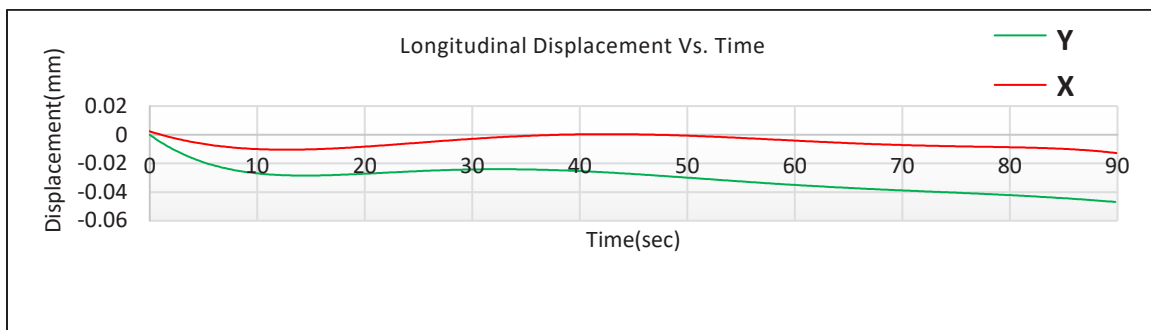
The steel casting was allowed to solidify prior to shakeout. After casting shakeout, the casting was sectioned near the disc-shape specimen/steel interface. These surfaces were then examined using a 3D Macroscope.<sup>4</sup> Images of the specimen/metal interfaces were captured and surface roughness was measured to infer surface texture.

**RESULTS AND DISCUSSION**

TDT results and images from the specimen/steel casting interface are presented in Table 2. In addition, TDC plots related to the investment shell specimens are presented in Fig. 4 and 5.

**TDT**

The TDCs for both specimens tested showed thermo-mechanical changes in the investment shell composite at elevated temperature. The longitudinal distortion curve for specimen X was stable with little undulation, but specimen Y showed greater plastic displacement (Fig. 4). The radial distortion clearly indicated greater expansion for specimen Y compared to specimen X (Fig. 5). Table 2 ascertains that the investment shell material used in specimen Y showed greater thermal distortion compared to that of specimen X.

**Figure 4. Longitudinal TDC for investment shell specimens X and Y**

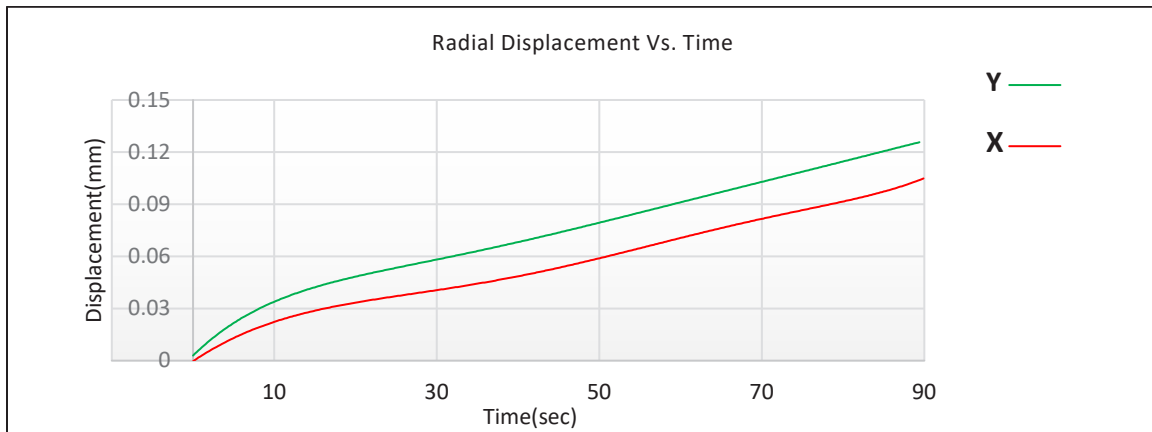


**Figure 5. Radial TDC for investment shell specimens X and Y**

Table 2 compares the thermo-mechanical and physical properties between the investment shell material. Specimen X had the greater toughness, retained strength, and superior abrasion resistance compared to specimen Y. Moreover, specimen X was more thermally stable compared to specimen Y.

**Table 2. Thermo-Mechanical and Physical Properties of the Investment Shell Specimens**

Investment Shell	Specimen 50 mm dia. by 8 mm thick	
First Coat Material	X	Y
S/f. Rough. Sa $\mu$ in. ( $\mu$ m)	236 (6)	708 (18)
Casting Trial Picture 4130 Steel 1600 °C at 10 cm Head →		
Specimen Wt. (g)	45.2	43.1
Impact Strength (J)	1.94	1.54
Retained Str. (J)	1.52	1.31
Abrasion (% Loss)	0.2	0.8
Long. Disp. (mm*sec)	0.032	0.056
Radial Disp. (mm*sec)	0.101	0.125
Total Disp. (mm*sec)	0.133	0.181

The hot surface/specimen interface showed a slight discoloration, the discoloration was not present on the opposite side of the specimen; and the amount of discoloration was not significantly different between the specimen types. There were no heat induced surface cracks found on specimens after elevated temperature exposure and the percent change in mass values was negligible.

### **As-Cast Surface Condition**

The as-cast surface condition of specimen X was clean and there were materials adhering at the shell/alloy interface on specimen Y. Thus, the as-cast surface roughness was superior for specimen X. The as-cast surfaces for specimens X and Y are pictured and the surface roughness measurements are provided in Table 2.

### **LIMITATIONS**

The effects of metal chemistry on an investment shell were not considered in this study. The work in this paper characterizes just two investment shell composite material at an elevated temperature and pressure representative of a small steel casting.

### **CONCLUSIONS AND RECOMMENDATIONS**

The TDT was able to capture and record data which showed significant thermo-mechanical difference between the two investment shell specimens investigated. Additionally, a casting trial supported the TDT data in showing significant difference in as-cast surface roughness between the specimens studied.

The TDT along with the novel casting trial provides a new approach to qualify an investment shell composite. Various investment casting shell formulations can be readily compared using the TDT and investigated for thermos-mechanical stability. It is recommended that investment shell specimens be developed from industrial formulations for TDT. Furthermore, an improved technique is needed for the production of disc-shaped investment shell specimens.

### **ACKNOWLEDGMENTS**

The author thanks the UNI Metal Casting Center for 3D printing the mold used in this study and gratefully acknowledge technical support from Metal Casting Laboratory at WMU.

## REFERENCES

1. Ramrattan, S., “Thermal Distortion Testing of an Investment Shell Material” Investment Casting Institute 62nd Technical Conference & Expo, Schaumburg, IL, October 20, 2015.
2. AFS Mold and Core Test Handbook, 5th. Edition, AFS (2020).
3. Oman, A. J., S. N. Ramrattan, and M. J. Keil, “Next Generation Thermal Distortion Tester”, *AFS Transactions*, 13-1454 (2013).
4. Keyence 3D Macroscope  
[\[https://video.search.yahoo.com/yhs/search;\\_ylt=A0LEVj2VAUhaQOYAgzoPxQt.;\\_ylu=X3oDMTEybGpyazhvBGnVbG8DYmYxBHBvcwMxBHZ0aWQDQjQ5ODFfMQRzZWMDc2M-?p=keyence+3d+macroscope&fr=yhs-adk-adk\\_sbnt&hspar=adk&hsimp=yhs-adk\\_sbnt#id=4&vid=da6aae46c1a6b6b1194c31bae9f1af85&action=view\]](https://video.search.yahoo.com/yhs/search;_ylt=A0LEVj2VAUhaQOYAgzoPxQt.;_ylu=X3oDMTEybGpyazhvBGnVbG8DYmYxBHBvcwMxBHZ0aWQDQjQ5ODFfMQRzZWMDc2M-?p=keyence+3d+macroscope&fr=yhs-adk-adk_sbnt&hspar=adk&hsimp=yhs-adk_sbnt#id=4&vid=da6aae46c1a6b6b1194c31bae9f1af85&action=view)

# **INVESTMENT CASTING INSTITUTE**

## **Enhancing Porosity & Permeability of Ceramic Shells for Investment Casting through Pre-wetting**

Noel O'Sullivan  
University of Limerick

### **68<sup>TH</sup> TECHNICAL CONFERENCE & EXPO 2021**

Paper No 18

# Influence of porosity on permeability post primary layer of ceramic shells

N. O' Sullivan, J. Mooney, D. Tanner

## Abstract

This paper discusses the influence of porosity generated through pre-wetting of the ceramic shell to enhance permeability while analysing flexural strength. Pre-wetting consists predominately of an aqueous silica solution binder that improves inter-coat bonding. Porosity is developed in the ceramic shell where the pre-wetting is applied due to the evaporation of the aqueous phase. As porosity increases, both green and fired strength reduced on average by 8.7–15.6% and 18.7–28.5%, respectively, whereas hot strength is increased by 20–25%. Permeability increased by a factor of two when pre-wetting was applied between intermediate coatings, where mercury intrusion porosimetry displayed a stepwise increase in intrusion volume in the high-pressure regime. X-ray microtomography coupled with pore network modelling provided an observation of the porosity and differential pressure through the multilayer structures. Gas adsorption revealed the presence of micropores through the alpha-s method when bi-layers of pre-wetting solution were applied.

## 1. Introduction

Pre-wetting is generally used between the primary and secondary coating to enhance bonding between the multilayer structures. This enhances the rheology of the slurry in intricate geometries and reduces the occurrence of delamination or defects such as excess metal. Shell thickness is reduced through this method although higher viscosity secondary slurries may be used to provide sufficient slurry coverage of the primary layer. The use of fine powders in the primary and secondary slurry produce a high packing density that impedes gas flow during casting [1]; de-waxing [2]; and drying of the ceramic shell [3, 4]. However, pre-wetting enhances porosity through evaporation of the aqueous phase, while non-pre-wetting yields an ordered laminar structure [5].

The modulus of rupture (MOR) and permeability are intrinsic properties of the ceramic shell to prevent cracking during the shell build process [6] and to transmit fluid flow [7], respectively. The latter is influenced by the particle size distribution of both the refractory stucco and the matrix filler material and porosity of the multilayer shell [8, 9]. Research has

shown that increasing porosity is reported to reduce the green MOR by approximately 5–20% [10].

The aim of this paper is to compare the effects of non-pre-wetting and pre-wetting on shell strength and permeability post primary layer of a conventional (zircon-alumina) non-fibre shell, without the use of a seal coat. Furthermore, pre-wetting between two secondary coatings with one less back-up coat was employed to reduce the frequency of replenishing the tertiary slurry. The hypothesis is to generate porosity through evaporation of the liquid phase and create a pathway for enhanced fluid flow, where smaller pores may contribute less to a reduced MOR.

## 2. Experimental Procedures

The location of the pre-wetting solution in the multi-layer shell is predominantly employed between the first three coatings. Four ceramic shell-types were prepared and described from here on as shell-types S1, S2, S3, and S4, see Figure 1. Both the total number of layers and the size of the stuccoing material remained constant throughout the different shell build processes. The size of the refractory filler material (RFM) is normalized due to the proprietary shell. The effects of a non-pre-wetting shell were evaluated (shell-type S1), one layer of pre-wetting (shell-type S2), bi-layers of pre-wetting (shell-type S3), while also introducing pre-wetting between two secondary coatings (shell-type S4) with one less tertiary slurry coating.

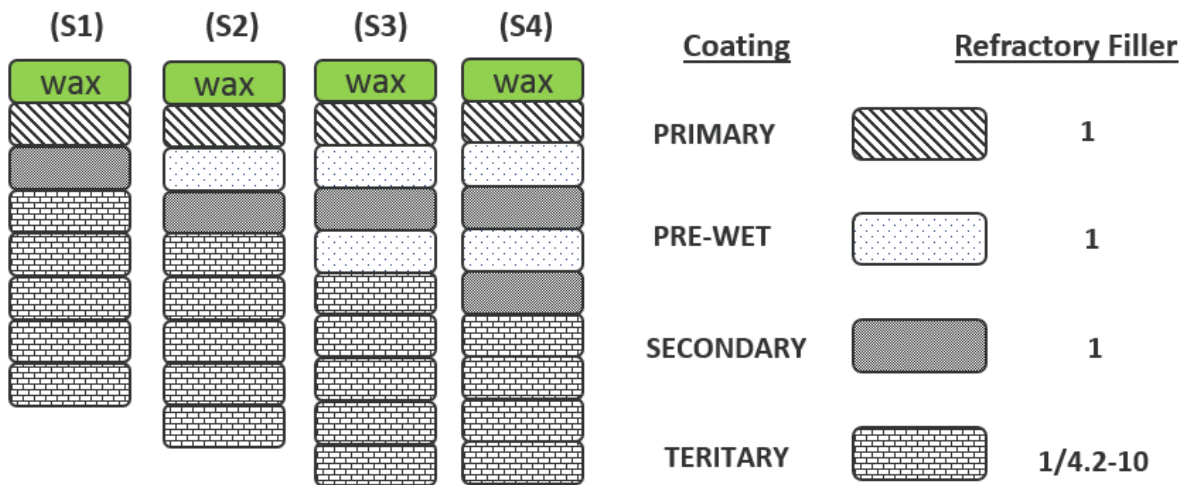


Figure 1, Schematic of the various shell build process

The pre-wetting solution consists of a colloidal silica binder in rotating tanks where a low quantity of zircon refractory filler is added. Preliminary investigations (not shown) showed with no refractory filler present leeching of the pre-wetting solution back to the wax surface was encountered, while excess powder produced insufficient coverage in intricate geometries. Therefore, the solids content of the pre-wetting solution was measured at 30% and is the standard set by the manufacturing process and can range from 29–32% over its pot-life.

### 2.1 *Modulus of Rupture*

Three-point flexural testing was carried out on six specimens of sample length of 70 mm using a Lloyd LRX tensile tester fitted with a calibrated load cell of 2.5 kN. The width and thickness varied from approximately 22–25 mm and 4.5–6.7 mm, respectively. The loading rate was 1 mm/min with an outer fixture span of 50 mm, where samples were measured with a micrometre post fracture. Green strength was analysed at room temperature before the samples were heated to 1000°C for hot strength determination while residual fired strength was determined when samples had cooled back to room temperature.

### 2.2 *Permeability Analysis*

Six specimens of each shell-type were prepared and permeability testing at high temperature (1000°C) was accomplished. Permeability of the specimens was determined in accordance with BS 1902-10.2, and derived from Darcy's law that defines fluid flow through refractory materials at high temperatures. The samples were fired to approximately 350°C over 1.5 hours to vaporize the ping-pong ball. Subsequently, the specimens are fired at 3°C/min up to 1000°C and then held at constant temperature for a further hour prior to testing.

### 2.3 *Mercury Intrusion Porosimetry*

Mercury intrusion porosimetry (MIP) was used to analyse the pore structure morphology of cylindrical fired specimens (O.D. 22 mm and 6 mm in height), using the Quantachrome Poremaster 60 in scanning mode. Samples were prepared as per Figure 1, where one sample from each of the shell build processes was analyzed by Anton Paar, Florida, U.S.A. MIP is described by the Washburn equation, and based on the non-wetting properties of mercury, where pore radius is a function of surface tension (485 mN/m), contact angle (140°) [11], and the applied capillary pressure [12]. The median diameter ( $D_m$ ) is obtained at the 50<sup>th</sup> percentile of the intrusion volume curve, whereas the mean pore diameter ( $D_{av}$ ) is calculated by  $4V_t/S_t$ , where ( $S_t$ ) denotes the total surface area and the total volume of mercury intruded is described by ( $V_t$ ) [13].

### 2.4 *Gas Adsorption*

Gas adsorption measurements by the static volumetric method were performed using the Quantachrome Autosorb AS-1 with nitrogen as the adsorbent at 77.35 K. Fired ceramic specimens (25 mm x 25 mm x 6 mm) were prepared as per Figure 1, and ground with a laboratory grade pestle and mortar. Samples contained a mixture of irregular shape material, where large clusters were screened out with using an AFS 16-mesh size aperture. Surface area

was determined using the Brunauer-Emmett-Teller (BET) method, where the monolayer corresponds to the inflection point in the BET adsorption isotherm where the amount of gas required for monolayer coverage indicates the total surface area. Pore size distributions were analyzed by the Barrett-Joyner-Halenda (BJH) method and based on the Kelvin equation under the assumption of cylindrical pores. Analysis of microporosity was conducted using the alpha-s method to determine the micropore volume [14].

### 2.5 *X-ray Microtomography*

The morphology of fired ceramic specimens was analyzed by x-ray microtomography (XMT) employing the Versa XRM-500. A monochromatic fan beam with a voltage rating of 140 kV is rotated through various angles and attaining 4000 exposures at a spatial resolution of 6.3  $\mu\text{m}$  per pixel. Samples were prepared into beam type geometries (6 mm x 6 mm x 50 mm). The attenuation of the x-ray beam is directly proportional to the density, thickness and composition of the material, where dark areas indicate pore void space [15]. This produces high contrast greyscale images to isolate and quantify pore space from the refractory material [16].

### 2.6 *Pore Network Modelling*

A set of techniques developed by Gostick [17] was applied to segment pores from the XMT images and extract a pore network model from a bulk volume of shell material. The algorithm extracted the pore space of the shell material in the form of a matrix of pores and throats, known as the pore network modelling (PNM) approach [18]. In PNM, the flow rate or pressure drop between two neighbouring locations is represented by the Hagen-Poiseuille equation and dictated by the medium's permeability coefficient based on Darcy's law. This approach allows the user to identify areas of low and high differential pressures through the ceramic shell material.

## 3. Results

### 3.1 *Modulus of Rupture*

Figure 2 shows the MOR results for the shell-types at the three different test conditions. The use of a single-layer of pre-wetting solution (shell-type S2) reduced green strength by approximately 8.7%, compared to the non-prewetting shell (S1). Similarly, utilizing bilayers of pre-wetting solution (shell-type S3 and S4) reduced green strength on average by approximately 14.4% and 15.6%, respectively. The use of bi-layers of pre-wetting provided a reduced bulk density and therefore resulting in a reduced MOR in the green state. Green

strength is reported as a function of silica concentration, alkali content, surface area [19, 20], and may be enhanced with polymeric additions to the silica solution binder [8] or fibres to the tertiary coatings [21-23].

In contrast, high temperature testing exhibited how hot strength increased as bilayers of pre-wetting solution were employed. Both shell-types S3 and S4 increased in hot strength by approximately 25% and 20% on average compared to the non-pre-wetting shell (S1). The use of a monolayer of pre-wetting solution increased hot strength of shell-type S2 by approximately 8% compared to shell-type S1. The increase in hot strength may be attributed to the increase in porosity that alters the diffusion process during firing and subsequently may restrict the propagation of cracks, and is affected by particle size distribution, packing density, pore size distribution, and aggregation of particles [24].

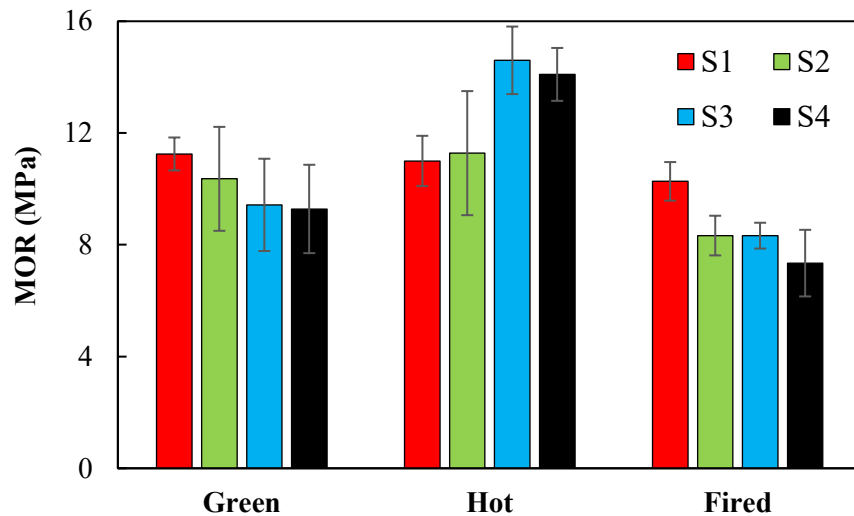


Figure 2, MOR results of shell-types with standard deviation of six samples shown

Residual fired strength reduced on average by 18.8%, 18.7%, and 28.5% for shell-types S2, S3, and S4, respectively, compared to the shell-type S1. A reduction in fired strength of 18.7–28.5% on average was observed when a pre-wetting solution was applied, where research displayed similar results of 18–30% [25]. The reduction in fired strength is reported from excess silica particles preventing particles from sintering at points of contact within the silica network [19], or irregular shaped pores creating inhomogeneities thus leading to differential densification [26].

### 3.2 Permeability

Figure 3 displays the results of permeability for six samples for each of the shell-types described in Figure 1, and accomplished over a range of gas flow rates ranging from 10–70 cm<sup>3</sup>/min. The highest permeability constant is characteristic to shell-type S4, employing

bilayers of pre-wetting solution between intermediate coatings and revealed a two-fold increase in permeability at the higher flow rate of 70 cm<sup>3</sup>/min.

At a lower flow rate of 40 cm<sup>3</sup>/min, permeability of shell-type S4 increased by approximately 56%, 47%, and 39% compared to shell type S1, S2, and S3, respectively. The non-pre-wetted shell (S1) exhibited the lowest permeable structure, whereas shell-type S2 and S3 exhibited an increase of approximately 16.1% and 27.6%, respectively, at a flow rate of 40 cm<sup>3</sup>/min. Shell-type S3 produced no significant increase in permeability compared to shell-type S4 even though both shells contained bilayers of pre-wetting. This suggests that an increase of porosity is observed without an increase in permeability.

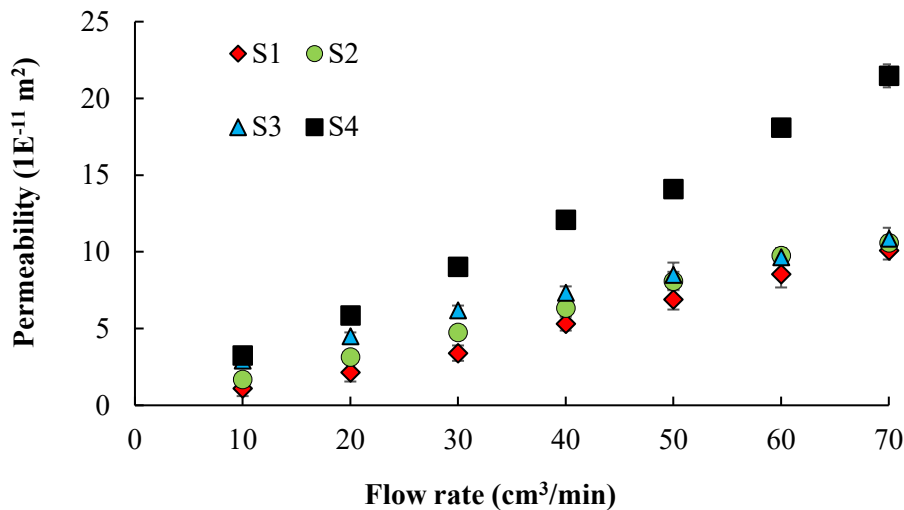


Figure 3, Permeability constant versus flow rate of six samples with standard error shown

### 3.3 Porosity

The increase in porosity of the shell-types described is observed by XMT methods coupled with imaging analysis, see Figure 4. Large clusters of pores are encountered in the first three coatings of the macrostructure of shell-type S3 compared to shell-type S4. Shell-type S3 also displays large volumes of pores encountered at the primary facecoat, possibly due to adsorption of moisture to previous coatings [27]. However, applying pre-wetting between two intermediate coatings post primary layer provided a two-fold increase in permeability, where permeability increases exponentially as open porosity is developed [24] and should increase with distance from the molten metal [28]. Porosity of the non-pre-wetted shell (S1) displayed the least presence of pores close to the primary layer, while the monolayer of pre-wetting shell-type S2 displayed an increase in porosity.

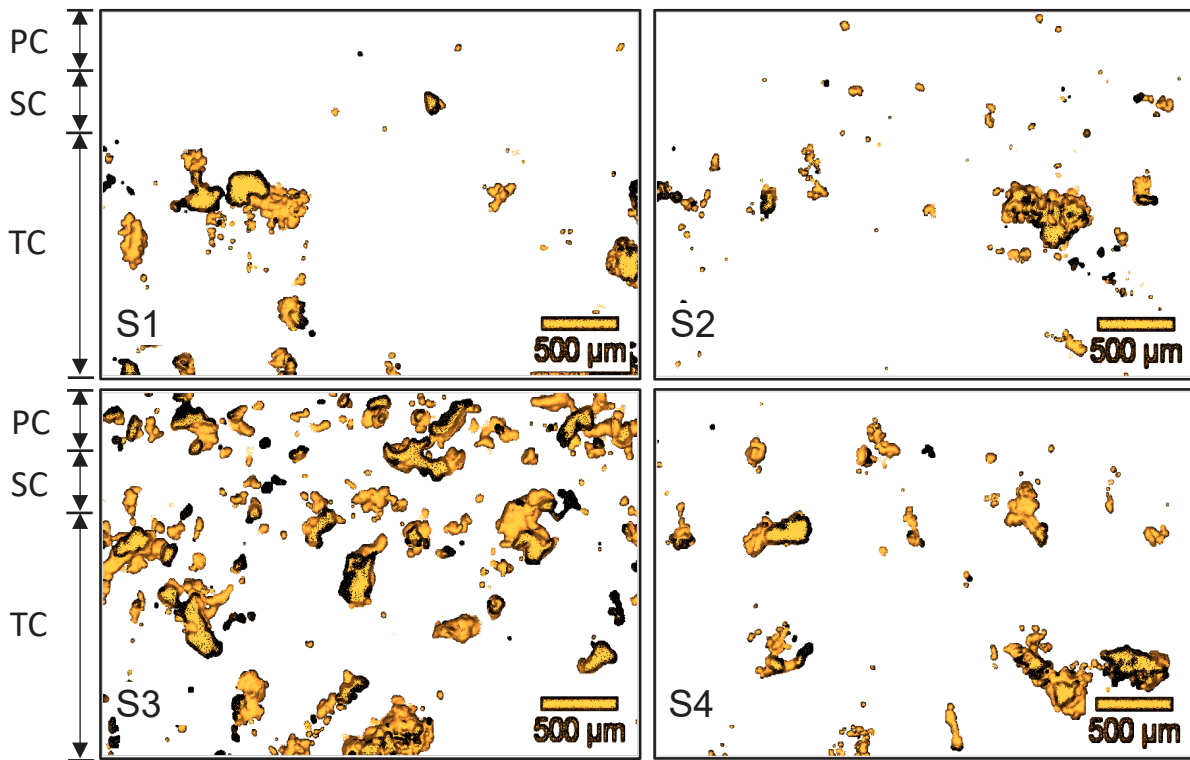


Figure 4, Image J (Version 1.52) analysis of 3D body volume of isolated pores in the first three coatings of the ceramic shell types from a stack of XMT 2D images, PC—primary coating, SC—secondary coating, and TC—tertiary coating

### 3.4 Mercury Intrusion Porosimetry

Figure 5 describes the volume of mercury intruded and extruded for the ceramic shell specimens, where the volume is normalized by sample weight. As mercury is intruded, large pores are initially filled at low pressures, where pressure is converted to a pore diameter on the x-axis through the Washburn equation [12, 29]. Interparticle voids are prevalent due to the packing density and the wide particle size distribution of the refractory stucco material. As pressure increases, smaller pores and deep narrow cavities are filled before a plateau is observed at an equivalent pore diameter of approximately 0.2–0.8  $\mu\text{m}$  for all samples.

The intrusion curves exhibited constant slopes that can be clearly seen in Figure 5b, corresponding to a pore diameter of approximately 0.7–5  $\mu\text{m}$ . This is recognized as constant filling (intruded volume) or emptying (extruded volume) of the volume of mercury in pores as pressure is increased or decreased. Shell-type S4 exhibited a noticeable step change in intrusion volume corresponding to a diameter of 3.5–10 nm in the high pressure region (137–275 MPa), while the extrusion curve exhibited no retraction in extrusion volume, see Figure 5d.

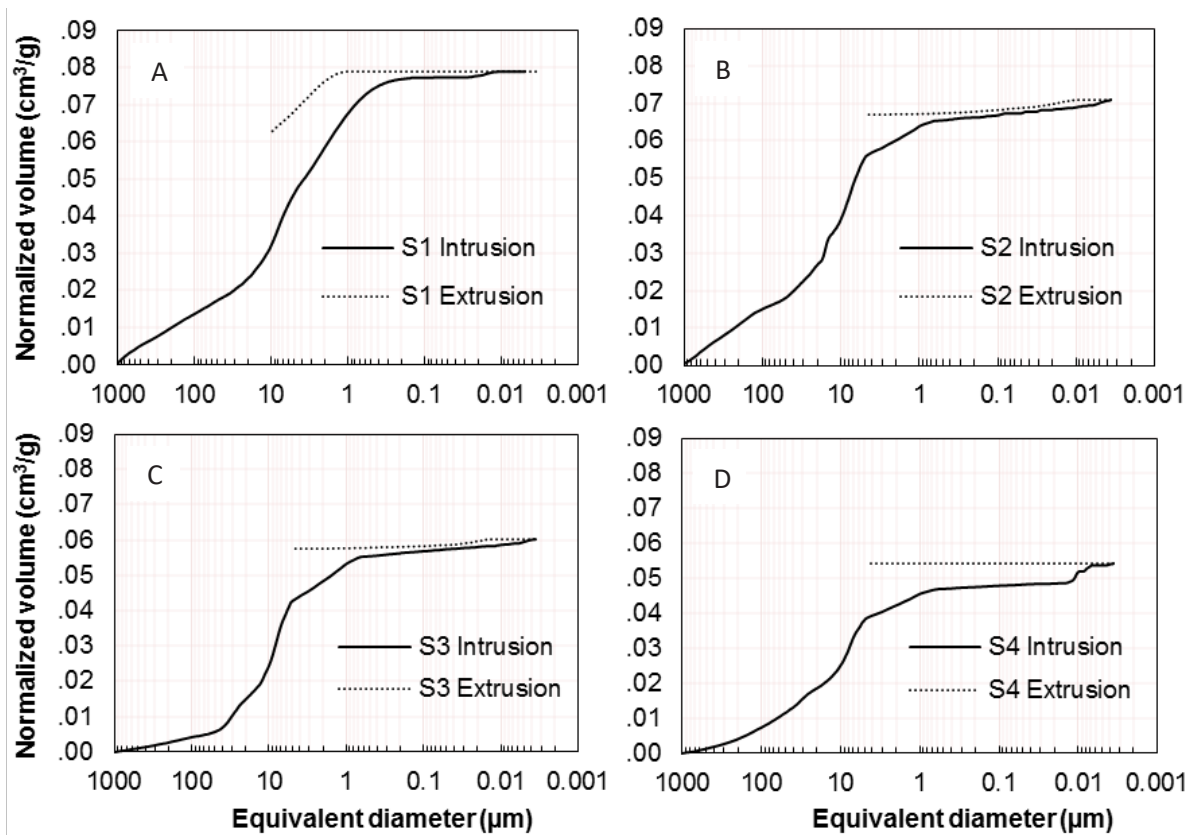


Figure 5, MIP intrusion/extrusion curves with equivalent pore diameter ranging from 0.0035–1000  $\mu\text{m}$

The hysteresis of shell-type S2 and S3 produced only a slight retraction of volume of approximately 5.5% and 4.5%, respectively, however, sample S1 exhibited a 21% reduction of volume extruded. The hysteresis of shell-type S1 possess a wide and constant range of pores and attributed to a needle type porous structure [30].

Table 3 shows the results of open porosity,  $\varepsilon$ , as a volume fraction of mercury intruded, where maximum porosity occurs at the smallest pore diameter or the highest applied pressures. Porosity was also analyzed through bulk density,  $\rho_b$ , and skeletal density,  $\rho_s$ , measurements, where the latter is a close approximation of the true density and measured post intrusion, where  $\varepsilon = (1 - \rho_b/\rho_s) \times 100$ . The true density,  $\rho_t$ , revealed a maximum deviation of 6.7% compared to skeletal density and may replace the skeletal density as a comparison of porosity [31]. As pointed out by [32] the analysis of surface area,  $S_t$ , by mercury intrusion ranges from 10–100  $\text{m}^2/\text{g}$  and only attainable in the intrusion curve, where results exhibited a maximum surface area of 2.7  $\text{m}^2/\text{g}$ . Shell-type S4 exhibited the lowest average diameter,  $D_{av}$ , and the highest surface area corresponding to smaller pores, thus indicating the generation of mesopores in the lower regime.

Table 1, Microstructure parameters obtained from MIP of fired ceramic shells-types

Sample	$\varepsilon$ %	$S_t$ m <sup>2</sup> /g	$D_{av}$ μm	$\rho_b$ g/cm <sup>3</sup>	$\rho_s$ g/cm <sup>3</sup>	$\rho_t$ g/cm <sup>3</sup>
S1	23.72	0.527	0.598	3.001	3.762	4.022
S2	20.78	1.899	0.149	2.936	3.691	3.954
S3	18.20	1.606	0.151	3.012	3.671	3.908
S4	18.11	2.721	0.079	3.336	4.038	3.906

Figure 6 represents the pore volume distribution attained by the derivative of the intruded volume with respect to the equivalent throat diameter and displayed as a logarithmic distribution. Results portrayed wide multimodal distributions between an equivalent pore diameter of 0.1–1000 μm with narrow and bimodal peaks occurring in the 5–8 μm region for all samples. Both shell-types S1 and S2 portrayed higher intruded volumes ranging from 30–1000 μm and exhibited the presence of larger pores.

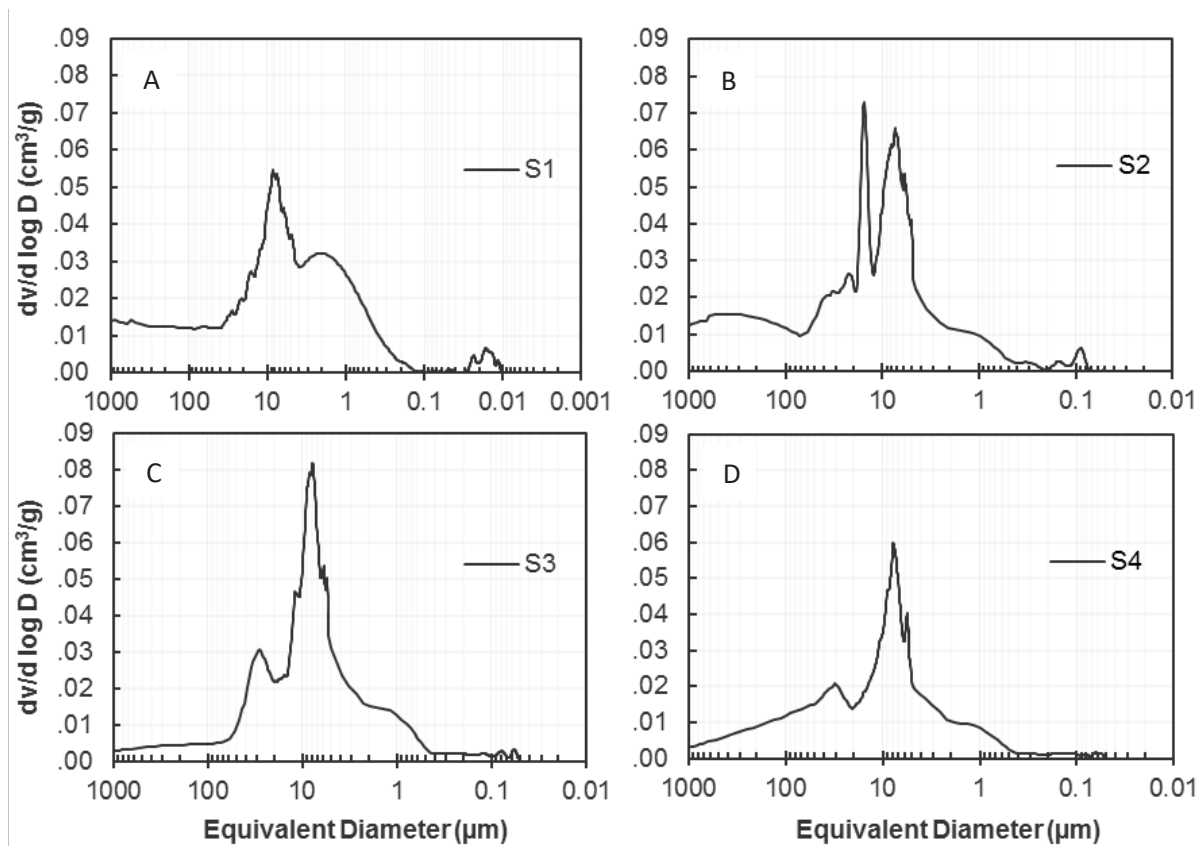


Figure 6, Differential volume curve versus equivalent pore diameter by MIP in the mesopore and macropore region

The higher intrusion volume encountered with shell-type S1 describe a wider pore size distribution and peaked at 7.57 μm with a median diameter of 7.2 μm. A bimodal distribution occurred at a peak value of 6 μm and 11 μm for shell-type S2 with a median diameter of 12.45 μm, suggesting the filling of a large pore as can be seen with the almost vertical slope in Figure 5b in that size regime. Shell-type S3 peaked at 7.81 μm with a median diameter of 8.35 μm,

while shell-type S4 exhibited a similar trend and peaked at 7.82  $\mu\text{m}$  with a median diameter of 9.05  $\mu\text{m}$ , exhibiting the presence of slightly larger pores shown in Figure 6d.

Figure 7 shows the volume of mercury intruded in the mesopore region (3.5–50 nm) accounting for approximately 2–5% of the total open porosity for all samples, except sample S4 accounting for 11% of the total porosity. Similarly, in the macropore region (0.05–400  $\mu\text{m}$ ) sample S4 exhibited the lowest volume occupied of 85.3 % compared to a maximum of 92.7% for shell-type S3. Both of these specimens contained bilayers of pre-wetting solution, although, shell-type S4 displayed a two-fold increase of intruded volume in the mesopore region. The porosity of shell-types with non-pre-wetting and a monolayer of pre-wetting (S1 and S2) displayed higher values in the 400–1000  $\mu\text{m}$  region. This may be attributed to less adsorption between coatings and thus producing thicker shells with increased void space available.

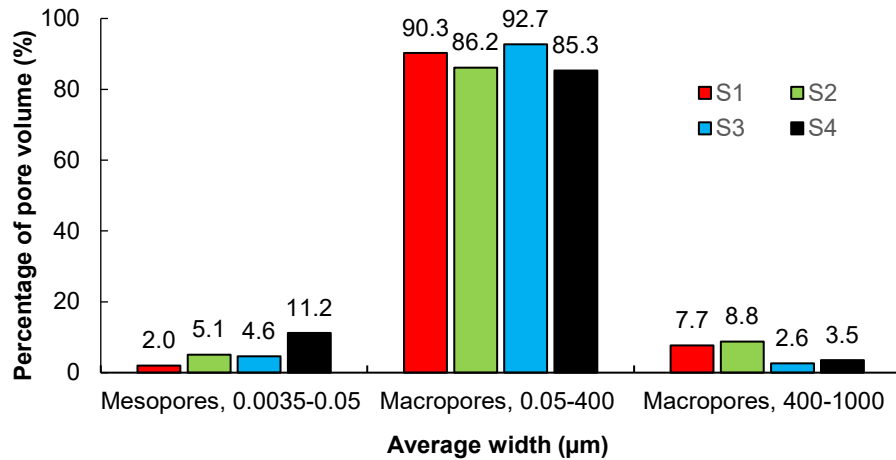


Figure 7, Percentage of intruded volume versus equivalent pore diameter in the mesopore and macropore realms by MIP

The stepwise increase in intrusion volume in the high-pressure regime of shell-type S4 may be on the verge of limitations of MIP and best suited to gas adsorption methods. However, Klobes and Munro [30] suggest good agreement is obtained from pore volume with an equivalent pore diameter down to 0.008  $\mu\text{m}$ .

### 3.5 Gas Adsorption

Gas adsorption provided analysis of the pore morphology of four ceramic shell-types, where the BET surface area is analysed over eleven points between relative pressures ranging from 0.05–0.35, see results in Table 2. The monolayer capacity,  $W_m$ , was then evaluated from the slope and intercept of the BET plot before determining the total surface area,  $St$ . The relative pressure at monolayer coverage ( $P/P_{0nm}$ ) of the adsorbent occurred from approximately 0.11–0.13. The acquired cumulative BET surface area exhibits less than 6% deviation between

shell types S2, S3, and S4, although, sample S1 showed a five-fold reduction in BET surface area. Correspondingly, the BET  $C$  constant deviated by 8.2% between samples, while shell-type S1 exhibited almost a two-fold reduction. As pointed out by Pendall [33], the general minimum BET  $C$  constant should be above 20 and the surface area should be between 40 and 120 m<sup>2</sup>, although, lower surface areas were obtained. Further work should involve krypton as the adsorbate that allows the analysis of surface area as low as 0.5 m<sup>2</sup> [34].

Table 2, Microstructural properties of the fired ceramic shell-types through gas adsorption

Sample	$S_t$ (m <sup>2</sup> /g)	BET $C$ (-)	Mass (g)	(P/Po) $n_m$ (-)	$W_m$ (cm <sup>3</sup> /g) 10 <sup>-3</sup>
S1	1.324	39.94	10.79	0.13	0.38
S2	6.722	71.78	9.45	0.11	1.94
S3	6.347	69.36	12.72	0.11	1.83
S4	6.675	66.30	11.48	0.11	1.93

Figure 8 shows the adsorption-desorption isotherms as relative pressure increases beyond those required for the BET plot (0.05–0.35) and displays the adsorption capacity of the material [35]. The slow increase in the adsorption isotherm at relative pressure of approximately 0.45–0.46 leads to multilayer formation of adsorbate on the surface of the adsorbent that corresponds to a pore diameter based on the Kelvin equation [36, 37]. Shell-type S2 and S4 exhibited near identical adsorption isotherms and the hysteresis of S3 is slightly skewed to a higher-pressure range due to the presence of smaller pores. The horizontal behaviour of the isotherm for sample S1 is attributed to less pore space present in the adsorbent material.

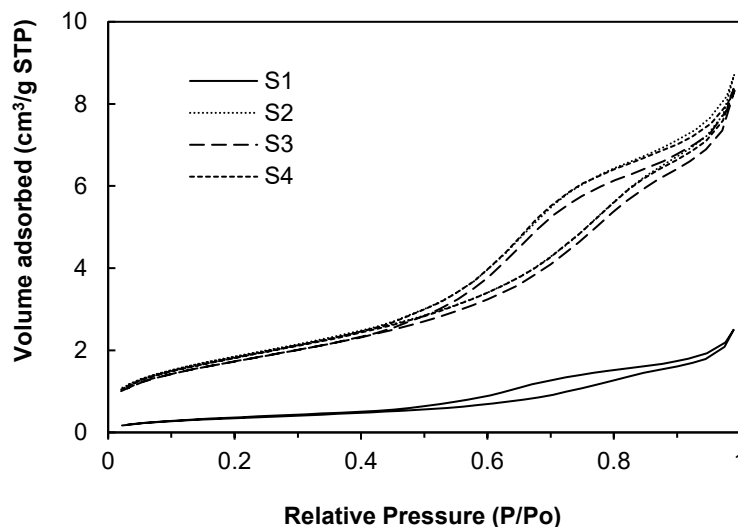


Figure 8, Gas adsorption-desorption isotherm at standard temperature and atmospheric pressure (STP)

Figure 9 was plotted using the alpha-s ( $\alpha_s$ ) method as the isotherm in Figure 8 did not portray a well-defined knee point and evaluates pore size in the micropore realm ( $< 2$  nm). Plotting of the  $\alpha_s$  isotherm in reduced form, where  $\alpha_s = (n/n_x)_s$ , versus the amount adsorbed  $n$  provided a comparison between actual and nonporous reference isotherms. Here,  $n_x$  is the amount adsorbed at a predetermined  $P/P_0$  of 0.4 [38]. The slope of the linear  $\alpha_s$  curve denotes the surface area of micropores present and the intercept signifies the specific micropore capacity ( $\eta_{p(mic)}$ ).

Shell-type S1 and S2 exhibited no presence of micropores as a negative and zero intercept occurred, respectively, see inset of Figure 9. A zero intercept is attributed to enhanced monolayer-multilayer adsorption while a negative intercept is unattainable. Shell-type S3 and S4 portrayed a positive intercept signifying the presence of micropores with a volume of  $1.29 \mu\text{m}^3/\text{g}$  and  $0.39 \mu\text{m}^3/\text{g}$  and a specific surface area of approximately  $4.23 \text{ m}^2/\text{g}$  and  $2.30 \text{ m}^2/\text{g}$ , respectively.

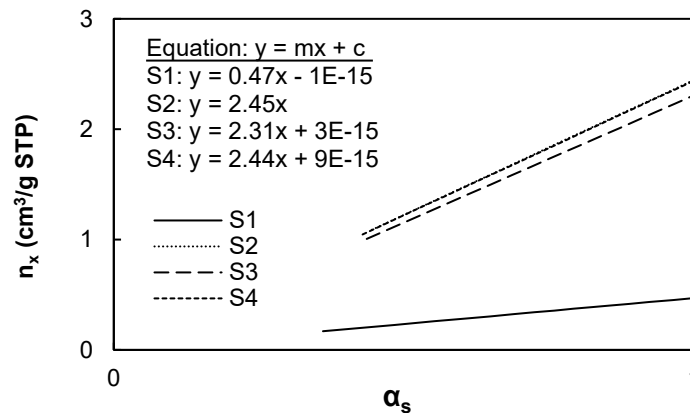


Figure 9, Surface area and micropore capacity of fired ceramic specimens

Figure 10a shows the results of pore size distribution with respect to pore volume. The lower volume obtained by shell-type S1 of  $8.63 \times 10^{-3} \text{ cm}^3/\text{g}$  at an equivalent diameter of 5.80 nm displays less adsorption sites available and thus less volume adsorbed. Therefore, the presence of pre-wetting solution is shown to enhance the volume of micropores in the shell structures. Total pore volume of each sample is determined from the volume of vapour adsorbed at a relative pressure close to unity under the assumption that pores are completely filled with liquid adsorptive [38]. Figure 10b displays the pore area distribution and showed similar trends to the pore volume distribution, where shell-types that contained a pre-wetting solution exhibited almost a four-fold increase in pore volume and pore area.

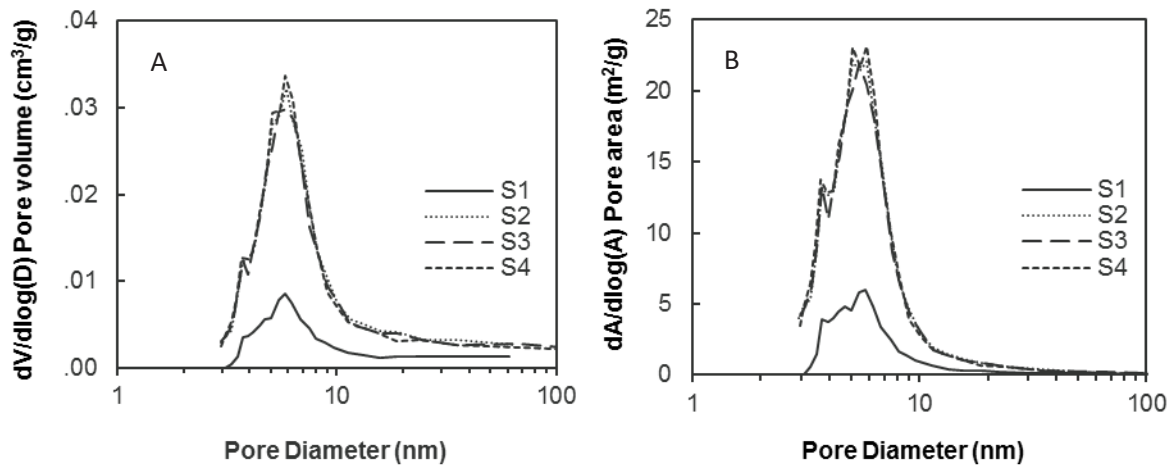


Figure 10, Pore volume distribution versus pore diameter (a) and pore area distribution versus pore diameter (b)

Figure 11 shows the percent frequency of pore sizes in the mesopore and macropore region of the ceramic shell-types. At an equivalent pore diameter of 50 nm, shell-types S1, S2, S3, and S4 adsorbed 86.3%, 95.8%, 88.5%, and 90.4% of their maximum pore volume capacity, respectively. The shell-type with no pre-wetting applied (S1) showed the least amount of mesopores present, whereas sample S4 utilized bilayers of pre-wetting and exhibited the highest occurrence of pore size in the 2–10 nm regime.

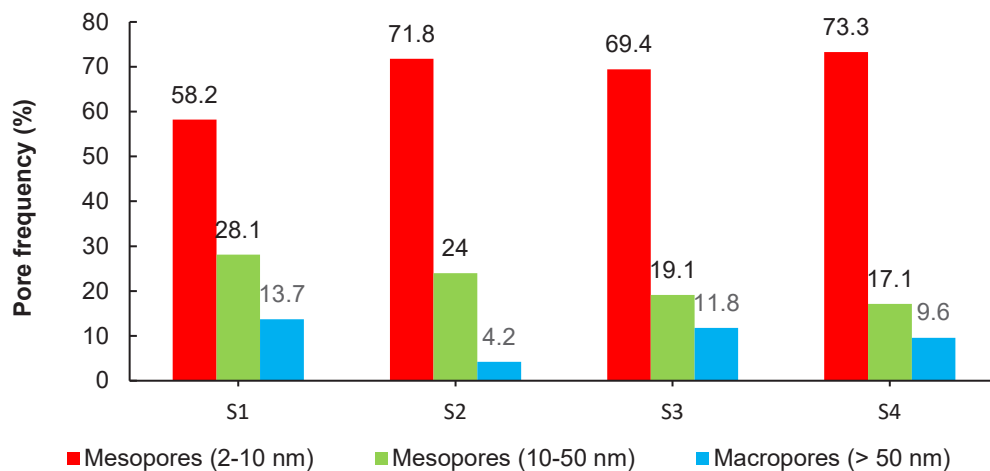


Figure 11, Percent pore frequency distribution of fired shell-types through gas adsorption

### 3.6 X-ray Microtomography and Pore Network Modelling

Results of porosity through XMT methods coupled with PNM displayed similar results to MIP, where shell-type S1 and S2 exhibited the largest porosity of the samples, see Table 3. The permeability constant,  $K$ , was analyzed with a nitrogen gas flow rate (70 cm<sup>3</sup>/min) orthogonally to the primary facecoat of known viscosity (1.76 x 10<sup>-5</sup> Pa.s) [39]. The average pore diameter,  $D_m$ , increased when bilayers of pre-wetting solution were applied (shell-types

S3 and S4). PNM methods provided a tortuosity factor for the ceramic structures that describe a real length scale for the flow of fluids compared to the orthogonal distance through the coatings.

Table 3, Microstructural parameters of fired ceramic specimens through PNM

Shell-type	$\varepsilon$ (%)	$K$ (m <sup>2</sup> )	$D_m$ ( $\mu\text{m}$ )	Tortuosity
S1	21.7	2.33 E-9	55	1.17
S2	19.3	1.53 E-9	64	1.24
S3	19.7	2.35 E-10	68	1.21
S4	18.7	6.07 E-10	74	1.17

Figure 13 displays the deviation of pore volume from the primary facecoat through the ceramic shell. The S1 shell exhibited the lowest porosity at the primary facecoat (15.4%) compared to the shells containing a pre-wetting solution (26%). This implies that porosity on the facecoat is enhanced through pre-wetting, as moisture adsorbs to previous layers during the drying process [27]. However, the standard production shell S2 provides adequate surface roughness of the cast components, signifying the increase of porosity post primary layer has minimal effect on surface roughness of the cast components.

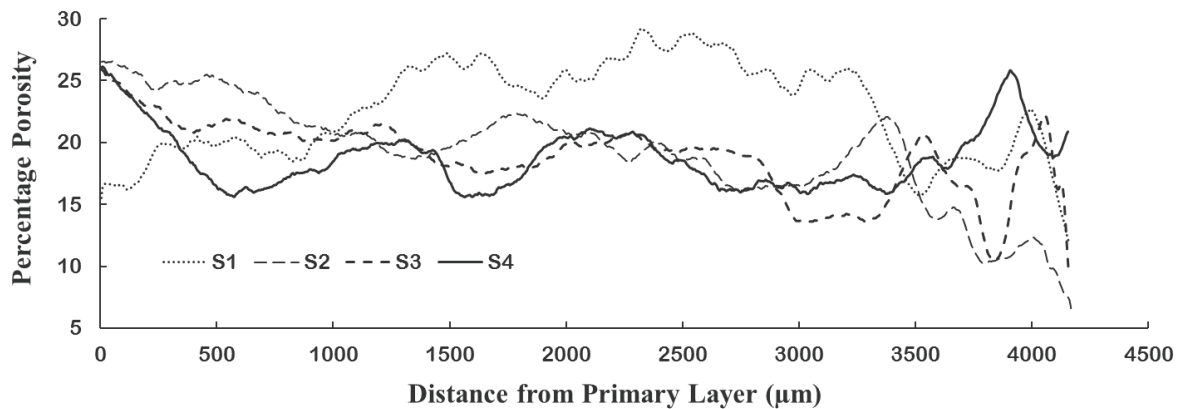


Figure 12, Variation of porosity through the thickness of the sintered ceramic shell types by PNM

Figure 14 shows a frequency distribution of the percentage of pore volume fraction to the total volume was plotted to analyse pore sizes ranging from 7–150  $\mu\text{m}$ , see Figure 17. This is accomplished by the sum of the pore area fractions of the 2D images to the total area in the region of interest, and then transposed to equivalent diameters. The frequency of pore diameters  $> 100 \mu\text{m}$  accounted for less than 0.5% of the total percent frequency distribution. The total percent of pores occurring below an equivalent pore diameter of approximately 20  $\mu\text{m}$  for shell-type S1, S2, S3, and S4 accounted for 52.22%, 55.6%, 45.4%, and 52.75%, respectively.

When the pore size distribution was analysed below 50  $\mu\text{m}$  shell-type S1 accounted for approximately 84.1% of the total occurrence of pores in that range. Similarly, shell-type S2 exhibited a result of 83.5%, whereas shell-types S3 and S4 showed signs of larger pores present with 81.6% and 81.1% of pore sizes present in that range.

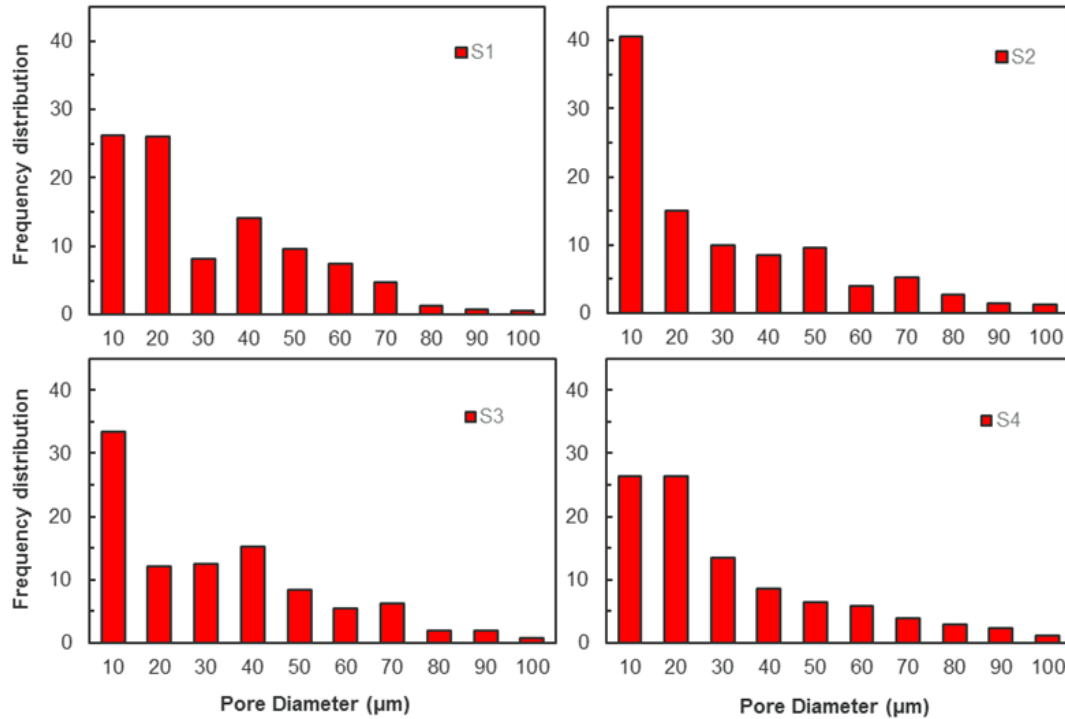


Figure 13, Pore frequency distribution versus pore diameter for the sintered shell specimens

## 4. Discussion

### 4.1 Modulus of Rupture

The use of a pre-wetting reduced green strength by approximately 8.7–15.6% compared to shell-type S1 that contained no pre-wetting solution between its refractory coatings, refer to Figure 2. A reduced green strength is undesirable feature of the ceramic shell and may be opposed by increasing the concentration of hydrophilic polymer as a low quantity of aqueous was used ( $< 2.5\%$ ). However, producing an increase in porosity provides a reduced bulk density and therefore resulting in a reduced MOR in the green body, depending on the pore size encountered. Hot strength increased by approximately 20–25% as pre-wetting was applied, where research by Lü [21] also showed an increase in hot strength as open porosity was developed. A reduction in fired strength of 18.7–28.5% occurred when pre-wetting was applied, where research displayed similar results of 18–30% [25].

#### 4.2 *Mercury Intrusion Porosimetry*

The pore morphology of the ceramic shell material were analysed by different techniques, each with their own advantages and limitations. MIP provides a wealth of information about key microstructural properties of the ceramic material under isostatic pressure, where pore size is generally reported from 3 nm to 400  $\mu\text{m}$  [13, 16, 40]. The intrusion process is dependent on cylindrical pore/throat diameter while the extrusion process resembles pore connectivity [41]. The shell-type with the highest permeability constant (S4) exhibited a sharp increase in intrusion volume in the high pressure region, see Figure 5d. This implies an interconnected network with narrow channels, while the extrusion curve displayed no extrusion volume.

#### 4.3 *Gas Adsorption*

Lower surface areas were encountered for the non-prewetting shell, whereas the higher surface area of the pre-wetting shells display the presence of smaller pores, see Table 2. Similarly, lower volumes adsorbed can be seen in the adsorption isotherm of Figure 8. The shape of isotherms and their hysteresis provide information on pore size, pore volume, and pore shape [38, 42]. The ceramic shell material displayed a Type IV isotherm with Type H3 hysteresis. However, there is no plateau in the higher pressure region, where a characteristic Type IV isotherm displays a plateau. Therefore, this isotherm can be further sub-classed as a Type II<sub>b</sub> isotherm with a hysteresis that displays a morphology of plate-like type structures [43]. The pore volume distribution and pore area distribution increased significantly when a monolayer or bi-layers of pre-wetting solution were applied, while the latter displayed the presence of micropores.

#### 4.4 *X-ray Microtomography and Pore Network Modelling*

XMT methods provides a non-destructive tool to analyse the inner 3D structure of the ceramic shell material obtained from 2D planar images and extracts quantitative information with micron resolution [44]. The density and thickness of the material is proportional to the attenuation of the x-ray beam that may alter the contrast of images, where pore sizes  $< 6.3 \mu\text{m}$  were unattainable due to the resolution used [15, 16, 45]. Pore size and its distribution is shown to increase where the pre-wetting solution is applied, where less pore space is present in the non-prewetting shell (S1), see Figure 4. When XMT imaging were coupled with PNM methods, porosity was shown to deviate through the macrostructure of the ceramic shell, see Figure 13. Furthermore, porosity reduced by approximately 35% at the primary facecoat when no pre-wetting solution was applied, while bi-layers of pre-wetting was shown to increase the frequency of pores greater than 50  $\mu\text{m}$ , refer to Figure 14.

#### 4.5 Pre-wetting

Enhancing permeability and adsorption between coatings through pre-wetting would be beneficial to reduce unintentional heterogeneities such as bulging, excess metal, gas-holes, and delamination. This may also provide a pathway for enhanced evaporation to occur during the timely drying and final drying process, while aiding with fluid flow during de-waxing. Although, pre-wetting has some negative effects in terms of producing a compositional change in subsequent slurry tanks, such as an increase in silica content. However, this may be regulated by replacing a volume fraction of the colloidal binder with de-ionized water when replenishing the slurry. This produces a colloidal binder with a lower specific gravity or silica content while allowing sufficient mixing time after refilling the slurry tank.

### 5. Conclusion

When porosity of the ceramic shell increased post primary layer no significant increase in permeability was observed. However, when porosity was developed between two intermediate coatings permeability increased by a factor of two. The shell-type (S4) with the highest permeability constant also displayed a stepwise increase in intrusion volume and showed the highest occurrence of pores ranging from 2–50 nm. Similarly, gas adsorption portrayed the largest present of pores in the 2–10 nm range and with the highest average pore diameter observed through XMT. Image analysis of the different shell-types displayed the influence of pre-wetting on porosity, where pores were generated in the mesopore range compared to non-prewetting. Lastly, as bi-layers of pre-wetting were applied the alpha-s method portrayed the presence of micropores in the ceramic shell material.

### 6. References

1. Kline, D.M., Lekakh, S.N. and Richards, V.L. *Improving Investment Casting Mold Permeability Using Graphite Particles*. Transactions of the American Foundry Society 2010 [cited 2021 25 Feb ]; Available from: <https://web.mst.edu/~lekakhs/webpage%20Lekakh/Articles/10-087.pdf>
2. Yuan, C., Compton, D., Cheng, X., Green, N. and Withey, P. *The influence of polymer content and sintering temperature on yttria face-coat moulds for TiAl casting*. Journal of the European Ceramic Society, 2012. **32**, 4041-4049 DOI: <https://doi.org/10.1016/j.jeurceramsoc.2012.06.010>.
3. Ewsuk, K.G., *Ceramic processing*, in *Encyclopedia of Chemical Physics and Physical Chemist*. 1999, U.S. Department of Energy Sandia National Labs U.S.A.
4. Kowalski, S.J. and A. Rybicki *The vapour-liquid interface and stresses in dried bodies*. Drying of Porous Materials, 2006. 43-58 DOI: [https://doi.org/10.1007/978-1-4020-5480-8\\_5](https://doi.org/10.1007/978-1-4020-5480-8_5).
5. Ferreira, J. and A. Mateus *A numerical and experimental study of fracture in RP stereolithography patterns and ceramic shells for investment casting*. Journal of Materials Processing Technology, 2003. **134**, 135-144 DOI: [https://doi.org/10.1016/S0924-0136\(02\)01034-8](https://doi.org/10.1016/S0924-0136(02)01034-8).

6. Kumar, S. and D.B. Karunakar *Enhancing the permeability and properties of ceramic shell in investment casting process using ABS powder and needle coke*. International Journal of Metalcasting, 2019. **13**, 588-596 DOI: <https://doi.org/10.1007/s40962-018-00297-7>.
7. Nickerson, S., Shu, Y., Zhong, D., Könke, C. and Tandia, A. *Permeability of porous ceramics by X-ray CT image analysis*. Acta Materialia, 2019. **172**, 121-130 DOI: <https://doi.org/10.1016/j.actamat.2019.04.053>.
8. Yuan, C. and S. Jones *Investigation of fibre modified ceramic moulds for investment casting*. Journal of the European Ceramic Society, 2003. **23**, 399-407 DOI: [https://doi.org/10.1016/S0955-2219\(02\)00153-X](https://doi.org/10.1016/S0955-2219(02)00153-X).
9. Stefanescu, D.M., Davis, J.R. and Destefani, J.D., *Metals Handbook, Vol. 15 Casting*. ASM International. 1988. 577-579.
10. Roberts, W.O., *Prewetting Effects on Shell Strength and Structure*. Investment Casting Institute, 38th Annual Technical Meeting, 1990: p. 1-12.
11. Groen, J.C., L.A.A. Peffer, and J. and Perez-Ramirez *Incorporation of appropriate contact angles in textural characterization by mercury porosimetry*. Studies in Surface Science and Catalysis, 2002. **144**, 91-98 DOI: [https://doi.org/10.1016/S0167-2991\(02\)80224-5](https://doi.org/10.1016/S0167-2991(02)80224-5).
12. Washburn, E.W. *The dynamics of capillary flow*. Physical review, 1921. **17**, 273 DOI: <https://doi.org/10.1103/PhysRev.17.273>.
13. Xue, S., Zhang, P., Bao, J., He, L., Hu, Y. and Yang, S. *Comparison of mercury intrusion porosimetry and multi-scale X-ray CT on characterizing the microstructure of heat-treated cement mortar*. Materials Characterization, 2020. **160**, 110085 DOI: <https://doi.org/10.1016/j.matchar.2019.110085>.
14. Barrett, E.P., Joyner, L.G. and Halenda, P.P. *The determination of pore volume and area distributions in porous substances. I. Computations from nitrogen isotherms*. Journal of the American Chemical society, 1951. **73**, 373-380 DOI: <https://doi.org/10.1021/ja01145a126>.
15. Ketcham, R.A. and W.D. Carlson *Acquisition, optimization and interpretation of X-ray computed tomographic imagery: applications to the geosciences*. Computers & Geosciences, 2001. **27**, 381-400 DOI: [https://doi.org/10.1016/S0098-3004\(00\)00116-3](https://doi.org/10.1016/S0098-3004(00)00116-3).
16. Tariq, F., Haswell, R., Lee, P.D. and McComb, D.W. *Characterization of hierarchical pore structures in ceramics using multiscale tomography*. Acta Materialia, 2011. **59**, 2109-2120 DOI: <https://doi.org/10.1016/j.actamat.2010.12.012>.
17. Gostick, J., Aghighi, M., Hinebaugh, J., Tranter, T., Hoeh, M.A., Day, H., Spellacy, B., Sharqawy, M.H., Bazylak, A. and Burns, A. *OpenPNM: a pore network modeling package*. Computing in Science & Engineering, 2016. **18**, 60-74 DOI: <https://doi.org/10.1109/MCSE.2016.49>
18. Banerjee, R., Bevilacqua, N., Eifert, L. and Zeis, R. *Characterization of carbon felt electrodes for vanadium redox flow batteries—A pore network modeling approach*. Journal of Energy Storage, 2019. **21**, 163-171 DOI: <https://doi.org/10.1016/j.est.2018.11.014>.
19. Rusher, R.L., *Strength factors of ceramic shell molds*, in *AFS Cast Metals Research Journal*. 1974. p. p. 149-153.
20. Alavala, C.R. *Thermo-mechanical Behaviour and Metal-to-Mould Reactions of Cristobalite Investment Shell Moulds to Cast Ti-6Al-4V Alloy*. International Journal of Advanced Research 2016 [cited 2020 18 Sep]; Available from: [https://www.academia.edu/23270578/Thermo\\_mechanical\\_Behaviour\\_and\\_Metal\\_to\\_Mould\\_Reactions\\_of\\_Cristobalite\\_Investment\\_Shell\\_Moulds\\_to\\_Cast\\_Ti\\_6Al\\_4V\\_Alloy](https://www.academia.edu/23270578/Thermo_mechanical_Behaviour_and_Metal_to_Mould_Reactions_of_Cristobalite_Investment_Shell_Moulds_to_Cast_Ti_6Al_4V_Alloy).
21. Lü, K., Liu, X., Du, Z. and Li, Y. *Properties of hybrid fibre reinforced shell for investment casting*. Ceramics International, 2016. **42**, 15397-15404 DOI: <https://doi.org/10.1016/j.ceramint.2016.06.188>.
22. Lü, K., Duan, Z., Liu, X. and Li, Y. *Effects of fibre length and mixing routes on fibre reinforced shell for investment casting*. Ceramics International, 2019. **45**, 6925-6930 DOI: <https://doi.org/10.1016/j.ceramint.2018.12.189>.
23. Wang, F., Li, F., He, B. and Sun, B. *Microstructure and strength of needle coke modified ceramic casting molds*. Ceramics International, 2014. **40**, 479-486 DOI: <https://doi.org/10.1016/J.CERAMINT.2013.06.027>.
24. Funk, J.E. and D.R. Dinger, *Predictive Process Control of Crowded Particulate Suspensions*. Applied to Ceramic Manufacturing. Vol. 4. 2001, London: Kluwer Academic. 237.
25. Dooley, G., Kavanagh, A., Jolly, M.R. and Williamson, K. *Development of Foundry Casting Methods for Cost-Effective Manufacture of Medical Implants*. 2014 [cited 2020 3 Mar]; Available from: <https://cordis.europa.eu/project/id/251269>.
26. Rahaman, M.N., *Ceramic Processing and Sintering*. 2nd ed. Vol. 1. 2003, London: Taylor and Francis Group. 1-875.
27. Leyland, S. and I. Smith. *Implementation of a water based shell mould investment casting process(replacement of an ethyl silicate system)*. in *9th World Conference on Investment Casting*. 1996.

28. Zych, J., Kolczyk, J., Jamrozowicz, Ł. and Snopkiewicz, T. *New Investigation Method of the Permeability of Ceramic Moulds Applied in the Investment Casting Technology*. Archives of Foundry Engineering, 2013. **13**, 107-112 DOI: <https://doi.org/10.2478/afe-2013-0047>
29. Rouquerol, J., Baron, G., Denoyel, R., Giesche, H., Groen, J., Klobes, P., Levitz, P., Neimark, A.V., Rigby, S. and Skudas, R. *Liquid intrusion and alternative methods for the characterization of macroporous materials (IUPAC Technical Report)*. Pure and Applied Chemistry, 2011. **84**, 107-136 DOI: <https://doi.org/10.1351/PAC-REP-10-11-19>.
30. Klobes, P. and R.G. Munro, *Porosity and specific surface area measurements for solid materials*. 2006, National Institute of Standards and Technology: Washington, U.S.A. p. 89.
31. Hasanuzzaman, M., Rashid, A. R., Mohammad H. and Olabi, A.G. *Characterization of Porous Glass and Ceramics by Mercury Intrusion Porosimetry*. 2017. **1**, 1-9 DOI: <https://doi.org/10.1016/B978-0-12-803581-8.09266-3>.
32. Rootare, H.M. and C.F. Prenzlow *Surface areas from mercury porosimeter measurements*. The Journal of physical chemistry, 1967. **71**, 2733-2736 DOI: <https://doi.org/10.1021/j100867a057>.
33. Pendall, K.D. *Specific Surface Area*. Reference Module in Earth Systems and Environmental Sciences, 2016. **1**, 7 DOI: <https://doi.org/10.1016/B978-0-12-409548-9.09583-X>.
34. Webb, P.A. and C. Orr, *Analytical methods in fine particle technology*. 1997, Norcross, GA.: Micrometric Instruments Corp: Georgia.
35. Virtanen, T., Rudolph, G., Lopatina, A., Al-Rudainy, B., Schagerlöf, H., Puro, L., Kallioinen, M. and Lipnizki, F. *Analysis of membrane fouling by Brunauer-Emmet-Teller nitrogen adsorption/desorption technique*. Scientific reports, 2020. **10**, 1-10 DOI: <https://doi.org/10.1038/s41598-020-59994-1>.
36. Horikawa, T., Do, D.D. and Nicholson, D. *Capillary condensation of adsorbates in porous materials*. Advances in colloid and interface science, 2011. **169**, 40-58 DOI: <https://doi.org/10.1016/j.cis.2011.08.003>.
37. Bertier, P., Schweinar, K., Stanjek, H., Ghanizadeh, A., Clarkson, C.R., Busch, A., Kampman, N., Prinz, D., Amann-Hildenbrand, A. and Krooss, B.M. *On the use and abuse of N<sub>2</sub> physisorption for the characterization of the pore structure of shales*. 2016. **21**, 151-161 DOI: <https://doi.org/10.1346/CMS-WLS-21-12>.
38. Sing, K.S.W., Haul, R.A.W., Pierotti, R.A. and Siemieniewska, T. *Reporting physisorption data for gas/solid systems with special reference to the determination of surface area and porosity* International Union of Pure and Applied Chemistry (IUPAC), 1982. **54**, 2201-2218 DOI: <https://doi.org/10.1351/pac198254112201>.
39. Evers, C., H. Lösch, and W. Wagner *An absolute viscometer-densimeter and measurements of the viscosity of nitrogen, methane, helium, neon, argon, and krypton over a wide range of density and temperature*. International journal of thermophysics, 2002. **23**, 1411-1439 DOI: <https://doi.org/10.1023/A:1020784330515>.
40. Porcheron, F., Thommes, M., Ahmad, R. and Monson, P.A. *Mercury porosimetry in mesoporous glasses: a comparison of experiments with results from a molecular model*. Langmuir, 2007. **23**, 3372-3380 DOI: <https://doi.org/10.1021/la063080e>.
41. Giesche, H. *Mercury porosimetry: a general (practical) overview*. Particle & particle systems characterization, 2006. **23**, 9-19 DOI: <https://doi.org/10.1002/ppsc.200601009>.
42. Liu, P. and G. Chen *Characterization Methods: Basic Factors*. 2014. 411-492 DOI: <https://doi.org/10.1016/B978-0-12-407788-1.00009-5>.
43. Rouquerol, F., J. Rouquerol, and K. Sing *Adsorption by powders and porous solids*. Academic Press, 1999. **11**, 1-191 DOI: <https://doi.org/10.1016/B978-0-12-598920-6.X5000-3>.
44. Withers, P.J., Bouman, C., Carmignato, S., Cnudde, V., Grimaldi, D., Hagen, C.K., Maire, E., Manley, M., Du Plessis, A. and Stock, S.R. *X-ray computed tomography*. Nature Reviews Methods Primers, 2021. **1**, 1-21 DOI: <https://doi.org/10.1038/s43586-021-00015-4>.
45. Wildenschild, D., Vaz, C.M.P., Rivers, M.L., Rikard, D. and Christensen, B.S.B. *Using X-ray computed tomography in hydrology: systems, resolutions, and limitations*. Journal of Hydrology, 2002. **267**, 285-297 DOI: [https://doi.org/10.1016/S0022-1694\(02\)00157-9](https://doi.org/10.1016/S0022-1694(02)00157-9).



# **INVESTMENT CASTING INSTITUTE**

## **Tensile Bar Castings**

Mark White  
IMPRO Industries USA

## **68<sup>TH</sup> TECHNICAL CONFERENCE & EXPO 2021**

Paper № 19

# “Tensile Bar Castings”

Mark A. White

Impro Industries USA, Inc.

## *Abstract*

In new casting projects there exists an agreement between the casting purchaser and the casting manufacturer which outlines technical requirements beginning with the qualification and also covering production. These agreements may range from comprehensive specific dimensional and metallurgical requirements associated with aerospace fixed processes ranging to a lone AS9102 dimensional requirement, for example, which may apply to an industrial part. PPAPs are mostly not covering metallurgical specifics. Oftentimes, there exists a gap, where the casting designer/purchaser assume metallurgical requirements including the notion that machined from casting (MFC) test bars are intended to and must meet ASTM mechanical property requirements. Oftentimes, the designer/purchaser requires MFC expecting ASTM properties. Many times casting houses agree, because they think there is no other choice and the designer must be correct. This can cost the casting producer in terms of excessive mechanical testing and lost production at a high cost, without a reasonable and economical solution. This review covers why the case for MFC test bars does not work as a standalone good/bad criterion and then provides a practical solution to this problem.

## **INTRODUCTION**

The metallurgical differences of cast shapes are responsible for the inimitability of castings with different geometries. This includes test bars, because fundamentally, test bars are castings. There are factors which contribute to this inconsistency, which we discuss here. Then we will review casting data and conclude with discussion, for moving forward. We touch on how it may be possible to close the gap between test bar properties and MFC; based on recent work. The standard for these discussions should be that separately cast then subsequently machined test bars are the preferred way to material assessment. Key to this discussion is this-all cast shapes are inimitable, including test bars. This is why we should discuss and agree on a mechanical properties testing plan, at the beginning of each new project.

## **BACKGROUND**

The first critical factor in making a sound casting is the essential solidification ratio. This is expressed in **Figure 1** where the width a “W” should not exceed  $B/2$ . This shows that we need to gate wider at the top, for example. The part geometry and the casting surface area factor into how well this ratio can be met. The keel block, on the right meets the essential solidification ratio. ASTM mechanical properties are developed using this ideal casting shape that provides good solidification, good grain and no isolated shrink. **Figures 2 / 3** show a keel block compared with a small casting. These two may not show the same metallurgical “DNA”. Not a sound comparison of the small casting which does not meet the essential solidification ratio and the keel block that does. Testing to ASTM standards is intended to verify the quality of the steel, not to establish actual casting properties. Each casting shape has different solidification ratios, different gating, different geometry size effect, different metallurgical size effect

and different heat effects. These factors lead to differing amounts of microporosity, different locations of shrinkage, dendrite arm spacing, grain size and grain directionality which impact mechanical properties. The importance of interpreting tensile results, is to review test bar data determining the quality of the steel from which the castings have been poured. Castings themselves have been effected by rate of cooling post casting and during subsequent heat treatment which are in turn influenced by casting design-thickness, size and shape. Grain size and heat treating impact mechanical properties, in steel. As section size increases, grain size increases. Properties reduce. Grain also affects fracture strength, fatigue. Heat treatment alters as-cast microstructure. Thick sections and edge conditions provide different cooling, microstructure and properties. Variation – surface to center. The single most important and least avoidable effect of section size is the coarseness of the microstructure. Cooling internally, may not be rapid.

Specifications A781 and A703 recognize that castings and test bars exhibit different properties. The mechanical test requirements are intended to verify the quality of the steel. They are not intended to establish actual casting properties which are impacted by solidification conditions, in casting and in cooling conditions, in heat treatment which can be influenced by part mass.

**Table 1** shows that even with the essential solidification ratio being met, precise test bar machining and no “lab effect” impacting mechanical results, ASTM A370 observed intrinsic variation in an alloy’s tensile testing results. Even though every operation was done in the same laboratory and by the same technicians, the results were not the same. There was variation. It was observed by ASTM, that foundries could see 95% assurance of being within 1000 psi for ultimate tensile strength, within 95% assurance to be within 1,600 psi in yield strength, +/- 3% variation in elongation and +/- 5% in reduction of area. This level of variation can alone disqualify metal. We can look to the non-equilibrium factors at work during solidification to understand why there is variation in tensile properties within the same casting shape. For example, if a casting freezes more quickly there may be grain size, grain directionality and chemical segregation differences occurring which may influence casting outcomes. Microporosity and dendrite arm spacing can be impacted. Metallurgical differences occur within controlled foundry conditions, too. With intrinsic variation occurring in property testing, mechanical test results can become less meaningful. A370 goes as far as to describe basic riser conditions in an attempt to establish consistency in addressing this problem.

Castings are inimitable. Metallurgical effects ensure that each shape solidifies differently. In **Figure 4**, the casting, on the left, will experience different solidification than the thin walled part on the right. Comparatively, the middle drawing is the shape that is used to cast then subsequently excise ASTM test bars from. Each of the three unique shapes has different solidification, different grain, different shrink and unique-to-itself mechanical properties. Cast shapes are impacted by: 1) Geometrical size effect – dimensions 2) Metallurgical size effect – surface area and cooling in casting and in heat treatment where thinner sections cool faster than thicker sections. The rate of cooling determines the austenite transformation during heat treatment. Effects like grain size; through grain temper embrittlement and microshrinkage, vary with section sizes. 3) Mass effect – solidification and heat transfer in casting solidification and in heat treatment and 4) Bi-film effect – Bi-films occur especially in castings with turbulent metal flow. The surface oxidizes, create a 1mm sized shell -a solidified flat section- that gets folded as metal continues to flow. Usually in a much too choppy metal flow. With a smooth pour and no “waterfall” gate connections, there are no interrupted surfaces. In a calm pour, metal flow surface

tension can be enough to prevent bifilms from turning into rejectable defects. If not, defects are formed internally, usually in the form of cracks.

**Figure 5** shows an ASTM E8 sub-sized test bar required by various customers. Compared with standard specimens which are a number of times larger, the Keel block test bar is larger than some customer-required test bars. The keel block test bar was used by ASTM to establish the mechanical properties we are usually working toward. Some customer test bar requirements require sub-sized MFC bars from a thin wall casting which may only be capable of netting a sub-sized test bar, for example 0.125" diameter. There is now the problem of not having established properties to meet or compare to. Different sized test bars going for the same mechanical result may not be realistic in an accept / reject scenario.

**Figure 6** We have shown, in this test, there is intrinsic variation in a cluster of parts. In this cluster, the top casting (A) exhibited lower properties than the bottom casting (B). We expected the bottom casting to be better, and it was. Different locations on a cluster can be likened to different ice cubes in an ice cube tray, freezing differently. Completely examine test bars. We continued our intrinsic variation test with fracture morphology exam, metallography, texture corrosion, X-ray and MPI, surface visual and straightness, prior to testing. (**Figures 7, 8, 9, 10**)

A look into the testing effects brings out the importance of test bar condition. **Figure 11** outlines necessary conditions. The extensometer **Figure 12** is handled meticulously and we call out precise and consistent settings to specific work instructions. Note too, that mechanical testing machines generally have a margin of error of approximately +/- .5% accuracy, as manufactured.

Within the industry, between casting producers and casting purchasers, there can be an array of test bar variations, which may not be fully understood. Each variant can produce different results. When flowed down these requirements are oftentimes, accepted. It's essential to have mechanical property test plans discussed before starting a new project. Separately cast then subsequently machined test bars are the best path forward for material assessment. These are examples of different test bar variants customers may use or casting producers may allow:

- 0.250" diameter, cast to size (CTS) bars on a separately cast mold, with 10 test bars per mold, top and bottom gated.
- 0.250" diameter, separately cast mold, with 10 test bars per mold, top and bottom gated, then subsequently machined.
- 0.250" diameter CTS, cast within a tree of parts, side gated, attached to the side of the sprue.
- 0.250" diameter, cast within a tree of parts, side gated, attached to side of the sprue, then subsequently machined
- 0.125" diameter, CTS test bars on a separately cast mold with 10 test bars per mold, top and bottom gated.
- 0.125" diameter, separately cast mold with 10 test bars per mold, top and bottom gated, then subsequently machined.
- 0.125" diameter, CTS cast on tree of parts, side gated, attached to the side of the sprue.

- 0.125" diameter, cast within a tree of parts, side gated, attached to the side of the sprue, then subsequently machined.
- 0.125" diameter, excised from the centerline of a thick casting section (MFC).
- 0.125" diameter, excised from a thin section, at (1/4T) of a casting (MFC).
- Flat test bar excised from the centerline of a thick section of a casting (MFC).
- Flat test bar excised from a thin section at (1/4T) of a casting (MFC).

Centerline shrink is a casting certainty. **Figure 13** Intrinsic centerline shrink will be present in any casting. Centerline shrink impacts ultimate tensile. Differing casting shapes result in unique-to-that-shape centerline shrink and ultimate tensile properties. The surface of the casting impacts yield strength and the strongest part of the casting is at 1/4T. Midway between the surface and the centerline. Customers use the terms shrink and shrinkage. These expressions have multiple meanings. Shrinkage is the decrease in volume that occurs during the transition from liquidus to solidus. The reason it occurs is because the specific volume of alloys is highest in the liquid state. All metals, except bismuth, have a higher density in a solid state. Therefore, castings undergo contraction as they cool. As castings cool from the outside inward, all castings will have microporosity much of which is concentrated in the centerline region. As we have said, different cast shapes, including test bars, will have differing microporosity impacting ultimate tensile. **FIGURE 14**

Inter-dendritic shrink is shrinkage between the feather-like features which form when castings solidify. When shrink occurs between the dendrite arms; it is called inter-dendritic shrink. Dendrite arm spacing is important because of its impact on casting properties. Another measure is secondary dendrite arm spacing. During some investigations we may assess SDAS. As metal solidifies, the liquid reforms into "tree-like" shapes called dendrites. As the arms close, metal may not be filled in. There is usually about 0.004" dendrite arm spacing in a normal cooling profile. Temperature gradient and cooling rate are important in addition to some of the more common variables to control. These effects manifest differently in various cast geometries.

**Figures 15, 16 and 17** are examples of microporosity typically in center sections. These examples are of automotive castings with microporosity shown at 100X. This testing was part of a study where a customer originally thought that .78% microporosity was a decent specification. That changed as we went through the project and showed them how to produce and how to properly assess excellent cast structures without intolerable specification call outs.

**(Table 2)** The Association of American Railroads, "Specification M-201-92..." shows that:

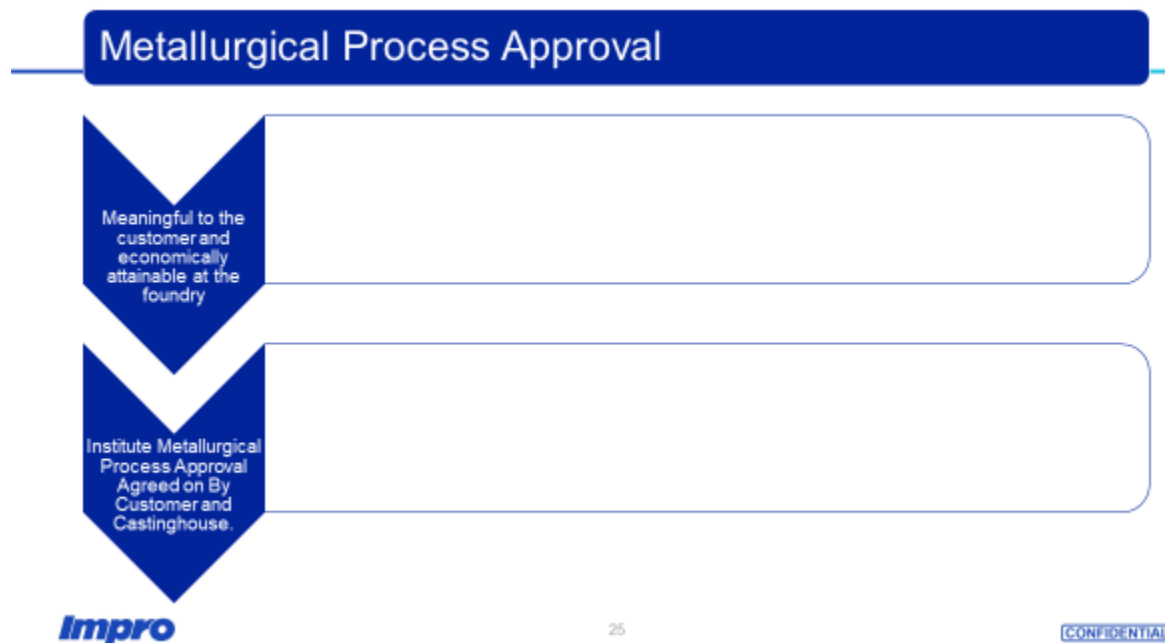
- Castings averaged 3% lower tensile versus test bars, in carbon steel.
- 6% less in elongation.
- 11% lower reduction of area.
- In section 7.2.5 it is shown that machined from casting test bars need to meet only 80% of the tensile and yield properties.

## DISCUSSION

Needed is an approval meaningful to the product and economically attainable at the foundry. It's typical having AS9102 for dimensional and PPAP for quality, for example. Oftentimes, creating a metallurgical and mechanical property approval, is needed, as well. This can occur in advance of new part kick-off. The material assessment is critical in this discussion. Being well-informed in the approximately ten critical factors discussed, in this paper, helps provide a path to a successful material assessment.

## LOOKING FORWARD

How do we, in investment casting, move forward working to attain MFC properties which are being shown at a sand foundry, in Canada, or at an investment casting foundry, in Ontario. These groups are excelling at properties, using new-to-investment casting metallurgical concepts. There is also, Dr. John Campbell's work to study, as well.



## REFERENCES

1. SFSA, "Steel Casting Handbook", (1941,1980, 1990, 1993)
2. Monroe, Raymond-SFSA "Steel Foundry Facts #354" February 1993
3. Reed, R.E.-Hill, "Physical Metallurgy Principles"
4. Campbell, John "Complete Casting Handbook; second edition
5. Roes, H.L. "Effects of Wall Thickness on Primary Structure and Mechanical Properties of Plain Carbon and Alloy Steels"; Metals Research Journal p.80-85 1968
6. ASTM A781 Section 6
7. Shank, M.E "Control of Steel Construction to Avoid Brittle Fracture; Welding Research Council
8. See, Allan and Hollandsworth, Bob Keokuk Steel Castings Company; SFSA Technical Conference

9. Association of American Railroads, Specification M-201-92, 1923-1992
10. Kun, Wang Acta Mechanica, "Effects of Crystalline Grain Structures on...Mechanical Property"
11. ASTM 703
12. ASTM A370
13. BG 3100 – 1976 Fig 5A and 5B for Steel Castings

FIGURE 1

The keel block, on the right meets the essential solidification ratio.

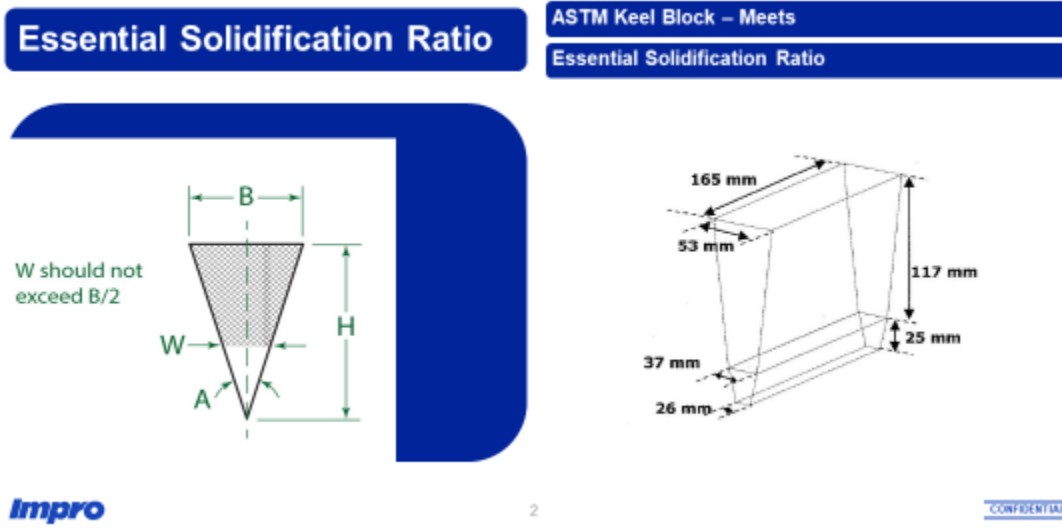
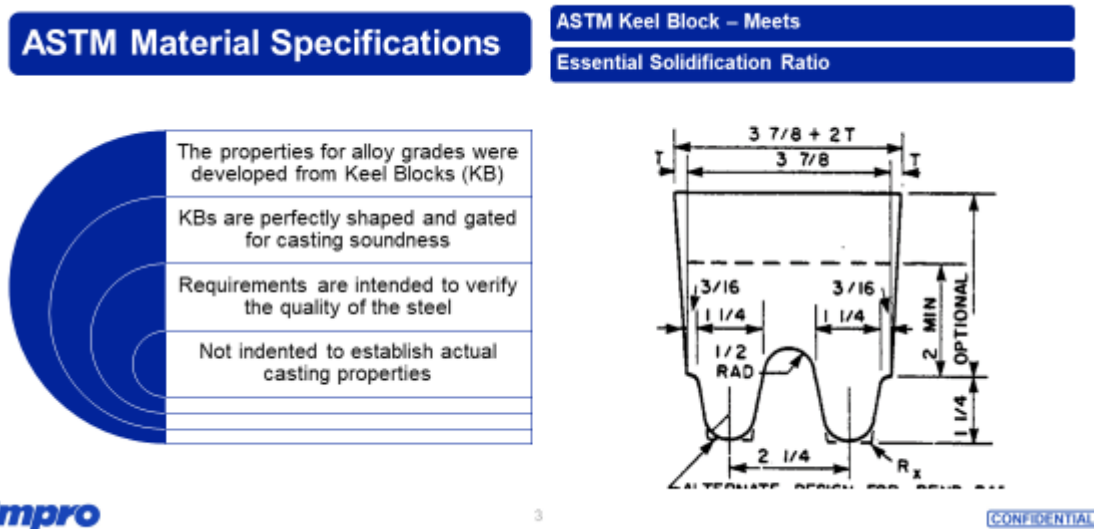


Figure 2

Testing to ASTM standards is intended to verify the quality of the steel. Not establish actual casting properties.

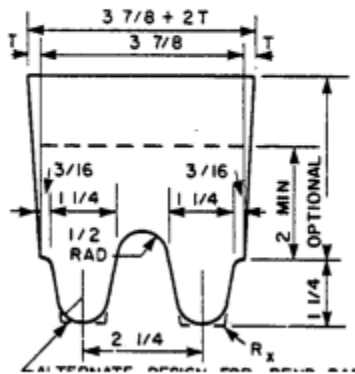


**FIGURE 3**

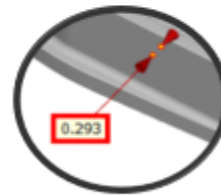
Not a sound comparison of the small casting which does not meet the essential solidification ratio and the keel block that does.

**CASTINGS ARE INIMITABLE**

- 1 1/4 " Diameter Keel Block



**0.293" Wall Thickness**



**Impro**

9

CONFIDENTIAL

**Table 1**

ASTM A370 observed keel block intrinsic variation in alloy's tensile results.

**Two Keel Blocks cast exactly the same**

- 95% Assurance with in 1,000psi UTS
- 95% Assurance with in 1,600psi Yield
- +/-3% Elongation
- +/-5% Reduction of Area

**1 1/4 " Diameter Keel Block**

**Impro**

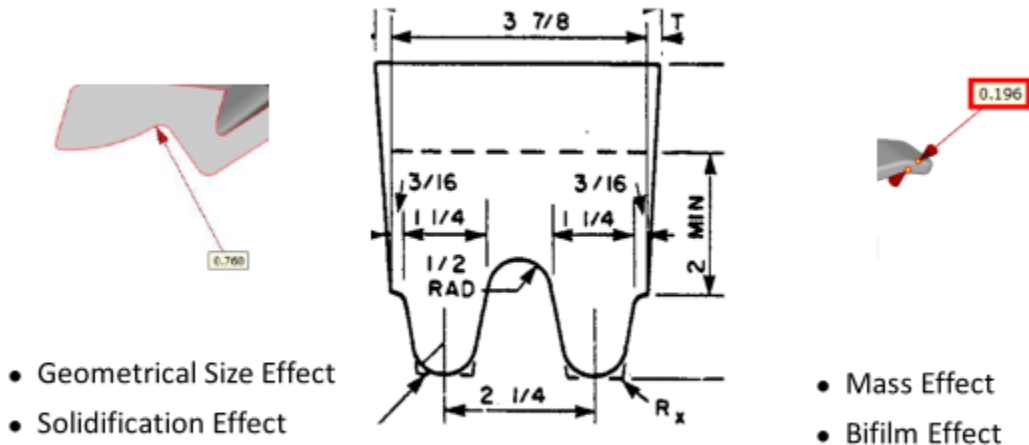
5

CONFIDENTIAL

Figure 4

Unique shapes have different solidification, different grain, different shrink and unique-to-itself mechanical properties.

### Metallurgical Effects



7

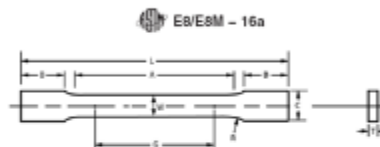
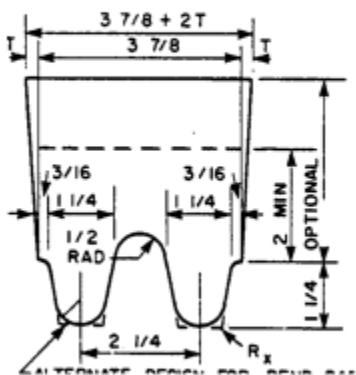
CONFIDENTIAL

FIGURE 5

Standard property requirements unavailable for several sub-sized specimens.

### Keel Block Vs. Casting - Different Size Test Bars

- 1 1/4 " Diameter Keel Block



Dimensions			
	Standard Specimen	Subsize Specimen	
Plate Type, 40 min [1,800 in.] Wide	Sheet Type, 13.5 min [3,150 in.] Wide	G min [0.280 in.] Wide	
mm [in.]	mm [in.]	mm [in.]	
G—Gauge length (Note 1 and Note 2)	280.0 ± 0.2 [8.93 ± 0.04]	50.0 ± 0.1 [2.800 ± 0.008]	25.0 ± 0.1 [1.000 ± 0.005]
W—Width (Note 3 and Note 4)	40.8 ± 2.0 [1,500 ± 0.102, -0.205]	12.5 ± 0.2 [500 ± 0.014]	6.8 ± 0.1 [270 ± 0.008]
T—Thickness (Note 5)	Thickness of material		
R—Radius of fillet, min (Note 6)	25 [1]	12.5 [0.500]	6 [0.250]
C—Crown length, min (Note 7, Note 8, and Note 9)	408 [16]	200 [8]	100 [4]
A—Length of reduced parallel section, min	225 [9]	57 [2.25]	28 [1.125]
B—Length of grip section, min (Note 10)	75 [3]	30 [1.2]	30 [1.25]
C—Width of grip section, approximate (Note 4 and Note 11)	68 [2]	29 [0.750]	19 [0.750]



8

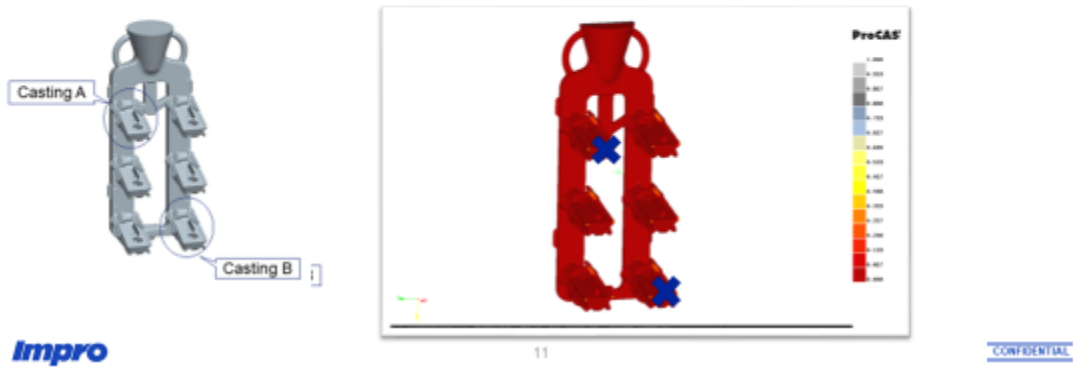
CONFIDENTIAL

**FIGURE 6**

Intrinsic variation occurrence within a cluster.

### Location Variation

Item	Tensile Rm/Mpa	Yield Rp/Mpa	Elongation A/%	Conclusion	Specification requirement
Casting A	514	307	25	OK	485-655 ≥250 ≥22
Casting B	521	310	27.7	OK	485-655 ≥250 ≥22



Figures 7, 8, 9, 10 Important to completely examine test bars which are going out for evaluation. We continued our intrinsic variation test with this fracture morphology exam, metallography, texture corrosion, X-ray and MPI, Surface Visual and straightness.

**FIGURE 7**

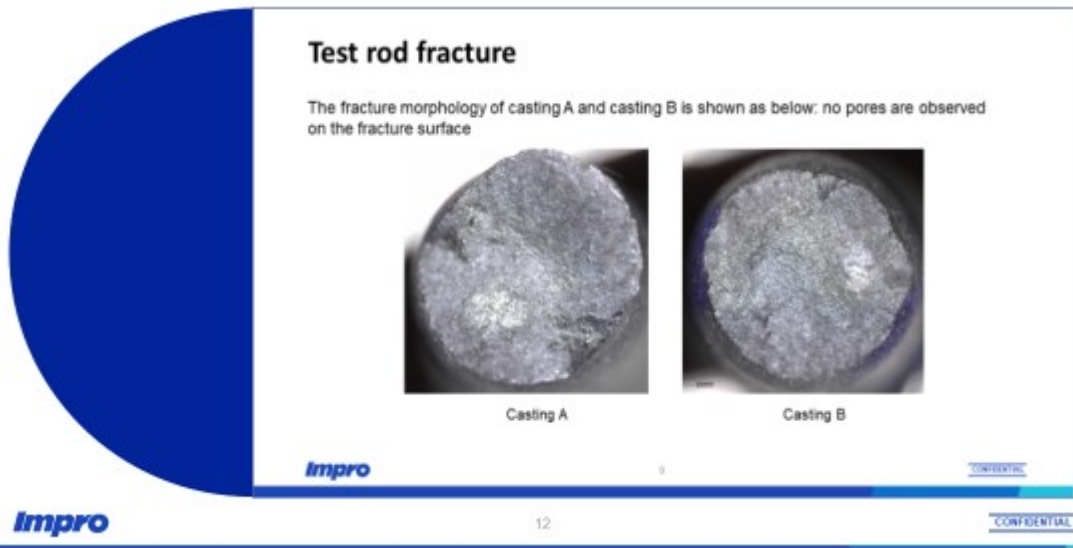
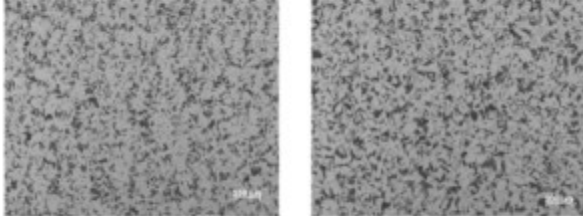


FIGURE 8

**Microscopic metallography**

The microscopic metallography of casting A and casting B is shown as below: the structure is ferrite pearlite with a uniform phase distribution.



Casting A                      Casting B

*Impro*                      10                      CONFIDENTIAL

*Impro*                      13                      CONFIDENTIAL

FIGURE 9

**Texture corrosion**

Proceed the texture corrosion of casting A and casting B sampling rods, the results all met the requirements of ASTM A703 level 4.



Casting A                      Casting B

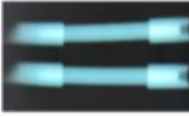
*Impro*                      11                      CONFIDENTIAL

*Impro*                      14                      CONFIDENTIAL

FIGURE 10

### X-ray and MPI check

The X-ray of casting A and casting B body sampling rods are both qualified.



X-ray photo of Casting A and casting B

The MPI of casting A and casting B sampling rods are both qualified.



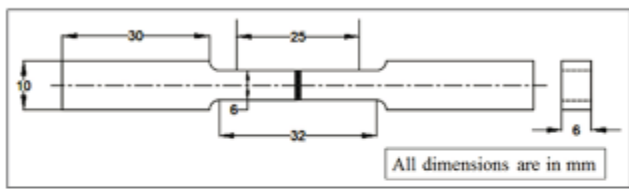

Casting A
Casting B

**Impro**
15
CONFIDENTIAL

FIGURE 11

Test bar surface conditions shall be defect free with no nicks, dents or notches.

## A Look Into Testing Effects



ASTM mechanical property specifications established from a near-perfect casting shape and an ideally gated keel block

The ASTM EB test bar came out of the soundest section near the lower portion of the keel block

Make certain the ASTM EB test bars are precisely machined with no knicks, dents or notches.

The ASTM EB test bar should be NDT'd-including straightness.

**Impro**
16
CONFIDENTIAL

**FIGURE 12**

Precise operation in the test bed; the extensometer, for example. Manufactured test machine accuracy factors into mechanical property accuracy, as well.

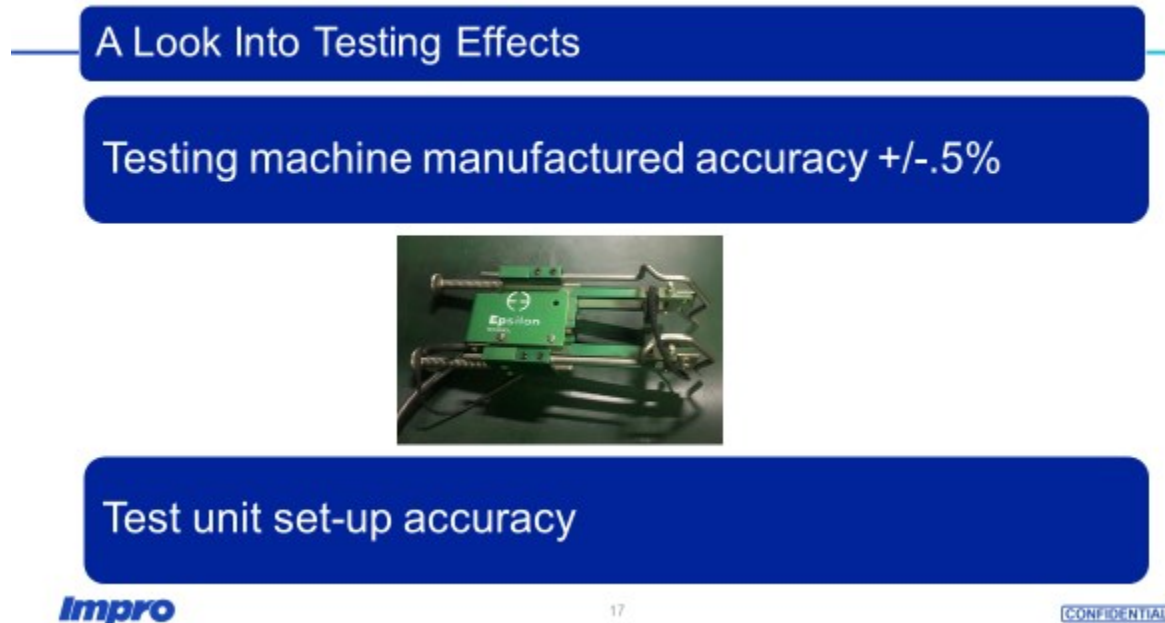


**FIGURE 13**

Centerline shrink can impact ultimate tensile.

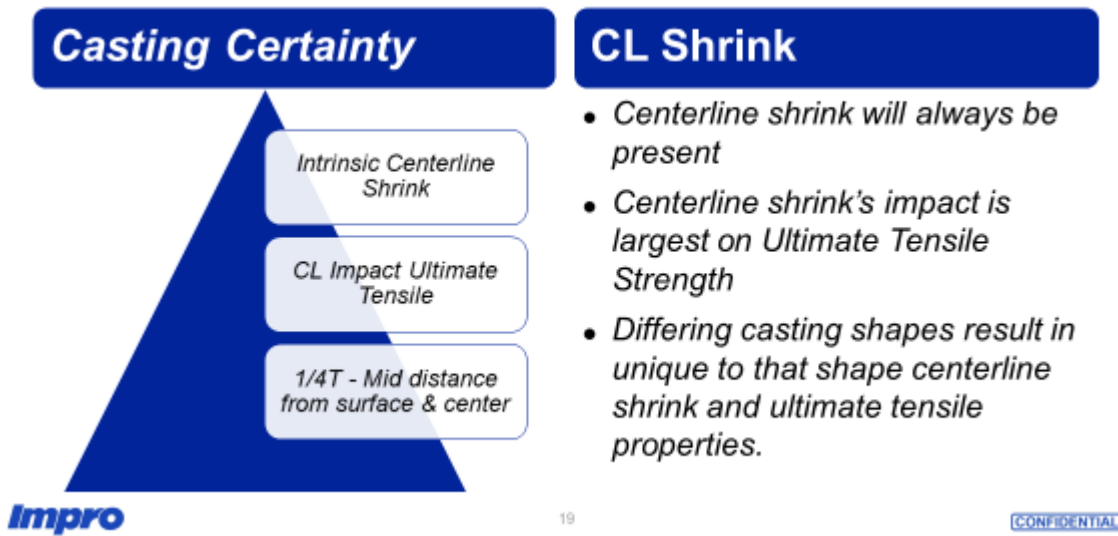


**FIGURE 14**

Shrinkage is the decrease in volume that occurs during the transition from liquidus to solidus. The reason it occurs is because the specific volume of alloys is highest in the liquid state.

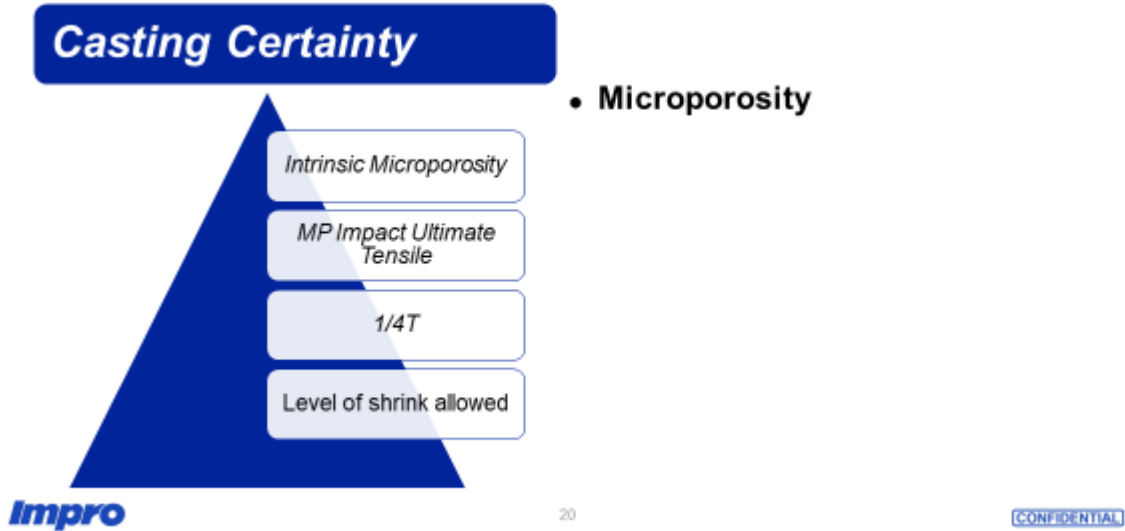


**FIGURE 15**

Example of an automotive casting showing microporosity typically in center sections.

**Example No.1**

Metallographic check in the direction of wall thickness



Fig 1: L=0.14031 mm  
Fig 2: L=0.41008 mm

(100X) the sum of all discontinuity areas of the whole analyzed section: 1.11%

**FIGURE 16**

Example of an automotive casting showing microporosity typically in center sections.

**Example No.2**

Metallographic check in the direction of wall thickness

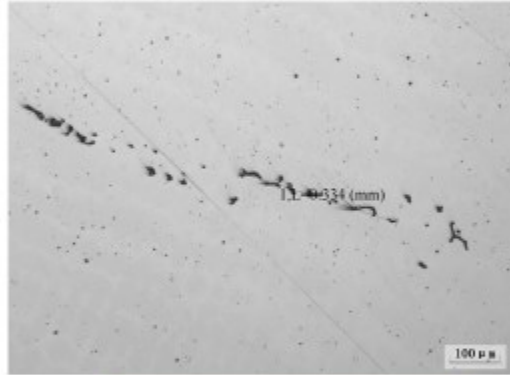


Fig 2: L=0.334 mm

(100X) the sum of all discontinuity areas of the whole analyzed section: 0.78%



CONFIDENTIAL

**FIGURE 17**

Example of an automotive casting showing microporosity typically in center sections.

**Example No.3**

Metallographic check in the direction of wall thickness

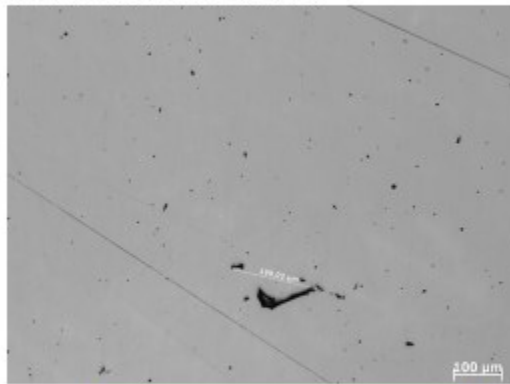


Fig 2: L=0.198 mm

(100X) the sum of all discontinuity areas of the whole analyzed section: 0.35%



CONFIDENTIAL

**FIGURE 18**

The Association of American Railroads, "Specification M-201-92..." shows that castings averaged lower properties compared with test bars.

**Casting vs. Test Bar Tensile Spec – 80%**

- The Association of American Railroads, "Specification M-201-92..."
  - Castings averaged 3% lower tensile versus test bars, in carbon steel
  - 6% less in elongation
  - 11% lower reduction of area.
  - In section 7.2.5 it is shown that machined from casting test bars are to meet 80% of the tensile and yield properties.